Study of Organic Semiconductors for Device Applications

Marco Stella

ADVERTIMENT. La consulta d'aquesta tesi queda condicionada a l'acceptació de les següents condicions d'ús: La difusió d'aquesta tesi per mitjà del servei TDX (www.tesisenxarxa.net) ha estat autoritzada pels titulars dels drets de propietat intel·lectual únicament per a usos privats emmarcats en activitats d'investigació i docència. No s'autoritza la seva reproducció amb finalitats de lucre ni la seva difusió i posada a disposició des d'un lloc aliè al servei TDX. No s'autoritza la presentació del seu contingut en una finestra o marc aliè a TDX (framing). Aquesta reserva de drets afecta tant al resum de presentació de la tesi com als seus continguts. En la utilització o cita de parts de la tesi és obligat indicar el nom de la persona autora.

ADVERTENCIA. La consulta de esta tesis queda condicionada a la aceptación de las siguientes condiciones de uso: La difusión de esta tesis por medio del servicio TDR (www.tesisenred.net) ha sido autorizada por los titulares de los derechos de propiedad intelectual únicamente para usos privados enmarcados en actividades de investigación y docencia. No se autoriza su reproducción con finalidades de lucro ni su difusión y puesta a disposición desde un sitio ajeno al servicio TDR. No se autoriza la presentación de su contenido en una ventana o marco ajeno a TDR (framing). Esta reserva de derechos afecta tanto al resumen de presentación de la tesis como a sus contenidos. En la utilización o cita de partes de la tesis es obligado indicar el nombre de la persona autora.

WARNING. On having consulted this thesis you're accepting the following use conditions: Spreading this thesis by the TDX (www.tesisenxarxa.net) service has been authorized by the titular of the intellectual property rights only for private uses placed in investigation and teaching activities. Reproduction with lucrative aims is not authorized neither its spreading and availability from a site foreign to the TDX service. Introducing its content in a window or frame foreign to the TDX service is not authorized (framing). This rights affect to the presentation summary of the thesis as well as to its contents. In the using or citation of parts of the thesis it's obliged to indicate the name of the author.

UNIVERSITAT DE BARCELONA

DEPARTAMENT DE FÍSICA APLICADA I ÒPTICA
Martí i Franquès 1, 08028 Barcelona

STUDY OF ORGANIC SEMICONDUCTORS FOR DEVICE APPLICATIONS

Marco Stella

Programa de doctorat: Tècniques Instrumentals de la Física i la Ciència de Materials

Bienni: 2004-2006

Tutor: Joan Esteve Pujol

Directors: Jordi Andreu Batallé, Joaquim Puigdollers Gonzalez

Memòria presentada per optar al grau de Doctor
Barcelona, desembre 2009

Alla mia famiglia

This work has been carried out in the Solar Energy Group of the Laboratory of Thin Film Materials of the Department of Applied Physics and Optics of the *Universitat de Barcelona*. The Solar Energy Group is a member of the *Xarxa de Referència de Materials Avançats per a l'Energía* (XaRMAE). The present work has been supervised by Dr. Jordi Andreu Batallé (*Universitat de Barcelona)* and Dr. Joaquim Puigdollers Gonzalez (*Universitat Politècnica de Catalunya*) in the framework of the project ENE2004-07376-C03-01 of the Spanish Government and with the support of a pre-doctoral grant from the Spanish Government (Beca FPI).

Table of contents

Acknowledgments

After about five years of work on this thesis I would like to thank all the people without the help of which it would have not been possible:

First of all, I am grateful to Dr. Ignacio Juvells Prades, Director of the Department of Applied Physics and Optics at the University of Barcelona, for accepting me as a Ph.D. student to participate in this interesting work and for his kindness.

I thoroughly acknowledge Dr. Jordi Andreu and Dr. Joaquim Puigdollers, co-directors of this thesis, for involving me in this interesting research, for their essential help and for their friendship.

I also want to thank Dr. Joan Bertomeu, Dr. José Miguel Asensi, Dr. Cristobal Voz, Dr. Joan Esteve and Dr. Arturo Lousa for their hints and help in difficult moments, to Dr. David Soler for being my PDS master and Dr. Marta Fonrodona for help and for introducing me to the secrets of Eindhoven.

I acknowledge Xavier Alcobé Ollé and his colleagues of the laboratory of x-ray diffraction of the *Serveis Cientificotècnics* for the X-ray diffraction measurements.

I express my gratitude to Prof. René Janssen and Dr. Martijn Wienk for accepting me in the Group of Molecular Materials and Nanosystems at the *Technische Universiteit Eindhoven* (TU/e) for three months during which I have really learned a lot and to Dr. Dirk Veldman for helping me with the work I developed there.

Special thanks go to Dr. Jordi Escarré, Fernando Villar, Fredy Rojas and Rubén Roldán, a group of colleagues that during these years have become friends. It would be nice if we could keep in touch in the future.

I acknowledge the members of the Jury, for accepting our invitation and reading this manuscript.

Finally, I want to thank Anabel and Adrià for tolerating to have only half a husband/father for many months.

OUTLINE OF THIS THESIS

This thesis is focused on the characterization of organic semiconductors for their application in electronic devices and is the result of the collaboration between the Solar Energy Group of Physics Faculty of the University of Barcelona and the Group of Research in Micro and Nanotecnologies (MNT) of the Electronic Department of the Polytechnic University of Catalunya (UPC). Despite the fact that organic semiconductors are long known, much work still remains to be done in order to completely understand the mechanisms regulating their function. Both research groups involved in this work have broad experience in the fields of inorganic semiconductors and electronic devices, among which silicon photovoltaic technology has always had a central role. The great knowledge accumulated during the years in these fields has been employed here to study this relatively novel category of semiconductors and to fabricate organic devices. This thesis started in 2004 and has been developed in the framework of the project "New Photovoltaic Technology Based on Silicon (NTS)" (ENE2004-07376-C03-01) financed by the Spanish government. The present work concerns the optical characterization of some semiconductors with the aim to discover parameters of great importance. Special attention will be paid on the study of the stability of these materials, given that it is a fundamental requirement for realizing electronic devices. Finally, the first electronic devices fabricated with some of the materials here treated will be presented.

Chapter 1. Introduction

In the first chapter the technological interest of the research on organic semiconductors as an interesting alternative to silicon will be discussed. The perspective to obtain flexible and lightweight solar cells, fabricated by cheap techniques justifies the great effort that the scientific community is putting in the organic technology.

Chapter 2. General review on organic semiconductor theory

This chapter is dedicated to a brief description of the characteristics that make an organic material a semiconductor. The mechanisms that regulate charge carriers generation and transport in the materials are introduced as they are currently accepted by the scientific community. The experimental aspects that are still not completely clear will be also briefly discussed. This section is concluded by a short description of the materials studied in this work.

Chapter 3. Technological aspects

The third chapter is focused on the technological aspects related with the doping mechanisms and the current photo-generation in organic cells. The deposition techniques that can be employed for these materials will be briefly described. Eventually, a description of the structure evolution that the organic photovoltaic devices have suffered in the last two decades will be also given.

Chapter 4. Experimental

This section is about the equipments and the experimental techniques that have been used in this work. Thermal vacuum evaporation is the technique employed to deposit organic thin films and will be briefly described in this chapter together with the characterisation techniques employed to study the materials and the devices. For the materials, optical techniques like Photothermal Deflection Spectroscopy (PDS) and Optical Transmission and other techniques as X-ray diffraction have been employed. The devices have been studied by the basic I-V characterisation.

Chapter 5. Material analysis

The fifth chapter is dedicated to the characterisation of five organic semiconductors deposited in thin film on glass. The materials under study are two *p*-type semiconductors, copper phthalocyanine (CuPc) and pentacene, and three *n*-type semiconductors, fullerene (C_{60}), Perylene-3,4,9,10-tetracarboxylic dianhydride (PTCDA) and *N,N*-ditridecyl-3,4,9,10-perylenetetracarboxylic diimide (PTCDI-C_{13}). Fundamental parameters like their optical gap and the Urbach energy will be calculated and their structural order will be evaluated by X-ray Diffraction (XRD). The effects of degradation on the optical properties of the materials will be also investigated.

Chapter 6. Bulk heterojunctions

A systematic study, similar to the one performed on pure materials, has also been done on co-deposited materials with all the possible combinations between the *p*-type semiconductors and the *n*-type ones. Their optical parameters and structural order have been investigated, along with their response to the degradation processes. In the final part of the chapter, the results obtained by annealing treatments will be described.

Conclusions

In this section the general conclusions about all the work will be presented together with a description of the technical aspects that need further improvement, in order to be able to obtain better organic devices.

Appendix A

The first organic devices that have been fabricated in our laboratories are presented in this chapter. Thin film transistors (TFTs) have been studied using PTCDI-C_{13} as a semiconductor. Moreover, Schottky *p*-type diodes have been fabricated by using CuPc.

CHAPTER 1

INTRODUCTION

The discovery of electrical conductivity in organic materials, a category of materials that previously was thought to be exclusively isolating, opened a new fascinating research field. In 2000 the Nobel Prize in Chemistry was awarded to Alan J. Heeger, Alan G. McDiarmid and Hideki Shirakawa for "The discovery and development of conductive polymers"[1]. Their experiments performed in the 70s with *trans*-polyacetylene revealed that it was possible to determine the conductivity of this covalent organic material by exposing it to vapours of chlorine, bromine or iodine[2]. Nevertheless, previous studies conducted by Weiss and co-workers in the early 60s had already demonstrated electrical conductivity in iodine-doped oxidized polypirrole[3].

Organic materials show mechanical and chemical properties that radically differentiate them from inorganic ones and that justify the great effort put into the research on their possibilities as semiconductors and conductors for device applications. Nowadays, organic semiconductors have found commercial application in organic light-emitting diodes (OLEDs). An 11-inch television, with a thickness of 3 mm, based on OLED technology is currently available from Sony, demonstrating that organic technology will be able to compete, in the near future, with the ones of liquid-crystal and plasma ones. Nevertheless, the stability of such devices, when exposed to high current densities over extended time, still remains an important issue to deal with. Thin film transistors (TFTs) and organic photovoltaics (OPV) seem to require more time to jump from research to commercialization phases. In any case, the former have demonstrated good qualities for display applications[4] while, regarding the latter, companies as Konarka and Solarmer Energy Inc. have risen with the aim of commercializing organic photovoltaic technology both in the field of power generation and gadgets production.

1.1 Overview on photovoltaic technology

In the next paragraph the state of the art of photovoltaic technology will be briefly presented with the aim to illustrate the evolution that PV technology has suffered during the last decades. The

actual efficiency records are also given, according to the last version of "Solar Cells Efficiency Tables" (version 33) published in 2009 by Martin A. Green and co-workers[5].

Monocrystalline silicon

Single crystal silicon solar cells are the most mature of all photovoltaic technologies that are currently available on market. Many advances have been achieved by investigating materials and device structure that allowed to obtain 25% efficiency, one of the highest values. The main drawback of such technology is the high cost of high quality monocrystalline silicon, which is obtained by means of techniques like Czochralski, where a crystal is put in contact with liquid silicon, causing its crystallization. The forming solid is extracted from the liquid and rotated very slowly and, as a result, a solid cylinder is obtained which then is cut into wafers.

Multycrystalline silicon

A low cost alternative to monocrystalline silicon, polycrystalline silicon is obtained by pouring the liquid material into a mold. During solidification, crystallites, separated by amorphous grain boundaries, are formed. Also in this case the material is cut into wafers. The current efficiency record for multycrystalline solar cells is 20.4%.

Amorphous silicon

Amorphous silicon can be deposited by thin film techniques like Plasma Enhanced Chemical Vapour Deposition (PECVD) and Hot Wire Chemical Vapour Deposition (HWCVD) resulting in important savings in material and production costs. The higher density of defects in the completely unordered structure of the semiconductor makes the efficiency of this technology sensibly lower than the ones of the previous cases, resulting in values of 9.5%. A great advantage of such technology is the possibility to fabricate flexible modules, few examples of which are already available on market.

III-V materials

Notable results have been obtained by using a combination of materials belonging to groups III and V in the periodic table of the chemical elements. One important example of such technology is gallium arsenide (GaAs) with an efficiency of 26.1%, while cells made of indium phosphide (InP) have reached efficiency values of 22.1%. GaAs cells are fabricated by Metal Organic Chemical Vapour Deposition (MOCVD) and in the beginning were developed especially for space applications due to their high cost.

Thin film chalcogenides

Absorber materials based on other, in some cases more complex, combinations of materials have also been studied. Thin film CIGS ($Cu(In:Ga)(S:Se)_2$) cells have reached efficiency values of 19.4%, while cadmium telluride (CdTe) cells values of 16.7%. Flexible modules can be obtained by proper selection of substrate and barrier materials.

Multijunction cells

Devices composed of junctions between more than one cell have been extensively studied in order to search for alternatives to obtain efficiency improvement with the already known technologies. The concept is based on taking advantage of the differences between the optical gaps of the different semiconductors, resulting in a more efficient absorption of the solar spectrum. GaInP/GaAs have reached efficiencies of 30.3%, while GaInP/GaAs/Ge cells values of 32.0%.

Photochemical cells

Radically different from the other photovoltaic structures, Dye Solar Cells (DSC) belong to a category of devices that employ organic materials. The active layer is constituted by porous titania (TiO_2), a dye and an electrolyte. Such cells have reached efficiencies of 10.4% and are being introduced in the market by some important companies, principally in the field of little portable modules. The fabrication process is completely different from the ones employed for fully inorganic technologies making use of techniques like screen printing for the TiO_2, and chemical bath for the dye. Two drawbacks that present such type of solar cells are the high sintering temperatures (450 ºC) needed to obtain porous TiO_2 and the presence of a liquid electrolyte which requires sealing the device. Currently solid electrolytes are being developed and commercialized.

Organic semiconductors

The newest category of solar cells is the one that includes small molecule, polymeric and hybrid organic/inorganic devices. Despite the low efficiency value obtained till now of 5.15% with a polymeric cell and the stability problems, this kind of solar cells presents several advantages like easy processability, flexibility, lightweight and low production cost. Organic Photovoltaics technology (OPV) will be described more in detail in chapter 3.

The results considered here have been obtained under the global AM1.5 spectrum (1000W/m2) at 25ºC (IEC 60904-3: 2008, ASTM G-173-03 global). With organic solar cells, even better results, than the ones listed, have been claimed by the company Solarmer Energy, Inc., which announced a power conversion efficiency of 7.9%[6]. This result has been certified by the National Renewable Energy Laboratory (NREL) recently.

1.2 Why investigate a new photovoltaic technology?

OPV is the youngest existing photovoltaic technology. The relatively low efficiency values demonstrate that much work still remains to be done to improve performance but this technology begins to be attractive for the market, especially if we consider the power generation target. Such performances can be ascribed to several issues that are currently object of intensive research. Among all of these factors, the low charge carrier mobility (10^{-8}-10^{-2} $cm^2V^{-1}s^{-1}$)[7] and the short exciton diffusion length (50-100 nm)[8,9] are probably the most important. Nevertheless, mobility values similar to the ones of hydrogenated amorphous silicon have been observed for pentacene[10,11] (0.7 $cm^2V^{-1}s^{-1}$), a small molecule *p*-type organic semiconductor.

If we do not limit our view to only efficiency, there are many other aspects that contribute to make organic semiconductors potentially competitive with inorganic ones:

1. The device fabrication techniques offer great variety, flexibility and, in some cases, low cost processes. Moreover, they allow to easily scale-up the production to great surface making this technology potentially interesting for the industry.
2. The possibility to easily obtain flexible and lightweight modules gives organic photovoltaics good properties of adaptability and integration.
3. The great varieties of materials available and of new materials that can be synthesized justify the expectance for a great improvement in electrical properties and stability.

1.3 Natural processes of solar energy storage

Chlorophyll-based photosynthesis is an extremely robust and efficient natural process in which light energy is captured and stored by an organism, and the stored energy is used to drive cellular processes. The conversion efficiency from photonic energy to chemical energy of such process has

been evaluated around 20-25%[12]. A natural reference for the photovoltaic process in OPV, the photosynthesis process can be divided into four steps[13]:

1. Light absorption and energy delivery by antenna systems
2. Primary electron transfer in reaction sites
3. Energy stabilization by secondary processes
4. Synthesis and export of stable products

To compare photosynthesis and photovoltaic processes the first two steps, dedicated to photon capture and charge carriers generation, are the ones to be considered, since the second ones are constituted by chemical processes. In the first step photons are captured by the antennas: a group of pigments that absorb light and transmit its energy through a cascade energy transfer process to the reaction center. The energy migrates from molecule to molecule, from the exterior molecules to the core, favoured by good relative orientation of the transition dipole moments of donor and acceptor and by a good spectral overlap of the two pigments involved in the step. In times of picoseconds the energy can be transferred through a distance of several tens of angstroms. In the second step the energy is transferred to the reaction center in which the separation between electrons and holes takes place. The electrochemical potential that is generated this way is the force which makes the chemical reactions necessary to drive cellular processes to be completed. An interesting aspect is that the photosynthetic systems are provided with protections from degradation that allow them to work for a very long time without suffer any damage. The carotenoids are pigments that quench undesired and extremely reductive excited states (triplet states and singlet oxygen) that can form in the system, preventing the pigments from photooxidative damage.

The existence of very complex and efficient natural photosynthetic processes suggests that behind OPV science there is something more that simply realizing photovoltaic technology by substituting inorganic semiconductors with organic ones. Several aspects of the photosynthetic mechanisms are in common with the ones that regulate the organic photovoltaic process, making, once more, nature an example for us.

CHAPTER 2

GENERAL REVIEW ON ORGANIC SEMICONDUCTORS THEORY

Organic semiconductors can be divided into two categories: polymers and small molecule materials. From a chemical point of view there are big differences between these two kinds of materials and this is reflected also in technological aspects. Polymeric macro-molecules are constituted by the repetition of a fundamental unit, the monomer, and are soluble in organic solvents, so they can be treated in liquid state. The materials belonging to the second category are in some cases named *molecular materials*, are composed of small molecules and can be divided into two sub-groups: pigments, not soluble in organic solvents, and dyes, which are soluble. As a result of their chemical properties, polymers can be solution processed, for example being spin-coated from a solution of appropriate organic solvents, while little molecule materials mostly must be thermally evaporated and in some cases can be solution processed. In this work thermally evaporated molecular materials have been studied, nevertheless in this chapter a general introduction to all kinds of organic semiconductors will be given, beginning with a description of their structures and properties (paragraph 2.1), followed by an introduction to the working principles of these materials (paragraph 2.2). To think about organic semiconductors starting from inorganic bases is a very common procedure, but it is also often confusing: concepts like *n* and *p*-type semiconductors, energetic bands model and Fermi energy level are slightly different concepts in the organic case. A true comprehension of this relatively novel category of semiconductors requires keeping into account other concepts like solitons, polarons and excitons and non-linear optical properties, only to make a few examples.

At the end of this chapter (paragraph 2.3) a description of the materials studied in this work will be presented, with their molecular structure and their optical properties.

2.1 Materials and their chemical properties

Polymeric materials are formed by large, weighty molecules, constituted by the repetition of a basic unit called *monomer*. Like all organic compounds, organic semiconductors are based on carbon atoms, which, in the case of polymers, form the main chain. Other elements or functional groups can be attached to the backbone and influence its chemical properties. Each carbon atom is covalently bonded to other carbon atoms and by partially ionic interactions to atoms of other elements.

The electronic configuration of C is He[$2s^2 2p^2$], which means that two of the four valence electrons, the *p* ones, are available to form chemical bonds. Such configuration would give raise to two equivalent bonds, while experimental experience shows that carbon atoms are able to make four. To explain such behaviour, the theory of valence orbitals hybridization is employed, which assumes that one *s* electron is promoted to the last free *p* orbital, thus obtaining four singly occupied valence orbitals; than the remained *s* and some or all of the *p* orbitals are mixed together to obtain new equivalent orbitals. As a result, the hybridized orbitals are a linear combination of the initial ones. The number of *p* orbitals used in the hybridization process defines the type of polymer and many of its chemical and structural properties. Three hybridizations are possible: sp^3, sp^2 and sp^1, where the superscript refers to the number of *p* orbitals involved in the hybridization. In Figure 2.1 a scheme explains the concept of the hybridization:

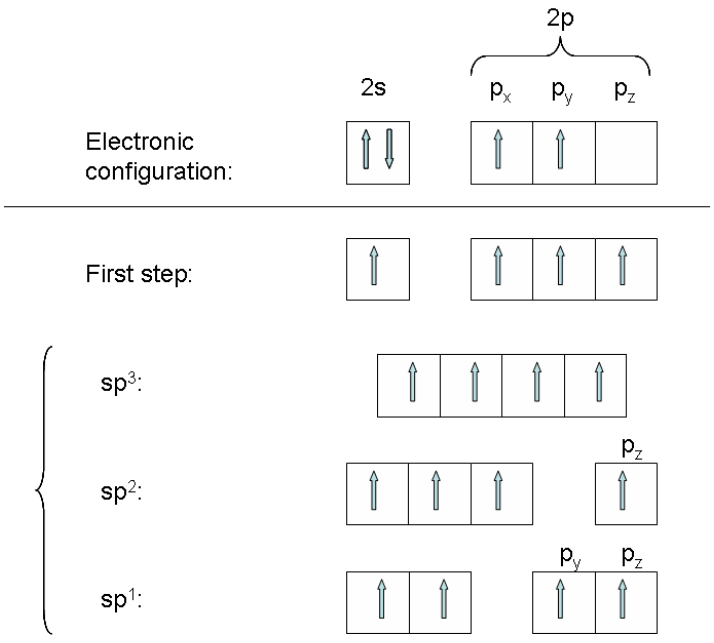

Figure 2.1. Types of hybridization of the valence orbitals in a carbon atom.

In the case of hybridization sp^3 we obtain four singly occupied orbitals able to make an equal number of σ bonds, with an electronic cloud distributed around the bond axis, obtaining a tetrahedral structure. In Figure 2.2 the structure of methane is shown as an example:

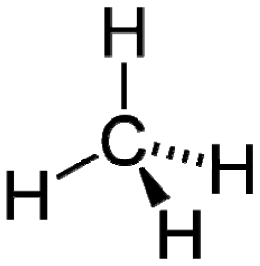

Figure 2.2. The methane molecule has tetrahedral geometry with a carbon atom in the centre and four hydrogens at the vertexes.

Polymers based on sp^3 hybridization contain only single bonds along its backbone. Materials belonging to this category can not have semiconductor properties because to employ a σ-electron in conduction means breaking the bond in which it was involved and decompose the material. Moreover the energy needed to promote an electron from a bonding σ-orbital to an anti-bonding σ^*-orbital is at least 6 eV[14].

The sp^2 hybridization is the condition to have double bonds in the molecule structure: three electrons from carbon are employed to form σ bonds; while the fourth, no hybridized, one is employed to give a π-bond. In Figure 2.3 the structure of ethylene is presented as en example:

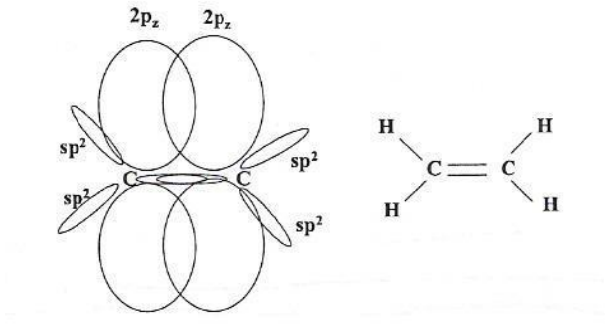

Figure 2.3. Carbon atoms are bonded with a double bond.

The π-electron is delocalized between the two atoms, above and below the molecule axis. An important characteristic of the double bond is that it is shorter than a single one: while the former is 1.34 Å long, the latter reaches the value of 1.54 Å[15].

Where sp^1 hybridization is adopted, triple bonds, with a length of 1.21 Å[15], are constituted as it is shown in the case of acetylene molecule in Figure 2.4:

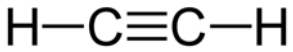

Figure 2.4. Acetylene molecule.

Polymeric semiconductors are based on sp^2 hybridized carbon atoms and are also called *conjugated polymers* because of the alternation of single and double bonds along their backbone. Similarly, such a structure can be found in dyes and pigments where a net of cyclic elements composes the entire molecule. In Figure 2.5 and Figure 2.6 the structure of some polymers and molecular materials is presented:

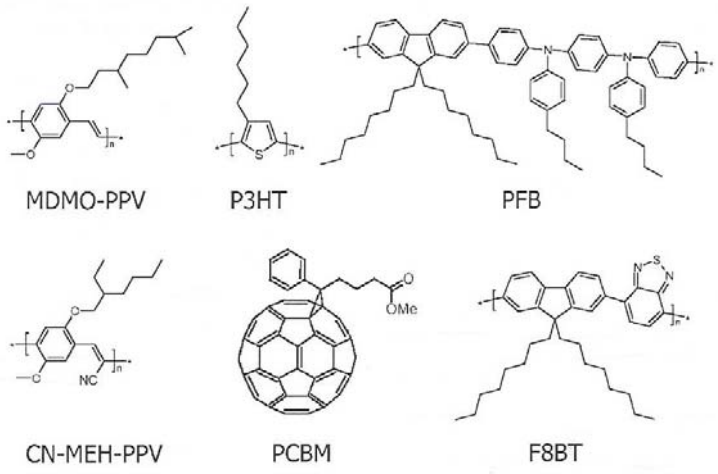

Figure 2.5. Examples of polymeric semiconductors.

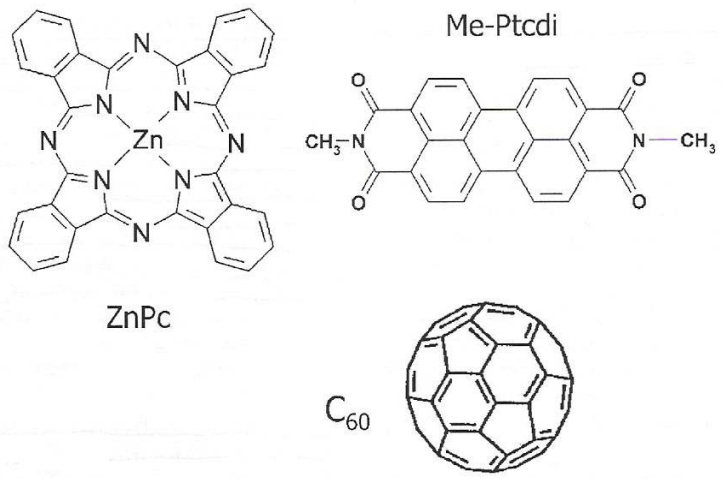

Figure 2.6. Examples of small molecule materials.

The overlap of the p_z wavefunction of each carbon atom with the one from the nearest neighbour is what allows to have electron delocalization along the molecule backbone. As it can be seen in Figure 2.5, PCBM ([6,6]-phenyl C_{61} -butyric acid methyl ester, in) is an exception among polymers because it is formed by a C_{60} molecule (fullerene, in Figure 2.6) with a side chain attached to the sphere. The lateral chain serves to make fullerene soluble in organic solvents and this material in many cases it is not considered properly a polymer.

Both polymers and molecular materials have in common an extended delocalized π-electron system, which allows to transport photogenerated charge carriers[16]. The molecule of benzene, represented in a few equivalent ways in Figure 2.7, is a simple example of such electronic structure:

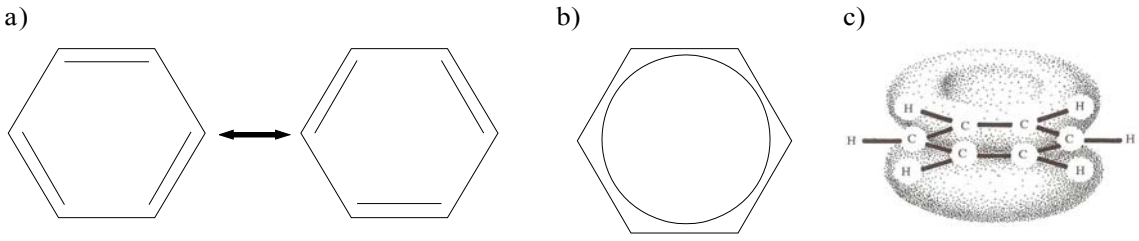

Figure 2.7. Different ways of drawing the structure of the benzene molecule: a) resonance structures; b) the circle that represents the delocalized electrons; c) the electronic cloud distributed above and below the molecule plane.

The benzene molecule can oscillate between two equally stable ground states due to the possibility to interchange the position of single and double bonds. The structure with a circle drawn

in Figure 2.7-b resumes schematically the delocalization of the 6 electrons which form an electronic cloud distributed above and below the molecular plane (Figure 2.7-c).

Organic semiconductors are divided into *n*-type and *p*-type categories, like the inorganic ones. Nevertheless, as it will be seen in the next chapter, the doping mechanisms are substantially different from the ones employed in inorganic materials, like silicon, so a direct comparison with them at this level could be misleading.

MDMO-PPV (poly[2-metoxy-5-(3',7'-dimethyl-octyloxy)-p-phenylene vinylene]), P3HT (poly-3-hexylthiophene) and PFB (poly(9,90-dioctylfluorene-co-bis-N,NO-(4-butylphenyl)-bis-N,NO-phenyl-1,4-phenyldiamine)) act as *p*-type semiconductors; while CN-MEH-PPV (poly(2-methoxy-5-ethylhexyloxy-1,4-phenylenecyanovinylene)), PCBM and F8BT poly(9,9-dioctylfluorene-co-benzothidiazole) act as *n*-type semiconductors. Regarding the pigments shown in Figure 2.6, ZnPc (zinc phtalocyanine) is a *p*-type semiconductor, while C_{60} (fullerene) and Me-Ptcdi (N,N′-dimethylperylene-3,4,9,10-dicarboxyimide) are *n*-type semiconductors.

Given the structural properties of these materials, it is possible to define which conditions are necessary in order to obtain a good organic device:

- the presence of a conjugated system
- in a solid, the π-electron clouds should be the most overlapped possible
- good thin film structural properties
- chemical purity
- material stability

The first condition has been discussed above; the second and the third ones are more concerning thin film properties, the deposition technique and its parameters: the more compact is a structure, the more overlapped are the electron clouds and better the charge transport. Similarly, the more ordered is a micro-structure, the better the electric properties in the thin film. To perform further material purification is necessary, in many cases, in order to obtain good devices[7,17]. Material stability against exposure to atmosphere and light is also an important issue in research on photovoltaic technology. The reactivity of the excited species generated in organic semiconductors could represent a problem, especially in the case of *n*-type semiconductors[18,19].

2.2 Basic working principles

In this section some fundamental concepts about organic semiconductors will be introduced. A theoretically deep discussion about this topic is not an aim for this thesis, but an intuitive explanation of the band structure and the primary excitations in organic semiconductors will be given. Even if only pigments have been used in this work, both polymers and molecular materials will be briefly discussed as a general review. It is worth taking into account that many details are still under discussion but some text can be found where an introduction to such important concepts is given[20,21,22].

On one side, according to some reference[20], it is convenient to divide organic semiconductors in three categories: polymers with degenerate ground state, polymers with non-degenerate ground state and small molecule materials. The nature of the primary stable excitations, (solitons, polarons, bipolarons and excitons) changes as a function of the material.

On the other side, another view of the problem suggests that in all types of organic semiconductors exposed to illumination, excitons are first created, which are then dissociated into separated charge carriers (for example polarons). The difficulty in interpreting some experimental results has contributed to the uncertainty about such an important distinction. Nevertheless, the charge generation mechanism through the formation of excitons is the most commonly cited in the literature dedicated to applied research on organic photovoltaics.

2.2.1 Molecular orbital theory

In presence of molecular systems the model of the molecular orbitals is employed. According to such model, when two atoms with the same energy are brought to interact, their energies are splitted, creating two different molecular energy levels: one with lower energy than the original ones and another with higher energy. Such new molecular orbitals are impossible to calculate exactly for most molecules and so an approximation called *Linear Combination of Atomic Orbitals* (*LCAO*) is used for that purpose. According to LCAO, in proximity of an atom the molecular orbital can be considered as the one of the isolated atom. In the case of two hydrogen atoms, the wavefunction would be the following:

$$\Psi_{\pm} = \Psi_{1s}(A) \pm \Psi_{1s}(B) \tag{2.1}$$

$$\text{with } \Psi_{1s}(A) = \sqrt{\frac{1}{\pi a_0^3}} \cdot e^{-r_A / a_0} \tag{2.2}$$

where A and B are the atoms and r_A the distance between electron and atom A. The wavefunction for atom B is equal to (2.2) but with r_B as the distance between electron and atom. By linearly combining the atomic wavefunctions in (2.1), two molecular orbitals have been obtained: the *bonding orbital* (Ψ_+) and the *anti-bonding orbital* (Ψ_-).

In Figure 2.8 the amplitude of the atomic orbitals and of the molecular ones is depicted. The sum of the atomic orbitals gives the bonding molecular orbital with an electron density higher than zero in between the two nuclei. Such configuration keeps the atoms bound and is energetically favourable since its energy (E_+) is lower than the one of the isolated atomic orbitals. On the contrary, the difference between the atomic orbitals gives the anti-bonding molecular orbital, with zero electron density in the centre between the nuclei. This configuration is unfavourable for the molecule stability since its energy (E_-) is higher than the one of the isolated atomic orbitals.

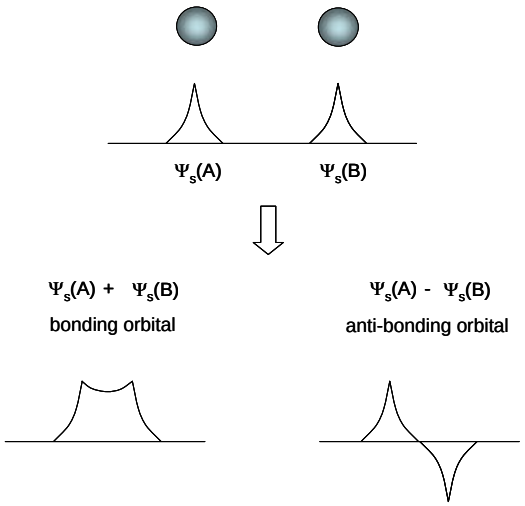

Figure 2.8. 3D representation and wavefunction amplitude of the atomic orbitals (upper part in the figure) and the molecular orbitals (lower part).

In Figure 2.9 the generation of molecular orbitals energetic levels is shown:

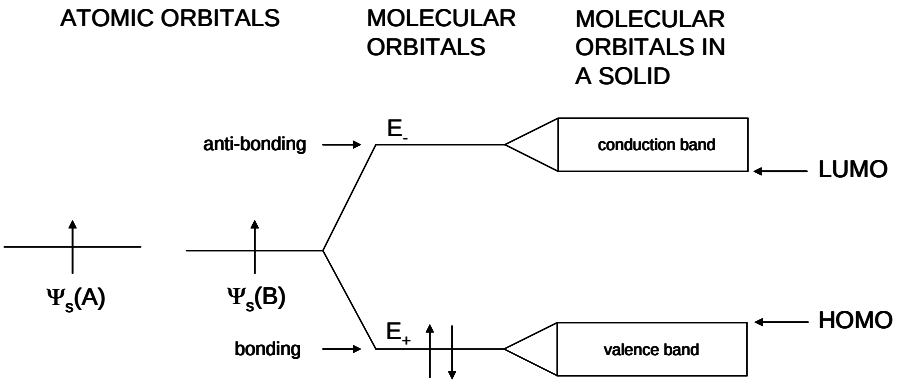

Figure 2.9. Scheme of the energetic levels of two isolated atoms, a biatomic molecule and a solid.

The energies of the two molecular orbitals are the followings:

$$E_{+} = \frac{\beta - \gamma}{1 - \alpha}$$
$$E_{-} = \frac{\beta + \gamma}{1 + \alpha} \qquad (2.3)$$

where β is the *coulombic integral*, which represents the energy that the electron has on the isolated atoms, γ is the *exchange (or resonance) integral*, which represents the interaction between the electrons, and α the amplitude of the wavefunction.

Since in the example depicted in the above figure there are two electrons (one per atom), both of them occupy the bonding molecular orbital, which has the lowest energy, assuming opposite spin. A third electron should begin to occupy the anti-bonding level and, in presence of a fourth, the total molecular energy would not be lower than the sum of the ones of the isolated atoms and the molecule would not be energetic favourable. In fact helium atoms (He), which have two valence electrons, are more stable in their atomic form. In the case of a solid composed of many molecules, the superposition of all of the molecular orbitals, interacting between them, results in a farther splitting (see bands in Figure 2.9) with the appearance of bands. The highest occupied molecular orbital in the valence band is defined as *HOMO* and the lowest unoccupied molecular orbital in the conduction band is defined as *LUMO*. The difference between HOMO and LUMO corresponds to the *energy gap* (E_g).

2.2.2 Polyacetylene: band structure and primary excitations

Polyacetylene is a polymer with two possible structures represented in Figure 2.10: *trans*-polyacetilene and *cis*-polyacetilene. Only the first one has semiconducting properties and it is a good starting point in order to understand the semiconducting properties of polymers as it was the first one to be studied.

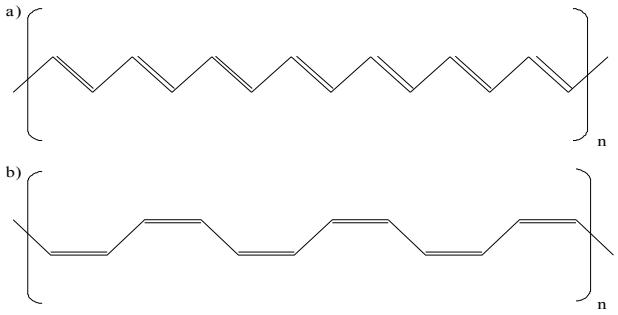

Figure 2.10. Structure formulas of a) *trans*-polyacetilene and *cis*-polyacetylene.

Considering the structure of *trans*-polyacetylene, every carbon atom gives one p_z electron to form the π-band. The band would be half-filled and the material should be a metal, but experimental evidences demonstrate that polyacetylene is a semiconductor with a gap of more than 1.5 eV. The real properties of this material are due to the fact that it undergoes structural distortions due to a phenomenon called *Peierls instability*[23], which consists in a dimerization of the molecule. Peierls instability has a periodicity of $\Lambda = \pi/k_F$, where k_F is the Fermi wave-vector. With a half-filled π-band we have $k_F = \pi/2a$ and, as a result of the Peierls distortion, the basic unit is not $(CH)_x$ but $(\text{-HC=CH-})_x$, i.e. that the unit cell is doubled: dimerization. Such dimerization is represented schematically in Figure 2.10 as an alternation of single and double bonds. The half-filled band is split into a full-filled π-band, similar to the valence band in inorganic semiconductors, and an empty π-band, similar to the conduction band.

In general, more than two π-bands are present and their number depends on the number of carbon atoms composing the repeat unit[14]. In the case of polyacetylene, as a result of the dimerization we have two carbon atoms and two π-bands indicated as π and π^*.

To describe polyacetylene the SSH Hamiltonian, from Su, Schrieffer and Heeger theory, has been proposed starting from two assumptions:

1. The π-electronic structure can be treated in tight-binding approximation which states that the bands have a width of W = 2*zt*, where *z* is the number of nearest carbon atoms neighbours and *t* the transfer integral. In the case of polyacetylene, *z* equals 2, while for *t* a value of 2.5 eV is taken. As a result, and keeping into account that we have two bands, the band width is W ~ 5 eV, for each one.
2. The molecular chain is coupled to the local electron density through the length of the chemical bonds between carbon atoms.

Single and double bonds are constantly interchanged and this interchange introduces a perturbation in the structure that propagates as a particle: the soliton.

A complete description of the theory is behind the scope of this thesis, so only the conclusions will be presented here. A more detailed dissertation is given by A.J. Heeger and co-workers[22].

The system continuously oscillates between the two possible configurations and around an equilibrium value for the bonds length. This factor is introduced in the Hamiltonian in the form of a hopping integral as follows:

$$t_{n,n+1} = t_0 + \alpha\left(u_{n+1} - u_n\right) \tag{2.4}$$

where u_n is the displacement from equilibrium position of the nth carbon atom. This term couples the electronic states to the geometry of the molecule and expresses the interaction between electron and phonon. The final form for the SSH Hamiltonian is than as follows:

$$H_{SSH} = \sum_{n,\sigma}\left[-t_0 + \alpha\left(u_{n+1} - u_n\right)\right]\left(c^{+}_{n+1,\sigma}c_{n,\sigma} + c^{+}_{n,\sigma}c_{n+1,\sigma}\right) + \sum_n \frac{p_n^2}{2m} + \frac{1}{2}K\sum_n\left(u_{n+1} - u_n\right)^2 \tag{2.5}$$

where p_n are the nuclear momenta, u_n the displacements from equilibrium, *m* is the carbon mass, *K* is the effective spring constant, $c^{+}_{n,\sigma}$ and $c_{n,\sigma}$ are the fermion creation and annihilation operators for site *n* and spin σ. The system undergoes a spontaneous breaking of the symmetry, the Peierls distortion, and the total energy is minimized for $|u_n| > 0$. So we can use the mean-field approximation as follows:

$$u_n \rightarrow \langle u_n \rangle = (-1)^n u \tag{2.6}$$

Within such approximation it is possible to calculate the value u_0, which minimizes the energy, using equation (2.6). Considering that the energy is minimized for both u_0 and $-u_0$ values, there are two possible configurations, depending on the position of the double bonds, and polyacetylene has a twofold degenerate ground state.

The energy of the system is depicted in Figure 2.11. The two states can be seen as two different phases, phase *A* and phase *B*, equal in energy. The excitation of the polymer forces it to change from one phase to the other one. The primary excitation in polyacetylene is the *soliton*.

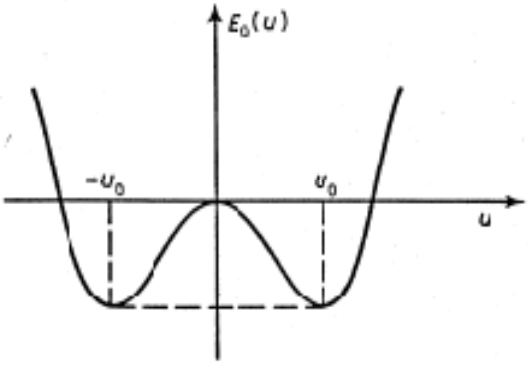

Figure 2.11. Energy of the system in function of the dimerization coordinate *u*.

This soliton represents the domain boundary between the two phases and in Figure 2.12 is given a graphical representation of it:

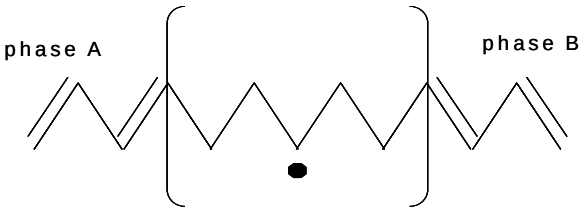

Figure 2.12. The generation and displacement of a soliton causes the change from phase A to phase B.

SSH theory predicts that the structural relaxation between phase *A* and phase *B* extends over 7 carbon atoms as it has been represented in the figure above. Nevertheless, for simplicity this factor is not always kept into account when drawing a scheme of the soliton particle.

Associated with the generation of a soliton a state with energy in the centre of the gap appears which can be occupied by zero, one or two electrons: with no electron the soliton is positively charged and has no spin; with one electron the soliton has no charge and spin equal to ± ½; finally,

with two electrons the soliton has negative charge and no spin. In Figure 2.13 the band diagram for each case with the molecule representation is sketched.

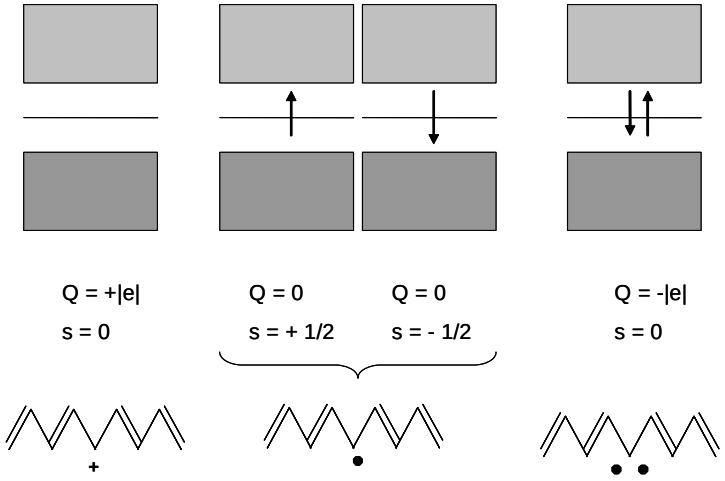

Figure 2.13. Electronic structure for the three types of solitons, with charge and spin values and structure representations.

In polyacetylene the degeneration is a consequence of the linear symmetry of the macro-molecule. An important aspect to be kept into account is that the introduction of energetic levels into the gap, as a result of the formation of solitons in the material, influences its optical properties. After the generation of solitons new transitions are possible with energy in the sub-gap range: the near infrared (NIR) region. Non-linear optical properties are another of the peculiarities of organic semiconductors and will be briefly described in the last paragraph of this chapter.

2.2.3 Polymers with non-degenerate ground state

Polymers like poly(phenylene vinylene) (PPV) and polyparaphenylene (PPP) have no degenerate ground state. It is not clear yet if the species generated under illumination are polarons and bipolarons directly or via formation and successive dissociation of excitons. In Figure 2.14 the structures of PPV and PPP are shown: since the two structural isomers are not energetically equivalent, the degeneracy is split.

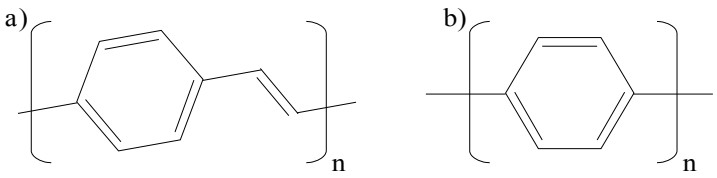

Figure 2.14. Molecular structures of two polymers with non-degenerate ground state: a) PPV (poly(phenylenevynilene); b) PPP (polyparaphenylene).

As it has been explained in paragraph 2.2.2, the number of carbon atoms in the unit cell determines the number of bands for the π-electron system. The unit cell of PPV, for instance, contains 8 carbon atoms: 6 in the cyclic part of the structure and two in the other part (Figure 2.14-a). Such structure leads to have 8 π-sub-bands: 4 bonding and 4 anti-bonding ones. As every carbon atom contributes with 1 electron to the π-system, there are a total number of 8 electrons occupying the four bonding π-orbitals, while the other orbitals, characterized by a higher energy, are empty. A detailed description of the theory of electronic states in PPV is given by S. Brazovskii et al.[24].

A polaron can be thought as a bound state of a charged soliton and a neutral anti-soliton. Since there is only one stable phase (no degeneration), the couple soliton/anti-soliton (S-AS) does not yield a change from one phase to the other. So the soliton is compensated by an anti-soliton and the two energetic levels coming from the two particles are split into a bonding less energetic level and an anti-bonding more energetic one.

In Figure 2.15 the band diagrams of polarons are shown:

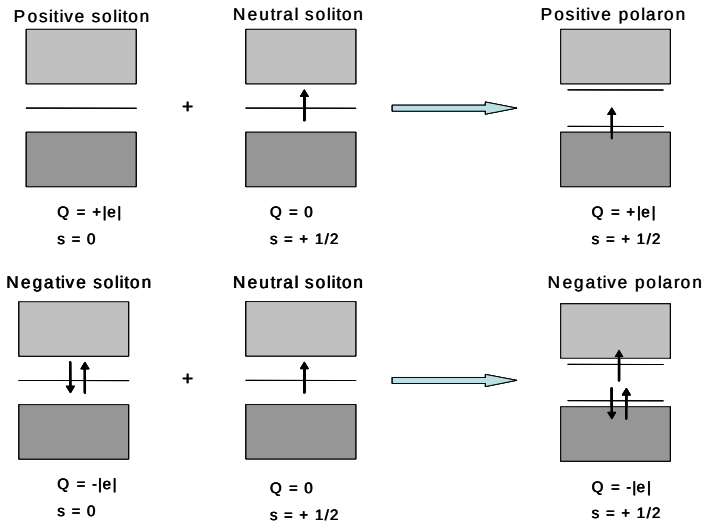

Figure 2.15. Band diagrams of positive and negative polarons: both are charged and have spin.

A positive and a neutral soliton give a polaron with positive charge and with spin, while a negative and a neutral soliton result in a polaron with negative charge and with spin. The new energetic states that appear in the gap give rise to new possible optical transitions. In Figure 2.16 there is a sketch representing a negative polaron in a PPP molecule:

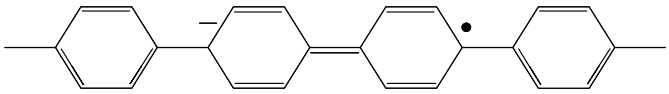

Figure 2.16. Schematic picture of a negative polaron in a PPP molecule.

A bipolaron is a bound state of two charged solitons of equal charge and also yields two energy levels in the gap between HOMO and LUMO. In Figure 2.17 there is the band diagram of bipolarons:

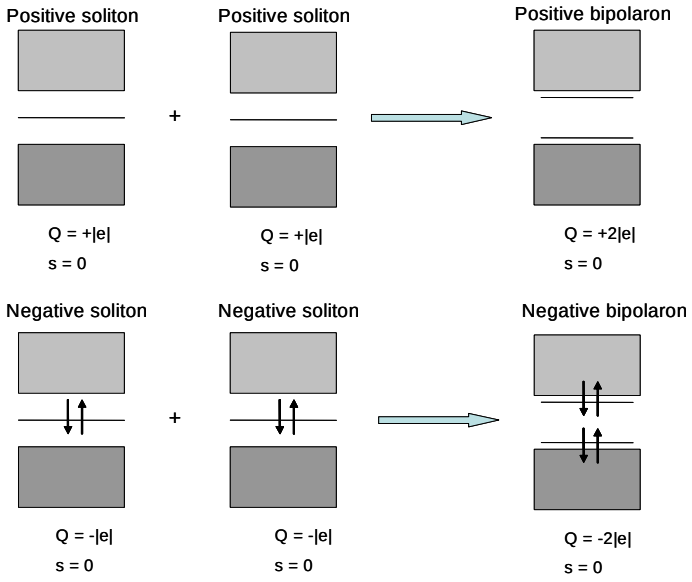

Figure 2.17. Band diagrams for positive and negative bipolarons: both are charged and spinless.

In Figure 2.18 a picture of a negative bipolaron in a PPP molecule is shown:

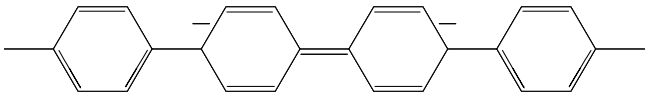

Figure 2.18. Schematic picture of a negative bipolaron in a PPP molecule.

Like solitons, both polarons and bipolarons are strictly coupled with structural relaxation and, moreover, are charged particles. Directly by illuminating a material, excited species are generated and the charged particles are able to move along the molecules. Viewed in another way, polarons are formed by charged particles surrounded by lattice distortions that stabilize the system. From this point of view, the electron-phonon interaction is what characterises polarons.

Polarons and bipolarons are not always the most stable primary excitation in polymers. Experimental evidences have indicated that in polydiacetilenes (PDAs) the most stable excited species are the excitons[25,26]. Such issue is evidently not easy as it could seem, since for every material a good experimental characterization should be performed in order to know how it works. It is than important to know the response of a material to the light in order to understand if it is useful for the application desired.

2.2.4 Small molecules

Another category of organic semiconductors, small molecules, must be treated in a separated section. Pigments and some dyes belong to this group, since their molecules are relatively small and symmetric. Molecular solids are composed of discrete molecules, kept together by Van der Waals force. Such force is weak and is the origin of a few peculiar characteristics that distinguish molecular solids from others (metals, ionic solids…). A general law is that in presence of a weak force maintaining molecules bound, the properties of the individual molecules are still retained in the solid[27].

The stable primary excitations in molecular materials are excitons[28,29]. Excitons are a known phenomenon in semiconductors and insulators and are particles composed of an electron/hole pair, interacting by Coulomb force. The total charge of the particle is zero, as the total spin, so in order to obtain electric current it is necessary to break the exciton. Three types of such particles have been observed: Frenkel, Wannier-Mott type and charge-transfer (CT) excitons. In Figure 2.19 a scheme shows the differences between them. What characterizes each type of exciton is the distance between electron and hole, i.e. the radius of the particle: when it is of the order of the crystalline constant (a_L) the exciton is a Frenkel type; when the distance is higher we have a charge-transfer (CT) exciton; for distances much higher than a_L then we have a Wannier-Mott exciton[28]. This last

type of particle is the most common in inorganic semiconductors and it is detectable only at low temperature, since at room temperature the thermal energy is higher than its binding energy and is strong enough to dissociate it. In polymers like PDAs[25,26] and in *organic molecular crystals* (*OMC*) Frenkel and charge-transfer excitons are the most stable and their binding energy has a value around 0.5 eV[30,31]. The stability of the excitons in this kind of organic semiconductors is due to their low dielectric constant: the material is not able to screen enough the two opposite charges[32]. In a Frenkel exciton the two carriers are located in the same molecule, while in charge-transfer exciton the two carriers are located in two different molecules; although they keep bound.

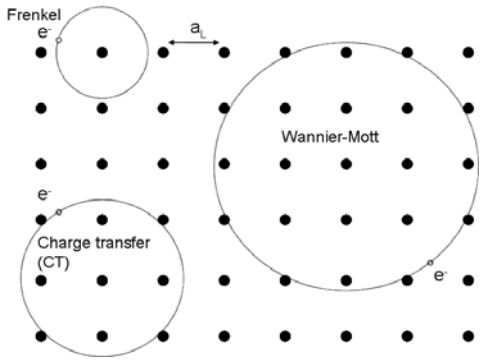

Figure 2.19. Picture of the three types of excitons in semiconductors and insulators: a_L is the lattice constant.

In Figure 2.20 a representation of the band scheme for an exciton is given[9]:

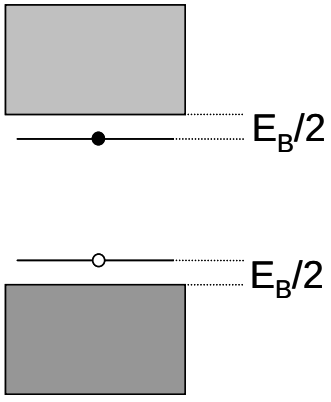

Figure 2.20. Intragap energetic states of the exciton The black filled circle is the electron, the white filled one is the hole and E_B is the exciton binding energy.

As it will be explained in the next chapter, the existence of excitons is a very important factor to be kept into account when fabricating a solar cell with organic semiconductors. When an OMC is illuminated and excitons are generated, energy levels appear in the gap, like for solitons, polarons and bipolarons. Nevertheless, in this case electron and hole are still bound and randomly move together along the molecule and from one molecule to another one: the exciton is not affected by the electric field because it has no charge. Another interesting aspect is that the existence itself of the exciton supposes that the electron-hole interaction is stronger than the electron-phonon interaction that characterizes polarons. Excitons can move, but the charge carriers are not free yet. A force is required to break the exciton into a free electron and a free hole that can flow to the respective electrodes. The mechanisms by which the excitons are dissociated in a solar cell will be explained in detail in chapter 3.

The mechanism regulating the function of organic semiconductors is known from nature in the case of the photosynthesis process, in which photonic energy is taken from the incident light to be converted into chemical energy by means of a similar process.

2.2.5 Experimental proofs and an alternative model

Experimental evidences demonstrate the existence of the excited species described in the paragraphs above. Each particle is characterized by having a charge and/or a spin value, thus are detectable by employing different techniques.

Neutral solitons have no charge, but spin equal to ±1/2 (see Figure 2.13). The presence of spin in a material can be detected by Electro Spin Resonance (ESR)[33,34] and Electron-nuclear Double Resonance (ENDOR) [35]. Charged solitons, which have no spin, can be analyzed by sub-gap optical absorption[36,37,38] and photoconductivity measurements[39,40,41]. The appearance of energetic levels in the gap is responsible for absorption features that can be usually registered in the near infra-red region of the spectrum. The generation of charged solitons is a consequence of photo-absorption and immediate separation of electron and hole into two oppositely charged solitons which give electric current.

If the primary excitations are polarons and bipolarons, charge-storage can be probed by a combination of electrical, magnetic and optical measurements. Remembering that polarons have charge (±|e|) and spin (±1/2), while bipolarons have charge (±2|e|) but not spin (see Figure 2.15 and Figure 2.17), ESR[42] and Optically Detected Magnetic Resonance (ODMR)[43,44] can be used to distinguish between the different values of spin; the optical measurements are useful to detect the absorption due to these particles in infrared region. Detection of polarons and bipolarons have been performed also via optical measurements[45,46,47].

Finally, in presence of excitons optical and photocurrent measurements can help with the problem of distinguishing such electron-hole pairs from the other particles: the optical absorption onset, when measured by photocurrent means, is higher than the one obtained by purely optical means[48]. This is due to the neutral nature of excitons which require an extra energy in order to be dissociated and obtain electric current. In the case of PDAs (polydiacetilenes), for example, the absorption onset occurs at 1.8-1.9 eV, value at which no photoconductivity is observed. The photoconductivity onset occurs at 2.3-2.5 eV, i.e. at energies high enough to break electron-hole pairs[48] which, by this way, have been detected. The binding energy of the excitons can be obtained by Electroabsorption (EA) measurements[49,50,51]. A useful technique is also the measurement of transient photoconductivity in pico- and nanosecond regimes[52,53].

Despite the great quantity of experimental work that has been done to understand which mechanisms determine the nature of the excited species in organic semiconductors, many doubts are still remaining. For example, the interpretation of the real causes for the onset difference between photoconductivity and optical measurements is still not clear. According to a more simple view of the problem, even in polymers or in molecular materials excitons are generated under illumination and then it is necessary to dissociate them into two separated charge carriers in order to obtain current flow.

As a conclusion, in Table 2.1 a comparison between chemical and physical terminology for the excited species that are generated in organic semiconductors is shown[54]:

Physical term	**Chemical term**
Neutral soliton	Neutral radical
Positive soliton	Spinless cation
Negative soliton	Spinless anion
Positive polaron (hole with associated lattice distortion)	Radical cation
Negative polaron (electron with associated lattice distortion)	Radical anion
Positive bipolaron	Spinless dication
Negative bipolaron	Spinless dianion

Table 2.1 Comparison between physics and chemistry terms: what for a physicist is a particle, for a chemist is an excited chemical species.

2.3 Optical properties

The optical properties have relevant importance in photovoltaic technology. In Figure 2.21 there is a scheme of the possible photo-physical processes in a conjugated molecule or polymer. Such processes characterise the molecular system and are also present in a solid, due to the low interactions between molecules. In the cited image, all the photo-physical processes that can occur in a conjugated molecule or polymer when excited by light irradiation are represented. The broad arrow indicates the excitation; S_0, S_1 and S_n are the singlet states, while T_1 and T_n are the triplet ones; k_{nr} and k'_{nr} are the rate constants for non-radiative processes, k_r and k'_r the constants for radiative processes and k_{ISC} the constant for *inter system crossing* (ISC) process. All of these mechanisms are in competition and are characterized by a time of decay (time of life, τ, of the excited species).

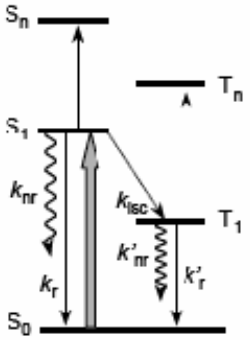

Figure 2.21. Excitation and possible decay processes in an organic molecule.

Traditional absorption and transmittance techniques allow to determine the amount of absorbed (or transmitted) light in relation to transitions over the optical gap of the analyzed material. Only photons with energy equal or superior to the energy gap (E_g) can be absorbed. In presence of impurities new energy levels are placed in the prohibited gap and more sensible techniques, as Photothermal Deflection Spectroscopy (PDS), are required to detect the absorption due to these features.

Once the material has absorbed the light, it returns to its ground state via several relaxing mechanisms (see Figure 2.21). The radiative decay processes from singlet (S_1) and triplet (T_1) states

to the ground state give rise to photoluminescence phenomena. The former process ($S_1 \rightarrow S_0$) is known as *fluorescence* and has a decay time of the order of ns (10^{-9} s); the latter ($T_1 \rightarrow S_0$) is known as *phosphorescence* and has a decay time of the order of μs-ms (10^{-6}–10^{-3}). The reason for such higher decay times in the case of phosphorescence is that this process requires the system to change spin, as it has to relax from the triplet state T_1 to the ground singlet one S_0. Transitions between two states with different spins are much less probable than transitions between two states with the same spin. Photoluminescence processes can be detected spectroscopically even as a function of time, in order to observe the evolution of the decay, or in *steady-state* mode, i.e. measuring the total intensity emitted during a determined time range. Transitions between excited states ($S_n \rightarrow S_0$ and $T_n \rightarrow T_1$) can be detected, for example, by Photoinduced Absorption Spectroscopy (PIA).

As it will be explained in chapter 3, solar cells made of organic materials require the use of a heterojunction between a donor semiconductor and an acceptor one. The scheme of the possible photophysical processes is, in this case, more complex and is represented in Figure 2.22.

Donor and acceptor energy levels are represented together with the levels associated to *charge separated states* (CSS). In a donor/acceptor system transitions from one material to the other one are also possible, yielding to a greater number of photophysical processes. CSS are states in which electron and hole are separated and two charged polarons are obtained and free to flow to the respective electrodes.

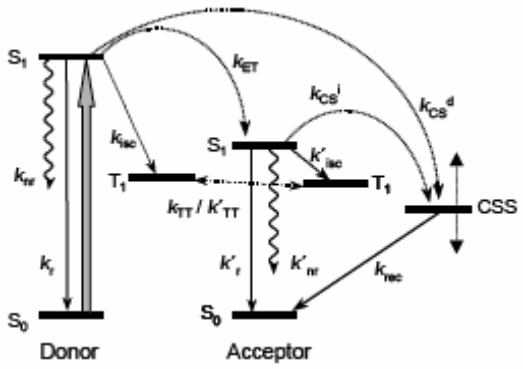

Figure 2.22. Excitation and decay processes in a donor/acceptor system.

As already commented before, organic semiconductors are characterized by non-linearity of their optical properties. The appearance of energetic levels in the gap, as a consequence of the generation of excited particles, yields new optical transitions not present before absorption has

taken place. When photons are absorbed, after a period of the order of less than a picosecond (10^{-12}), midgap energetic levels, associated with the new particles, appear. In Figure 2.23 a scheme shows the mechanisms described above. Upon photon absorption a band-to-band transition occurs, but after 10^{-13} s the system relaxes with the generation of a polaron, here considered as an example. The new energetic states in the gap, associated with the polaron, are the origin of new optical transitions located in the near infrared region (for energy values inferior to the optical gap of the material). It is then necessary to employ time resolved characterization techniques in the sub-picosecond range in order to understand which mechanisms are working immediately after the absorption. This *ultrafast relaxation* of the photo-excited carriers plays an important role in the optical properties of the organic semiconductors.

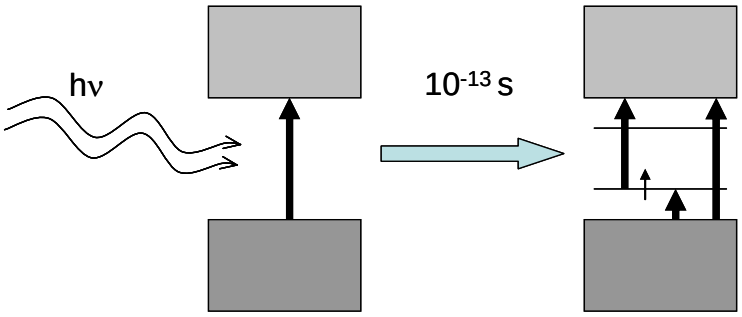

Figure 2.23. Scheme showing a nonlinear optical phenomenon in the case of a positive polaron: the vertical and sharp arrow indicates one electron, while the narrow ones indicate the possible optical transitions.

In the case of organic molecular crystals (OMCs) the intragap states are related with the generation of excitons (Figure 2.20). The excited singlet (S_1) and triplet (T_1) states correspond to excitonic species, the nature of which (Frenkel or charge transfer type) must be investigated case by case[55]. As a result, the high-level absorption part of the absorption coefficient α of such materials is composed of several features due either to exciton generation and to band-to-band transitions[55].

2.4 Materials investigated in this work

The experimental work of this thesis is based on the characterization of a group of small molecule materials which are listed below:

- **donors**: copper phthalocyanine (CuPc) and pentacene ($C_{22}H_{13}$)
- **acceptors**: fullerene (C_{60}), perylene tetracarboxylic dianhydride (PTCDA), *N*,*N*-ditridecyl-3,4,9,10-perylenetetracarboxylic diimide (PTCDI-C_{13})

These molecules are insoluble in organic solvents and must be evaporated or sublimated from a powder. The good optical and electrical properties shown make them interesting semiconductors for some device applications like for example solar cells[17,56,57] and organic field effect transistors[10,58]. In this chapter a brief description will be given for each of the materials treated in this work. Such materials have been bought from Sigma-Aldrich, Fluka and Merck Corporation and have been evaporated without performing any purification treatment.

The materials defined as *donors* are *p*-type, which means that they are good hole conductors; the materials defined as *acceptors* are *n*-type, good electron conductors. This is an intrinsic property, not a result of any doping process.

The choice of these materials is motivated by the fact that they have an important role in research on organic solar cells. Efficiencies of 3.6 % have been obtained with a bi-layer cell composed using CuPc and C_{60}[17].

As it will be seen, each molecule is based on cyclic structures that allow to have electron delocalization over almost the whole molecule.

Copper Phthalocyanine

Copper phthalocyanine ($Cu_{32}H_{16}CuN_8$) belongs to a group of compounds in which the simplest molecule is the one with a hydrogen molecule (H_2) occupying the central site. When deposited in thin film its colour is blue. Other types of phthalocyanines are characterized by the presence of other transition metals than Cu, like Fe, Co, Ni, Zn and Mg. In Figure 2.24 the structure of the copper substituted phthalocyanine is shown:

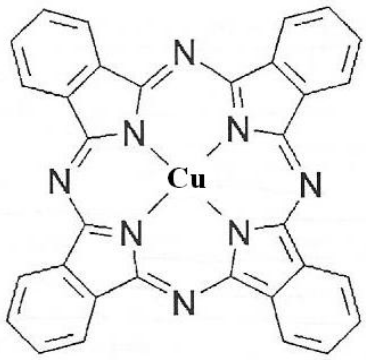

Figure 2.24. Structure of copper phthalocyanine.

The metal contained in the centre of the molecule yields different electronic properties[59]. All of these molecules are planar conjugated aromatic macrocycles that can form crystals with conductivities ranging from 10^{-12} up to 10^{-4} Sm^{-1} [60]. CuPc has a molecular mass of 576.07 a.u. (atomic mass units), an optical gap of 1.7 eV and a transport gap of 2.3 eV[15,61]; it is a stable compound and begins to evaporate at around 350ºC. Several polymorph phases have been observed[62] , two of which are the most stable ones and are defined as α and β, respectively. Such phases have monoclinic structures with the lattice parameters reported in Table 2.2[60]:

Phase	a (Å)	b (Å)	c (Å)	β (º)
α	25.92	3.79	23.92	90.40
β	19.41	4.79	14.63	120.00

Table 2.2. Structural parameters of the two stable crystallographic phases of CuPc.

Generally CuPc powder has β structure, while the micro-structure of thin films depends on the type of substrate and deposition conditions: a deposition process performed with the substrate at room temperature yields α structure, while a deposition at higher temperature (210ºC) yields to the formation of β phase[63]. The possibility to change the phase from α to β by applying a post-deposition annealing treatment at 250ºC has also been demonstrated[63].

Pentacene

Pentacene ($C_{22}H_{14}$) in another blue hole semiconducting material that has received much attention in the last few years for its high hole conductivity: 1 cm^2 /Vs[58]. Such a high conductivity makes this semiconductor one of the organic compounds with the highest conductivity and a good competitor for amorphous silicon. Pentacene belongs to the groups of polyacenes with other compounds represented in Figure 2.25. These molecules, in their ground state, are flat and its π-system counts for (4n+2) delocalized electrons, one per carbon atom, where *n* is the number of aromatic rings. So pentacene has 22 electrons delocalized along the molecule.

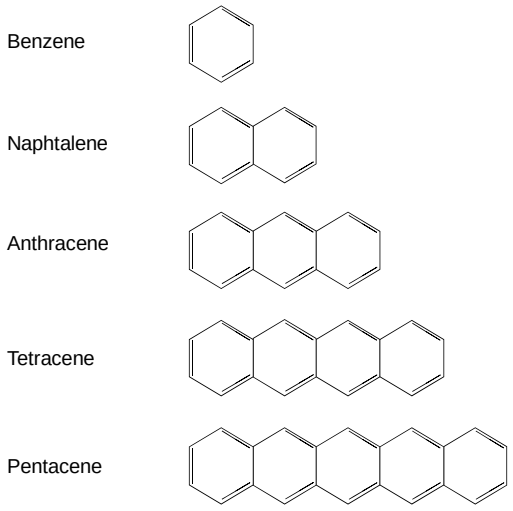

Figure 2.25. Molecular structure of the first five polyacenes.

Pentacene has a molecular mass of 278.35 a.u. and one of the lowest evaporation temperatures of molecular organic semiconductors, as it begins to evaporate at around 130ºC. This semiconductor has also several polymorph structures; among them, two stable ones that are defined as polymorph C and polymorph H, the lattice parameters of which are listed in Table 2.3[64]:

Phase	a (Å)	b (Å)	c (Å)	α(º)	β(º)	γ (º)
C	6.06	7.90	14.88	96.74	100.54	94.20
H	6.27	7.78	14.53	76.47	87.68	84.68

Table 2.3. Structural parameters of pentacene stable crystallographic phases. Both structures are triclinic.

Two phases called *thin film* and *bulk* phases have also been described with lattice parameters *c* equal to 15.4 and 14.4 Å respectively[65]. The former polymorph is normally observed for thicknesses below a critical value of around 150 nm, while the latter phase for thicker films. The different phases can be obtained, as for CuPc, varying the substrate type and its temperature during the deposition process[66]. Nevertheless it is common to have more than one in the same film[65].

Pentacene is known to interact with oxygen which diffuses into it, but some research demonstrated that the diffusion process is reversible and that the material overcomes irreversible degradation only when irradiated with UV light, due to the formation of very reactive chemical species in the atmosphere like ozone[67]. On the other hand, studies have been performed to demonstrate that water molecules can diffuse into the crystal and, by interacting with charges, decrease the current, while oxygen can work as an impurity injecting holes (trapping electrons)[68].

Fullerene (C_{60})

Observed for the first time by H.W. Kroto and his co-workers during '80s[69], a fullerene is a big cluster composed of only carbon atoms. In Figure 2.26 the molecule composed of 60 carbon atoms is presented:

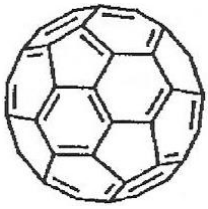

Figure 2.26. Molecule structure of C_{60}.

The cluster clearly resembles a football ball, with alternating hexagons and pentagons building its surface. Its molecular mass is 720.64 a.u., its diameter about 7 Å[69] and, due to such dimensions, large space is left to interstitial impurities like oxygen[70].

The net of cyclic elements builds up an extended π-system with delocalized electrons circulating all over the molecule surface. Fullerene is an accepting organic semiconductor and it has been demonstrated that in it excitons have a diffusion length of about 70 nm[71], characteristic that makes this material a good choice as an acceptor. Fullerene derivatives, modified with a lateral

functional chain in order to make them soluble in organic solvents, are employed also in solution-processable solar cells fabricated with semiconductor polymers[72].

Perylenes: PTCDA and PTCDI-C_{13}

Perylene-3,4,9,10-tetracarboxylic dianhydride (PTCDA) and *N*,*N*_-ditridecyl-3,4,9,10-perylenetetracarboxylic diimide (PTCDI-C_{13}) belong to the group of compounds known as perylenes and their molecular structures are shown in Figure 2.27.

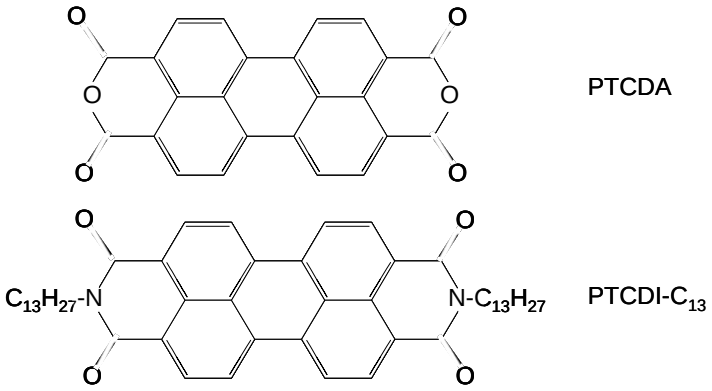

Figure 2.27. Molecular structure of PTCDA and PTCDI-C_{13}.

These molecular materials are acceptor semiconductors and present good crystalline quality, which gives a good overlap of the π-π^*, and transport properties[55,73].

Phase	a (Å)	b (Å)	c (Å)	β (º)
α	3.72	11.96	17.34	98.8
β	3.87	19.30	10.77	83.6

Table 2.4. Lattice parameters for the two crystalline phases of PTCDA.

Two crystalline phases have been observed for PTCDA, both with monoclinic structure, called α and β[74,75]. In Table 2.4 the lattice parameters for the two phases are indicated[76,77].

PTCDI-C_{13} is a derivative of the more simple 3,4,9,10-perylenetetracarboxylic diimide (PTCDI) which is a semiconductor known for having high field-effect electron mobility[78]. A mobility of 0.6 $cm^2V^{-1}s^{-1}$ has been measured for *N*,*N*-dioctyl PTCDI (PTCDI-C_8H)[79]. The linear alkyl group

that characterizes the molecule of PTCDI-C_{13} gives better self-assembling and alignment properties to the molecules, due to its better adaptability respect to rigid aromatic structures[78]. Such effect is especially observed when thermal treatments are performed and allows the obtainment of higher crystalline fractions. Moreover, electron mobility equal to $1.7 \cdot 10^{-2}$ $cm^2V^{-1}s^{-1}$ has been measured in a thin film transistor where the active layer was made of such material[80].

CHAPTER 3

TECHNOLOGICAL ASPECTS

In this chapter technological issues about organic device fabrication will be treated. Processes like doping an organic semiconductor are done in a radically different way, compared with the ones that are usually employed for inorganic semiconductors like silicon. The differences with respect to inorganic semiconductors are mainly related to the chemical properties of the organic ones, but also with their different charge storage mechanisms. As a result, after sections about the chemical and the electrical properties of such materials, another one dedicated to processing methods will be offered.

Section 3.1 is dedicated to the doping mechanisms in organic semiconductors; section 3.2 is about the charge carrier transport; the most common deposition techniques will be described in section 3.3; finally, a view on the evolution of organic solar cells will be given in section 3.4.

3.1 Doping mechanisms

Organic semiconductors can be classified as *n*-type and *p*-type semiconductors like doped silicon. Nevertheless, the doping process is in this case substantially different from the one which is usually employed in the case of silicon. Silicon is doped by introducing substitutional impurities as phosphorus (P) or boron (B) in order to obtain *n*-type and *p*-type semiconductors, respectively. The process is done by substituting a few silicon atoms with atoms of the other elements. Given that one silicon atom has four valence electrons, P with its five is a donor impurity, while B with its three is an acceptor one. So when doped with phosphorus, silicon becomes an *n*-type semiconductor and new energetic levels, associated with the impurity, appear in the gap near to the conduction band; when doped with boron, silicon becomes a *p*-type semiconductor and new energetic levels are introduced in the gap near the valence band.

When talking about organic semiconductors, it is worth emphasizing that the mechanisms by which it is possible to "dope" them are different and that the terminology taken from inorganic science is often misleading.

An alternative definition for organic semiconductors is *donor* (D) for the *p*-type and *acceptor* (A) for the *n*-type. In the case of organics the *n*- and *p*-type definitions refer to the fact that *n*-type semiconductors are good conductors for electrons, while *p*-type ones are good conductors for holes[16]. In an organic solar cell the donor gives electrons to the acceptor (see paragraphs below). So, for example, while *n*-type silicon is obtained by introducing *donor impurities*, an organic *n*-type semiconductor is to be called *acceptor* and this must be kept into account in order to avoid confusing with terms. Moreover, the action to dope an organic semiconductor, i.e. to introduce charge carriers in it, has the double mean of introducing polarons, from a physical point of view, and to generate reactive chemical species as radical ions, from a chemical point of view[20].

The mechanisms for doping organic semiconductors are four[20]:

1. Chemical
2. Electrochemical
3. Photo-doping
4. Interfacial

The nature of the species that are generated in a doped organic semiconductor explains how it is possible to have such variety of doping mechanisms. Such a variety is useful when characterizing new materials, since charge carriers can be formed and characterized by different ways.

1. Chemical doping

This type of doping involves oxidation (*p*-type doping) and reduction (*n*-type doping) reactions. The mechanisms are illustrated in the following examples for polymers:

p-type: $$(\pi - polymer)_n + \frac{3}{2} ny(I_2) \rightarrow \left[(\pi - polymer)^{+y}\left(I_3^-\right)_y\right]_n \quad (3.1)$$

n-type: $$(\pi - polymer)_n + \left[Na^+(Naphthalide)^\bullet\right]_y \rightarrow \left[\left(Na^+\right)_y(\pi - polymer)^{-y}\right]_n + (Naphth)^0 \quad (3.2)$$

By chemical means it is then possible to generate charge carriers in the molecules. As it has been shown in the previous chapter, what for chemists means to create charged and reactive

chemical species (radical ions), for physicists means to create charged particles (polarons) useful for electric conductivity in technological applications.

With this method it is quite easy to obtain high doping levels and a material can turn from semiconducting to metal when the doping level is high enough. A drawback of this technique is that it is difficult to control, making often impossible to obtain intermediate and homogeneous levels of doping.

2. Electrochemical doping

Due to the problems of controlling the doping level that affect the chemical method, in many cases the electrochemical technique is more convenient. An electrode supplies redox charge to the semiconductor, while ions diffuse into or out of it from the nearby electrolyte to compensate the electronic charge. The voltage between the polymer and the electrode allows to control the doping level. The mechanism is illustrated in the following examples:

p-type: $$(\pi - polymer)_n + \left[Li^+\left(BF_4^-\right)\right]_{sol'n} \rightarrow \left[(\pi - polymer)^{+y}\left(BF_4^-\right)_y\right]_n + Li(electrode) \qquad (3.3)$$

n-type: $$(\pi - polymer)_n + Li(electrode) \rightarrow \left[\left(Li^+\right)_y(\pi - polymer)^{-y}\right]_n + \left[Li^+\left(BF_4^-\right)\right]_{sol'n} \qquad (3.4)$$

3. Photo-doping

The generation of an electron-hole pair by photo-absorption and the subsequent charge separation leading to the formation of separated charge carriers results in a local oxidation and a nearby reduction of the material. The mechanism can be resumed by the following equation:

$$(\pi - polymer\ )_n + h\upsilon \rightarrow \left[(\pi - polymer\ )^{+y} + (\pi - polymer\ )^{-y}\right]_n \qquad (3.5)$$

where *n* is the number of electron-hole pairs. If photo-absorption results in the generation of free carriers or bound excitons is a theme still under discussion[81] and, in any case, seems to depend on the material (see chapter 2). It is, in conclusion, something to be experimentally determined case by case.

After photon absorption many photo-physic processes compete to determine the response of the material (see chapter 4). Charge separation and the resulting generation of free carriers can be enhanced by coupling a donor with an acceptor (see paragraphs below). In any case, it is worth pointing out that while chemical mechanisms allow charge carrier generation of the required sign,

the photo-doping yields to the generation of both charge carriers and requires a mechanism to separate them.

4. Interfacial carriers injection

Charge carriers can be injected into a semiconductor at the interface with a metal contact. The charges are introduced directly into the π and π^* bands as indicated by the following equations:

$$p\text{-type:} \qquad (\pi - polymer)_n - y(e^-) \rightarrow [(\pi - polymer)^{+y}]_n \tag{3.6}$$

$$n\text{-type:} \qquad (\pi - polymer)_n + y(e^-) \rightarrow [(\pi - polymer)^{-y}]_n \tag{3.7}$$

where y is the number of injected particles. Equation (3.6) refers to the injection of a hole into an otherwise filled π-band, or the extraction of an electron, which corresponds to an oxidation reaction. Equation (3.7) refers to the injection of an electron into an empty π^*-band, which consists in a reduction of the material.

The different mechanisms described above lead to different situations in the materials. In the case of chemical and electrochemical doping the induced current is permanent until the charges are compensated, while in the case of photo-doping the current is limited by decay and recombination mechanisms. Finally, in the case of interfacial carrier injection, the durability of the free carriers is limited by the presence of a bias applied to the contacts.

3.2 Current generation in an organic solar cell

Current generation in an organic solar cell is obtained through four steps that will be discussed in detail below[9]:

1. photon absorption and exciton generation
2. exciton diffusion
3. exciton dissociation and charge carriers generation
4. charge carriers collection at the electrodes

1. The light absorption process depends on the optical properties of the active layer and of other components, like the transparent contact. A low optical band gap for the semiconductor is preferable in order to have higher light absorption. Moreover, the absorption spectra of the materials composing the active layer should fit the best possible the solar spectrum the best possible.

   A transparent electrode is needed on the side where light enters. Normally, *transparent conductive oxides* (TCO) like *indium tin oxide* (ITO) or *zinc oxide* (ZnO) are commonly used for such purpose.

   The photo-absorption process leads to excitons generation with efficiency η_A.

2. The second step involves the diffusion of the excitons through the active layer towards the interface between the two semiconductors which works as a dissociation site. Such process is limited by the diffusion length of the excitons in the material, which normally rounds a few tens of nanometres[82,83]. In order to allow the excitons to get to the interface without recombining, an active layer with a thickness comparable to the exciton diffusion length is necessary. This requirement could limit the absorption in the cell and a compromise between the two needs must be found.

   One aspect influencing the exciton diffusion is the structural quality of the active layer: the more ordered the structure, the more easily the particles diffuse in it.

   It is worth focusing the attention on the fact that the excitons are made of an electron-hole pair and have no charge. As a consequence, their transport is not obtained by applying an electric field, but simply by random diffusion.

   For the diffusion process we define the efficiency $\eta_{ED.}$

3. The third step involves the dissociation of the exciton into separated charge carriers. In order to achieve the purpose, a dissociation site is required and this is normally the interface with an electrode or with another semiconductor. The kind of dissociation centre is determined by the structure of the device, issue that will be discussed in the next paragraph.

   For the dissociation step the efficiency η_{CT} is defined.

4. The last step is the collection of the charge carrier at the contacts. Depending on where the dissociation has taken place, the carriers will simply be injected into the contacts or will have to reach them. Such process is strongly dependent on the structure of the device, which

could include a heterojunction between two semiconductors or the presence of more layers that have the function to facilitate the charge injection.

For the charge carriers collection at the contacts an efficiency η_{CC} is defined.

The efficiency η of the global process can be calculated as the product of the efficiencies of the single steps:

$$\eta = \eta_A \cdot \eta_{IQE} = \eta_A \cdot \eta_{ED} \cdot \eta_{CT} \cdot \eta_{CC} \tag{3.8}$$

where η_{IQE} is the *internal quantum efficiency* defined as the number of charge carriers collected at the electrodes per number of incident photons.

3.3 Deposition techniques

In chapter 2 a classification of the organic semiconductors based on the type of charge carrier has been given. Another classification of such materials can be based on their solubility properties and is shown in Figure 3.1[84]:

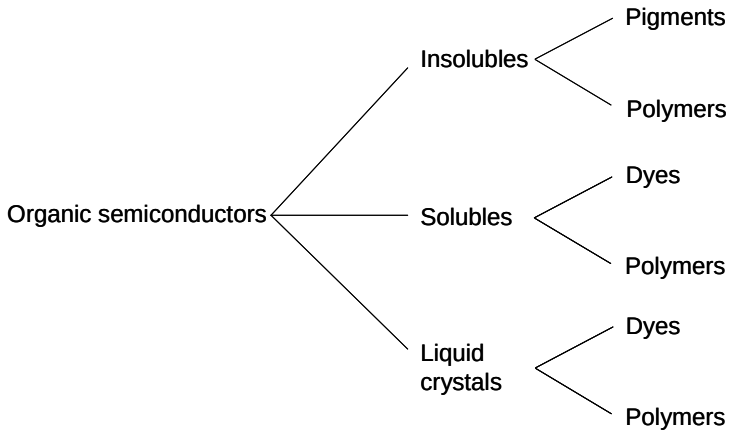

Figure 3.1. Classification of the organic semiconductors based on their solubility properties.

The chemical properties of the materials determine which deposition technique can be used. In the next paragraph a brief description of the most used processes will be given. Two kinds of

deposition processes are known: the thermal evaporation, for the insoluble materials, and the group of wet processes for the soluble ones and for pigments dispersions.

Thermal vacuum evaporation or sublimation

This technique is commonly used for depositing organic semiconductors that are insoluble in organic solvents: the most common small molecule materials. The evaporation equipment will be described more in detail in chapter 4 with all the experimental equipments used in this work. It consists in a vacuum chamber in which a pressure of the order of 10^{-3} Pa is generally maintained to obtain a long mean free path for the evaporated molecules. The source material is heated up to its melting or sublimation temperature that can be of the order of a few hundred ºC. As a consequence, thermal stability is required for the molecules to be deposited with this technique. Small molecules are normally stable enough, while the polymers could undergo degradation.

Thermal evaporation offers the possibility to control some properties of the thin film to be deposited by controlling some deposition parameters, like substrate temperature and deposition rate (the amount of material deposited on the substrate per time unit). In this way, it is possible to control the thickness of the thin film and also its micro-structure. If needed, two or more materials can be evaporated in sequence or at the same time.

Films deposited by vacuum evaporation have generally good homogeneity and structural properties. Nevertheless, this technique is more expensive than the ones where the material is processed from solution and also requires longer deposition times.

Wet processing

In this type of processing techniques, the organic material has to be dissolved in one or more solvents, that could be water or organic solvents. In general, polymers and dyes are soluble in certain solvents or, in the other cases, their molecular structure can be slightly modified to make it more adequate for interacting with solvent molecules. Many pigments (insoluble materials) can also be processed by a wet technique through the formation of a dispersion of nanoparticles. This is a very common procedure with metals, for instance.

The most used techniques, in this field, are spin-coating, doctor-blading, screen printing and inkjet printing. In Figure 3.2 two of them are presented:

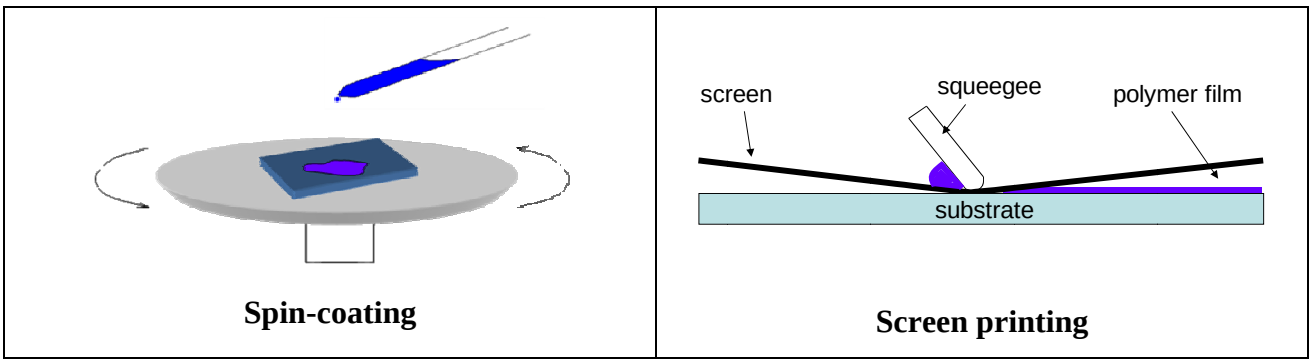

Figure 3.2. Scheme showing spin-coating and screen printing techniques.

Largely used to fabricate lab-scale solar cells, spin-coating (left part of Figure 3.2) takes advantage from the centrifuge force generated on a rotating plate in order to deposit the material that is left to fall onto the substrate. Solvent evaporation time, rotation speed and rotation time are the main parameters to take into account for determining the thickness and the crystalline quality of the film, together with thermal post-deposition treatments. The rotation speed determines the final thickness, while the time of rotation is influenced by the vapour pressure of the solvent: for solvents that have low vapour pressure, more rotation time could be needed.

Screen printing (right part of Figure 3.2) uses a squeegee to disperse the solution on the substrate surface through a screen. Doctor-blading technique makes use of a blade to deposit the film directly onto the substrate surface, while inkjet printing produces drops of the ink that are jetted onto the substrate surface.

For all these techniques solvent properties have an important role. The most important are the interactions between solvent and polymer molecules and solvent vapour pressure. Good interactions between the molecules results in good polymer solutions. A low vapour pressure leads to a long evaporation time, and vice versa for a high vapour pressure. Such parameters can have a great influence on the resulting structure of the film and on solar cells performance, but a specific study must be done for each technique in order to find the best solvent and to define the deposition conditions.

These deposition techniques have in common low cost, fast processing time and some of them can be easily scaled up to bigger surfaces.

Solution processable materials make it possible also to operate using roll-to-roll technique. This method works by depositing on a flexible rolled substrate that is moved through the machine which executes all the phases of the process continuously. At the end of the whole process the coated substrate is rewound again.

A simplified scheme of a roll-to-roll system is shown in Figure 3.3:

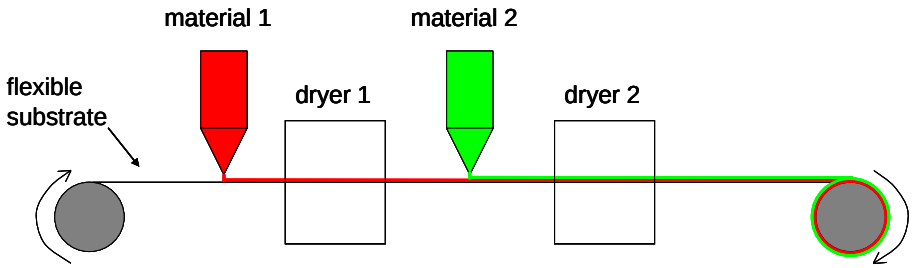

Figure 3.3. Scheme of a roll-to-roll system depositing and drying two films.

In the figure above the deposition of two materials and their subsequent drying are sketched.

The surface output of such technique is very high (some meters per minute), and several deposition techniques can be employed in function of the material to be deposited and of the application. Two examples of deposition techniques are slot die coating and gravure coating. A slot die system is constituted by a slit through which the ink is made to flow by means of a pumping system. By using masks and regulating the liquid flow it is possible to create a direct pattern onto the substrate, i.e. without the need to use lithography techniques. A gravure system consists of a patterned metallic roll which collects the ink from a tray and releases it onto the substrate with the same pattern. The method to be used is chosen depending on the viscosity of the ink and of the pattern to be obtained.

Roll-to-roll method requires stable materials in order to be able to operate in atmospheric conditions. On one side, there is still much work to be done in the field of materials stability in order to be able to manipulate them in presence of atmospheric air. On the other side, the great surface output of the roll-to-roll technique allows to think at very low cost production for photovoltaic technology.

The printing methods have the great advantage of making it possible to directly pattern the film, without needing any post-deposition process. An example of investigation in this field is given by the work done in Risø centre in Denmark[85].

A drawback of these deposition techniques is the difficulty to obtain polycrystalline structures with high crystalline fractions and a good homogeneity in the films. Post-production annealing treatments can help with this problem, causing a partial phase segregation and crystallization[91].

3.4 Device structures

In the last decades the research on organic solar cells has been focused on all the aspects that regulate their way to work. The four steps described in previous sections suggest which aspects should be investigated to improve the efficiency of the solar cells. Solar spectrum coverage and carrier mobility are, for example, characteristics of the semiconductors. Nevertheless, there are other aspects, like exciton diffusion and dissociation, which have been improved by investigating devices geometry. As a result, during the last 20 years, a few different device structures have been developed with the objective to make the generation of free charge carriers more efficient.

3.4.1 Single layer device

The first geometry to be studied is the one with an organic layer sandwiched between two electrodes, one of the contacts interface acting as a rectifying barrier according to the Schottky model.

In Figure 3.4, a band diagram for a *p*-type Schottky device is shown, including the steps of free charge carrier formation, as described in the previous section. The active layer, a *p*-type semiconductor in the figure, is sandwiched between the two electrodes: an anode with higher work function and a cathode with lower work function. When the three elements are put in contact, the Fermi levels of the metals get aligned, there is band bending at the interface between the semiconductor and the cathode and a depletion region *W* is formed. Such region of the device is the dissociation site where the excitons, the ones which have succeeded in arriving, are dissociated in electrons and holes. The coulombian interaction that keeps electron and hole bound is broken by the electric field that is generated in the region *W*. Once the charge carriers are separated, the hole has to move back to the anode through the active layer[16].

The performance of such type of device is strongly dependent on the diffusion length of the excitons in the material composing the active layer. Only the excitons generated at a distance from the dissociation region comparable to the exciton diffusion length will give free charge carriers. In other words, only the photons absorbed in those conditions contribute to the photocurrent.

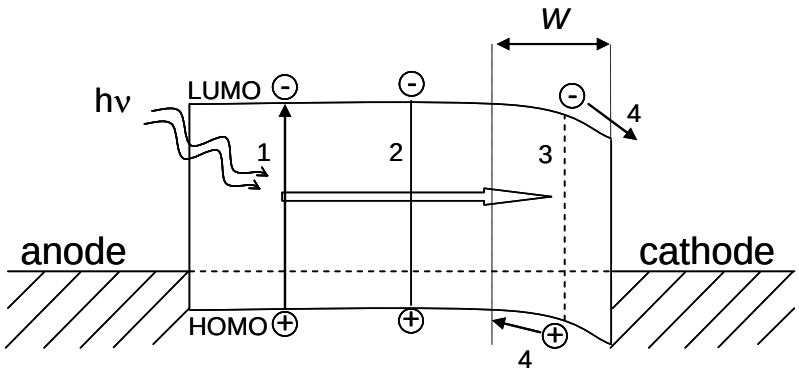

Figure 3.4. Band scheme of a *p*-type single layer solar cell and steps of formation of free charge carriers: absorption and exciton formation (1), exciton diffusion (2), exciton dissociation (3) and charge carriers collection. The arrow in step 1 indicates the jump of the electron to the LUMO, the line in step 2 the coulombian interaction between electron and hole and the dashed line in step 3 the suppression of such interaction, followed by the jump of the electron into the cathode.

From a qualitative point of view, two kinds of behaviours are observed: the symbatic and the antibatic behaviour[86,87]. The symbatic behaviour is characterized by a quantum efficiency spectrum (see chapter 4) that fits the absorption spectrum, which means that in correspondence with an absorption maximum, there is a maximum in the quantum efficiency too. This kind of behaviour is observed when a device like the one reported in Figure 3.4 is illuminated from the cathode. The photons, respect to which the material has a high absorption coefficient α, are immediately absorbed within a few nanometres of material. In these conditions the absorption occurs near the dissociation site, the excitons are then able to arrive to the interface without recombining and the photons that have originated them contribute to the photocurrent. The photons with energy respect to which the material has low α penetrate deeper into the active layer and hardly contribute to the current. On the contrary, the antibatic behaviour is observed when the *p*-type Schottky device is illuminated from the anode: in correspondence of an absorption maximum, a minimum of quantum efficiency is observed. The photons that correspond to a higher α are absorbed far away from the dissociation region and recombine before to arrive there. These photons do not contribute to the photocurrent. The other photons enter deeper into the material and are absorbed closer to the interface with the cathode and can contribute to the photocurrent.

From an efficiency point of view, the search for good performances requires that the active layer is thin enough to allow all the excitons to arrive to the dissociation site, without recombining. Such requirement forces to deposit very thin active layers that, on the other side, could have low optical absorption.

In general, single layer devices show high series resistances, low *fill factor* (*FF*, defined in paragraph 4.4) and a field dependent charge carrier collection[16]. Since the recombination probability is proportional to the concentration of electrons and holes, the *short circuit photocurrent* (I_{sc}, also defined in paragraph 4.4) dependence on the illumination intensity is sublinear[16].

3.4.2 Bilayer heterojunction device

In a bilayer device, the active layer is composed of two semiconductors, a *donor* (*D*) and an *acceptor* (*A*). In Figure 3.5 the band diagram of this kind of device is presented, together with excitons dissociation mechanism. In the figure any phenomenon of band bending has been neglected[16]. The main dissociation site is, in this case, the interface between the two semiconductors. Such device is based upon the mechanism of the *charge transfer* (*CT*) from donor to acceptor. The photo-generated excitons have to move towards the interface where the potential drop between the energetic levels of the two materials favours the breaking of the coulombian interaction. As a result, the electrons accumulate in the acceptor and the holes in the donor. The charge carriers are separated, located in two physically different phases.

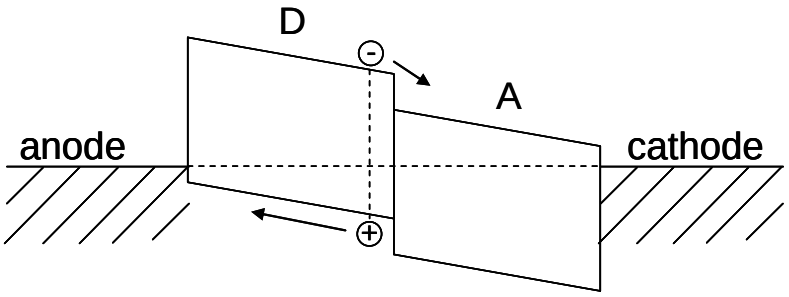

Figure 3.5. Band scheme of a bilayer solar cell. The dissociation site is the interface between the donor (D) and the acceptor (A). No band bending has been here considered.

The dissociation mechanism is favourable and spontaneous if the following condition is verified[88]:

$$I_{D^*} - A_A - U_C < 0 \tag{3.9}$$

where I_{D^*} is the ionization potential of the photo-excited donor state, A_A the electron affinity of the acceptor and U_C the effective Coulomb interaction.

The *charge transfer* mechanism is known to be ultra fast and occurs in a time of the order of tens of femtoseconds (fs)[89]. The recombination rate between electrons in *A* and holes in *D* is several orders of magnitude smaller than the one of the charge transfer, making the *CT* mechanism extremely favourable. Once the charge carriers are separated in the two phases, their recombination only depends on defects concentration (traps). For this reason, and being the charge carrier generation independent from the field, the dependence of I_{sc} with light intensity can be linear[16] and the fill factor greater than in single layer devices[90].

3.4.3 Bulk heterojunction device

In a bulk heterojunction donor and acceptor are physically mixed, in order to obtain the maximum possible interfacial surface between the two materials. In Figure 3.6 the band diagram of such a device is shown. In a situation like the one depicted in the figure, the interface is dispersed in the whole bulk volume of the active layer, making the path through which the excitons have to diffuse for dissociating shorter and also making the charge transfer mechanism much more effective. The dissociation site is still the interface between donor and acceptor, but in this case the active layer is optimized to improve the charge carrier generation.

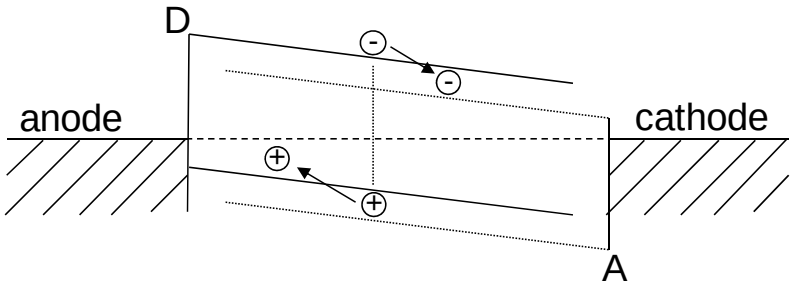

Figure 3.6. Band scheme of a bulk heterojunction: the interpenetrated bands symbolize the materials mixing. Also in this case no band bending has been considered.

All photo-generated excitons are expected to dissociate and contribute to the photocurrent. Once the carriers are generated, they need a free path, in the corresponding phase, to reach the electrode. As a result, the formation of two interpenetrating phases, with percolated paths, is a necessary requirement for the cells to work properly. Moreover, a tendency to grow with an extended amorphous phase has been observed in bulk heterojunctions made of polymers and in some cases an

improvement in cells performance is obtained with post-deposition annealing treatments[91]. Such phenomenon confirms how the bulk heterojunctions are nanoscale morphology dependent.

The control of the morphology can be achieved through several strategies, the principles of which are[16]:

1. Use of a plasticizer

   This method is useful when working with materials to be processed in solution. The plasticizer is formed by molecules that have a part interacting with the donor and another part interacting with the acceptor, making it possible to mix them.

2. The choice of a good solvent

   In case of working with dissolved polymers, the solvent influences the nanomorphology without changing the absorption spectra of the materials. Apart from the chemical properties of the solvent, also its evaporation time can play a role.

3. Deposition parameters

   In the case of vacuum evaporated materials, parameters such as the substrate temperature and the deposition rates of the two materials determine the final morphology. In the case of solution processed materials, the parameters must be investigated case by case depending on which technique is employed.

4. Post-production annealing

   As it has been introduced above, it has been demonstrated that annealing treatments, performed after the deposition process, in some cases allow to obtain phase separation and enlargement in crystals dimension. As a result, the charge carrier transport is facilitated.

5. Use of A-B diblock-copolymers

   Polymers with a donor and an acceptor part in the same molecule have demonstrated self-organizing properties. Moreover, such kind of molecules guaranties the most complete contact between donor and acceptor.

6. Polymer nanoparticles

   Polymer spheres with nanometric dimensions have been obtained by miniemulsion preparation. The particles are obtained in aqueous solution and stabilized by using surfactants and ultrasound treatments; then they are spin cast.

In Figure 3.7 the energetic position of HOMO and LUMO for all of the materials investigated in this work is presented together with the work function of two typical electrodes[92,93,94]: ITO and aluminium. In the lower part of the figure the optical gap (E_g), obtained from the difference between HOMO and LUMO levels, is also indicated.

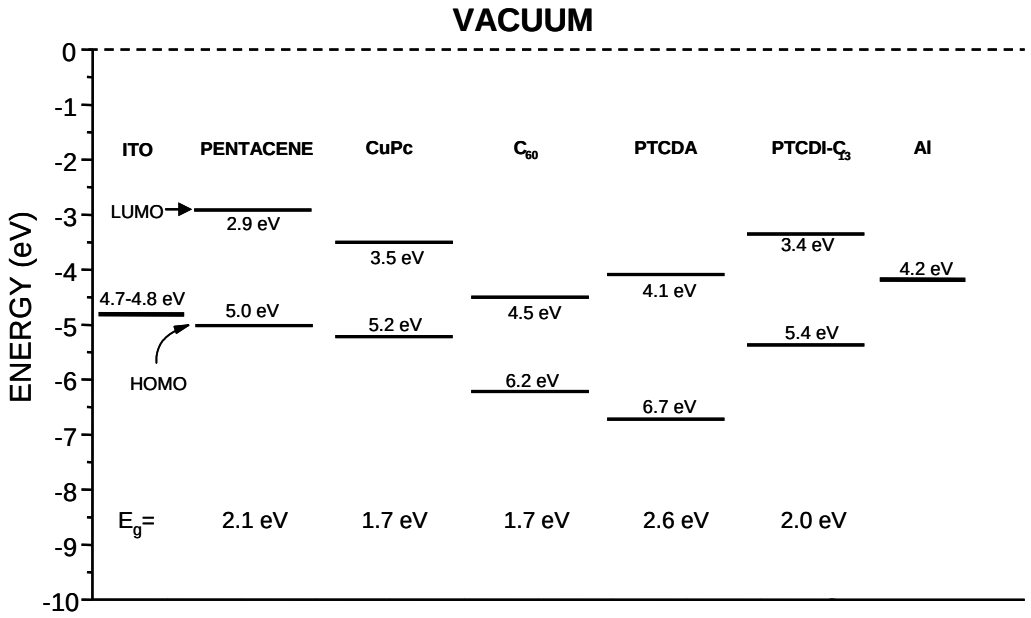

Figure 3.7. HOMO and LUMO positions for pentacene, CuPc, C_{60}, PTCDA and PTCDI-C_{13} together with the work function values of ITO and aluminium. The difference between HOMO and LUMO levels corresponds to the optical gap (E_g), also indicated in the image.

3.4.4 Other device structures: hybrid solar cells

Other types of solar cells involving organic semiconductors are the hybrid structures. Inorganic materials are, for the moment, the best known semiconductors. The objective is to unify materials of proven efficiency as silicon with materials with a great versatility like organic materials.

An example of hybrid heterojunctions are the cells made of an organic donor material deposited on nanoporous TiO_2. The nanopores of the inorganic matrix are filled by the spin cast polymer,

creating an extended interfacial area. Cells of this type have been fabricated by using poly(3-hexylthiophene) P3HT as the organic semiconductor[95,96].

Another type of hybrid heterojunction has been obtained by blending acceptor inorganic nanoparticles in an organic material. An example of such cell is the one made of CdSe crystals dispersed in P3HT[97].

Hybrid silicon/organic cells are another type of cell that has been tried. Silicon is the most common semiconductor and its properties and deposition techniques are well known. Moreover, the use of silicon could solve the difficulty to find stable *n*-type organic semiconductors[18,19]. Hybrid cells have been fabricated with a *p-i-n* type structure, where the layer *p* was made of PEDOT:PSS [*poly(3,4-ethylenedioxythiphene) : poly(styrenesulfonate)*] while *i* and *n* layers were made of hydrogenated amorphous silicon (Si:H) deposited by *Plasma Enhanced Chemical Vapour Deposition* (PECVD)[98]. Another field of investigation is focalized on the research on electronic memories with a *p-n* structure, made of PEDOT:PSS/n-type silicon[99]. Nevertheless, such kind of devices present several questions about important issues like the interface between silicon and organic materials, the way the organic molecules deposit on silicon and the band structure at the interface[100].

The most important hybrid technology at the moment is the *Dye Sensitized Solar Cell* (DSSC). A dye acts as a photosensitizer for mesoporous titanium oxide (TiO_2) and the presence of an electrolyte (I^-/I_3^-) is needed to compensate the charge in the system. With this technology efficiencies of 10% have been reached. DSSC has the drawback of containing a liquid electrolyte which requires hermetic sealing. Anyway, new solid electrolytes are under study and are available on the market.

CHAPTER 4

EXPERIMENTAL

In this chapter the deposition and characterization techniques used in this work will be described. Section 4.1 is dedicated to the thin film deposition equipment; in section 4.2 a description of the optical characterization techniques is given: Photothermal Deflection Spectroscopy (PDS) and Optical Transmittance Spectroscopy; in section 4.3 a description of X-ray Diffraction (XRD) technique is presented; finally, an introduction to the electrical characterization equipment is given in section 4.4. With the description of the equipments, a brief introduction about the treatment of the data will be given, paying special attention to PDS due to its central importance for this work.

4.1 Organic thin film deposition

As it has been introduced previously, small molecule organic materials are commonly deposited by thermal vacuum evaporation. The equipment employed in this work is located in the Department of Electronic Engineering laboratories of the *Universitat Politècnica de Catalunya* (UPC). Two different evaporation chambers are in use: one for the evaporation of metallic contacts and one for the evaporation of all kind of organic semiconductors. In Figure 4.1 there are photos of the systems used. The employment of two different chambers is due to the need to avoid mixing two kinds of materials, such as metals and organic semiconductors, with an evident risk of contamination.

Both evaporation systems are equipped with a mechanical pump and a turbo-molecular pump, pirani and penning systems for measuring the pressure in the chamber and the corresponding crucibles for the thermal evaporation.

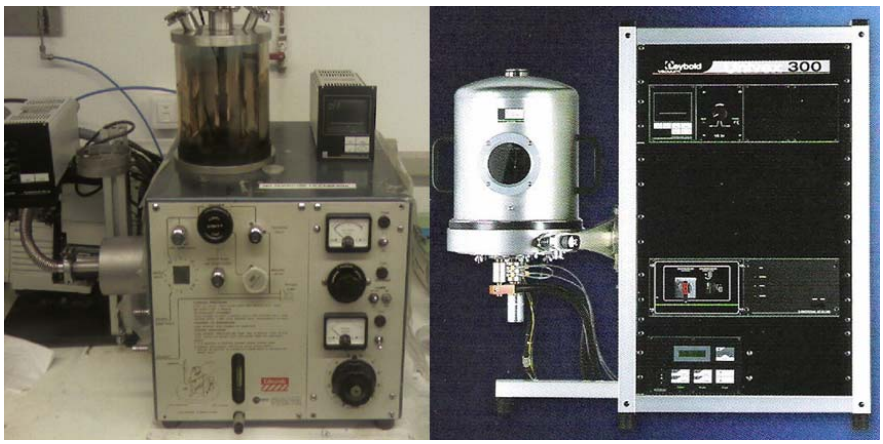

Figure 4.1. Pictures of the system used for evaporating metals (left side) and of the system employed for organics (right side).

The system destined to metals deposition is equipped with a homemade molybdenum crucible through which an electric current flow is activated when ready to deposit. Because of the Joule effect the crucible becomes hot, reaching metals melting temperatures. In this case we have no shutter, no control on the source temperature or on film thickness. The deposition processes are normally carried out without heating up the substrates. There is no special requirement for the crucible shape, given that metals firstly melt and then evaporate, avoiding problems that are common with materials that directly sublimate, in which case a crucible with a more closed aperture is needed to prevent from clusters to be projected directly onto the substrate surface. The deposition process is performed with a base pressure of 10^{-4} Pa.

The system for organic semiconductor deposition is by Leybold, model Univex 300, and is equipped with two cylindrical ceramic crucibles by Kurt Lesker, located on the base of the chamber, which allow the deposition two different materials without having to break the vacuum. The crucibles are rounded by spiral resistances that produce heat when the electrical current flow is activated. The temperature of the two sources is regulated by two separated PID (proportional-integrate-differential) controllers and measured by thermocouples. Heating up the substrate is also allowed by means of a resistance controlled by another PID system. When necessary, it is possible to deposit a third material by using a metallic crucible placed near the ceramic ones. The metallic crucible is only employed to evaporate bathocuproine (BCP), a material used to obtain better contact properties when deposited in between organic *n*-type semiconductors and metal contacts. Film thickness is measured by an oscillating quartz crystal: the more material is getting deposited on its surface, the more its oscillation frequency changes. This variation is used to estimate the thickness through the use of three parameters: the *tooling factor*, the density of the material and the

acoustic impedance of the material. The data regarding the material can be often found in literature, while the tooling factor can be calculated from the geometry of the system composed by source, substrate and quartz crystal.

The steps followed during a deposition process are listed below:

- cleaning of glass substrates using acetone and isopropyl alcohol
- UVO (ultraviolet generated ozone) treatment of the substrates for half an hour
- evaporation of organic materials
- when required, evaporation of metals

After the deposition process, the samples are introduced into a vacuum box to keep them as safe as possible from contact with water and oxygen and to keep them in the dark. Finally, the samples are immediately taken to the measurement equipments.

4.2 Optical characterization techniques

In this section the optical characterization techniques employed in this work are presented with a brief theoretical description. Optical Transmittance Spectroscopy has been used to have a rapid view on films optical properties. Moreover, these measurements have been necessary to calibrate measurements performed by PDS. PDS is a very sensitive technique which allows the measurement of low-level absorption, in the sub-gap region of the spectrum. The features found in this region are due to transitions that involve energetic levels generally associated with defects.

4.2.1 Photothermal Deflection Spectroscopy (PDS)

INTRODUCTION

Traditional Optical Transmittance Spectroscopy is able to reach a sensitivity of $\alpha d = 10^{-2}$, where α is the absorption coefficient and d the thickness of the absorbing film. Photothermal Deflection Spectroscopy can reach sensitivity values near to $\alpha d = 10^{-5}$ and detects the absorption due to recombination defects associated with energetic states located in the gap of the semiconductor[101].

The measurement is carried out by indirect means, i.e. by measuring the deflection of a laser beam passing in front of the sample, which is proportional to the heat produced as a consequence of light absorption (see paragraph below). Non-radiative recombination of the photo-generated charge carriers in the sample is the origin of the heat, which is then transmitted to a transparent, inert liquid (Fluorinert^{TM} FC-40) in which the sample is submerged. The variation of refractive index in the liquid causes the deflection of the laser beam which is measured by a position-sensitive detector. The amplitude of the deviation is proportional to the amount of absorbed light. The mechanism, also known as the mirage effect, is depicted in Figure 4.2:

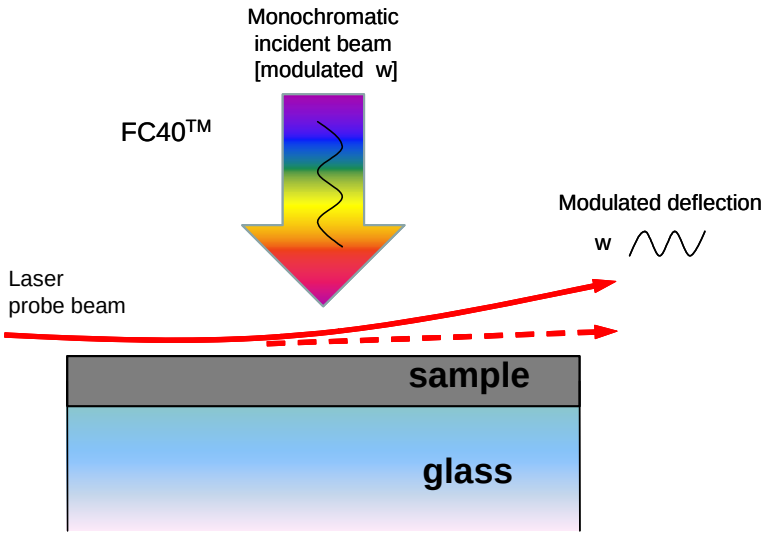

Figure 4.2. Sketch of the modulated deflection of the laser beam.

As the system installed in our laboratory was 20 years old and suffering from several problems due to noise and mechanical stability, long time was dedicated to building a new one. New optical components were acquired from Thorlabs Inc. and mounted on an optical breadboard in order to obtain a better mechanical stability of the system. In Figure 4.3 a picture of the system is showed with a description of all of the components.

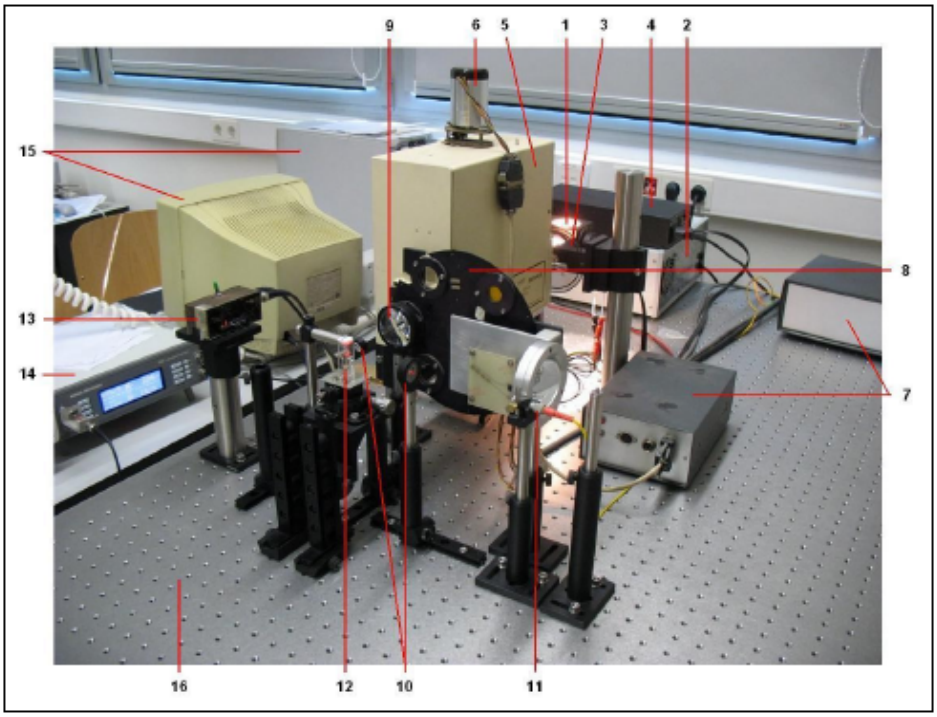

Figure 4.3. Picture of the PDS system: (1) light source, (2) power supply for light source, (3) opto-mechanical chopper blade, (4) opto-mechanical chopper controller, (5) monochromator, (6) monochromator stepping motor, (7) control units for monochromator and filter wheel motors, (8) filter wheel and its motor, (9) plano-convex lens, (10) bi-convex lenses, (11) laser, (12) quartz cuvette with sample, (13) position-sensitive detector, (14) lock-in amplifier, (15) computer, (16) optical table.

The light source (component nº 1 in Figure 4.3) is a 100 W halogen bulb, while the laser (nº 11) is a solid state one, with a 635 nm wavelength. The monochromator (nº 5) is from PTI and is equipped with two diffraction gratings with 1200 lines/nm and 600 lines/nm and with a mechanical scanning range of 0-1100 nm and 0-2200 nm respectively. As a result, it is possible to measure from 400 to 2000 nm (3.1 - 0.62 eV) just by changing the grating during the measurement. This operation has to be done manually, since there is no automatic control for it. An opto-mechanical chopper blade (from Thorlabs Inc.), positioned in between the light source and the monochromator (nº 3), modulates the incident light with a frequency of 8 Hz and is controlled by an electronic unit (nº 4) which sends a reference signal, with the same frequency to the lock-in amplifier (nº 14). The position-sensitive detector (nº 13) consists of two photo-diodes which give a current signal proportional to the amount of light illuminating them. The lock-in amplifier is an AMETEK, model 7265, connected to a computer (nº 15). The role of the lock-in is to calculate the difference between the signals originated by the two photo-diodes and to filter them from signals with a frequency different from 8 Hz. The PC collects the signal and the phase, respect to the reference, and depicts a

graph automatically. The data are then used to calculate the absorption coefficient (see paragraphs below). In front of the monochromator exit slit there is a filter wheel (nº 8) equipped with three dichroic filters which eliminate unwanted diffraction orders from the incident light. The sample is placed into a quartz cuvette, containing Fluorinert™. This is a transparent liquid and is necessary to obtain good heat transmission in the deflection medium. The most common liquids used for PDS spectroscopy are *carbon-tetrachloride* (CCl_4) and Fluorinert™. The former has better thermal properties: thermal capacities are equal to 0.87 and 1.03 J/g·K respectively, while thermal diffusion lengths are equal to 49 and 32 μm. Nevertheless CCl_4 is dangerous for health, being carcinogenic, so Fluorinert™ is the one we chose to employ. Two lenses (nº 10) focus the monochromatic light onto sample surface.

The new system is isolated from the external environment by black curtains mounted on a rigid structure made of aluminium profiles. Such coverage prevents the measurements from being affected by temperature variations and air movement around the cuvette. As the system is extremely sensitive to any mechanical vibration, the optical table is placed on a thick table that absorbs most of the vibrations coming from the ground.

The software used to manage the equipment has been programmed with Visual Basic and the interface is a GPIB IEEE controlled by Microsoft Excel.

PDS is a system that could require a lot of time to align the sample with the laser and the incident light. The alignment process begins with the search of the signal maximum, in order to obtain easy detection. For this purpose, data obtained from an optical transmittance measurement, could be of use.

PHYSICS OF PDS

In this paragraph the physical mechanisms of PDS will be described in detail. As it has been said above, the sample is illuminated by a monochromatic light, the absorption of which causes heat generation as a consequence of non-radiative recombination of the charges. This heat is transmitted to the liquid, into which the sample is dipped, with the consequent appearance of gradients in its temperature and refractive index. When the laser crosses the gradient it is deflected an angle proportional to the absorption in the sample. Moreover, a chopper modulates the monochromatic light with a frequency of 8 Hz which is also transmitted to the temperature gradient and the laser deviation. The position-sensitive detector allows to quantify the amplitude of the deflection that is proportional to the temperature gradient and to the amount of light absorbed by the sample. The use of the chopper is motivated by the need to use a lock-in amplifier in order to filter this signal from

all the signals present in the environment like external light, changes of temperature, mechanical vibrations, etcetera. The lock-in receives a signal reference from the chopper and eliminates all the signals with a frequency different from the one set in the chopper controller.

The total process, formed by the excitation followed by non-radiative recombination of the photo-generated charge carriers, is much faster than a single cycle of the incident light. Therefore, the intensity measured in each single cycle is the result of many recombined charges carriers. Moreover, the time constant set in the lock-in allows to average many cycles and the higher the time constant, the lower the noise affecting the measurement.

In Figure 4.4, a scheme represents the system composed by sample, monochromatic light and laser. Considering the magnitude of the laser spot much smaller than the surface illuminated by the monochromatic light, we can solve the differential equation just in one dimension. So it is possible to calculate the amount of heat developed as follows:

$$q = -\frac{dI}{dz} = \alpha I e^{-\alpha z} e^{i\omega t} \tag{4.1}$$

where α is the absorption coefficient of the material, I the intensity of the incident light, ω the angular frequency and z the coordinate along the direction of propagation.

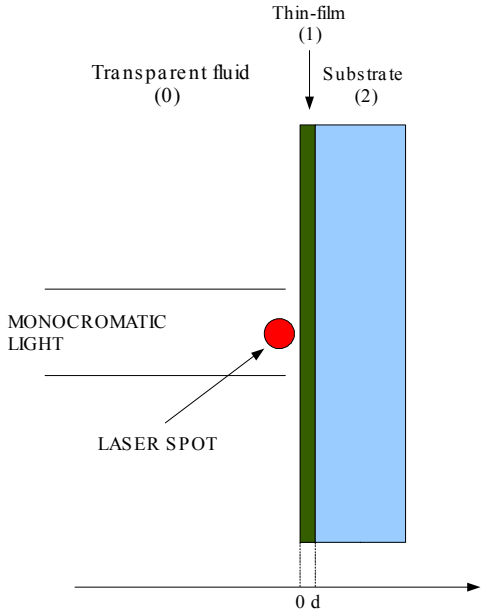

Figure 4.4. Side view of the system composed by liquid/thin film/substrate. The monochromatic light and the laser spot are also shown.

Then for the three media composing the system we have:

$$\frac{\partial^2 T_0}{\partial z^2} - \frac{1}{k_0}\frac{\partial T_0}{\partial t} = 0 \qquad \frac{\partial^2 T_1}{\partial z^2} - \frac{1}{k_1}\frac{\partial T_1}{\partial t} = -\frac{q}{K_1} \qquad \frac{\partial^2 T_2}{\partial z^2} - \frac{1}{k_2}\frac{\partial T_2}{\partial t} = 0 \tag{4.2}$$

with $k_j = \dfrac{K_j}{\rho_j C_j}$, where K_j is the thermal conductivity of the medium, ρ_j the medium density and C_j the specific heat. The subscripts *0*, *1* and *2* refer to the media as indicated in Figure 4.4. If we consider the extreme media (*0* and *2*) semi-infinite, the solutions for equations (4.3) are the following:

$$T_0 = Ae^{\beta_0 z}e^{i\omega t} \qquad T_1 = \left(\Gamma e^{-\alpha z} + Ce^{-\beta_1 z} + De^{\beta_1 z}\right)e^{i\omega t} \qquad T_2 = Be^{-\beta_2 (z-d)}e^{i\omega t}$$

$$\beta_j^2 = i\frac{\omega}{k_j} \qquad \beta_j = \sqrt{\frac{\omega}{2k_j}}(1+i) = \frac{1}{L_j}(1+i) \qquad \Gamma = \frac{\alpha}{\beta_1 - \alpha^2}\frac{1}{K_1} \tag{4.3}$$

The next step is then to calculate the coefficients *A*, *B*, *C* and *D* by applying the boundary conditions, i.e. temperature and heat must be continuous at the interfaces:

$$T_0(0) = T_1(0) \qquad T_1(d) = T_2(d)$$

$$K_0\left(\frac{\partial T_0}{\partial z}\right)_0 = K_1\left(\frac{\partial T_1}{\partial z}\right)_0 \qquad K_1\left(\frac{\partial T_1}{\partial z}\right)_d = K_2\left(\frac{\partial T_2}{\partial z}\right)_d \tag{4.4}$$

$$A - C - D = \Gamma \qquad B - e^{-\beta_1 d}C - e^{\beta_1 d}D = \Gamma e^{-\alpha d}$$

$$K_0\beta_0 A + K_1\beta_1 C - K_1\beta_1 D = -K_1\Gamma\alpha \qquad K_2\beta_2 B - K_1\beta_1 e^{-\beta_1 d}C + K_1\beta_1 e^{\beta_1 d}D = K_1\Gamma\alpha e^{-\alpha d}$$

So the coefficients have the following values:

$$C = -\left[(g+r)(1+b)e^{\beta_1 d} + (1-g)(b-r)e^{-\alpha d}\right]\frac{\Gamma}{E}$$

$$D = -\left[(1+g)(b-r)e^{-\alpha d} + (1-b)(g+r)e^{-\beta_1 d}\right]\frac{\Gamma}{E} \tag{4.5}$$

$$E = (1+g)(1+b)e^{\beta_1 d} - (1-g)(1-b)e^{-\beta_1 d}$$

$$g = \frac{K_0\beta_0}{K_1\beta_1} \qquad b = \frac{K_2\beta_2}{K_1\beta_1} \qquad r = \frac{\alpha}{\beta_1}$$

The real part of the coefficient β is equal to the inverse of the thermal diffusion length (L) in the medium: Re(β) = 1/L. Such value represents the distance in which the heat is attenuated and is characteristic for the material in which it is propagating. The imaginary part of β corresponds to the propagation constant of the plane wave.

Considering that in semiconductors the light diffusion length normally has values around some hundreds of nanometres, when modulating the incident light with frequencies of tens of Hz, we can employ the following approximation:

$$e^{\pm\beta_1 d} \approx 1 \tag{4.6}$$

so we can calculate the coefficient A as follows:

$$A = \Gamma + C + D \approx \frac{b-r}{b+g}\left(1 - e^{-\alpha d}\right)\Gamma \tag{4.7}$$

Taking z as the direction perpendicular to the film surface and parallel to the monochromatic light path, the temperature of the liquid in this region suffers a variation dT going from position z to position $z+dz$. Thermal changes imply also variations in the refractive index of the liquid and, as a result of this, the laser is deviated from its original path by an angle $d\varphi$ (Figure 4.5).

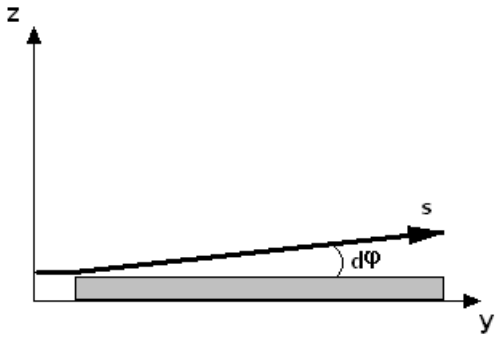

Figure 4.5. The laser follows trajectory *s* in front of the sample surface.

The refractive index *n*, the trajectory *s* and the deflection angle φ come from the following equations:

$$\begin{aligned} c = n\nu \Rightarrow \nu dn + n d\nu = 0 \Rightarrow |d\nu| = \left|\nu \frac{dn}{n}\right| \\ d^2 s = d\nu dt = \nu \frac{dn}{n} dt = \nu \frac{dn}{n}\frac{dy}{\nu} = \frac{dn}{n} dy \\ d\varphi = \frac{d^2 s}{dz} = \frac{1}{n}\frac{dn}{dz} dy = \frac{1}{n}\frac{\partial n}{\partial T}\frac{\partial T}{\partial z} dy \end{aligned} \tag{4.8}$$

If the angle φ is small enough to consider that the refractive index and the thermal gradient are constant along the trajectory *s*, then we can compute the angle as follows:

$$\varphi = \int_0^s \frac{1}{n}\frac{\partial n}{\partial T}\frac{\partial T}{\partial z} dy = s\frac{1}{n}\frac{\partial n}{\partial T}\frac{\partial T}{\partial z} \tag{4.9}$$

As it has been said before, the incident light is modulated using a chopper and so is the signal received by the lock-in. The signal with angular frequency ω and intensity proportional to the laser deviation amplitude through a factor η, which depends on the detector, is:

$$S = \eta\varphi = \eta s \frac{1}{n}\frac{\partial n}{\partial T}\frac{\partial T}{\partial z} \tag{4.10}$$

By changing the direction of the z axis, it is possible to make the calculation using positive coordinates and, in this case, the temperature gradient in the deflecting medium is given by the following expression:

$$\frac{\partial T}{\partial z} = -A\beta_0 e^{-\beta_0 z} e^{i\omega t} \tag{4.11}$$

By using equation (4.11) we can calculate the signal as follows:

$$S = -\eta s \frac{1}{n}\frac{\partial n}{\partial T}\frac{b-r}{b+g}\left(1-e^{-\alpha d}\right)\Gamma\beta_0 e^{-\beta_0 z} e^{i\omega t} \tag{4.12}$$

For a system composed of Fluorinert/silicon/glass, and working with chopping frequencies of around 10 Hz, we obtain an approximated expression for the signal as follows:

$$S \approx -\eta s \frac{1}{n}\frac{\partial n}{\partial T}\frac{1}{K_2\dfrac{L_0}{L_2}+K_0}\left(1-e^{-\alpha d}\right)Ie^{-z/L_0}e^{i(\omega t - z/L_0)} \tag{4.13}$$

CALCULATION OF THE ABSORPTION COEFFICIENT

In this paragraph, the method used to calculate the α will be discussed, using silicon measuring as a reference.

Equation (4.13) can be rewritten in a more simple way:

$$|S| = FA(\lambda)I(\lambda) \tag{4.14}$$

where F has a constant value during the whole measurement and depends on z, ω and on the thermal properties of the substrate and the liquid medium. In the absorbance $A(\lambda)$, multiple internal reflections between the interfaces are kept into account.

The measurement procedure begins by taking a spectrum of a graphite sample as a reference. Being black, the reference is supposed to absorb all the light. In this case the signal detected is:

$$|S_r(\lambda)| = F_r I(\lambda) \tag{4.15}$$

Given that the only absorbing component is the thin film, and that any effect due to the substrate is avoided, we can calculate the absorbance as indicated below:

$$A(\lambda) = \frac{F_r}{F} \frac{|S(\lambda)|}{|S_r(\lambda)|} \tag{4.16}$$

The absorption coefficient is then calculated as indicated below:

$$\alpha_{PDS} = C \cdot \left(- \frac{\ln(1 - A)}{d} \right) \tag{4.17}$$

where C is a constant and d the thickness of the film. In order to calculate the value of C, a calibration with Optical Transmittance Spectroscopy is necessary. The procedure followed is then to measure a transmittance spectrum and to calculate the absorption coefficient by using the following expression:

$$\alpha_T = - \frac{\ln(T)}{d} \tag{4.18}$$

where T is the transmittance spectrum measured in a range between 400 and 1100 nm. The measurement is performed with the system described in the paragraph that follows, which can only work in the visible and a part of the near infrared ranges. The constant C is then calculated by multiplying α_{PDS} by a factor in order to equalize it with α_T as it is shown in Figure 4.6. As it can be seen, PDS technique is more reliable in the sub-gap region (red part of the thinner line), while the optical transmittance spectroscopy in the high-absorption region (red part of the thicker line).

The final α spectrum is constructed by taking α_{PDS}, corrected as explained above, for the sub-gap region of the spectrum and α_T for the band-to-band transition region (the red line in the figure). The reason for such procedure is that PDS is a very sensitive technique that allows the measurement of low-level absorption but is not reliable to measure intense absorptions like the ones associated with band-to-band transitions. In this part of the spectrum transmittance spectroscopy is better performing. Since PDS is very time consuming, the measurements have been performed with a lower resolution than in the case of the optical transmittance.

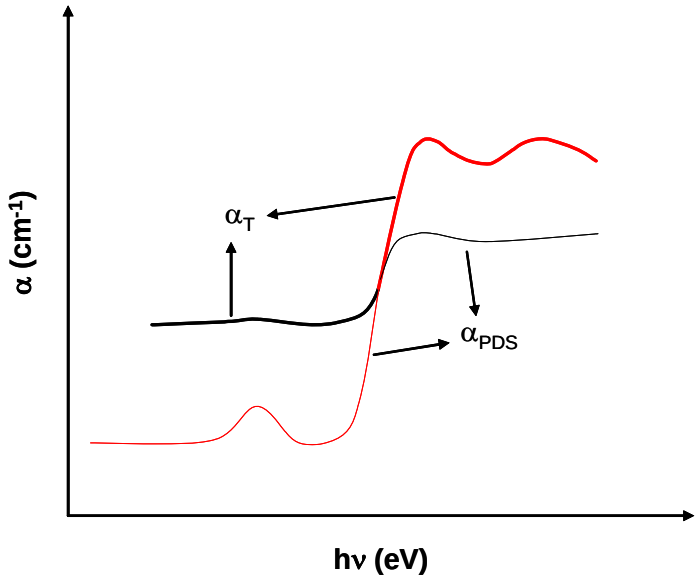

Figure 4.6. Graphical reproduction of the calibration of PDS curve (thin line) with the one measured by optical transmission (thick line). In red the selected parts which compose the final absorption coefficient curve.

The spectrum is composed of three regions: the low-absorption region (low energy: NIR-near infrared), the exponential region (NIR+visible) and the high-absorption region (high energy: visible). In Figure 4.7, the absorption spectra of hydrogenated amorphous and crystalline silicon are shown as two examples (Figure 4.7-a), along with the density of states diagram for the two materials (Figure **4.7**-b).

In the case of crystalline silicon only band-to-band transitions are possible because there are no available states in the gap. As a consequence, the absorption coefficient α goes down to zero for energies lower than its optical gap (E_{og} = 1.12 eV). In Figure 4.7 the transitions between valence band and conduction band are depicted in blue for crystalline silicon.

In the case of hydrogenated amorphous silicon (a-Si:H), non-zero absorption is measured for energies lower than the optical gap of the material (E_{og} = 1.8-1.9 eV). In the low-energy region the absorption is due to intra-gap localized states usually caused by the presence of structural defects and/or impurities. We have exponential increase of the absorption coefficient due to transitions that involve the band tails, where extended states are located. In the high-absorption region, absorptions due to band-to-band transitions are detected.

The scheme here proposed is typical for disordered semiconductors like a-Si:H [102]. In the case of organic materials, the second and third regions can also contain absorptions due to the generation of excitons (see Figure 2.20).

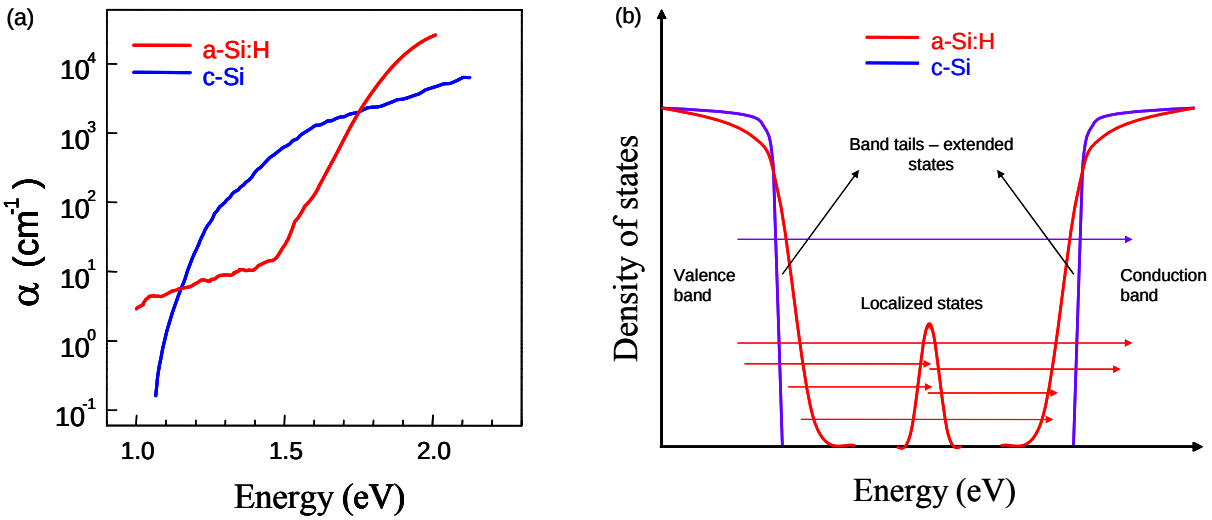

Figure 4.7. (a) Absorption coefficient spectra of crystalline (blue line) and hydrogenated amorphous silicon (red line); (b) density of states of crystalline (blue line) and hydrogenated amorphous silicon (red line): the former has no states in the gap, while the latter has band tails and localized states. The blue and red arrows indicate all the possible transitions between these states.

4.2.2 Optical Transmission Spectroscopy

Optical Transmittance has been used as a complementary spectroscopy, in order to complete the information regarding the optical properties of our materials.

A transmittance measurement is performed in the following way: a reference T_0 is taken with air, in order to measure the intensity of the incident light; than a new spectrum T_1 is taken with the sample. The ratio between the sample spectrum and the reference one is called transmittance (T) and indicates the amount of light that has passed through the sample:

$$T = \frac{T_1}{T_0} \tag{4.19}$$

The equipment used is an USB2000 by Ocean Optics. It is constituted by two optical fibres, the first one taking the light from a lamp to the sample, the second one taking the light that passed through the sample, to the detector. Software given by Ocean Optics with the instrumentation calculates the transmittance spectra. With this equipment it is only possible to measure the optical transmittance in a wavelength range between 400 and 1000 nm. In Figure 4.8 there are two pictures of the system:

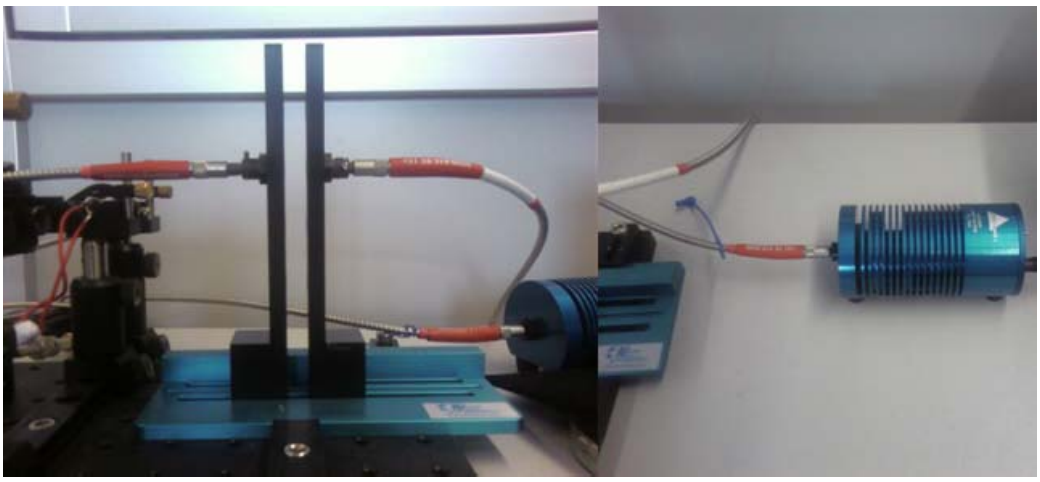

Figure 4.8. Picture of the Ocean Optics system for transmittance measurements: in the left side the two optical fibres between which the sample is placed for the measurement, in the right side the lamp.

4.2.3 Calculation of optical gap and Urbach energy

Important parameters of a material like the optical gap and the Urbach energy can be calculated from its absorption coefficient. For this purpose a fit of the exponential part of the spectrum must be done by using the adequate models, the choice of which depends on the kind of material under study (amorphous, polycrystalline...).

The optical gap of semiconductors in presence of direct allowed transitions follows the next expression[103,104]:

$$\alpha(h\upsilon) = B \cdot \left(h\upsilon - E_{og}\right)^{1/2} \tag{4.20}$$

where B is a constant, $h\nu$ the energy of the incoming photon and E_{og} the optical gap. Such model comes from the general theory of inorganic semiconductors, considering that valence and conduction bands follow a parabolic law. Few examples can be found in literature about its employment with organic semiconductors[105,106,107].

In the case of disordered semiconductors, Tauc's law is more adequate to evaluate the optical gap. Tauc's equation can be written, in the case of parabolic band edges, in the following way[108]:

$$\left[\alpha(h\upsilon)\cdot h\upsilon\right]^{1/2} = A \cdot \left(h\upsilon - E_{og}\right) \tag{4.21}$$

where A is a constant.

The presence of deep and band-tail localized states modifies the optical absorption in disordered semiconductors. The optical transitions caused by localized states (see Figure 4.7) in the gap give rise to the Urbach front (or Urbach tail), as illustrated in Figure 4.9:

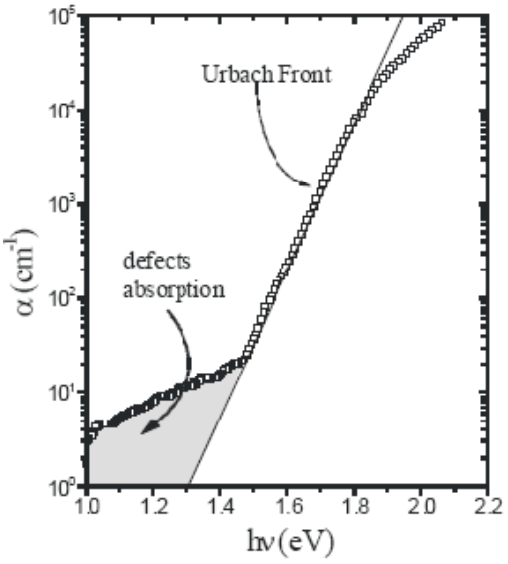

Figure 4.9. Absorption coefficient of a-Si:H: the presence of defects causes absorption in the sub-gap region, highlighted in the figure, as well as the slope in the Urbach tail.

The Urbach energy gives information about the structural order of a material and can be calculated as follows[109]:

$$\alpha(h\upsilon) = \alpha_0 \exp\left(\frac{h\upsilon}{E_u}\right) \tag{4.22}$$

where α_0 is a constant, $h\nu$ the energy of the incoming photon and E_u the Urbach energy. Such value is generally interpreted as a quality indicator in inorganic amorphous semiconductors. In the case of a-Si:H values around 50 meV indicate device quality material[108]. The higher the density of states in the gap, the higher the Urbach energy value. An example of the use of this model with organic semiconductors is given by Tamihiro Gotoh and co-workers for the case of fullerene[110].

In this thesis the values obtained by the models described above will be taken just as qualitative indicators, since a specific model for organic semiconductors has not been yet developed.

4.2.4 Important aspects of PDS measurement

It is worth discussing about some features of measuring with a PDS system, especially in view of an interpretation of the results. As it has been explained, PDS is a very sensitive technique and it is used to detect absorptions in the sub-gap region of the semiconductors (NIR). The signal is, in this case, so low that the ratio between signal and noise becomes very critical. The use of a lock-in amplifier allows the signal to be filtered and amplified, but in many cases this is not enough to obtain a good measurement if the films are very thin. A thickness of the order of one micron is typically necessary in order to obtain a good quality measurement. The signal of such kind of films is usually high enough to be detected, with our system, using time constants between 2 and 10 s, allowing to complete a measurement in a reasonable time (~3 hours).

When the conditions are not optimal, higher time constants must be used and the time to complete an entire measurement can increase up to ten hours. This is the case, for example, of films with thicknesses of the order of 100 nm. Moreover, when, for any of the causes here discussed, the sample absorption is low, absorptions in the substrate could be detected.

The absorptions detected by PDS in the sub-gap region are due to both bulk and surface components[111]. If the sample is very thin (a few tens of nanometres) the resulting absorption could be strongly determined by superficial defects. On the contrary, in a thick sample (one micron) the bulk, possibly more ordered, phase takes relevance. Some difference is then to be expected between measurements in function of the thickness.

Another aspect that must be taken into account is connected to the optical transmittance in the visible region (band-to-band optical transitions). Thick samples can have zero transmittance in a part of the spectrum, making the calculation of α by using these data impossible. This phenomenon will be clearly shown in CHAPTER 5. In such cases, measuring a thin film helps to define all the absorption features present in the high-energy part of the spectrum (band-to-band optical transitions).

4.3 Other characterization techniques

4.3.1 X-ray diffraction spectroscopy (XRD)

X-ray Diffraction (XRD) has been used to know some details about the micro-structure of the thin films. The equipment used in this work is located at the *Serveis Cientificotècnics* of the *Universitat de Barcelona*.

A detailed identification of the crystalline structure was not an aim of this thesis. XRD has been employed to establish if the films were amorphous or polycrystalline and, moreover, to identify the crystalline phases just by comparing the results with the literature. For this purpose, the Bragg-Brentano geometry has been used. In Figure 4.10 a scheme of this kind of configuration is shown:

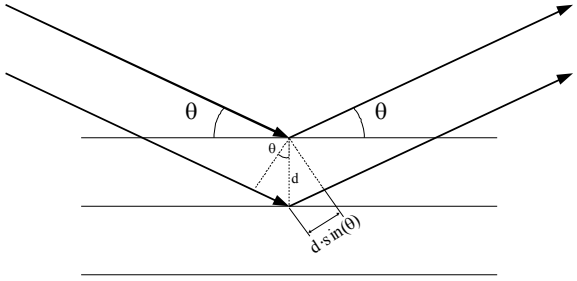

Figure 4.10. Scheme of the Bragg-Brentano geometry for XRD: the incident and reflection angle (θ) are equal; *d* is the distance between the crystallographic planes.

In this case, the X-ray source and the detector are positioned at an equal angle with respect to the sample surface.

In this figure, the horizontal lines represent the families of crystallographic planes. The possibility to have or not a reflection, and so a peak in the spectrum, is regulated by Bragg's law:

$$n\lambda = 2d_{hkl}\sin\theta \tag{4.23}$$

where n is the diffraction order, λ the wavelength, d_{hkl} the distance between the planes (d-spacing) and θ the incident (and reflection) angle. From equation (4.23) it is possible to correlate the d-spacing and the reflection angle. Since the spectra are composed of intensity counts as a function of the detection angle, from the experimental data it is possible to calculate the interplanar distance of the planes that have given that reflection. In this work the angular positions of the diffraction peaks and the corresponding d-spacings have been compared with data found in literature.

In some cases it is useful to calculate the dimension of the crystalline grains that have given rise to a diffraction peak. The dimension of the crystals *t* is related with the shape of the diffraction peak through Scherrer's equation[112]:

$$t = \frac{0.9 \cdot \lambda}{FWHM \cdot \cos\theta} \tag{4.24}$$

where λ is the wavelength of the incident radiation (1.54 Å for X-rays), θ the angular position of the peak and *FWHM* is the full width at half maximum high of the peak and must be expressed in radians.

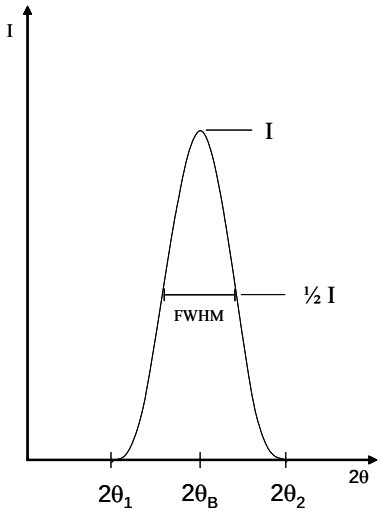

Figure 4.11. Representation of a diffraction peak: $2\theta_1$ and $2\theta_2$ are the angular positions at the base extremes, $2\theta_B$ the position of the peak, I its maximum intensity and FWHM its full width at half maximum.

A fit of the diffraction peak is calculated in order to obtain the data about the angular position of the peak and its FWHM. The fits have been performed by using the software Origin® using a pseudo-Voigt function that is the sum of a Lorentzian (*L*) and a Gaussian (*G*) functions and has the following form:

$$y = y_0 + A\left[m_u \cdot L + \left(1 - m_u\right) \cdot G\right]$$
$$= y_0 + A\left[m_u \frac{2}{\pi} \frac{w}{4\left(\theta - \theta_B\right)^2 + w^2} + \left(1 - m_u\right) \frac{\sqrt{4\ln(2)}}{\sqrt{\pi} w} e^{-\frac{4\ln(2)}{w^2}(\theta - \theta_B)^2} \right] \quad (4.25)$$

where w is the *FWHM*, A the area of the peak and m_u ($0 < m_u < 1$) the lorentzian component of the peak.

In a first approximation, the X-ray radiation has been considered monochromatic and no contribution from the $K_{\alpha,2}$ radiation of copper has been considered. Similarly, no instrumental contribution has been taken into account.

4.4 Electrical characterization of the devices

After a characterization phase of the optical and structural properties of the materials, devices have been fabricated by thermal vacuum evaporation. The devices studied in this work are Organic Thin Film Transistors (OTFTs) and diodes (see Appendix A). A detailed description of the electronic devices and their theory is not the objective of this thesis and may be found in literature[113]. In this section, the tools used to electrically characterize TFTs and diodes are briefly introduced.

All the electrical measurements on TFTs have been performed at the UPC laboratories in vacuum conditions (10^{-1} mbar) by means of a HP5156 parameter analyzer. The measurements on diodes have been done using an Agilent 4156 C system a scheme of which is shown in Figure 4.12. The whole system is composed of two golden smooth tips contacting the electrodes of the samples, an optical microscope to place the tips, the Agilent 4156 C to collect all the data and a computer to control all the equipment and for the data treatment. It is very important for the tips not to be too much aggressive with the surface of the sample in order to avoid any possible perforation of the organic materials and, therefore, short circuits. In the case of solar cells, the contacts are 1 mm^2; a small area that diminishes the probability to find short circuits. From this point of view, the thickness of the active layer is also important: the thinner the layer, the higher the probability to have short circuits.

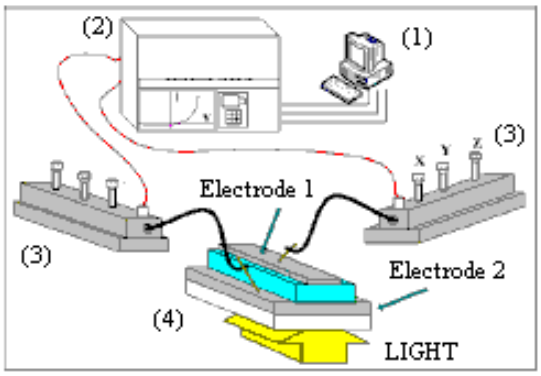

Figure 4.12. Scheme of the system for measuring the I-V curves: computer (1), Agilent 4156 C for data collection (2), golden smooth tips systems (3) and sample (4).

4.4.1 Thin film transistors

The OTFTs fabricated for this work have inverted staggered (top contact) geometry. The structure of such devices is shown in Figure 4.13.

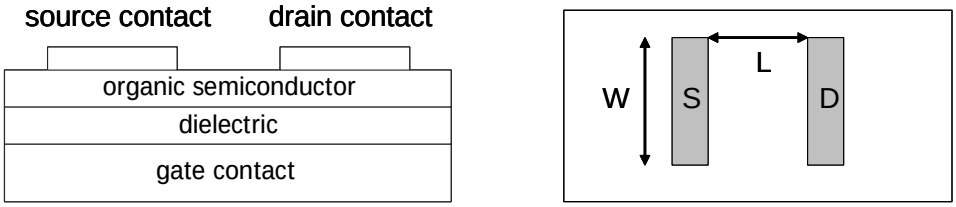

Figure 4.13. Side and top view of a TFT with inverted-staggered geometry. L is the length of the channel between source contact (S) and drain contact (D) and W is its width.

To characterize OTFT's, the same applications that are used for inorganic NMOS and PMOS transistors have been employed in this work.

In the saturation regime the current that flows between source and drain (I_{DS}) as a function of gate-source voltage can be written in the following way:

$$I_{ds} = \frac{WC_{ox}\mu}{2L}\left(V_{gs} - V_t\right)^2 \Rightarrow \sqrt{I_{ds}} = \sqrt{\frac{WC_{ox}\mu}{2L}\left(V_{gs} - V_t\right)^2} = \sqrt{\frac{WC_{ox}\mu}{2L}}\cdot V_{gs} - \sqrt{\frac{WC_{ox}\mu}{2L}}\cdot V_t \qquad (4.26)$$

where W is the channel width, L its length, μ the filed-effect mobility of the charge carriers, C_{ox} the capacity of the dielectric per unit area and V_t the threshold voltage.

The mobility and the threshold voltage can be calculated by fitting the experimental results with equation (4.26) as follows:

$$y = A + B \cdot x$$
$$A = \sqrt{\frac{WC_{ox}\mu}{2L}} \cdot V_t ;\ B = \sqrt{\frac{WC_{ox}\mu}{2L}} \tag{4.27}$$

The conductivity in semiconductors is thermally activated and follows an Arrhenius type of law:

$$\sigma = \sigma_0 \cdot e^{-\frac{E_a}{K_B T}} \tag{4.28}$$

where E_a is the activation energy, K_B the Boltzmann constant and σ_0 a constant of the material. The drain-source current can be then calculated using the following expressions:

$$\sigma = \frac{L}{W \cdot d}\frac{I_{DS}}{V_{DS}} \Rightarrow I_{DS} = \frac{W \cdot d}{L} V_{DS}\sigma_0 e^{-\frac{E_a}{K_B T}} = I_0 e^{-\frac{E_a}{K_B T}} \tag{4.29}$$

$$\ln(I_{DS}) = \ln(I_0) - \ln\left(\frac{E_a}{K_B T}\right) \tag{4.30}$$

The activation energy of the conductance indicates the position of the Fermi level in the semiconductor channel (in the case of an *n*-type semiconductor: $E_a = E_C - E_F$) providing information about the localized states in the band gap of the semiconductor on the energy scale. T. Globus and co-workers proposed a connection between the derivative of the activation energy and the density of states for devices fabricated from a-Si:H[114]. According to that work and within the hypothesis that energy variations around k_BT do not cause important changes in the density of states, the charge density of the states that have been occupied by applying a gate-source tension (V_{GS}) is given by the following expression:

$$Q_t = q\int_{E_C - E_{F0}}^{E_C - E_{F0} + qV_S} g(E)dE \tag{4.31}$$

where q is the electronic charge, V_S the surface potential and E_{F0} the equilibrium Fermi level in the semiconductor. The charge Q_t can also be expressed in the following way:

$$Q_t = \frac{qn_t}{d_t} = \frac{\varepsilon_i}{d_t d_i}\left(V_{GS} - V_{FB}\right) \tag{4.32}$$

where qn_t is the surface charge, V_{FB} is the flat-band voltage, ε_i and d_i are the permittivity and the thickness of the dielectric, respectively, and d_t is the thickness of the space charge layer.

By substituting equation (4.32) into (4.31) and differentiating with respect to V_{GS} we obtain

$$\frac{d}{dV_{GS}}\left(\frac{n_t}{d_t}\right) = g\left(E_a\right)\frac{dqV_s}{dV_{GS}} = -g\left(E_a\right)\frac{dE_a}{dV_{GS}} \tag{4.33}$$

where the activation energy E_a equals E_c - E_{F0}- qV_s. In the energy range qV_s, the density of states $g(E)$ is constant and equal to $g(E_a)$, so the result of the integral (4.31) is $g(E_a)qV_s$. The density of states in the band-gap can be calculated by using the following expression:

$$g\left(E_a\right) = -\frac{-\frac{d}{dV_{GS}}\left(\frac{n_t}{d_t}\right)}{\frac{dE_a}{dV_{GS}}} \tag{4.34}$$

In the case where the dielectric layer is thick and the semiconductor layer is thin, we can make the approximation $d_t \approx t$, where t is the thickness of the semiconductor, and obtain

$$g\left(E_a\right) = -\frac{\varepsilon_i}{qd_i t\frac{\partial E_a}{\partial V_{GS}}} \tag{4.35}$$

where ε_i is the dielectric constant.

4.4.2 Diodes

The diodes have been characterized by measuring the I-V curve using the equipment described above. Moreover, their response with light has been tested repeating the curve with light conditions. Such characterization allows to determine the parameters of efficiency (η), open circuit voltage (V_{oc}), short circuit current (I_{sc}) and fill factor (FF). In this work this measurement has been

performed by using a halogen lamp with 248 W/m^2 power density. The device is exposed to the light just for the time needed for the measurement, to avoid any degradation.

In Figure 4.14 an example of I-V curves, measured in obscurity (dark current) and light (light current) conditions, is presented:

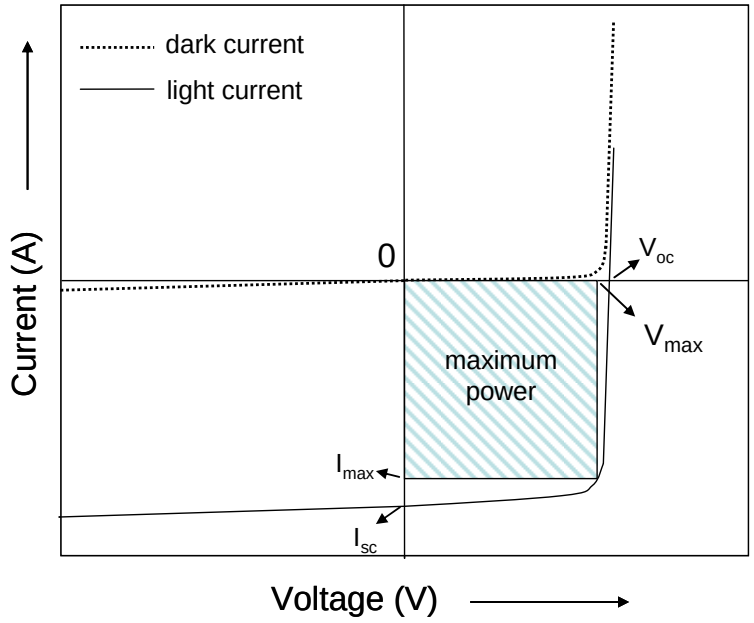

Figure 4.14. Example of an *I vs. V* curve in obscurity and with light irradiation.

When the device is illuminated, current is generated in it. Four parameters characterizing the solar cells are measured by taking the I-V curve: the already cited I_{sc} and V_{oc} and the values of maximum current (I_{max}) and voltage (V_{max}), calculated from the maximum power produced by the cell. The ratio between these values defines a parameter called *fill factor* (*FF*) as follows:

$$FF = \frac{I_{\max} \cdot V_{\max}}{I_{sc} \cdot V_{oc}} = \frac{P_{\max}}{I_{sc} \cdot V_{oc}} \tag{4.36}$$

The efficiency of the cell is then calculated as indicated below:

$$\eta = FF \frac{I_{sc} \cdot V_{oc}}{G \cdot S} = \frac{P_{\max}}{P_{in}} \tag{4.37}$$

where G [$W \cdot cm^{-2}$] is the density of incident power and S [cm^{-2}] is the surface of the cell. Equation (4.37) gives the relationship between the power efficiency of the cell and the other parameters.

CHAPTER 5

MATERIAL CHARACTERIZATION

In this chapter the experimental results obtained from the characterization of five organic semiconductors will be presented. Since the optical characterization is the most important aspect of this thesis, in this chapter will be mainly focused on the results obtained by PDS and Optical Transmittance Spectroscopy.

Firstly, a basic optical characterization has been performed on thin films to know the absorption properties of the organic semiconductors under study between 400 and 2000 nm, which includes the range of interest for photovoltaic applications. XRD has been employed in order to know if the thin films have grown with polycrystalline or amorphous structure. XRD spectra have been measured to have a reference to choose the most adequate law to calculate the optical gap of the semiconductors. An evaluation of the Urbach energy will be also proposed, as a useful parameter to check the quality of the materials.

5.1 Thin film characterization

All of the films have been deposited in the conditions listed below:

- thickness: 1 μm
- substrate temperature: room temperature
- deposition rate: 3 Å/s
- base pressure: ~$6 \cdot 10^{-4}$ Pa

All the results presented in the present paragraph have been obtained for as-deposited samples, which means samples characterized right after their extraction from the evaporation chamber.

PDS is a characterization technique that requires thick samples that give intense enough signal to be measured in the low-absorption range. Nevertheless, saturation could occur in the high absorption part of the absorption coefficient, due to the high thickness of the films. Such result is a consequence of the fact that the optical transmittance, with which that region is calibrated, of a very thick sample goes to zero in the visible range and there is no possibility to distinguish any absorption feature. For this reason also 100 nm-thick samples have been deposited and characterized by optical transmittance spectroscopy and PDS.

Another reason to perform an experiment on thinner films is to characterize the materials deposited in similar conditions to the ones used for solar cells: low thickness and low deposition rate. For this experiment the following deposition conditions have been chosen:

- thickness: 100 nm
- substrate temperature: room temperature
- deposition rate: 0.4 Å/s
- base pressure: ~$6 \cdot 10^{-4}$ Pa

The thickness has been chosen similar to the values it should have in a cell in order to optimize the dissociation of excitons, taking into account their diffusion length. The low deposition rate of 0.4 Å/s has also been chosen to be similar to the values used to fabricate solar cells.

The thickness of each sample has been checked by a stylus profiler. The α spectra, obtained for each of the five materials deposited in the conditions described above, are presented and compared with the absorption coefficients of the thicker samples. The same comparison will be done for the transmittance spectra.

5.1.1 Pentacene

In Figure 5.1 the absorption coefficient (α) and the optical transmittance spectra are shown. The complete spectrum of the absorption coefficient (Figure 5.1-a) has been obtained by unifying the PDS part (ranging from 0.6 to 1.7 eV approximately) with the part measured by transmittance spectroscopy (1.7-3.2 eV approximately) (see chapter 4).

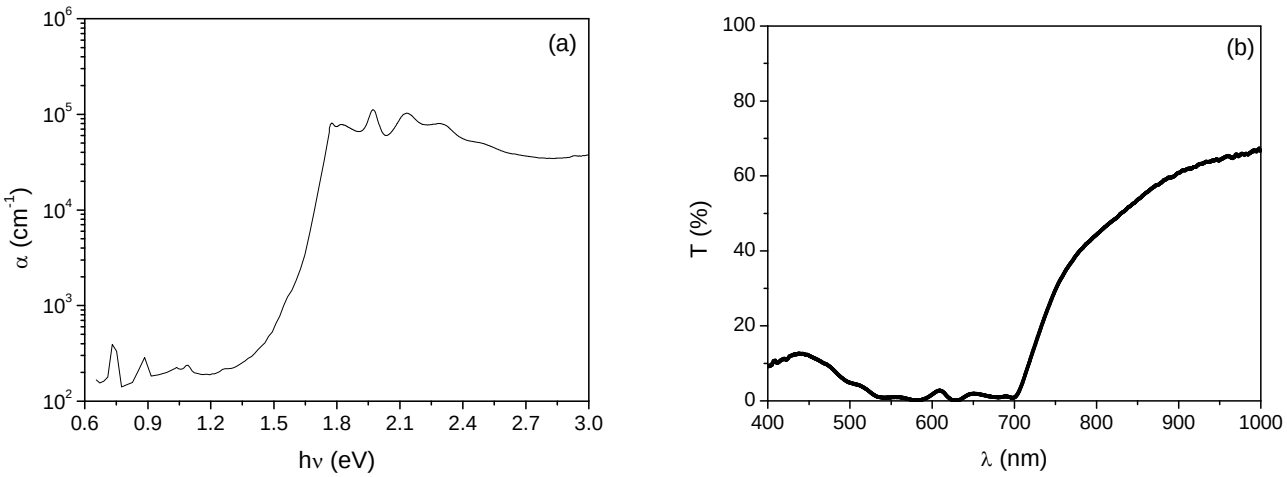

Figure 5.1. a) Absorption coefficient of pentacene measured by PDS and transmittance; b) Transmittance spectrum.

In the absorption coefficient spectrum three regions can be distinguished: a low-level absorption region ($h\nu < 1.5$ eV), a part with an exponential increase of the absorption ($1.5 < h\nu < 1.8$ eV) and, finally, a high-absorption region ($h\nu > 1.8$ eV). The absorption observed in the first region corresponds to energy values inferior to the optical gap of the semiconductor and is generally interpreted as due to localized states, coming from defects situated in the gap. The exponential part is similar to the shape observed for disordered semiconductors, like a-Si:H and is the result of optical transitions involving absorption from defects/localized states located in the band tails. The high absorption detected for energy values higher than 1.8 eV is due to band-to-band transitions (π-π^*). The peaks located at 0.74 and 0.88 eV are common in many of our samples and could be due to either substrate absorptions or vibrational overtones (vibrational orders) of C-H bonds[115].

In Figure 5.1-b the transmittance taken in the visible and the initial part of NIR is shown. An absorption band, localized in the visible range, can be observed between 500 and 700 nm and, as it will be seen for the next samples, such spectrum is typical for many organic thin film semiconductors. The shape and intensity of the transmittance in this region is strongly dependent on the thickness of the film, as it will be shown below.

An X-ray diffraction spectrum has been taken on the same sample already characterized by optical means. In Figure 5.2 the XRD spectrum up to $2\theta = 30^{\circ}$, since no important feature was observed for higher values, is shown:

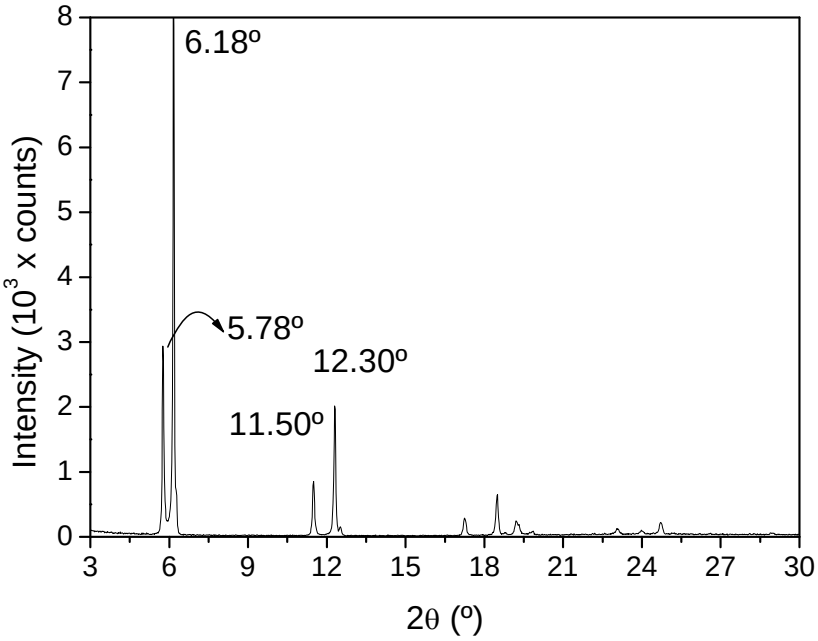

Figure 5.2. XRD spectrum of a pentacene thin film.

The diffraction peaks that characterize the spectrum indicate that the sample is polycrystalline. The first two of them are located at $2\theta = 5.78º$ and $6.18º$ respectively and are associated with family planes with a *d*-spacing of 1.53 and 1.43 nm, calculated using equation (4.23). Such features are due to the coexistence of two phases: the *thin film* and the *bulk* phases respectively (see paragraph 2.4). The values here calculated are in good agreement with the ones reported in literature[65]. Moreover, according to the literature, since the second peak is much more intense than the first one, the film could be principally composed of the phase known as the *bulk* phase. This result is not a surprise, since such phase is the one which dominates when the film thickness is higher than 100 nm[65] and our sample is 1 μm-thick.

The second couple of peaks, located at $2\theta = 11.50º$ and $12.30º$ respectively, is associated with plane families with interplanar distances equal to 0.77 and 0.72 nm. These reflections, and the following ones, are due to higher diffraction orders of the same phases described above.

Given that the XRD characterization has allowed us to exclude that the film is amorphous, Tauc's law (equation (4.21)) has been considered not adequate. So the law for direct allowed optical transitions in inorganic semiconductors (equation (4.20)) has been employed. The fits have been

calculated using Origin® which allows the definition of the equation to use and calculates the error that affects the parameters.

In Figure 5.3 the fit for the calculations of the optical gap (E_{og}) and the Urbach energy (E_u) for pentacene thin films, using equations (4.20) and (4.22), are shown:

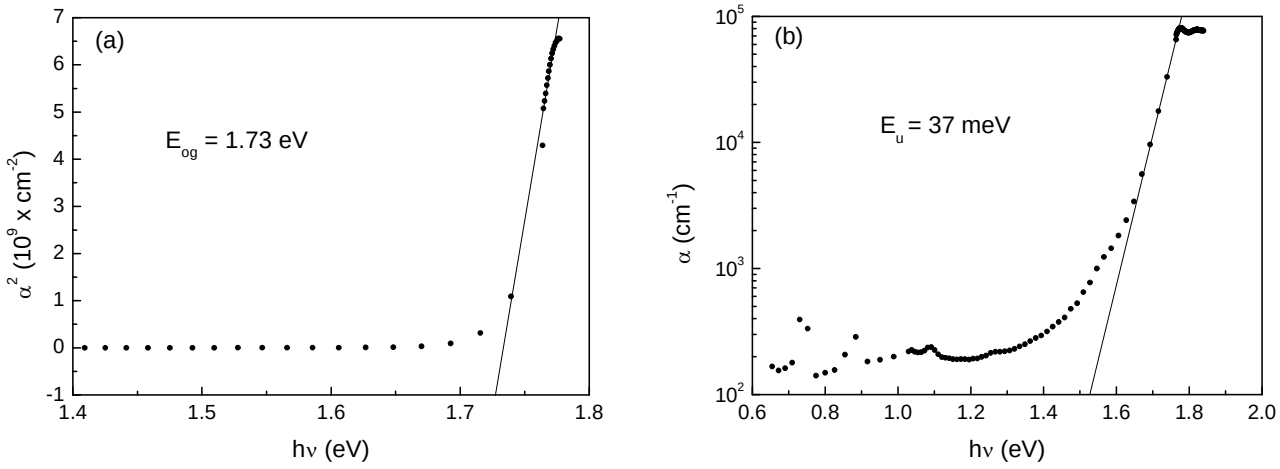

Figure 5.3. a) Plot of α^2 vs. $h\nu$ for the calculation of the optical gap of pentacene; b) Plot of α vs. $h\nu$ for the calculation of the Urbach energy.

The equations used for calculations were already introduced in chapter 4:

$$\alpha(h\upsilon) = B \cdot (h\upsilon - E_{og})^{1/2}; \qquad \alpha(h\upsilon) = \alpha_0 \exp\left(\frac{h\upsilon}{E_u}\right)$$

The value obtained for the optical gap is 1.73 eV with an error of 0.005 eV. The error estimated by the software is too low to be reasonable, probably due to the few experimental points available for the calculation in the range of interest. So a more realistic value of 0.01 eV has been considered in this case. Taking into account the difficulties to find in literature any other example of optical gap measurement for pentacene, a comparison with other experimental works can hardly be done.

The Urbach energy has a value of 37 ± 1 meV. As it has been explained in paragraph 4.2.3, this parameter is used to check the quality of inorganic amorphous semiconductors and is calculated in the exponential region of the α spectrum. Despite the fact that our pentacene sample is polycrystalline, in the absorption coefficient an Urbach front is clearly visible, making it possible to make the calculation. Also in this case, the absence of any reference in literature makes a comparison between our results with other ones impossible.

In order to check the differences between the two models to evaluate the optical gap, a fit has also been calculated using Tauc's law. In Figure 5.4 the plot of $(\alpha h\nu)^{1/2}$ vs. $h\nu$ is shown.

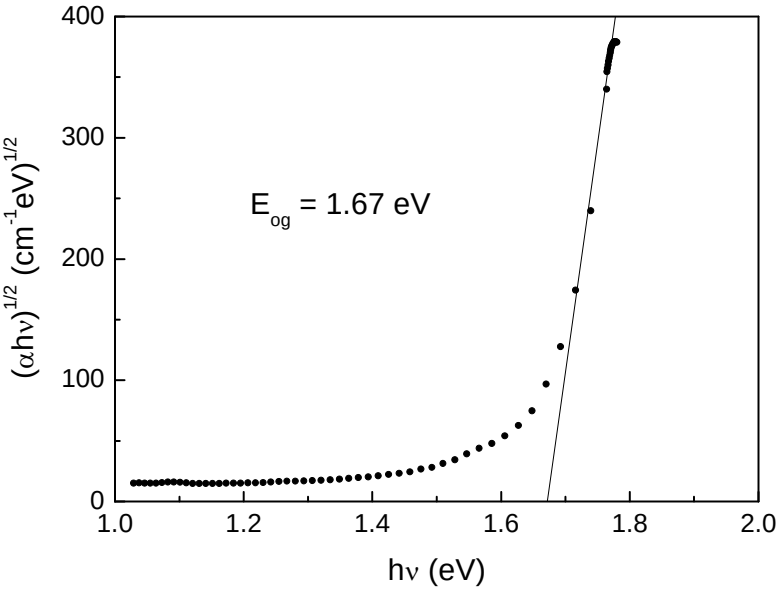

Figure 5.4. Calculation of the optical gap of pentacene using Tauc's law.

The optical gap obtained this way is 1.67 ± 0.01 eV. The value obtained using the Tauc model is lower than the one obtained using the general model for allowed direct transitions in inorganic semiconductors. The small error that affects the calculation of the gap indicates that both laws fit quite well the experimental data but since Tauc's law is for amorphous semiconductors, and our sample has polycrystalline structure, we take the value obtained in the first case (1.73 eV) as the good value for our sample.

In Figure 5.5 the measurements of absorption coefficient and optical transmittance of a 100 nm thick film are shown and compared with the ones presented in Figure 5.1, measured on the thicker one.

The absorption spectrum (Figure 5.5-a) clearly changes in all the part located at energies higher than 1.5 eV: the exponential part (between 1.3 and 1.85 eV approximately) is red-shifted, what could cause a change also in the optical gap, while in the band-to-band transition region ($h\nu > 1.85$ eV) the absorption level has decreased a little. The peaks that characterize this part of the spectrum are located at the same energy. The α in the sub-gap region is more affected by noise than in the

case of the first measurement indicating that, in such region and with a film that is so thin, the ratio signal to noise was less favourable.

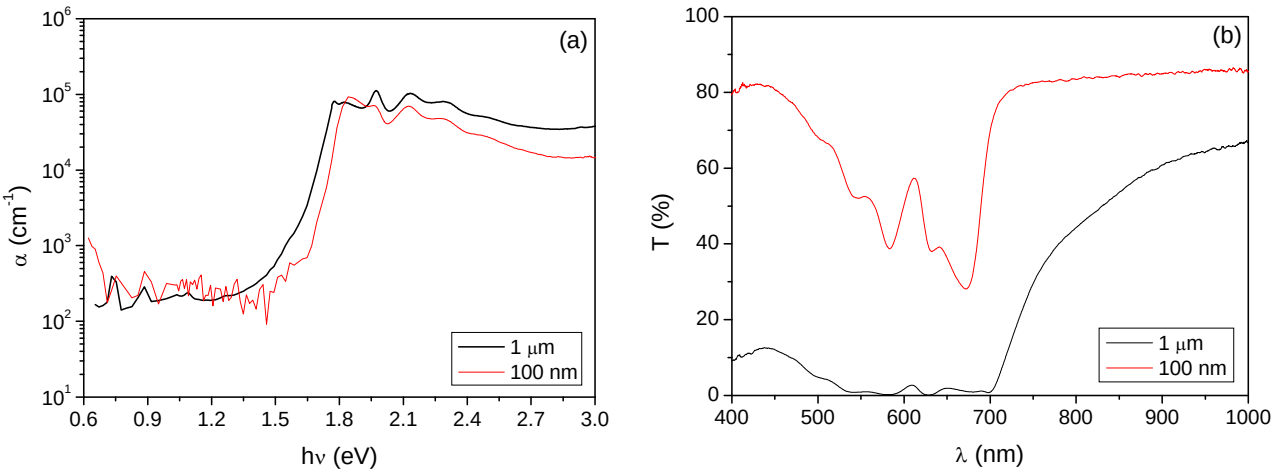

Figure 5.5. (a) Comparison between the α of pentacene with different thicknesses: 1 μm (black line) and 100 nm (red line); (b) Comparison between the two transmittances.

As it could be expected, the general level of the transmittance (Figure 5.5-b) is higher for the thinner film, but it is interesting to point out that in the range between 500 and 700 nm the shape of the curve changes a lot, evidencing more pronounced features. The characterization of a thin film allows to better define the absorption features.

The optical gap of the thinner film has been also calculated and is shown in Figure 5.6. The optical gap of the thinner film is 1.78 ± 0.01 eV, a little higher than the one calculated for the thicker one (1.73 ± 0.01 eV) with the same law. This could be related to the fact that a different composition of bulk and thin film phases could have been obtained due to the lower deposition rate and the lower thickness. This result could be useful, given that, when fabricating a solar cell, thickness and deposition conditions are normally similar to the ones employed in this last case.

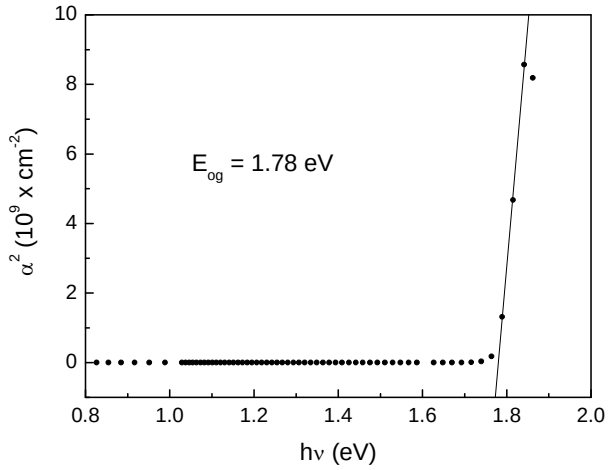

Figure 5.6. Calculation of the optical gap of a thin pentacene film.

5.1.2 Copper phthalocyanine (CuPc)

In Figure 5.7 the absorption coefficient and the transmittance of CuPc are shown:

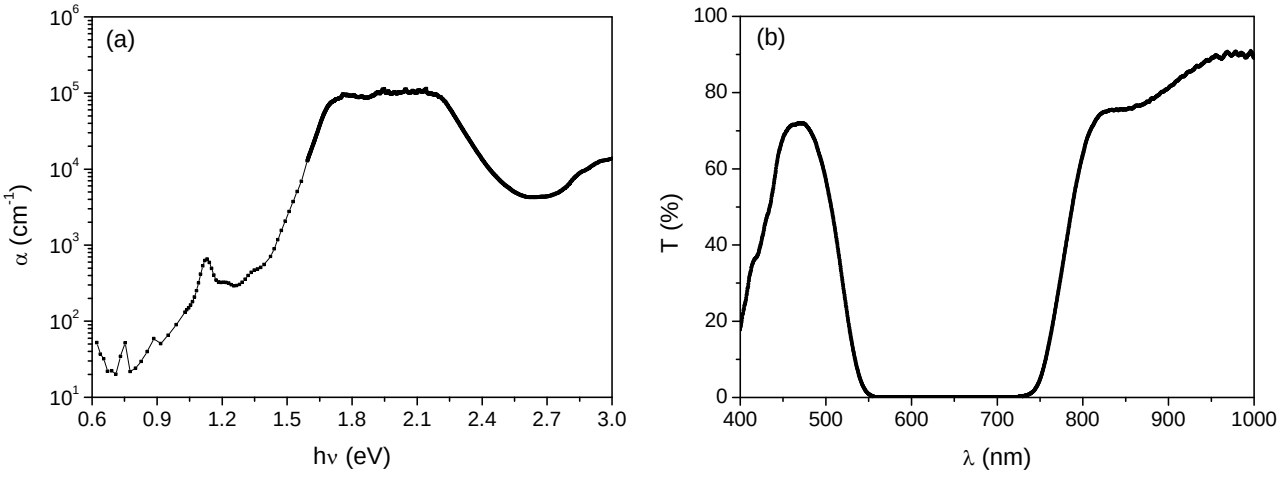

Figure 5.7. a) Absorption coefficient of CuPc measured by PDS and transmittance; b) Transmittance spectrum.

The absorption coefficient (Figure 5.7-a) evidences the presence of a strong saturated absorption band known as the Q-band between 1.5 and 2.7 eV and the beginning of the Soret band around the value of 2.7 eV[116,117,118]. These two features have been attributed to band-to-band transitions from the ground states in π-band to the excited π^*-bands[119]. The sharp absorption peak located at 1.13 eV and the three shoulders located at 1.04, 1.22 and 1.35 eV respectively, are probably due to

transitions between levels of ionic molecules[120]. Another absorption peak is observed at 0.75 eV, similar to the ones already discussed for pentacene.

The Q-band is also visible in the transmittance spectrum (Figure 5.7-b) for wavelengths between 550 and 750 nm.

An XRD analysis has been performed on the CuPc thin films. The X-ray diffraction spectrum is shown in Figure 5.8. A very intense diffraction peak has been observed at 2θ = 6.99º, associated with an interplanar distance of 1.26 nm. On one hand, the angular position of such feature is situated between the ones reported in literature for the family of planes (200) of the polymorphs α and β[60,63]: 6.83º and 7.02º, respectively. On the other hand, the values reported in literature concern thin films deposited on crystalline silicon with a very flat surface, whereas our film has been evaporated on amorphous glass. Since the deposition process has been performed with the substrate at room temperature, we conclude that our material is constituted by polymorph α with a slightly different *d*-spacing, respect to the examples reported in the references. The cited literature also reports the fact that such diffraction peak could be shifted as a function of the film thickness, being located at 2θ = 10º for a thickness of a few nanometers[63]. Another, much less intense, diffraction peak is located at 2θ = 7.47º (see the inset in Figure 5.8) associated with an interplanar distance of 1.18 nm. The extended band located at around 25º is due to the substrate.

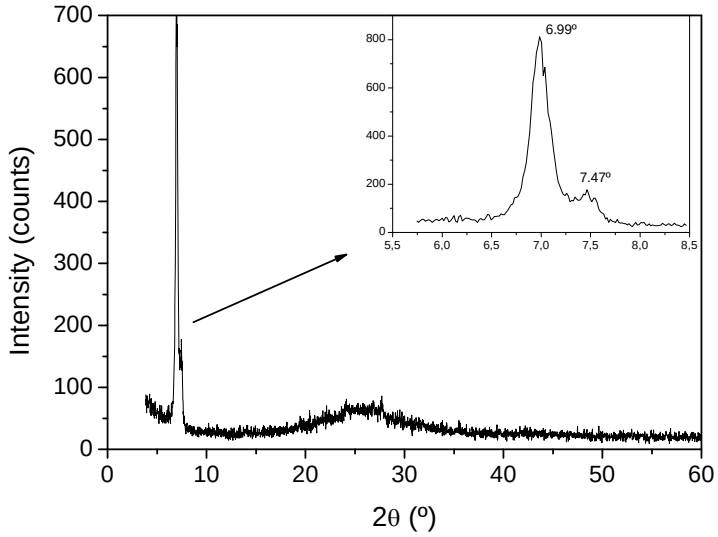

Figure 5.8. XRD spectrum of a CuPc thin film.

In Figure 5.9 the plots with the calculations of optical gap and Urbach energy are shown. The value obtained for the optical gap is 1.64 ± 0.01 eV (Figure 5.9-a), while for the Urbach energy a value of 53 ± 1 meV has been calculated (Figure 5.9-b).

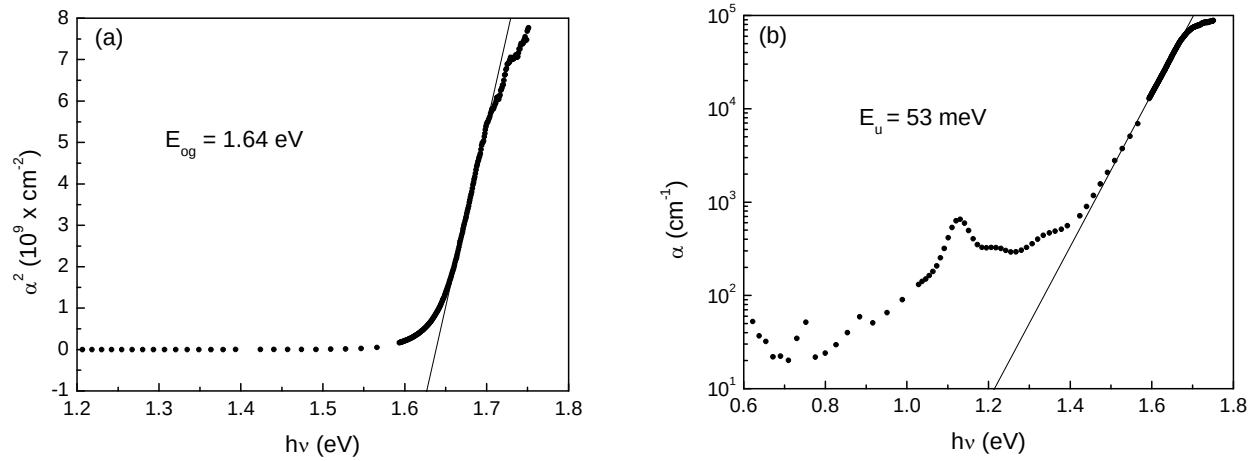

Figure 5.9. a) Plot of α^2 vs. $h\nu$ for the calculation of the optical gap of CuPc; b) Plot of α vs. $h\nu$ for the calculation of the Urbach energy.

In Figure 5.10 the absorption coefficient and the transmittance of a 100 nm film with is compared with the ones measured for the thicker film.

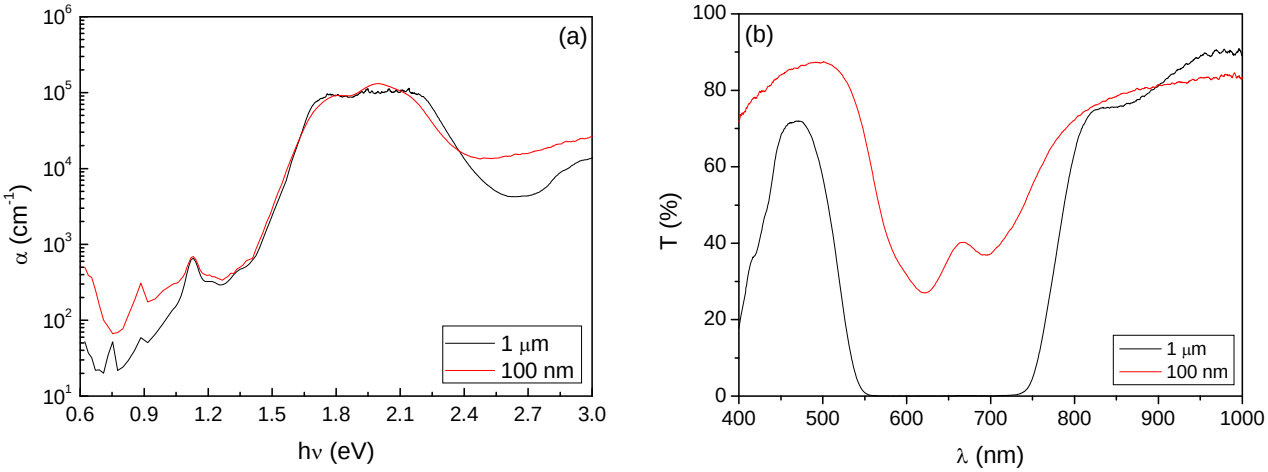

Figure 5.10. (a) Comparison between the α of CuPc with different thicknesses: 1 μm (black line) and 100 nm (red line); (b) Comparison between the two transmittances.

In the region below 1.5 eV the absorption level (Figure 5.10-a) is a little higher for the thin film than for the thicker one due to superficial states. In a thinner sample the ratio surface/bulk is higher

than in a thicker one[111] where the bulk component is more important. Another aspect that could explain such higher absorption in the sub-gap region for the thin sample is some absorption phenomena in the substrate that could be relevant in the low-absorption region when the film is very thin.

5.1.3 Fullerene (C_{60})

The absorption coefficient and the transmittance spectra of a fullerene thin film are shown in Figure 5.11.

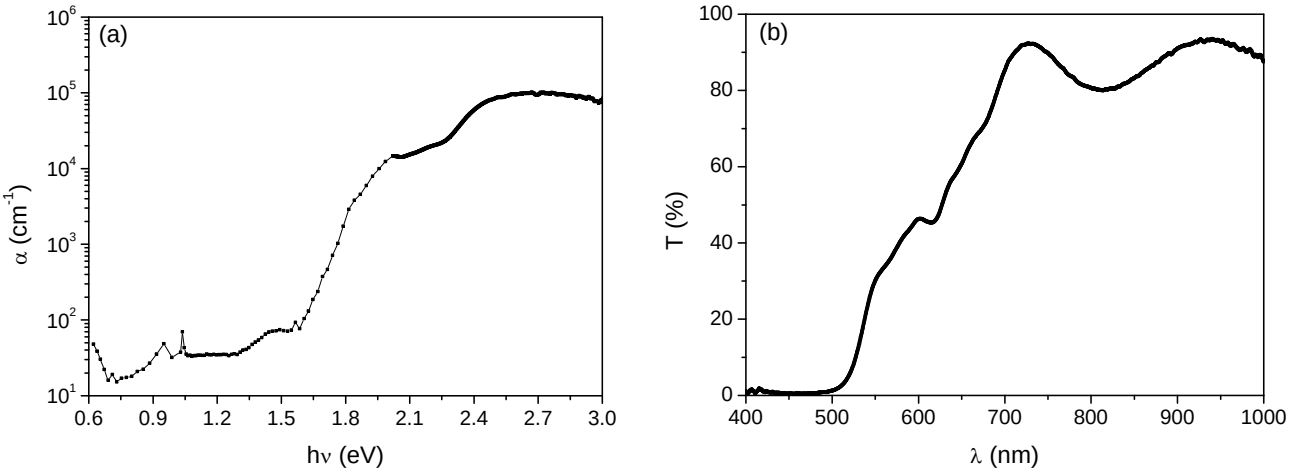

Figure 5.11. a) Absorption coefficient of fullerene measured by PDS and transmittance; b) Transmittance spectrum.

The exponential region in the spectrum of the absorption coefficient (Figure 5.11-a) is not as clear as in the previous cases (pentacene and CuPc). Two exponential regions can be observed: the first one located between 1.5 and 2 eV and the second one between 2.2 and 2.4 eV. Such situation makes it more difficult to identify the adequate range to calculate optical gap and Urbach energy, whose the values depend on the model used to calculate them. Finally, it is interesting to notice that no absorption peak is observed around 0.8 eV. If we considered that the peaks observed in the cases of pentacene and CuPc were due to the substrate, the absorption of fullerene should be much higher to cover it. Since a comparison between the spectra of the three samples indicates that this is not the case, the theory of the vibrational overtone of C-H bonds then acquires more relevance. Coherently with this hypothesis, in the case of fullerene, which does not contain any hydrogen atoms, the overtones are absent.

The optical transmittance of fullerene goes to zero below 500 nm and shows interferences due to multiple reflections for values higher than 650 nm.

In Figure 5.12 the X-ray diffraction spectrum of a fullerene thin film is shown. Only one diffraction peak is observed at $2\theta = 31.74º$, corresponding to an interplanar distance of 0.28 nm. Nevertheless, this feature could simply be a noise effect, as this result can hardly be compared with similar measurements in literature[121,122] and, moreover, the peak is very sharp and little intense. The film is amorphous and no evidence of crystalline structure can be inferred from this XRD measurement.

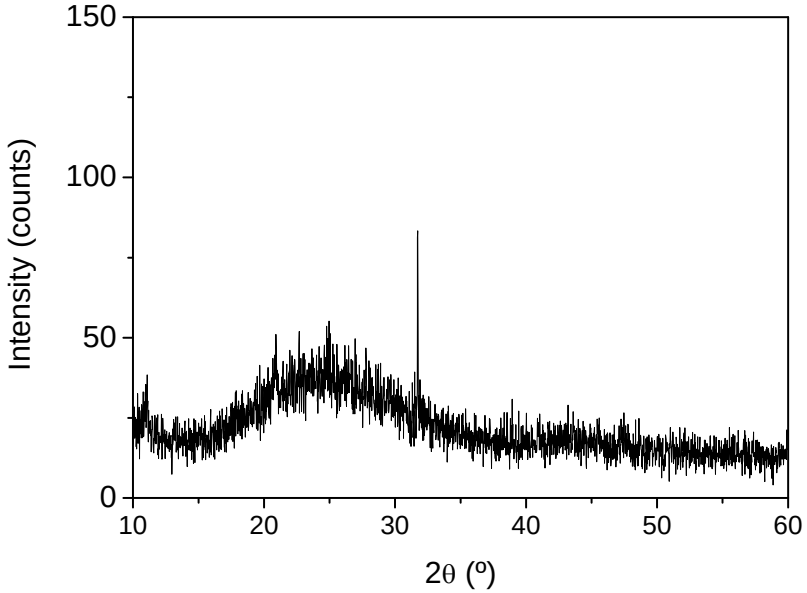

Figure 5.12. XRD spectrum of a fullerene thin film.

In Figure 5.13 the plots for the fits for the optical gap and the Urbach energy are shown. Just to check the result, despite the fact that the XRD spectrum demonstrates that the fullerene has grown with an amorphous-like structure, a first calculation of the optical gap with the general law for direct allowed transitions (equation (4.20)) has been performed.

By employing the law for direct allowed transitions, the optical gap of C_{60} has been found to be 2.31 ± 0.01 eV (Figure 5.13-a), a very high value for a semiconductor. Anyway, the law seems to fit quite well the experimental data in the exponential part of the spectrum. The Urbach energy is equal to 63 ± 1 meV (Figure 5.13-b).

The relatively high value, if compared with the ones obtained for polycrystalline pentacene and CuPc, found for the Urbach energy also supports the idea about a fullerene micro-structure with a big amorphous component and rich in defects.

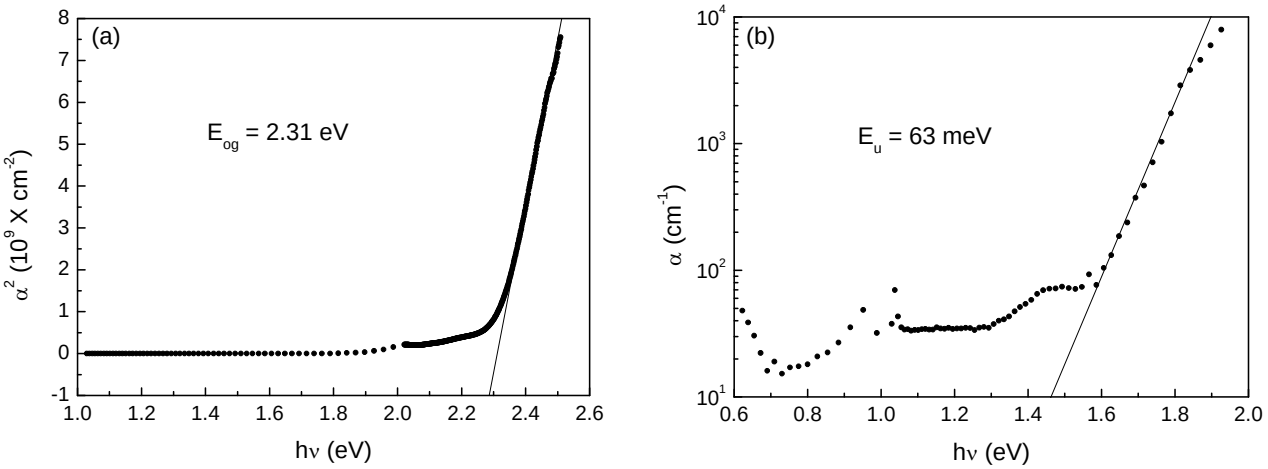

Figure 5.13. a) Plot of α^2 vs. $h\nu$ for the calculation of the optical gap of fullerene; b) Plot of α vs. $h\nu$ for the calculation of the Urbach energy.

Given that the micro-structure of this sample seems to be amorphous, it is worth trying to recalculate the optical gap of the material using Tauc's law (equation (4.21)), generally valid for such kind of materials.

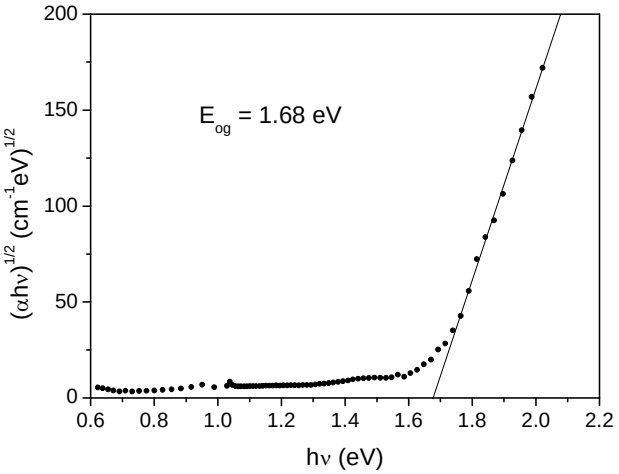

Figure 5.14. New calculation of fullerene optical gap using Tauc's law.

The striking difference of 0.63 eV between the values of optical gap obtained by the general law for semiconductors (2.31 eV in Figure 5.13-a) and by Tauc's law for amorphous ones (1.68 eV in Figure 5.14) is motivated by the fact that the latter estimates the linear region for lower energy values than the former. Anyway, the value obtained by Tauc's law is in good agreement with the value of 1.66 eV, measured at 300 K, reported by Gotoh at al.[110].

It is interesting to point out that in the case of pentacene the difference between the gaps calculated by the two models (0.06 eV) was smaller compared to the one obtained in fullerene (0.63 eV). So the choice of the correct model seems to be more critical for fullerene. In this case Tauc's law is probably the most adequate.

In Figure 5.15 a comparison between absorption coefficient and transmittance of the thick and the thin film of fullerene is shown.

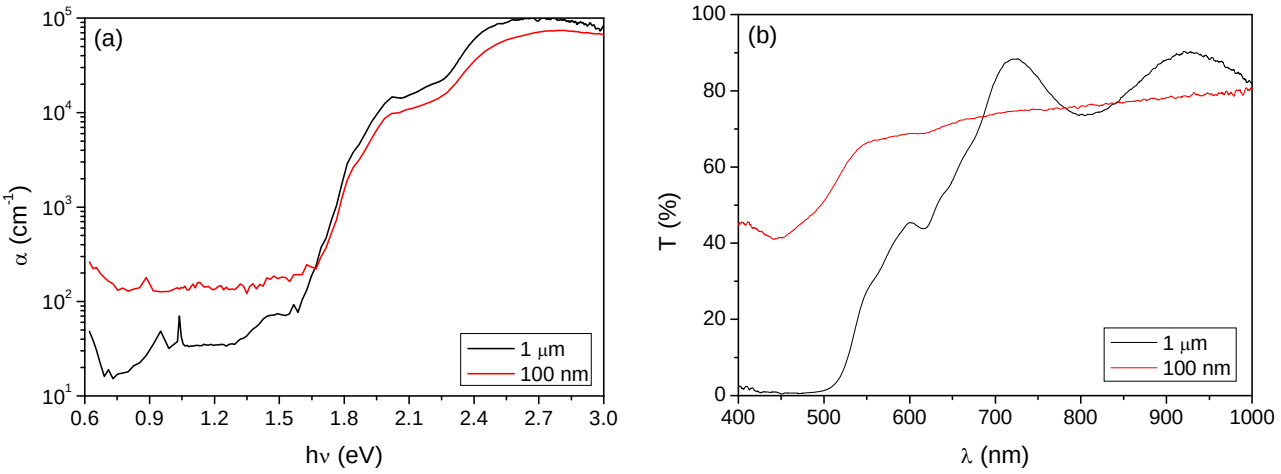

Figure 5.15. (a) Comparison between the α of fullerene with different thicknesses: 1 μm (black line) and 100 nm (red line); (b) Comparison between the two transmittances.

By comparing the two absorption coefficients (Figure 5.15-a), it seems that the high-absorption region was already well defined and not saturated in the spectrum of the thicker one. In the former case we have obtained a slightly lower absorption level. On the contrary, in the sub-gap region, the absorption is much higher for the thinner film, having increased by a factor 10 in some points. Such phenomenon can be explained by taking into account the higher contribution of the superficial states for the thinner sample.

The optical transmittance of the thin film (Figure 5.15-b) is higher than the one of the thicker sample in the region between 400 and 680 nm. Moreover, as it is to be expected, the interferences due to the multiple reflections in the film have disappeared for the thinner sample.

5.1.4 Perylene-3,4,9,10-tetracarboxylic dianhydride (PTCDA)

In Figure 5.16 the measurements of absorption coefficient and transmittance of perylene tetracarboxylic dianhydride thin films are shown.

The sharp peak located at 0.75 eV in the α spectrum (Figure 5.16-a) is originated by the same causes as for pentacene and CuPc. There are another absorption band at 1.27 eV and the exponential region is located between 1.8 and 2.2 eV. In the high-absorption region the absorption is saturated and a thinner film must be characterized in order to be able to observe any features. By comparing the α spectrum with the ones already commented for the other materials, we can observe that the exponential region of PTCDA is located at higher energies, indicating that this material has a higher optical gap.

The optical transmittance of PTCDA (Figure 5.16-b) is almost zero for wavelengths below 580 nm and then grows rapidly till the value of 80%.

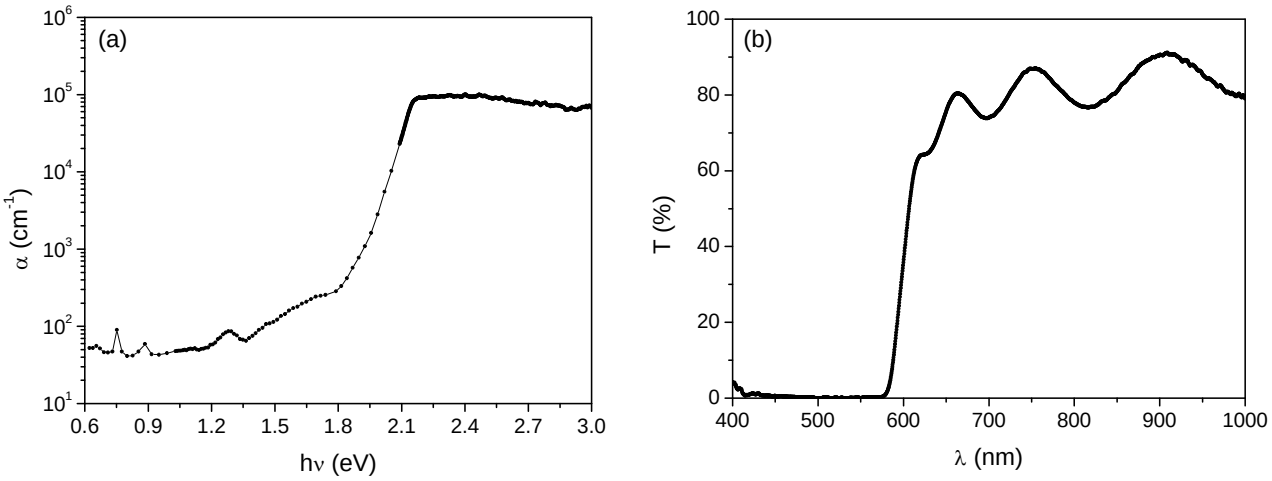

Figure 5.16. a) Absorption coefficient of PTCDA measured by PDS and transmittance; b) Transmittance spectrum.

In Figure 5.17 the XRD spectrum is shown. The sample is polycrystalline, as the presence of many diffraction peaks located at 2θ = 24.76º, 27.55º, 29.44º, 31.75º and 52.87º respectively indicates. Nevertheless, by comparing with literature, only the peak at 2θ = 27.55º seems really due to a crystalline form of PTCDA, being associated with the family of planes (102)[123], with a

d-spacing of 0.32 nm. This reflection is the most intense and could indicate a predominant fraction of material with this crystal orientation. The nature of the other reflections is uncertain, but, in case of being caused by some family of crystallographic planes and not by noise, the interplanar distances would be 0.36, 0.30, 0.28 and 0.17 nm, respectively. In these cases the dimensions of the crystals would be very small, aspect that would explain the low intensity of the diffraction peaks.

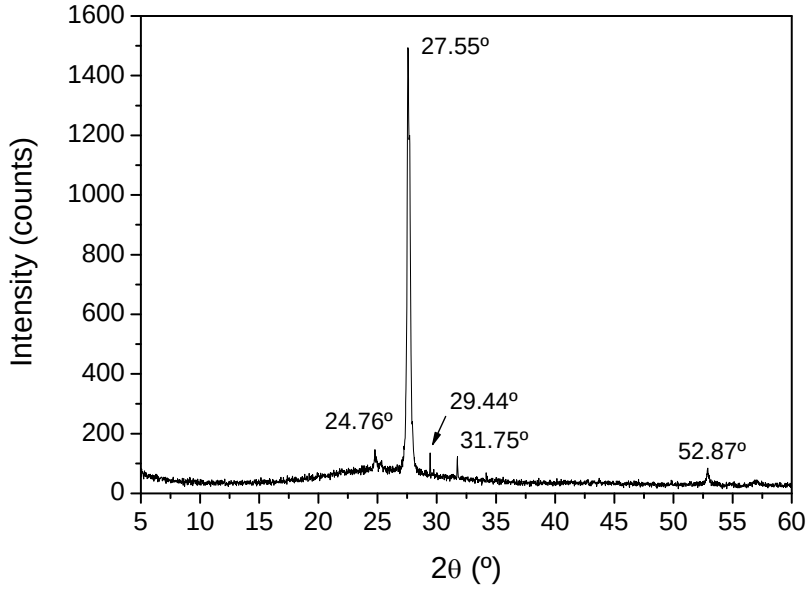

Figure 5.17. XRD spectrum of a PTCDA thin film.

In Figure 5.18 the results for the optical gap and the Urbach energy are shown:

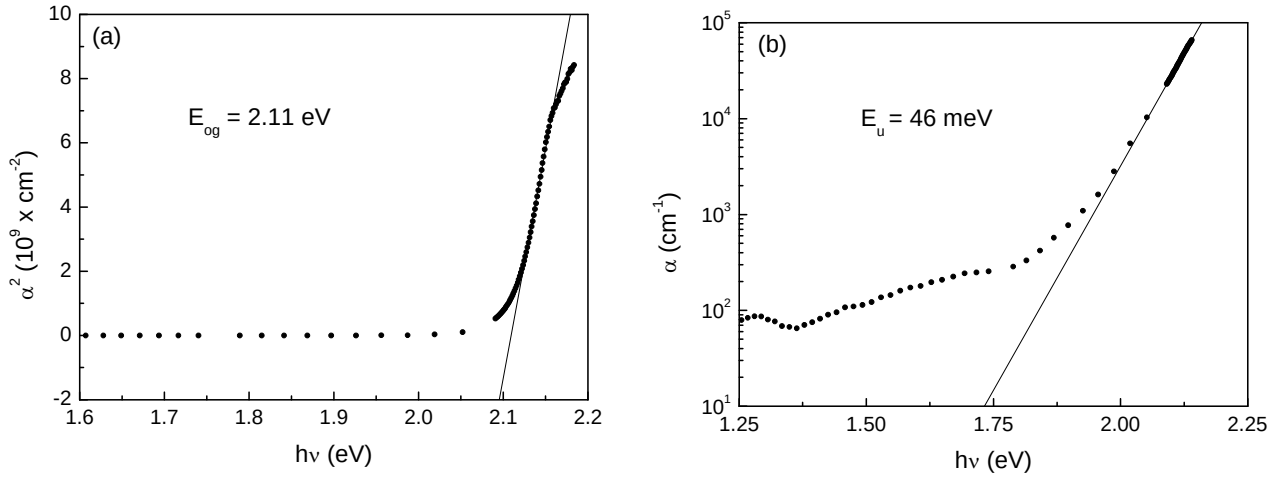

Figure 5.18. a) Plot of α^2 vs. $h\nu$ for the calculation of the optical gap of PTCDA; b) Plot of α vs. $h\nu$ for the calculation of the Urbach energy.

The optical gap of PTCDA has been found to be equal to 2.11 ± 0.01 eV (Figure 5.18-a), while the Urbach energy is equal to 46 ± 3 meV (Figure 5.18-b).

In Figure 5.19 a comparison between the absorption coefficients and the transmittances of 1 μm and 100 nm thick films is presented.

As usual, the thinner film has higher absorption in the sub-gap region probably due to the superficial defects and/or to possible absorptions in the substrate (Figure 5.19-a). In the high-absorption region we are able to better define the absorption bands of PTCDA, since the measurement is not saturated. We can observe one band centred at 2.24 eV and another broader one centred at 2.59 eV.

Also in the transmittance spectrum (Figure 5.19-b) the above mentioned features are clearly visible between 450 and 600 nm. It is worth remembering that α in this region is calculated from the transmittance. The transmission is much higher in this part of the spectrum, while for higher wavelengths the level of transmitted light is more or less the same but without interferences, due to the low thickness of the film.

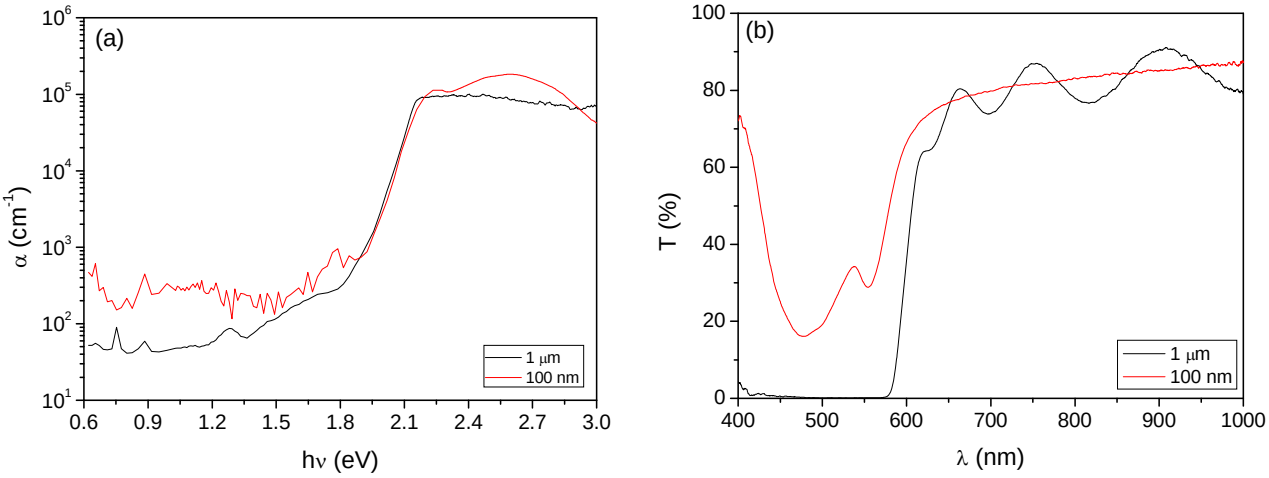

Figure 5.19. (a) Comparison between α of PTCDA with different thicknesses: 1 μm (black line) and 100 nm (red line); (b) Comparison between the two transmittances.

5.1.5 *N,N*-ditridecyl-3,4,9,10-perylenetetracarboxylic diimide (PTCDI-C_{13})

In Figure 5.20 the measurements of the absorption coefficient α and transmittance are presented for PTCDI-C_{13}. α (Figure 5.20-a) shows the typical absorption peaks for energy values inferior to 1 eV and a shoulder around 1.6 eV, the origin of which is not clear. The spectrum is clearly

characterized by the three typical regions of an absorption spectrum of a semiconductor: low-absorption (sub-gap) region, an exponential region (band tails) and a high-absorption (band-to-band) region. Nevertheless, the presence of what could be interpreted as an absorption band around 1.6 eV complicates the location of the Urbach tail. For energy values higher than 2 eV the absorption is saturated and any optical features are hardly visible.

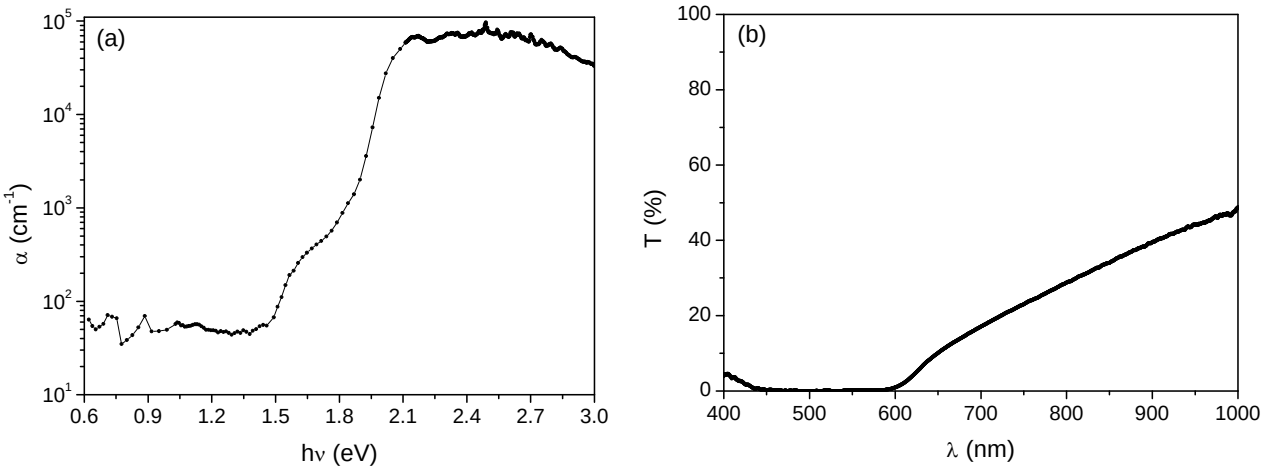

Figure 5.20. a) Absorption coefficient of PTCDA measured by PDS and transmittance; b) Transmittance spectrum.

The optical transmittance appears to be quite low, due to the high thickness of the sample. In the case of this kind of perylene the "visible" absorption band is located between the 450 and 600 nm.

In Figure 5.21 the XRD spectrum of PTCDI-C_{13} is shown. The PTCDI-C_{13} thin film is polycrystalline as indicated by the presence of a few diffraction peaks located at the following angular positions: $2\theta = 3.47º$, $6.81º$, $10.18º$ and $13.52º$, respectively. Such reflections are associated with family of planes characterized by the following interplanar distances: 2.54, 1.30, 0.87 and 0.65 nm. These peaks are associated to the (001), (002), (003) and (004) diffraction planes of the PTCDI-C_{13} crystalline structure[78].

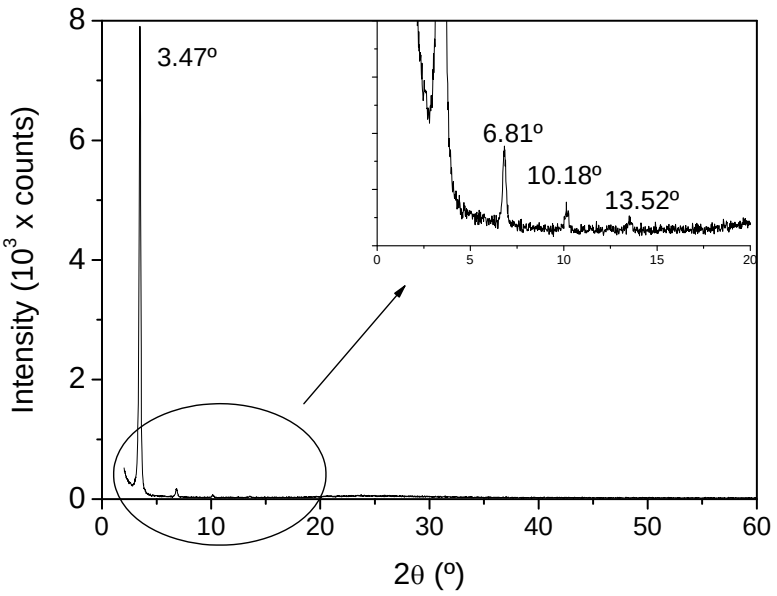

Figure 5.21. XRD spectrum of a PTCDI-C_{13} thin film.

In Figure 5.22 the fits for the calculation of the optical gap and the Urbach energy are shown.

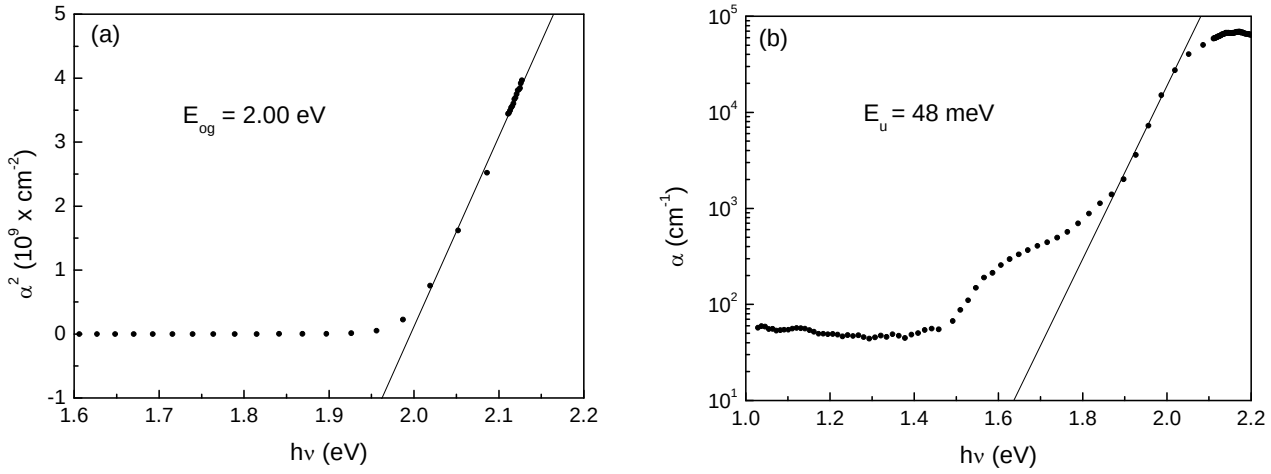

Figure 5.22. a) Plot of α^2 vs. $h\nu$ for the calculation of the optical gap of PTCDI-C_{13} ; b) Plot of α vs. $h\nu$ for the calculation of the Urbach energy.

The plot of α^2 vs. $h\nu$ (Figure 5.22-a) allows the estimation of an optical gap of 2.00 ± 0.01 eV, while the plot of α vs. $h\nu$ (Figure 5.22-b) a value for the Urbach energy of 48 ± 1 meV.

In the case of the Urbach tail, it is not clear where it is located due to the presence of the absorption band located at 1.6 eV. The higher part of the exponential part of the spectrum has been

chosen for homogeneity reasons with further calculations on PTCDI-C_{13}. Within such interpretation this band could be seen as an absorption band located in the sub-gap region the intensity and shape of which could change, as it will be seen, as a function of parameters like the quality of the material and its deposition parameters.

In Figure 5.23 the absorption coefficient and the transmittance of a 100 nm thick film are shown together with the spectra of a 1 μm thick film.

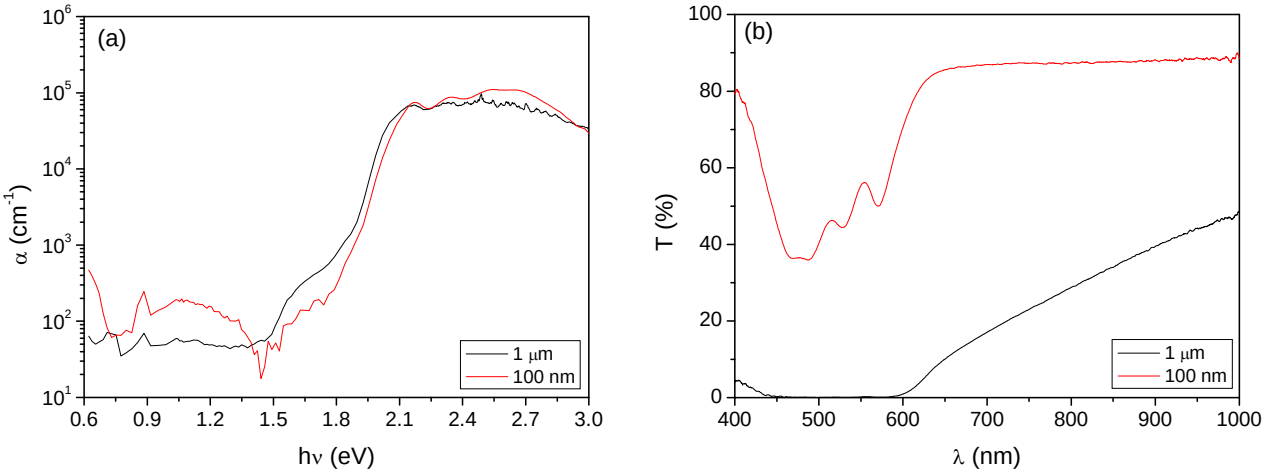

Figure 5.23. (a) Comparison between the α of PTCDI-C_{13} with different thicknesses: 1 μm (black line) and 100 nm (red line); (b) Comparison between the two transmittances.

In the high-absorption region α (Figure 5.23-a) is quite similar to the one measured on the thicker film. In this case absorption bands centred at 2.17, 2.35 and 2.59 eV are visible. The last one still appears saturated despite of the low thickness of the sample. The exponential part of the curve is only a little red-shifted, while in the sub-gap region the absorption appears radically different from the one measured on the thicker sample. A broad band is observed below 1.5 eV and is probably due to absorptions in the substrate and the presence of a higher density of states associated with superficial defects.

The transmittance (Figure 5.23-b) appears much higher in all the range of wavelengths, with clearly visible features between 400 and 600 nm.

5.2 Effects of degradation on the optical properties

In this paragraph the effects of the exposure of thin films to air and light will be discussed. This is an interesting issue, given that the stability of a semiconductor is an important issue to be considered when fabricating high efficiency solar cells. To our knowledge, there is no systematic study on how the optical properties of small molecule organic semiconductors vary as a consequence of the exposure to light and oxidizing agents, in the spectral range of interest for photovoltaic applications. The PDS technique will have a central importance in this discussion since it allows to measure the sub-gap absorption: the absorption due to energetic levels located in the gap and associated with defects that can actuate as recombination centres. We expect that, in the case of having defect generation in the materials, it will be detected mostly in the sub-gap region. Apart from providing us with valuable information about the stability of organic semiconductors, this experiment is of special interest when operating without an adequate technology to fabricate devices in nitrogen atmosphere, like in our case.

The experiment on the degradation effects has been performed on the same samples described in the previous paragraph. After finishing the optical measurements on as-deposited samples, they have been exposed to light irradiation for one week and their "twin" samples, deposited during the same process, have been left in ambient conditions (these sample will be labelled as "*n.c.*" that means "normal conditions"). The reason to expose samples to light was to observe if it was possible to accelerate degradation in our films in order to be able to identify its effects on the optical spectra. In particular, changes in the low-absorption level and in the value of the optical gap are two specific cases that will be checked. The light source our samples were exposed to was an UV filtered halogen bulb, regulated at 1 sun power approximately, with an extra IR filter added in order to avoid heating of the films. Given that it is well known that UV light degrades organic materials, we have studied the effects of visible light on ours, through the analysis of their optical properties. The treatment at normal conditions was expected to have less effect and to give us the information about what happens to the semiconductors if they have to be stored in normal laboratory conditions (*n.c.*).

PDS and optical transmittance measurements have been repeated after the degradation treatments and compared with the ones performed on as-deposited samples, already discussed in paragraph 5.1. In the cases in which no change has been found, the treatment has been prolonged and the measurements repeated. In the cases in which an important degradation has been observed annealing treatments have been performed on the films in order to see if the degradation process was reversible.

The indications extracted from this experiment could be of use when choosing, among all the materials under study, the most adequate to fabricate solar cells.

5.2.1 Pentacene

The PDS part of the α spectrum of pentacene is presented in Figure 5.24.

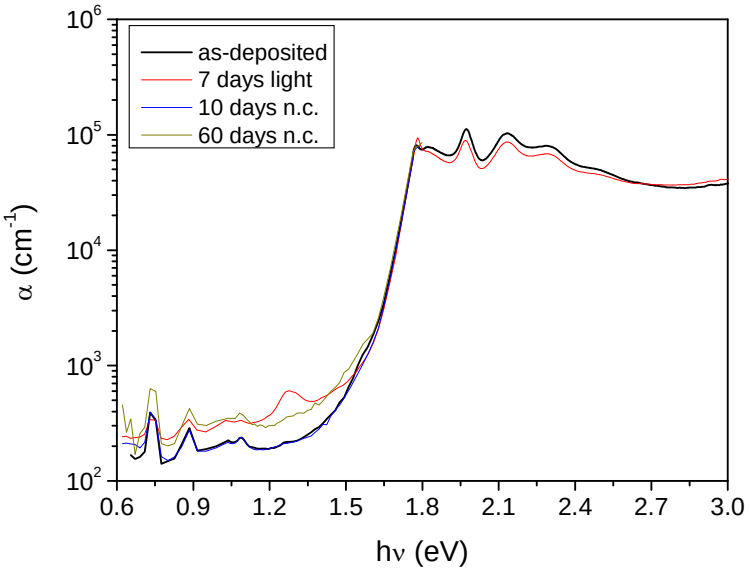

Figure 5.24. Absorption coefficient of degraded pentacene thin films: as-deposited film (black line), after 7 days of light treatment (red line), after 10 days of exposure to normal conditions (*n.c.*) of light and air (blue line) and 60 days of exposure to *n.c.* (dark yellow line).

The most remarkable effects of degradation on the optical properties are localized in the infrared region of the spectra, indicating that the density of states in the gap of the semiconductor has changed. In the case of the sample exposed to light irradiation for a week (red line in Figure 5.24), the sub-gap absorption level increases by a factor of 1.5, approximately. The absorption of the sample left in normal conditions of air and light (named "*n.c.*" in the figure) for 10 days (blue line) has not increased at all. In order to check if in this last case the degradation could depend on the exposure time, the same sample has been measured again after 60 days of exposure to *n.c.* from the day of its deposition. Its absorption level (dark yellow line in the figure) had increased up to the level of the sample degraded with light irradiation. The effects of the two processes are similar, with

the differences that the process with light irradiation is faster and causes the appearance of a broad absorption peak centred at 1.28 eV.

The observed increase in the low-level absorption could be related with oxygen impurities incorporated in the material. A similar phenomenon has already been observed for fullerene[110]. Moreover, the exposure to visible light seems to accelerate the degradation process.

Little changes were observed also in almost all the high energy region (energy higher than 1.7 eV) where, after the treatment with light for a week, the absorption had slightly decreased. The exponential part of the spectrum, located between 1.50 and 1.80 eV, experienced only little alterations.

The optical gap has been calculated also after the degradation processes by using equation (4.20) and all the results obtained are shown in Figure 5.25. The gap value increases from the original value of 1.73 ± 0.01 eV (Figure 5.3-a) to 1.75 ± 0.01 eV after irradiation (Figure 5.25-a), while it has remained unchanged (1.73 ± 0.01 eV) after undergoing the other treatment (Figure 5.25-b,c). In any case the variation is not very significant, taking into account an error of ± 0.01 eV affecting the calculation.

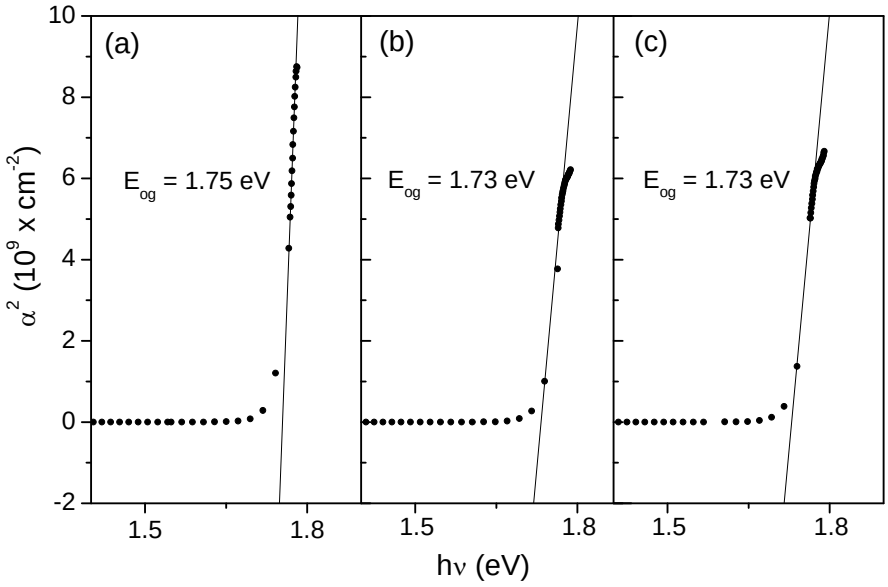

Figure 5.25. Calculation of the optical gap (E_{og}) after light irradiation for 7 days (a), after the exposure to *n.c.* for 10 days (b) and after the exposure to *n.c.* for 60 days (c). The vertical axis is the same for all the graphs.

The Urbach energy has also been calculated, using equation (4.22) and the results are shown in Figure 5.26:

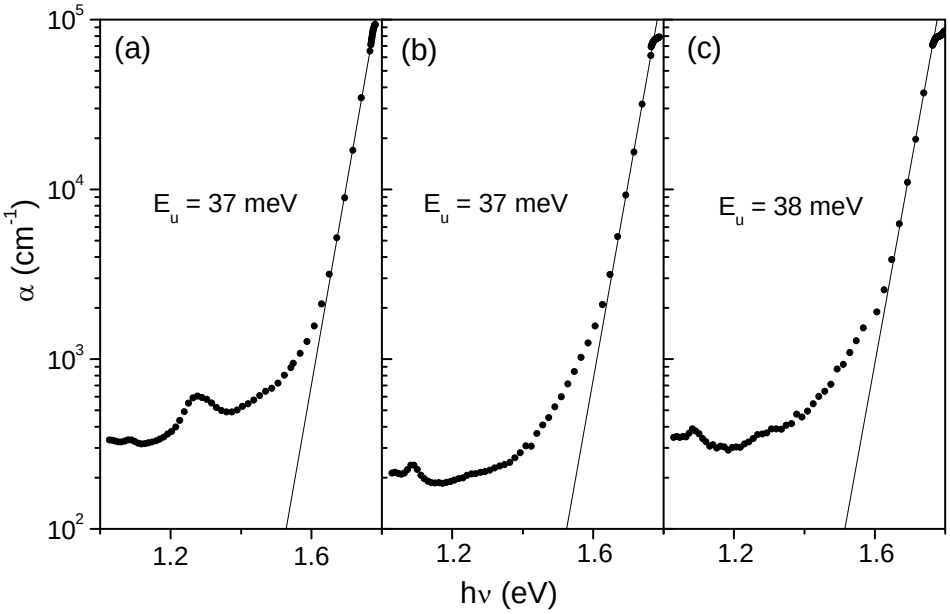

Figure 5.26. Calculation of the Urbach energy (E_u) after light irradiation for 7 days (a), after the exposure to *n.c.* for 10 days (b) and after the exposure to *n.c.* for 60 days (c). The vertical axis is the same for all the graphs.

The value of the Urbach energy for the as-deposited sample was 37 meV (Figure 5.3-b) and it has not changed after the process with light irradiation (Figure 5.26-a) and after 10 days of exposure to *n.c.* (Figure 5.26-b). After 60 days of exposure to *n.c.* the Urbach energy has increased to 38 meV (Figure 5.26-c), a change that is not distinguishable from the original one, being the error in calculating it ± 1 meV.

The optical transmittance spectra measured after the degradation processes are shown in Figure **5.27**. Some changes were observed after the treatments, especially in the regions located before 550 nm and after 700 nm. The level of light transmission keeps more or less the same for all the samples between those wavelengths. The treatment with light irradiation slightly increases the transmittance, while the treatment in normal environment conditions has the opposite effect.

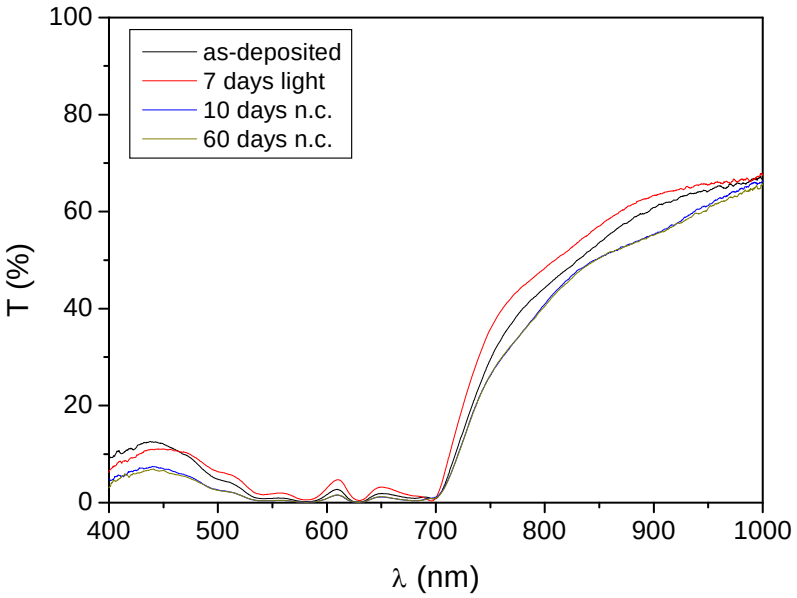

Figure 5.27. Transmittance spectra taken on as-deposited film (black line), after the light treatment (red line), after 10 days of exposure to *n.c.* (blue line) and 60 days of exposure to *n.c.* (dark yellow line).

The pentacene sample exposed to light has been annealed to check if it is possible to recover the original properties of the material. Taking into account the relatively low evaporation temperature of pentacene, the annealing treatment has been performed at 100ºC for 3 hours in a cryostat with a mechanical pump making vacuum in it. The annealing time was calculated starting from the instant in which the annealing temperature had been reached. After the annealing, the heater was switched off and the temperature was left to decrease to room temperature, before opening the cryostat.

PDS and optical transmittance spectroscopy characterizations have been executed on the sample annealed and the results are presented in Figure 5.28. The absorption coefficient of the annealed film (Figure 5.28-a) is almost identical to the one measured on the same sample after being exposed to direct light irradiation for 7 days. Also the transmittance spectrum (Figure 5.28-b) does not change much after the annealing especially in the range between 400 and 700 nm, where the transmittance is similar to the one of the degraded sample. Anyway, for wavelengths between 400 and 450 nm the transmittance has increased, while in the region after 700 nm it has decreased.

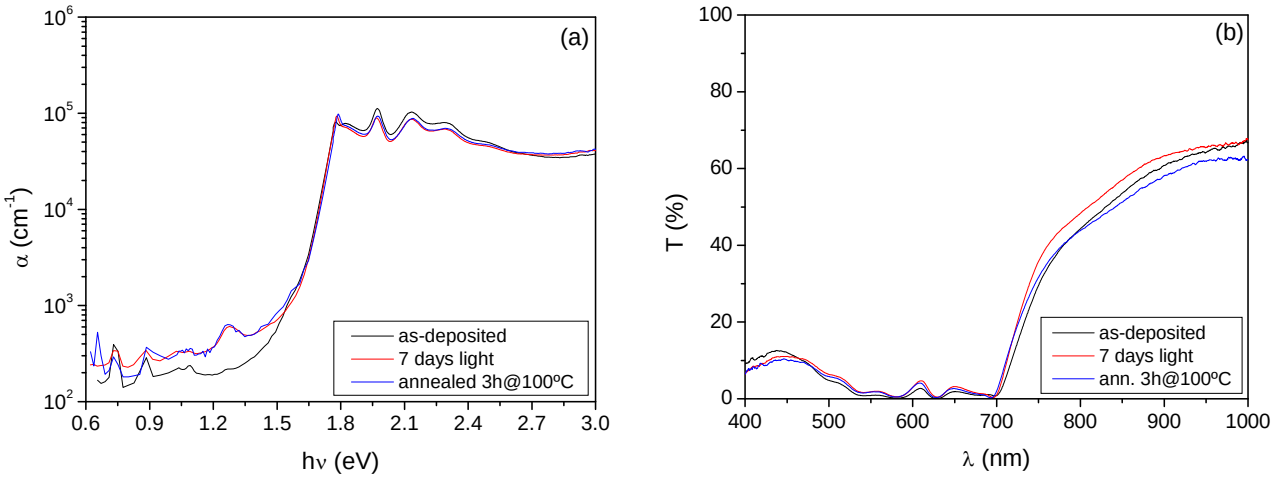

Figure 5.28. Absorption coefficient (a) and transmittance spectra (b) of as-deposited (black line), light degraded (red line) and annealed (blue line) pentacene at 100ºC for 3 hours.

These results mean that the treatment does not work to recover the properties of the degraded thin film or that the conditions employed are not the optimal. Since the evaporation temperature of pentacene is low, there is little margin to increase the annealing temperature, so if we wanted to improve the treatment one possibility would be to increase the time of exposure.

5.2.2 Copper Phthalocyanine (CuPc)

In Figure 5.29 the effects of degradation on the absorption coefficient of CuPc are shown:

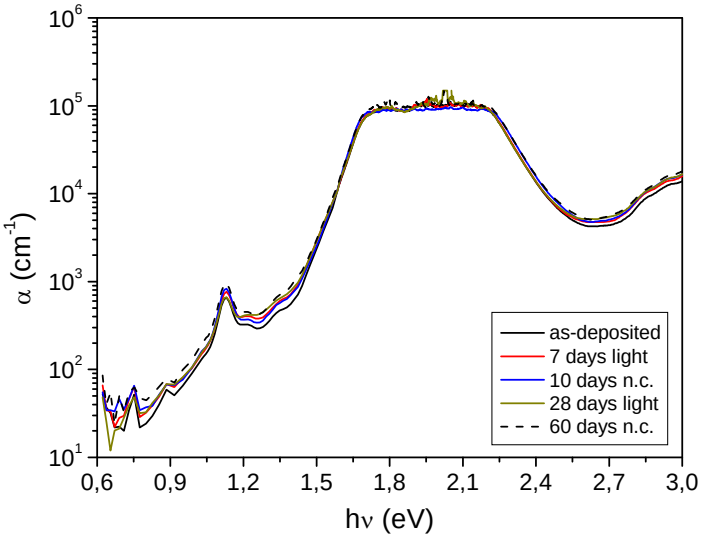

Figure 5.29. Absorption coefficient of degraded CuPc thin films: as-deposited film (black line), after 7 days of irradiation treatment (red line), after 10 days of exposure to *n.c.* (blue line), after 28 days of irradiation (dark yellow line) and 60 days of exposure to *n.c.* (black dashed line).

After a first exposure to the two types of treatment for 7 (light) and 10 (n.c.) days respectively, the alteration of the spectrum in the sub-gap region was so tiny that the treatments have been prolonged. The treatment with light irradiation has been prolonged to 28 days. The treatment of exposure to environmental conditions of air and light has been prolonged to 60 days. Only a small increase has been observed in the sub-gap absorption after applying the two treatments. This leads to the conclusion that copper phthalocyanine is a stable material, even when directly irradiated with light.

In Figure 5.30 the fits for the calculation of the optical gap of treated CuPc are shown. The optical gap has been found to be equal to 1.64 eV in all of the cases, the same value that was obtained for the as-deposited sample.

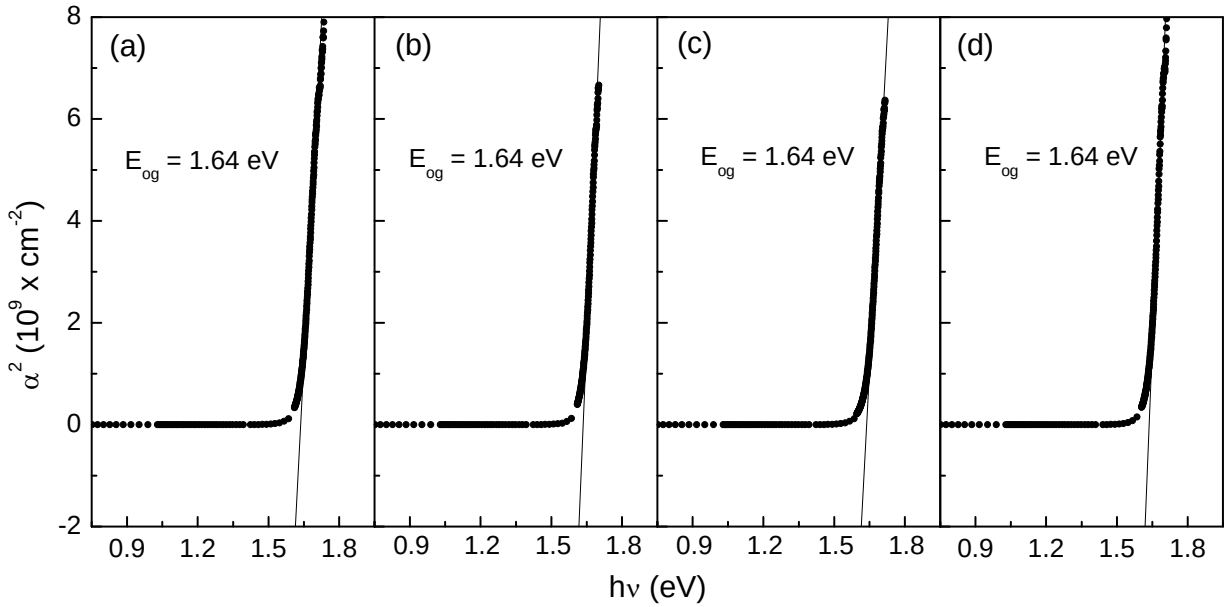

Figure 5.30. Calculation of the optical gap (E_{og}) after light irradiation for 7 days (a), after the exposure to *n.c.* for 10 days (b), after irradiation for 28 days (c) and after the exposure to *n.c.* for 60 days (d). The vertical axis is the same for all the graphs.

In Figure 5.31 the results obtained for the Urbach energy are presented. Such parameter undergoes an evolution depending on the treatment type and the time of exposure. The value for the as-deposited sample is 53 meV (Figure 5.9-b) and the irradiation with light does not cause any change after 7 days, but an increase to 57 meV is seen after 28 days. On the contrary the trend of variations of the parameter when the sample is exposed to environmental conditions is less clear, since after 10 days of exposure the Urbach energy decreases to a value of 50 meV, while after 60

days it increases again to a value of 53 meV. If we consider that the error affecting the results here presented is equal to ± 1 meV in all the cases, such variations only could indicate that the parameter under study slightly increases with the time of exposure to light.

Keeping a parallelism with hydrogenated amorphous silicon, the last result would indicate that the film, after being exposed to light irradiation, undergoes a worsening of its electronic properties with an increase of the extended states, revealed by an increase of the Urbach energy, and a slight increase of the localized states, indicated by the slight increase in the sub-gap absorption. In any case, all the variations are of little importance.

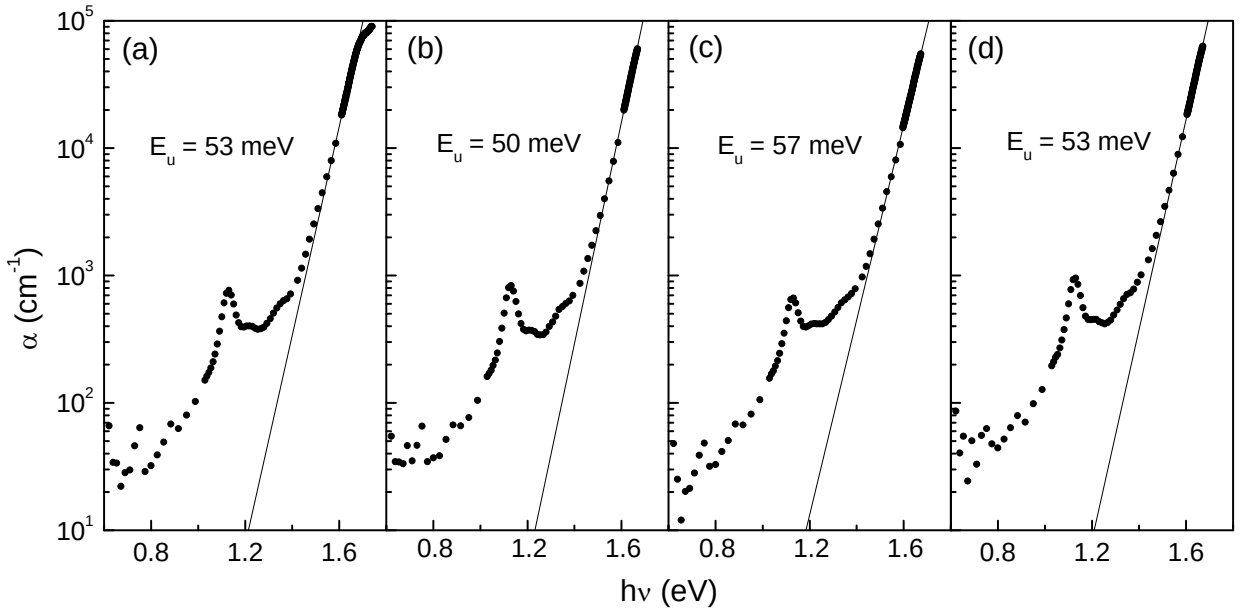

Figure 5.31. Calculation of the Urbach energy (E_u) after light irradiation for 7 days (a), after the exposure to *n.c.* for 10 days (b), after irradiation for 28 days (c) and after the exposure to *n.c.* for 60 days (d). The vertical axis is the same for all the graphs.

In Figure 5.32, the optical transmittance, measured after each degradation treatment, is shown. The most important alterations are visible for wavelengths higher than 800 nm and lower than 500 nm. In the former case it seems that the only thing that changes are the interferences caused by the multiple reflections at the interfaces. In such case the variation could be due to the fact that the measurement has been taken in a slightly different point of the sample. In the latter case, on the contrary, the transmittance decreases depending on the treatment: the longer the time spent under degradation conditions, the more the intensity of the transmittance peak located at around 470 nm diminishes. Depending on the treatment, different time is needed to obtain the same effect.

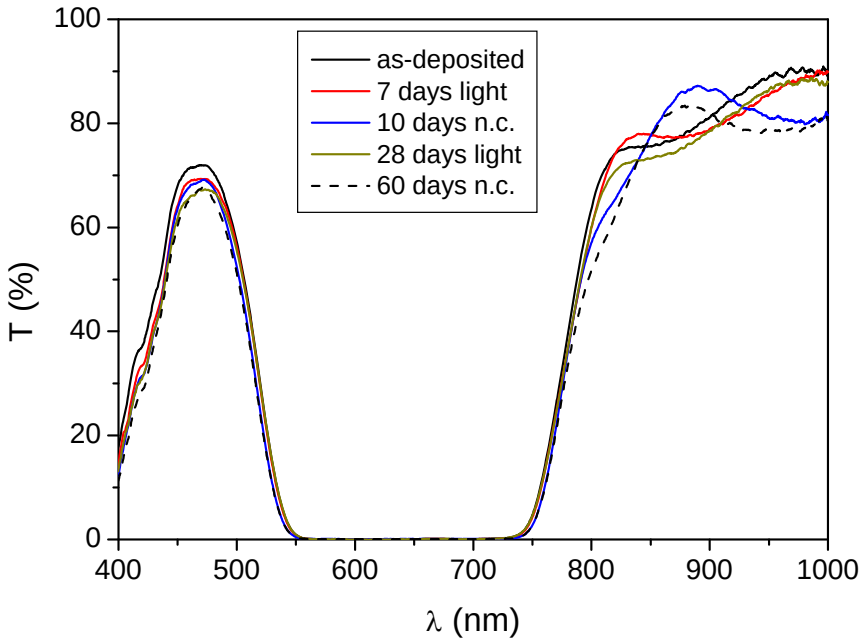

Figure 5.32. Transmittance spectra taken on as-deposited CuPc film (black line), after 7 days of treatment with light irradiation (red line), after 10 days of exposure to *n.c.* (blue line), after 28 days with illumination (dark yellow line) and 60 days at *n.c.* (black dashed line).

Given the negligible importance of the changes in the spectra, no annealing experiment has been performed on CuPc samples.

5.2.3 Fullerene (C_{60})

In Figure 5.33 a comparison between as-deposited and degraded fullerene thin films is shown.

The absorption of the material in sub-gap region suffers from important changes either if exposed to direct illumination or if simply exposed to environmental air and temperature conditions. As it could be expected, and similarly to what happened for pentacene (see Figure 5.24), the treatment with light irradiation has stronger effects than the one with normal conditions. In any case, the trend seems to be the same: a general increase in the absorption in the region between 0.9 and 1.8 eV.

These results are in good agreement with the ones obtained by Gotoh and co-workers[110] who observed that, in fullerene exposed to air, the sub-gap absorption level increases. The explanation that has been proposed for such phenomena is that the diffusion of O_2 molecules in the material yields the generation of states in the gap. It is worth observing that the sub-gap level absorption of our as-deposited sample is higher than the one measured by them. This could be explained by the fact that they have the possibility to deposit the thin film and then characterize it without taking it to

air, while, in our case, the samples must remain in contact with atmosphere for a few moments, before being characterized. Another important cause could be that they use quartz as a substrate that should be more transparent that our Corning glasses.

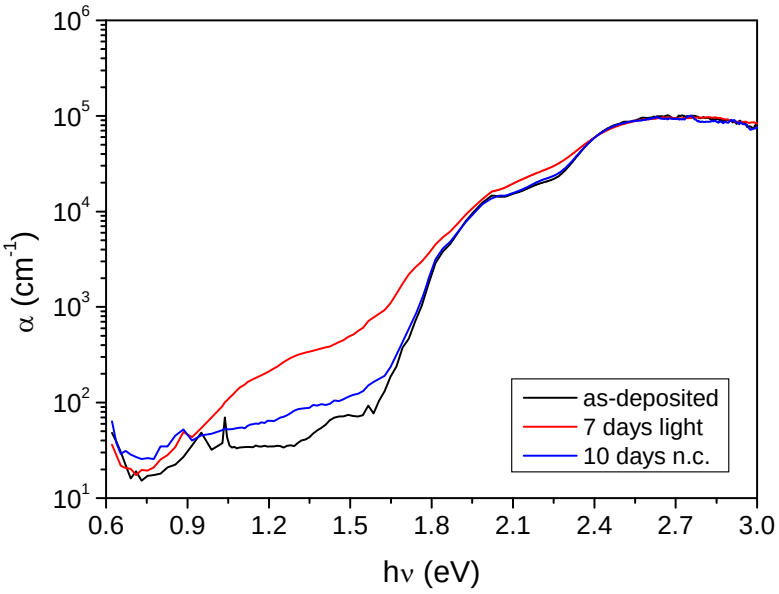

Figure 5.33. Absorption coefficient of degraded fullerene thin films: as-deposited film (black line), after 7 days of irradiation treatment (red line), after 10 days of exposure to *n.c.* (blue line).

In Figure 5.34 the fits for the calculation of the optical gap of degraded fullerene are shown.

The values of the optical gap have been calculated using Tauc's law and they have been found to be equal to 1.65 ± 0.01 eV for the irradiated sample and 1.66 ± 0.01 eV for the sample exposed to normal conditions (*n.c.*). These values are slightly lower than the one of as-deposited fullerene calculated with the same law (1.68 eV in Figure 5.14). Anyway, the differences are not very significant, when the error affecting the calculation is considered.

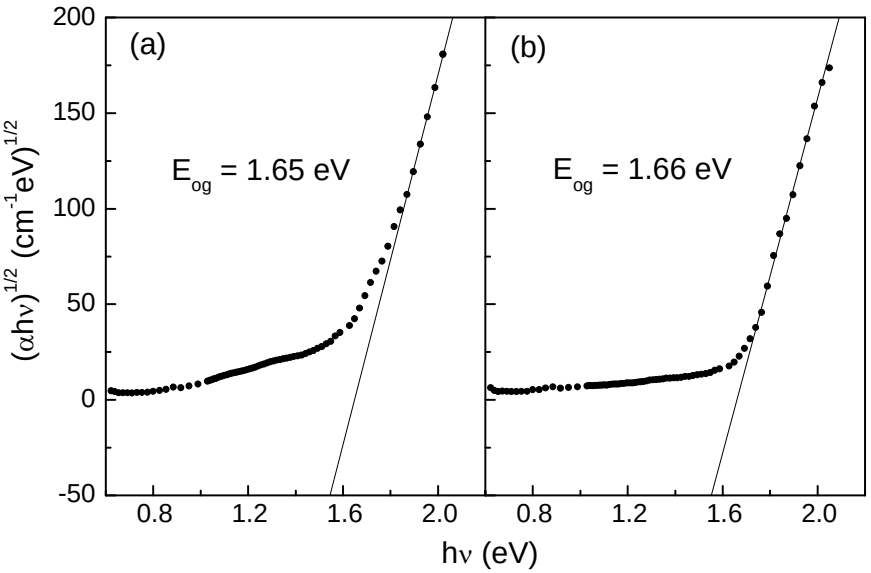

Figure 5.34. Calculation of the optical gap (E_{og}) after light irradiation for 7 days (a) and after the exposure to *n.c.* for 10 days (b). The vertical axis is the same for all the graphs.

In Figure 5.35 the calculations of the Urbach energy of fullerene after the degradation processes are shown.

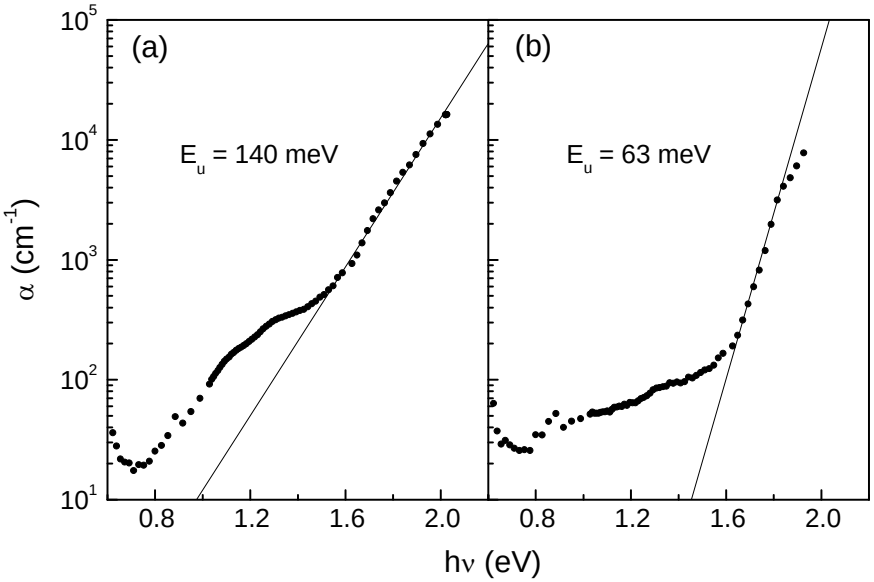

Figure 5.35. Calculation of the Urbach energy (E_u) after light irradiation for 7 days (a) and after the exposure to *n.c.* for 10 days (b). The vertical axis is the same for all the graphs.

As can be seen in Figure 5.35-a, an estimation of 140 ± 2 meV has been obtained for the sample when exposed to irradiation with light. This result indicates that the degradation causes the density of states in the gap to increase. An increase of the localized states in the gap had already been registered by observing an increase of the sub-gap absorption level (see Figure 5.33). When the material is simply exposed to normal environmental conditions of temperature and light (Figure 5.35-b), the Urbach energy stays constant at the original value of 63 meV (Figure 5.13-b).

In Figure 5.36 the evolution of the optical transmittance spectrum with the degradation processes is shown. Differences are visible from 530 nm, starting with a decrease of transmittance between 530 and 620 nm for the light irradiated sample. It is difficult to identify any change in the region located at wavelengths higher than 700 nm because of the interferences.

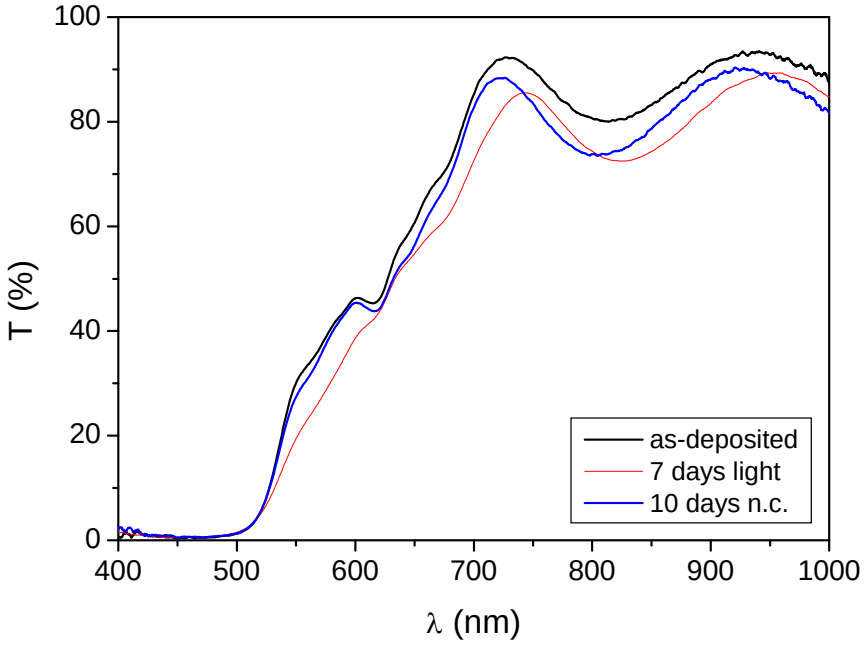

Figure 5.36. Transmittance spectra taken on as-deposited fullerene film (black line), after 7 days of treatment with light irradiation (red line), after 10 days of exposure to *n.c.* (blue line).

Since the effects of degradation were so clear also in the case of fullerene, the sample has been annealed in order to see if it was possible to reverse such effects. The annealing has been performed at 250ºC.

In Figure 5.37 the absorption coefficient and the transmittance spectra of the annealed sample are compared with the ones of the as-deposited film and the light degraded one:

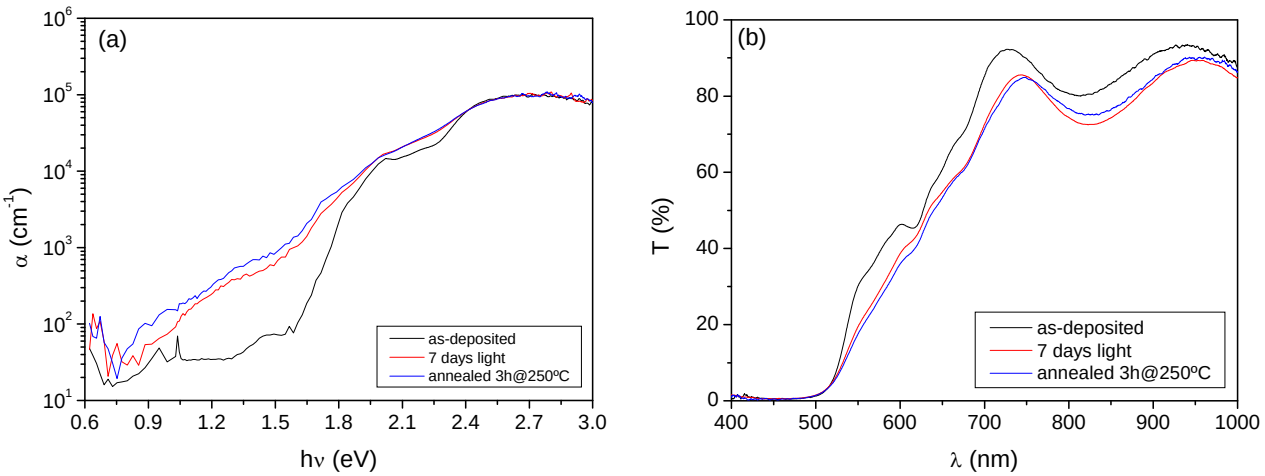

Figure 5.37. Absorption coefficient (a) and transmittance spectra (b) of as-deposited (black line), light degraded (red line) and annealed (blue line) C_{60} at 250ºC for 3 hours.

After the annealing at 250ºC for three hours the sub-gap absorption even increases and the optical transmittance suffers little changes, indicating that the temperature treatment did not have the desired effect.

5.2.4 Perylene-3,4,9,10-tetracarboxylic dianhydride (PTCDA)

In Figure 5.38 the effects of the degradation treatments on the absorption coefficient of PTCDA are shown. Only slight changes can be observed in the absorption: an increase between 1.55 and 2.06 eV, proportional to the exposure time, in the case of the sample exposed to light and a slight increase at lower energy values for the sample exposed to normal conditions for 10 days. On the contrary, after exposing to *n.c.* for 60 days the absorption coefficient seems to have recovered its original shape. In both cases the greatest variation of the alpha is nearly by a factor 2.

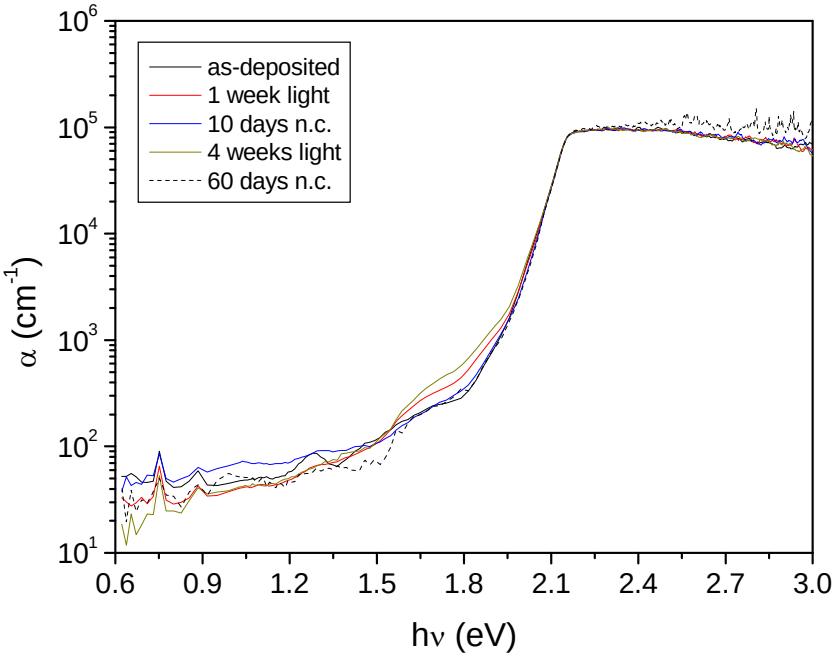

Figure 5.38. Absorption coefficient of degraded PTCDA thin films: as-deposited film (black line), after 7 days of irradiation treatment (red line), after 10 days of exposure to *n.c.* (blue line), after 28 days of irradiation (dark yellow line) and 60 days of exposure to *n.c.* (black dashed line).

In Figure 5.39 the calculations of the optical gap of PTCDA are shown. As it can also be guessed from Figure 5.38, the optical gap does not vary after performing the degradation processes. The value obtained is 2.11 ± 0.01 eV for all cases.

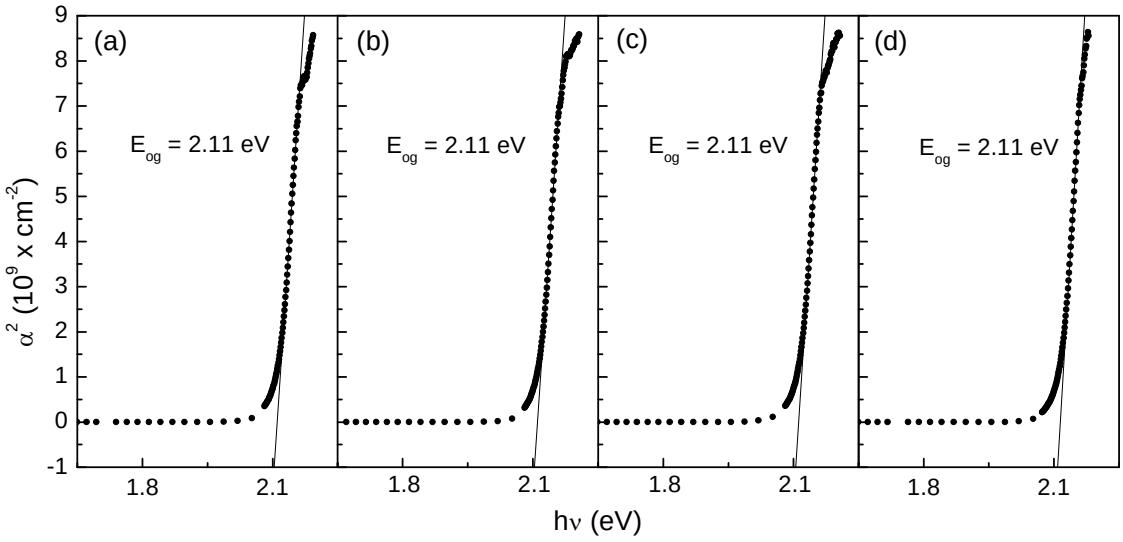

Figure 5.39. Calculation of the optical gap (E_{og}) after light irradiation for 7 days (a), after the exposure to *n.c.* for 10 days (b), after irradiation for 28 days (c) and after the exposure to *n.c.* for 60 days (d). The vertical axis is the same for all the graphs.

In Figure 5.40 the α is presented together with the calculated Urbach energy.

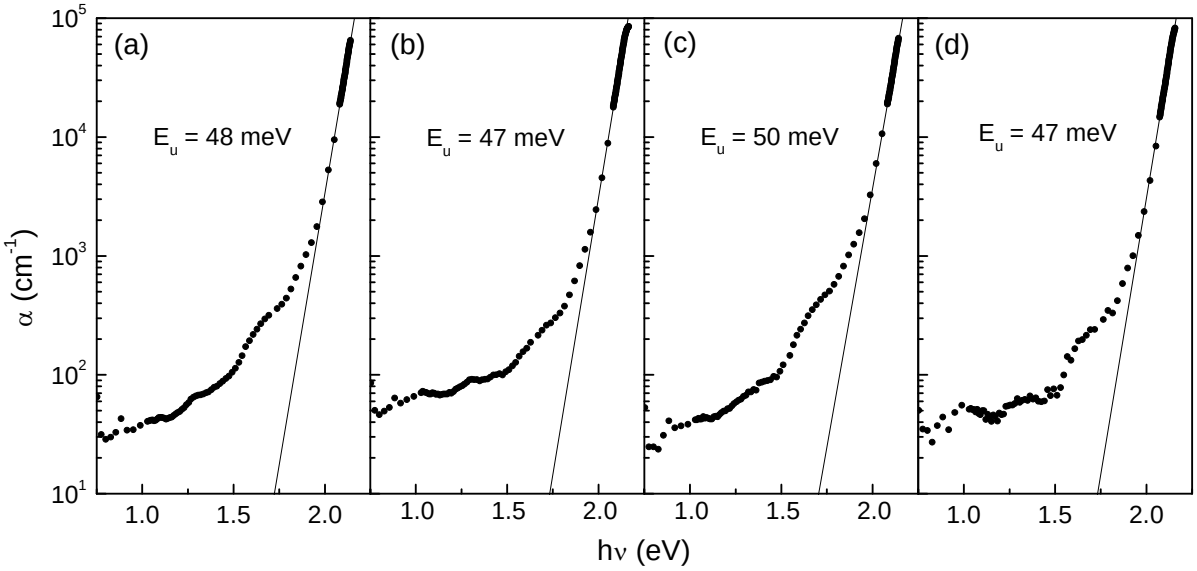

Figure 5.40. Calculation of the Urbach energy (E_u) after light irradiation for 7 days (a), after the exposure to *n.c.* for 10 days (b), after irradiation for 28 days (c) and after the exposure to *n.c.* for 60 days (d). The vertical axis is the same for all the graphs.

The process of degradation by exposure to environmental atmosphere and temperature has no evident effect, since the Urbach energy is 47 ± 1 meV, only 1 meV superior to the original value of 46 meV (Figure 5.18). On the contrary, light irradiation induces an increase in the value, given that it increases to 48 ± 1 meV after 7 days and to 50 ± 1 meV after 28 days of treatment. The last result would indicate an increase of the density of extended states, in the band tails.

In Figure 5.41 the transmission spectra of PTCDA before and after being treated is shown. As it can be seen, the transmittance does not change after the degradation processes, but in the region above 600 nm where the interferences peaks slightly change their position. Such variation could not be due to degradation phenomena in the material but to the fact that the measurements could have been performed in slightly different sites of the sample.

As a conclusion, PTCDA seems quite stable and demonstrates to maintain its optical properties reasonably unaltered during the first few days after the deposition.

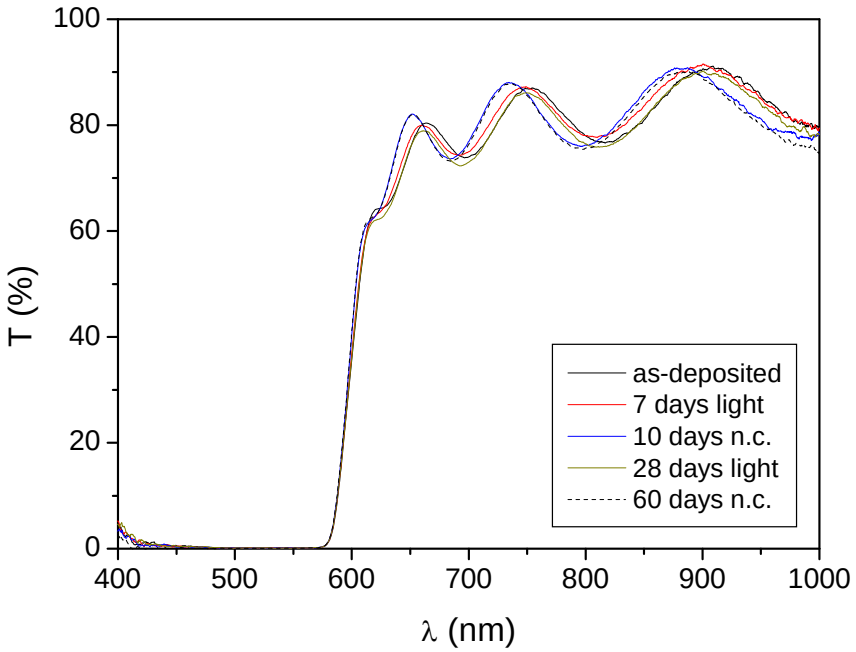

Figure 5.41. Transmittance spectra taken on as-deposited PTCDA film (black line), after 7 days of treatment with light irradiation (red line), after 10 days of exposure to *n.c.* (blue line), after 28 days with illumination (dark yellow line) and 60 days at *n.c.* (black dashed line).

5.2.5 *N,N*-ditridecyl-3,4,9,10-perylenetetracarboxylic diimide (PTCDI-C_{13})

Finally, in Figure 5.42 the absorption coefficient of as-deposited and degraded PTCDI-C_{13} are shown. Due to technical problems, the samples have been exposed to both treatments for two weeks.

When irradiated with light, the absorption coefficient of PTCDI-C_{13} (red line) undergoes alterations in the region located below 1.58 eV. In this part of the spectrum, α increases by a factor that reaches a maximum of approximately 2 at 1.3-1.4 eV. The rest of the spectrum is quite identical to the one of the as-deposited sample.

The changes in α are more pronounced after the treatment with environmental air and light conditions (blue line in Figure 5.42). The absorption level decreases in the region between 1.92 and 1.53 eV, while it increases for energy values higher than 1.53 eV. In the last case the difference reaches a maximum variation factor of 2.5 at approximately 1.37 eV. As a result, the shoulder centred at 1.6 eV disappears and this makes it easier to identify the Urbach tail.

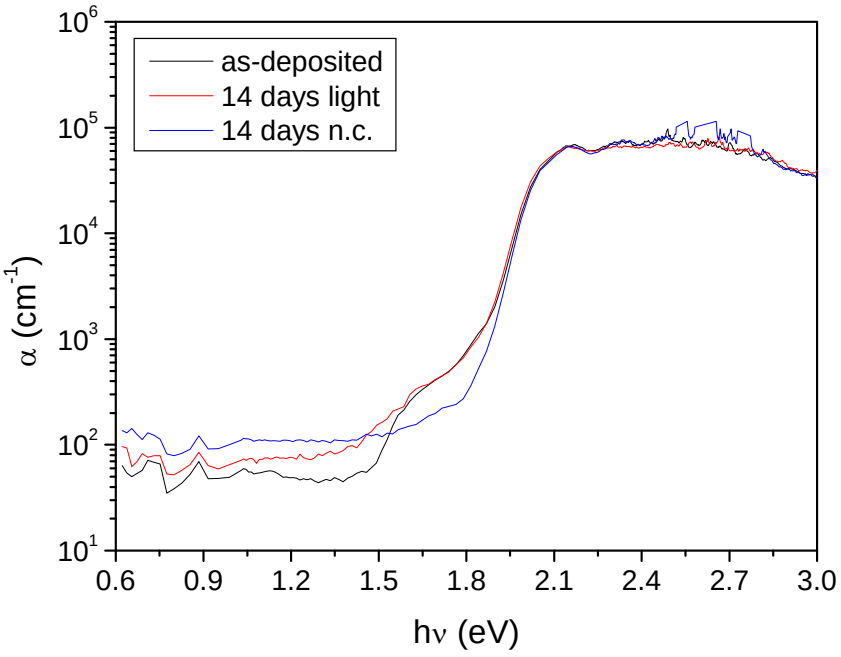

Figure 5.42. Absorption coefficient of degraded PTCDI-C_{13} thin films: as-deposited film (black line), after 7 days of irradiation treatment (red line), after 10 days of exposure to *n.c.* (blue line).

The optical gap has been calculated also after the degradation processes and in Figure 5.43 the results are shown:

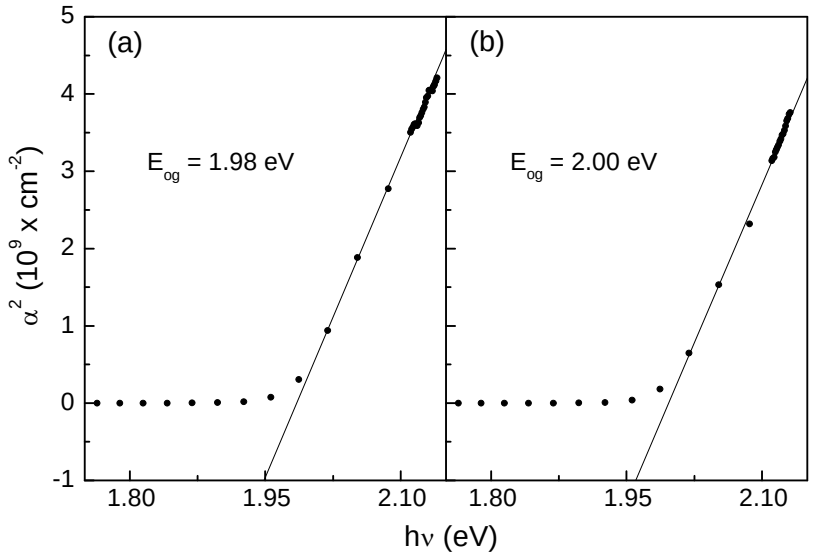

Figure 5.43. Calculation of the optical gap of PTCDI-C_{13} after the degradation processes: a) after treatment with light irradiation; b) after treatment in environmental conditions (*n.c.*). The vertical axis is the same for all the graphs.

The values obtained for the sample after light irradiation and exposure to *n.c.* treatments are 1.98 and 2.00 ± 0.01 eV, respectively. Such numbers are not significantly different from the one obtained for the as-deposited sample (2.00 eV), if we consider the error in evaluating them.

In Figure 5.44 the calculations of the Urbach energies after the degradation processes are shown. For the sample treated with light irradiation a value of 43 ± 1 meV has been found, while for the sample treated at *n.c.* a value of 39 ± 1 meV has been calculated. The second value is slightly lower than the first one and this could mean that a small improvement in the structural quality has taken place in the sample exposed simply to environmental light and air. Nevertheless, reminding that the absorption level in the sub-gap region has increased (see Figure 5.42), we could interpret that the density of localized states in the gap has increased too, while, having decreased the Urbach energy, the band tails have diminished.

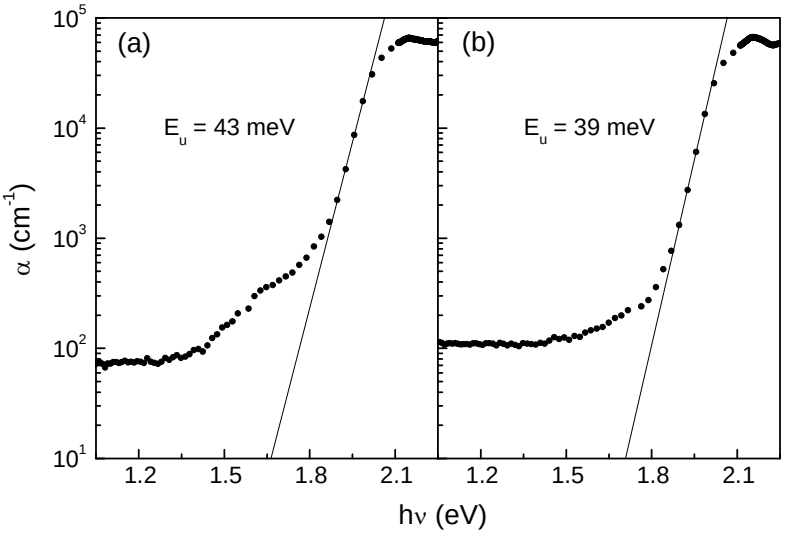

Figure 5.44. Calculation of the Urbach energy of PTCDI-C_{13} after the degradation processes: a) after treatment with light irradiation; b) after treatment in environmental conditions (*n.c.*). The vertical axis is the same for all the graphs.

In Figure 5.45 the evolution of the transmittance of PTCDI-C_{13} with degradation processes is presented. Few changes are observed in the transmittance of PTCDI-C_{13}, since there is a slight increase of transmittance for the sample exposed to *n.c.*, for wavelengths higher than 600 nm and a decrease, even less perceptible, for the irradiated sample, at the same wavelengths.

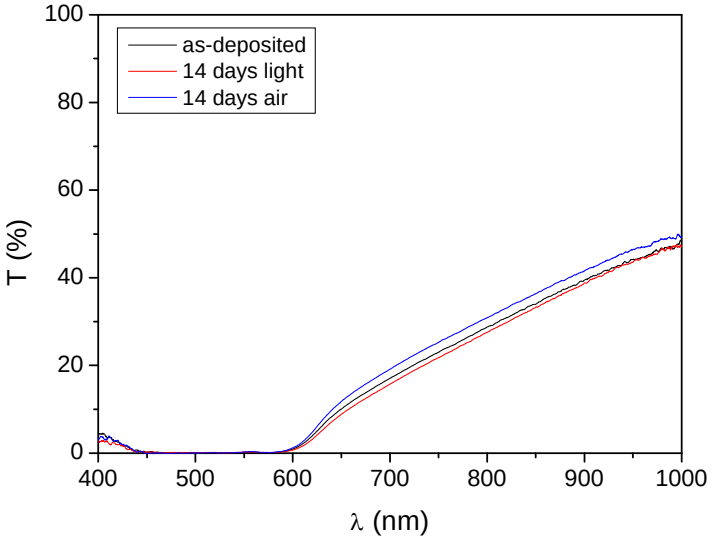

Figure 5.45. Transmittance spectra measured on the as-deposited PTCDI-C_{13} film (black line), after 14 days of treatment with light irradiation (red line), after 14 days of exposure to *n.c.* (blue line).

5.3 Conclusions about pure materials

Five organic semiconductors have been deposited in thin films and characterized by XRD, PDS and optical transmittance spectroscopy. XRD has been employed to observe if the thin films had polycrystalline or amorphous micro-structure. Almost all the materials investigated here have turned up to grow in a polycrystalline structure, in the deposition conditions used, except fullerene that was amorphous. The absorption coefficient has been evaluated in a range between 400 nm (3.1 eV) and 2000 nm (0.62 eV), which includes visible and NIR.

The general model for allowed direct transitions in inorganic semiconductors and the Tauc model for inorganic amorphous semiconductors have been analyzed for the calculation of the optical gap of our organic semiconductors. On one side, the absorption curves obtained in our experiments are similar to the ones of a-Si:H, with non-zero absorption in the sub-gap region, associated with localized states in the gap, and an exponential region that can be identified with the Urbach tail, associated with band tails. On the other side, the XRD spectra suggested that only fullerene is amorphous. To our knowledge there are not enough examples in literature of gap calculation by PDS, to compare. In our case, the choice between two models has been taken by considering the XRD indication. As a result, Tauc model has been used for fullerene, while for the other materials the more general model has been employed. The results obtained show that the

equations fit well the experimental data and, when it has been possible, the obtained gap values have been compared with the literature and are in good agreement with it. We have also evaluated the Urbach energy, the values of which are resumed, together with the ones obtained for gap, in Table 5.1:

	$E_g^{PDS/T}$ (eV)	$E_g^{fig.3.7}$ (eV)	E_u (meV)
Pentacene	1.73	2.1	37
CuPc	1.64	1.7	53
Fullerene	1.68	1.7	63
PTCDA	2.11	2.6	46
PTCDI-C_{13}	2.00	2.0	48

Table 5.1. Summary of the parameters calculated for pure materials: $E_g^{PDS/T}$ refers to the gap calculated from PDS and transmittance measurements in this work, $E_g^{fig.3.7}$ refers to results obtained by other techniques and already presented in Figure 3.7 and E_u is the Urbach energy.

In this table the calculated gap values ($E_g^{PDS/T}$) are compared with others ($E_g^{fig.3.7}$) estimated from Figure 3.7 where HOMO and LUMO energetic levels, obtained by other experimental techniques, have been reported. The difference between HOMO and LUMO has been taken, in this case, as the optical gap of the materials. A good agreement has been found for the values of CuPc, fullerene and PTCDI-C_{13}, but not for the ones of pentacene and PTCDA. The cause of these discrepancies is not clear yet. We only can argue that the experimental conditions and the type of sample (deposition parameters, substrate…) can influence the final result. The Urbach energy, related with the structural quality of a material, has been found coherently higher for the amorphous material (fullerene in Figure 5.13-b) than for the polycrystalline ones. These approximate the reference value of 50 meV for a good quality hydrogenated amorphous silicon, with the exception, once again, of pentacene, the value of which is surprisingly low (37 meV).

An investigation has been done to check the effects that the exposure to oxidizing agents and light can have on the optical properties of the materials. For each material a few samples have been deposited in a single process and then exposed to two different kinds of degradation treatments. One of them consisting in exposing the samples to direct irradiation with visible light and another one in

exposing the samples to normal laboratory air and light conditions. Pentacene and fullerene undergo much degradation when illuminated, having their absorption coefficient increased in the sub-gap region. Such result can be interpreted as caused by an increase in the density of states, associated with defects, in the gap. The process by exposure to normal conditions causes, in fullerene, similar effects but with less intensity. In the case of pentacene the only difference between the two treatments is the appearance of an absorption peak at 1.28 eV the origin of which we still do not know. It seems that a small band has risen in the gap, from which optical absorptions are possible. The absorptions of CuPc and PTCDA suffer only from little modifications after both processes, while for PTCDI-C_{13} the two processes introduce different changes: the process in normal conditions produces an increase in the absorption level below 1.5 eV, while the process with light irradiation causes a more intense increase in the same region but also a decrease between 1.5 and 1.9 eV.

The exact mechanism by which degradation occurs in our materials is still not well understood, but, as a starting point, we could make two hypotheses on the basis of the accumulated knowledge about a-Si:H and organic semiconductors. According to the first of them, the increase of the sub-gap absorption could be caused by the energy absorbed and re-emitted, not radiatively, by the electrons and which can then break some chemical bond creating new defects. Such hypothesis is normally the explanation for the degradation observed in amorphous silicon when it is exposed to light irradiation. According to the second hypothesis, when the material absorbs light, the excited species that are generated in it (radicals) could react chemically with the oxygen contained in the air[18,19]. Moreover, fullerene has been demonstrated as capable of incorporating oxygen molecules (O_2) in its interstitial sites. Specific analysis should be performed in order to analyze the real nature of the defects that are generated in an organic semiconductor exposed to air and light.

CHAPTER 6

BULK HETEROJUNCTIONS

In chapter 3 the importance of creating a heterojunction between a donor (D) and an acceptor (A) has been discussed as the fundamental requirement for an organic solar cell to work. As it has also been explained, the *bulk heterojunction*, obtained by physically mixing the two materials, yields the largest interface surface and the highest efficiency in dissociating the excitons. In such a kind of active layer, the excitons have the shortest distance to cover in order to dissociate and the probability for them to recombine is the lowest. In this paragraph a report about the first attempts to deposit bulk heterojunctions, in our laboratory, by co-evaporation will be presented. The samples have been characterized by PDS, optical transmittance and XRD. Moreover, the films have been exposed to the same degradation processes as the pure materials to analyze if the new configuration can influence, at some extent, the trend of the semiconductors to degrade.

Firstly, pentacene heterojunctions with each of the three acceptors (fullerene, PTCDA and PTCDI-C_{13}) will be presented, followed by the heterojunctions with CuPc as a donor. The samples have been deposited with the following conditions:

- thickness: 1 μm
- substrate temperature: room temperature
- global deposition rate: 3 Å/s (1.5 + 1.5 Å/s)
- base pressure: $6 \cdot 10^{-4}$ Pa

The thickness of each sample has been confirmed by using a stylus profiler.

In the first paragraph of this chapter (paragraph 6.1) the characterizations of the bulk heterojunctions will be presented, while in the second one (paragraph 6.2) the results obtained by performing annealing treatments on the same samples will be discussed.

6.1 Characterization of the bulk heterojunctions

6.1.1 Pentacene-fullerene

The absorption coefficient and the transmittance of a co-evaporated pentacene-fullerene thin film are compared, in Figure 6.1, with the ones measured on pure films:

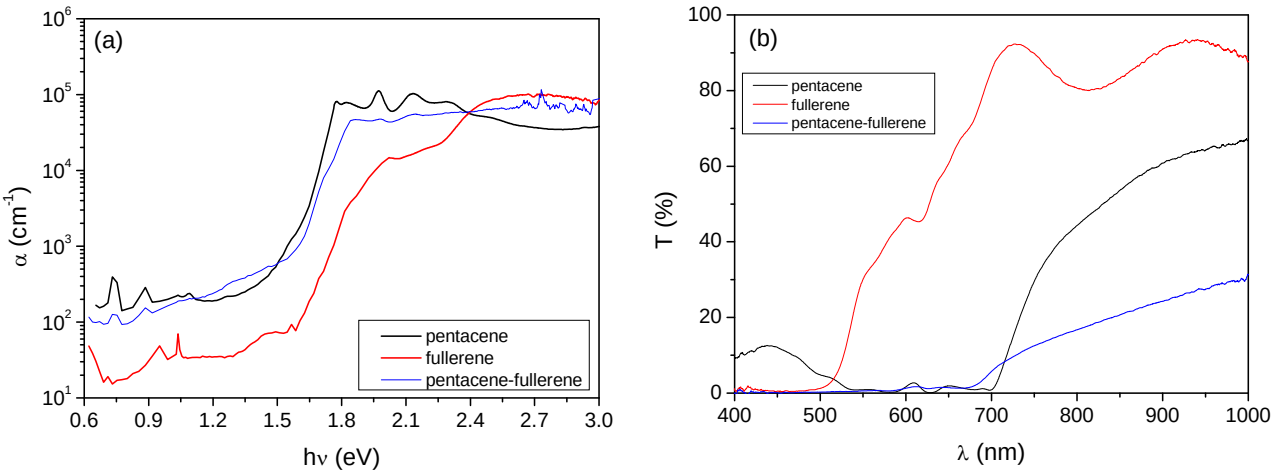

Figure 6.1. (a) Comparison between the absorption coefficients of pentacene, fullerene and the co-evaporated material; (b) Comparison between the transmittance spectra.

In the high-level absorption region, α of the co-evaporated material has values that seem to be the average of the ones of pure materials. On one side, in the other part of the spectrum the most absorptive material, which is pentacene, dominates in determining the absorption level of the co-evaporated thin film but without the features that are typical for that material. On the other side, in the part where there is exponential decrease of the absorption the shape of the spectrum recalls the one of fullerene.

In the sub-gap region the absorption level is near to the one of pentacene, exceeding it between 1.2 and 1.5 eV. Such a phenomenon has already been observed in a similar experiment performed on films of blended MDMO-PPV:PCBM[115]. The explanation proposed in that case for such unexpected absorption is that in the co-deposited material the interaction between the two components yields the formation of Charge Transfer Complexes (CTC), which would give rise to new absorption features. It is still not clear if the presence of CTC can explain also the increased sub-gap absorption observed in our sample.

The transmittance spectra reveal that the co-evaporated sample has a much lower transmission, with near to zero transmission from 400 to 675 nm.

The XRD spectrum of the co-evaporated sample is presented in Figure 6.2. The spectra of pentacene and fullerene are the ones already discussed previously (Figure 5.2 and Figure 5.12) where it had been noted that pentacene had a polycrystalline structure while fullerene was apparently amorphous. The co-evaporated material also seems to be characterized by an amorphous structure, since no diffraction peak is observed.

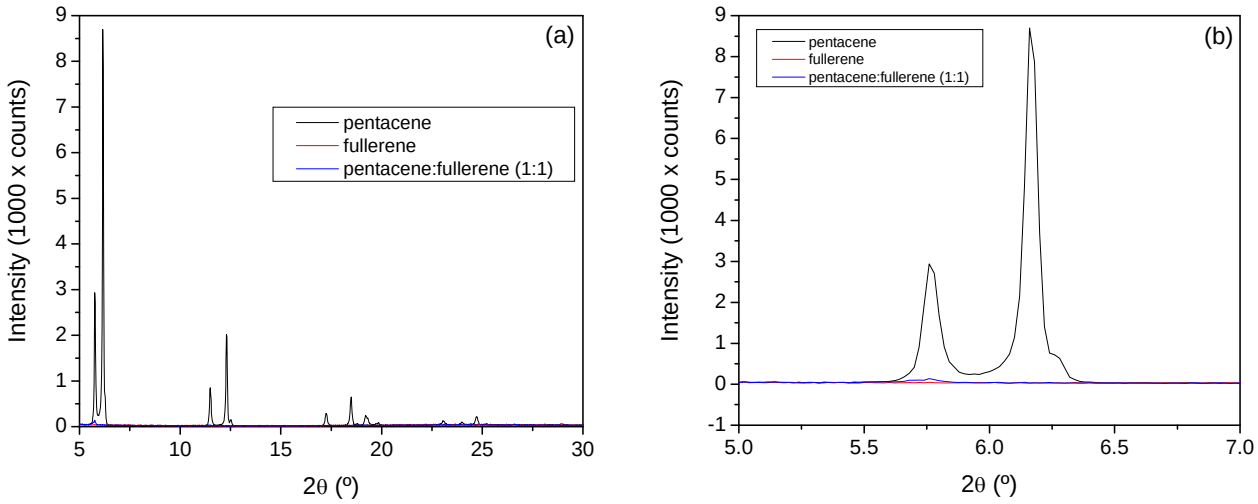

Figure 6.2. (a) Comparison between XRD spectra of pure pentacene and fullerene and co-evaporated pentacene-fullerene; (b) Detail of the first group of peaks.

The amorphous structure in the co-evaporated thin film is somewhat expected, since what we have been trying to do is to deposit two molecules with completely different shape (see Figure 2.25 and Figure 2.26) at the same time. It could be argued that the molecules do not have the possibility, or the time, to organize in an ordered structure. In literature there are examples of similar results with a polymer solar cell made by co-deposited P3HT:PCBM. In that case the deposition process, performed by spin-coating, is very different, since the molecules are dispersed in an organic solvent, but the result is similar to the one we have obtained by evaporation: an amorphous material.

The optical gap and the Urbach energy have been estimated for pentacene-fullerene thin films and the results are shown in Figure 6.3.

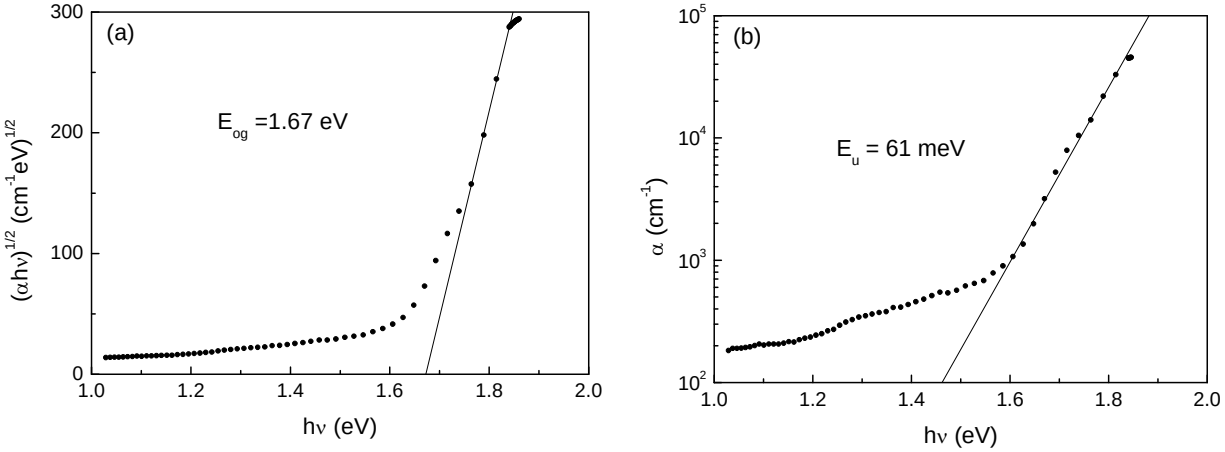

Figure 6.3. (a) Optical gap (E_{og}) of the co-evaporated pentacene-fullerene thin film; (b) The Urbach energy (E_u).

Given that the XRD characterization indicates that the thin film is amorphous, Tauc's law has been employed for the calculation of the optical gap with a result of 1.67 ± 0.01 eV (Figure 6.3-a). The Urbach energy has been found to be equal to 61 ± 2 meV (Figure 6.3-b). The optical gap is interestingly lower than the ones of pure materials: 1.73 eV for pentacene (Figure 5.3-a) and 1.68 eV (Figure 5.13-a). On the contrary, the energy of Urbach is much higher than the one of pentacene (37 meV in Figure 5.3-b), but slightly lower than the one of fullerene (63 meV in Figure 5.13-b). Like the case of pure materials, where amorphous fullerene showed the highest Urbach energy, the amorphous heterojunction here discussed also shows a high value for that parameter, if compared with the other ones.

Also in the case of the co-evaporated thin films the experiment of measuring the effects of the degradation processes on their optical properties, has been performed as in the case of the pure materials. The results obtained on two samples after 7 days of irradiation with light and after 10 days of exposure to normal environmental conditions of temperature and air (*n.c.*) are shown in Figure 6.4.

The thin film undergoes degradation mostly when exposed to direct light (red line in Figure 6.4) and with less intensity when exposed to environmental normal conditions (blue line). A trace of a new absorption peak, already seen in the case of pure pentacene, can hardly be observed around 1.28 eV, for the sample irradiated with light.

The transmittance spectra (Figure 6.4-b) indicate that, respect to the as-deposited sample, the optical transmittance increases after the treatment with light irradiation and decreases after the exposure to *n.c.* Apart from such considerations, the shape of the graphs remains unmodified.

In general, it seems that a co-evaporated film made of two materials that suffer from degradation, also degrades.

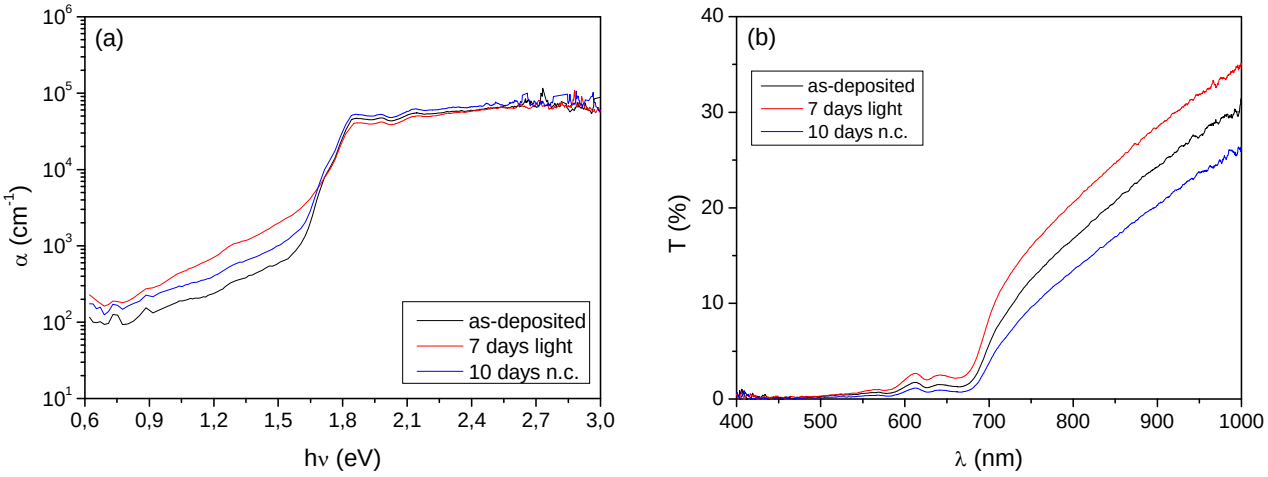

Figure 6.4. Absorption coefficient (a) and transmittance (b) of degraded pentacene-fullerene thin films: as-deposited film (black line), after 7 days of irradiation treatment (red line) and 10 days of exposure to *n.c.* (blue line).

The evolution of the optical gap in function of the degradation treatment has been investigated and is shown in Figure 6.5.

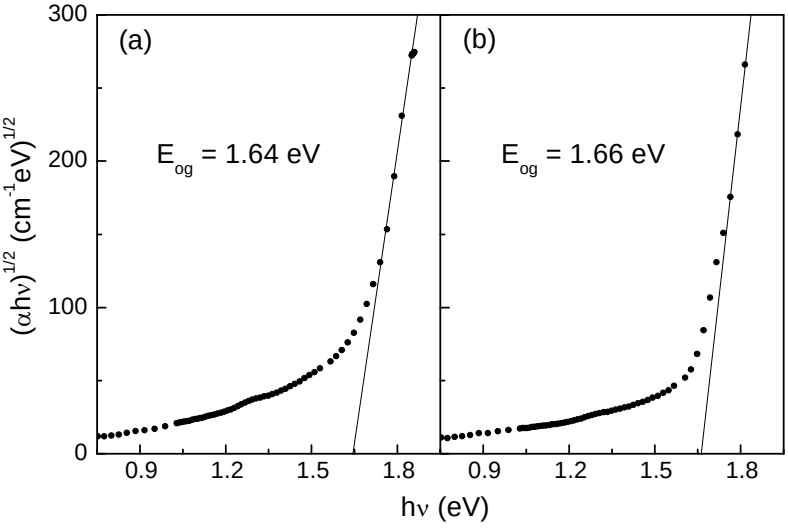

Figure 6.5. Optical gap (E_{og}) of the thin film exposed to light irradiation for 7 days (a) and of the one exposed to *n.c.* for 10 days (b).

The values obtained are 1.64 ± 0.01 eV for the sample exposed to light irradiation and 1.66 ± 0.01 eV for the sample exposed to *n.c*. In both cases the gap seems to have decreased, with respect to the as-deposited sample (1.67 eV in Figure 6.3-a), but the variation is not much significant, taking into account the error in calculating the parameter.

Also possible variations in the Urbach energy have been investigated and the results are shown in Figure 6.6.

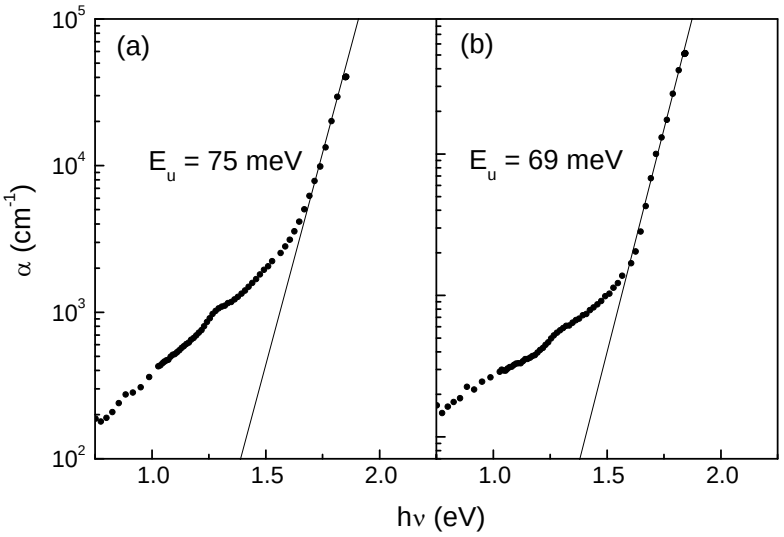

Figure 6.6. Urbach energy (E_u) of the thin film exposed to light irradiation for 7 days (a) and of the one exposed to *n.c.* for 10 days (b).

A value of 75 ± 1 meV has been estimated for the sample irradiated with light (Figure 6.6-a) and a value of 69 ± 3 meV for the sample degraded at *n.c.*(Figure 6.6-b). In both cases the Urbach energy has changed, respect to the original one (61 meV in Figure 6.3-b), by an amount that is clearly higher than the error affecting the calculation of such parameter.

These results indicate that a substantial increase, more pronounced for the irradiated sample, in the density of both localized and extended states has occurred, with a probable worsening in the structural quality of the films and their electrical properties.

6.1.2 Pentacene-PTCDA

The absorption coefficient and the transmittance of co-evaporated pentacene-PTCDA thin films are shown in Figure 6.7.

The absorption coefficient obtained for the co-evaporated material (Figure 6.7-a) is clearly different from the ones of the pure materials. For high energy values, the absorption level, induced by the more absorptive pentacene, is kept high for a range of energy that is wider than in the case of pure PTCDA. Nevertheless, as it happens for pentacene-fullerene thin films, the features that characterize pentacene are lost or modified. In the sub-gap region a wide absorption band, centred at 1.27 eV has appeared. Such band corresponds quite well to the absorption peak that had been found for pure PTCDA, exactly for that value of energy.

Also the optical transmittance (Figure 6.7-b) has been radically altered by mixing the two materials, as indicated by a remarkable increase around 600 nm.

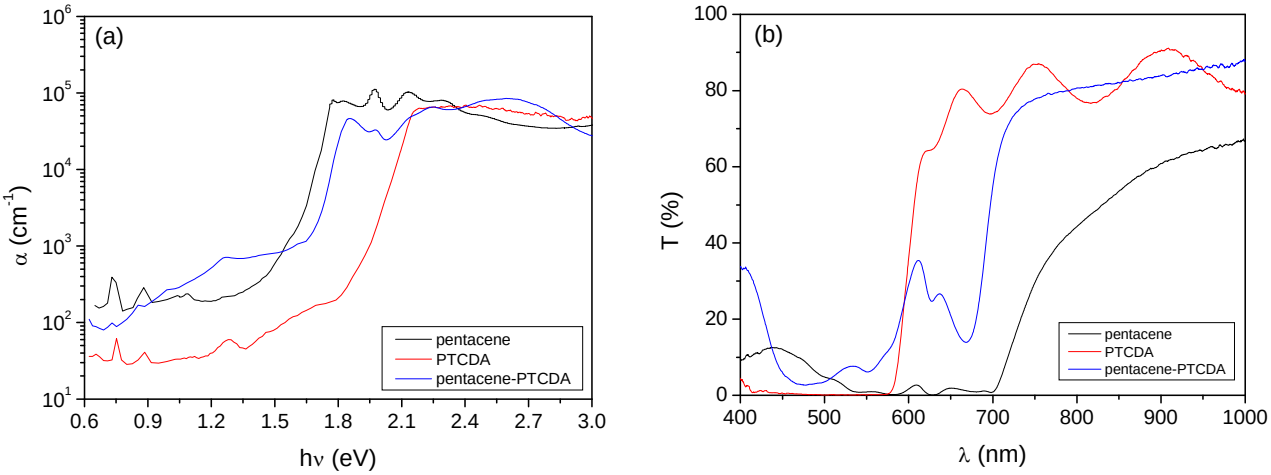

Figure 6.7. (a) Comparison between the absorption coefficients of pentacene, PTCDA and the co-evaporated material; (b) Comparison between the transmittance spectra.

The XRD spectrum of the co-evaporated material is compared with the ones of pure materials in Figure 6.8. The complete XRD spectrum, shown in Figure 6.8-a, indicates that the co-evaporated thin film is amorphous, since no peak either from pentacene or PTCDA, or even from other types of structures, is observed. The result is better visible in the zooms done on the first group of peaks (Figure 6.8-b) and on the last one (Figure 6.8-c). In the first case, only the known pair of peaks of pentacene is present, while in the second one only the diffraction peak due to PTCDA.

The results here reported are similar to the ones already described for co-evaporated pentacene-fullerene thin films. To deposit at the same time two kinds of molecules with different shapes and dimensions makes it difficult to obtain an ordered structure that could probably be obtained by using a lower deposition ratio, by heating up the substrate during the process or by performing post-deposition annealing processes.

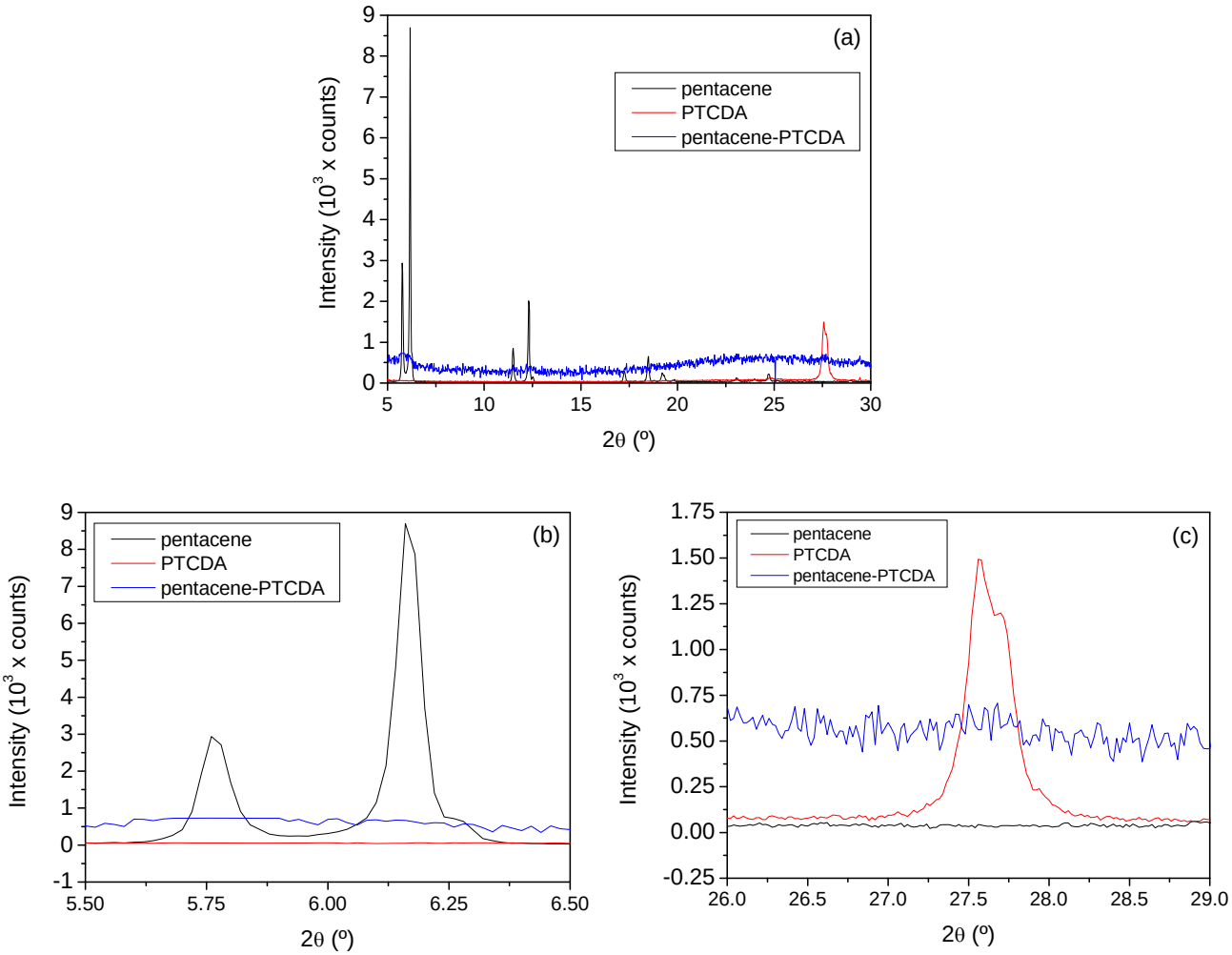

Figure 6.8. (a) Comparison between XRD spectra of pure pentacene (black line) and PTCDA (red line) and co-evaporated pentacene-PTCDA (blue line); (b) Detail of the first group of peaks; (c) Detail of the last group of peaks.

The calculations of optical gap and Urbach energy are shown in Figure 6.9. The optical gap has been found to be equal to 1.71 ± 0.01 eV, a value that is lower than both the ones of pentacene (1.73 eV in Figure 5.3-a) and PTCDA (2.11 eV in Figure 5.18-a). The Urbach energy is equal to 40 ± 2 meV, a value that is higher than the one of pentacene (37 meV in Figure 5.3-b), but lower than the one of pure PTCDA (46 meV in Figure 5.18-b). If compared with other values for such parameter calculated in the previous sections of this work, the one calculated here is a good value, especially if the amorphous nature of this material is considered.

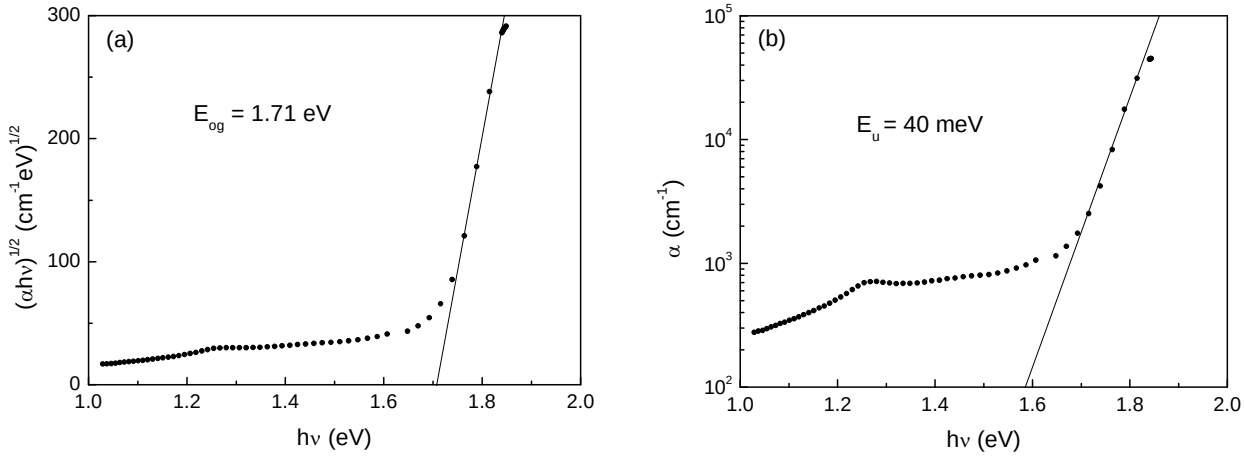

Figure 6.9. (a) Optical gap (E_{og}) of the co-evaporated pentacene-PTCDA thin film; (b) The Urbach energy (E_u).

In Figure 6.10 the effects of degradation on the absorption coefficient and the transmittance of pentacene-PTCDA are shown. The effects of degradation are extremely clear when the sample is exposed to light irradiation, since the absorption widely decreases in almost the whole range where the measurement has been performed, including the visible part (Figure 6.10-a). As it is to be expected, the change is more intense when the treatment is prolonged to 60 days, after which the exponential part of the spectrum results completely altered. At a glance, it seems that an important decrease in the sub-gap density of states has occurred, thing that in general is interpreted as a positive effect. Nevertheless, by analyzing the whole spectrum it is clear that the optical properties of the material have changed radically. On the contrary, the treatment at *n.c.* does not have great effects on α, but when the treatment is prolonged to 30 days. In this case we can observe a little decrease of the absorption around 1.26 eV and an increase below 0.93 eV.

The transmittance spectra confirm what has already been described for the absorption coefficient: the sample degraded for 60 days with light irradiation transmits much more light than before the treatment. The optical properties of the material have radically changed.

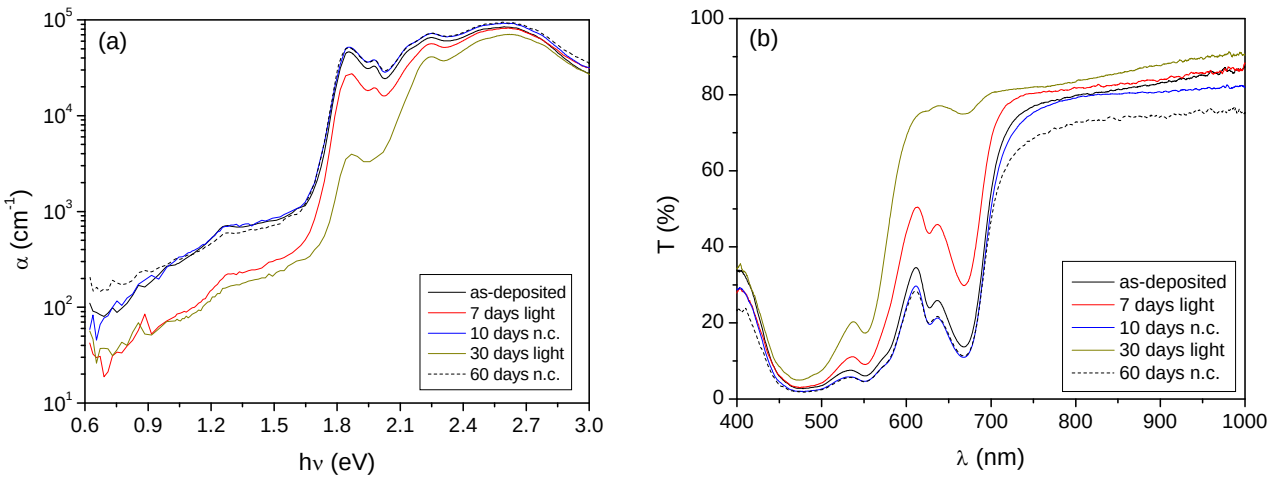

Figure 6.10. Absorption coefficient (a) and transmittance (b) of degraded pentacene-PTCDA thin films: as-deposited film (black line), after 7 days of irradiation treatment (red line), 10 days of exposure to *n.c.* (blue line), 30 days of irradiation (dark yellow line) and 60 days of exposure to *n.c.*

In Figure 6.11 the calculation of the optical gap after the degradation processes is presented.

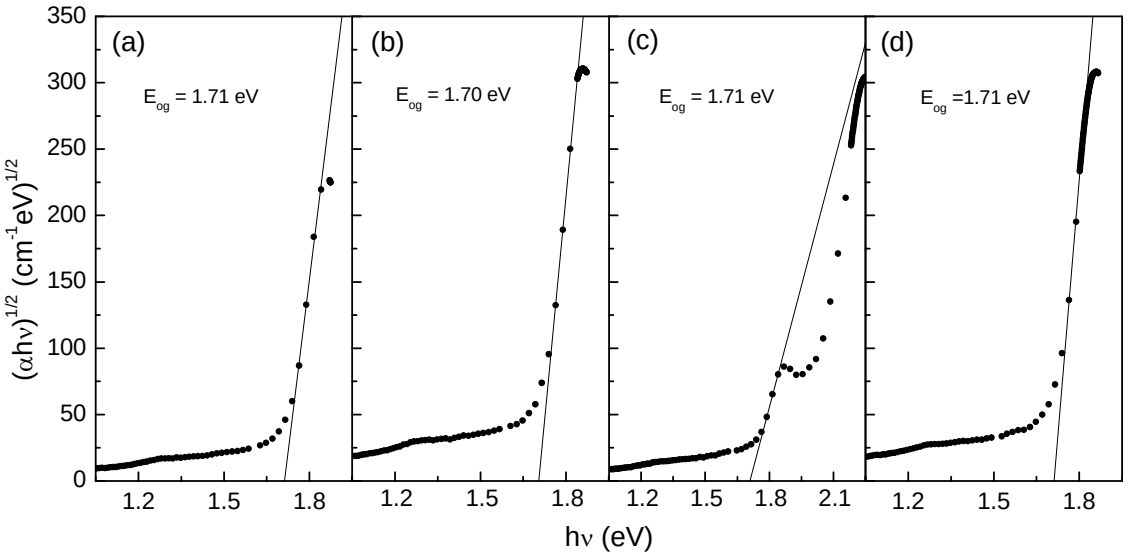

Figure 6.11. Optical gap (E_{og}) of the thin film exposed to light irradiation for 7 days (a), to *n.c.* for 10 days (b), to light irradiation for 30 days (c) and to *n.c.* for 60 days (d).

The value of the optical gap remains around 1.70-1.71 ± 0.01 eV, almost identical to the original one of 1.71 eV (Figure 6.9-a), in all of the cases. It is worth noting that in the case of the treatment with light irradiation for 30 days (Figure 6.11-c) a choice must be done about where to calculate the fit of Tauc. For analogy with the other cases, the range that has been chosen is the one a gap value

similar to the others. In any case, the shape of the curve suggests that a process of mutation of the gap is occurring, which we could argue that would yield a completely different value, for that parameter, in case of continuing the treatment for a longer time. An estimation, not presented here, has been done for the new gap, calculating it in correspondence of the highest part of the exponential region of the spectrum. The result obtained is 1.98 eV.

In Figure 6.12 the evolution of the Urbach energy after the degradation processes is shown.

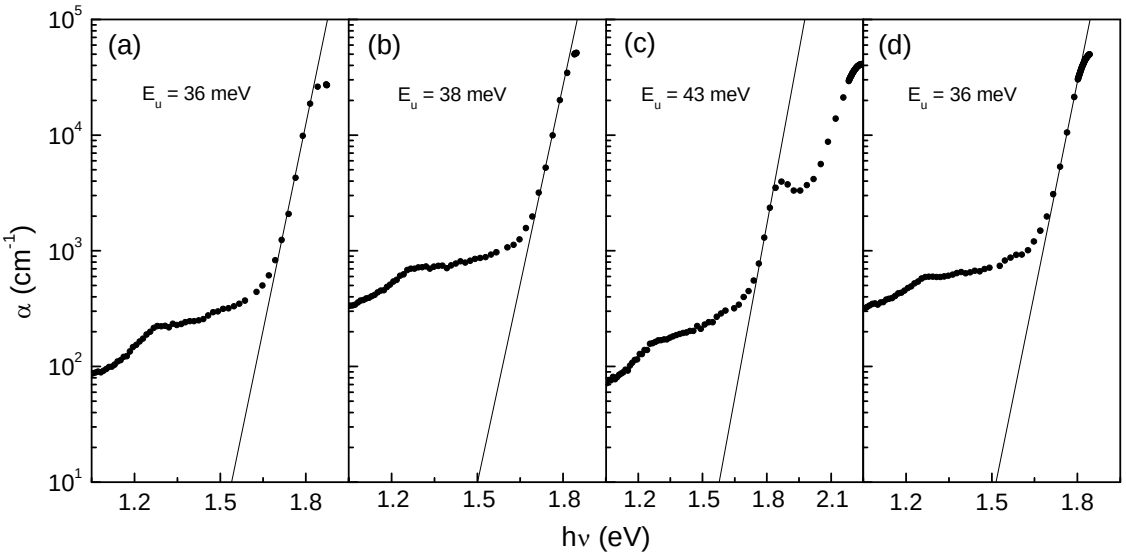

Figure 6.12. Urbach energy (E_u) of the thin film exposed to light irradiation for 7 days (a), to *n.c.* for 10 days (b), to light irradiation for 30 days (c) and to *n.c.* for 60 days (d).

The energy of Urbach decreases, from the original value of 40 meV (Figure 6.9-b), to 36 ± 2 meV, when the sample is exposed to light irradiation for 7 days, and increases to 43 ± 1 meV, when the same treatment is prolonged to 30 days. The trend seems not to have any coherence but the error affecting the calculations partially explains this fact. On the contrary, the treatment in *n.c.* causes a decrease to 38 ± 2 meV after 10 days and to 36 ± 1 meV after 60 days.

6.1.3 Pentacene-PTCDI-C_{13}

In Figure 6.13 a comparison between pure pentacene and PTCDI-C_{13} absorption coefficients and optical transmittances with the ones of the co-evaporated material is shown.

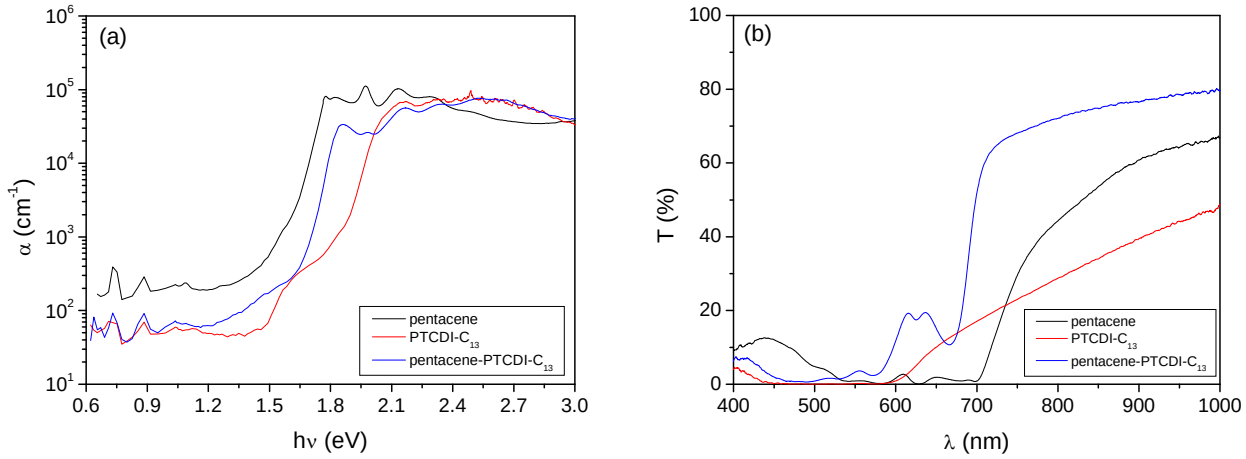

Figure 6.13. (a) Comparison between the absorption coefficients of pentacene, PTCDI-C_{13} and co-evaporated material; (b) Comparison between the transmittance spectra.

As it has been found in other cases, the spectrum of the mixed material contains features of both its components and some element differentiating it from them. In the high-absorption region, characteristics of the most absorptive material can be recognized, like the shape of the curve for energy higher than 2.4 eV that is similar to the one of PTCDI-C_{13}. Going to lower energy values, the high-level absorption extends below 1.8 eV, due to the presence of pentacene, but without its typical absorption peaks which here result strongly modified. For $h\nu < 1.8$ eV the absorption of the co-evaporated thin film remains in the middle of the ones of the pure components and it finally decreases to reach the one of the perylene derivate. This is a phenomenon that differentiates this material from the previous ones but it is interesting to notice that, even tending to the absorption of PTCDI-C_{13} for energy values lower than 1.2 eV, the shape of the curve recalls the one of pentacene, the most absorptive.

Regarding the transmittance, it is higher than the ones of pure materials in almost the whole range, with the exception of the region below 550 nm. In the range included between 570 and 670 nm a transmission band is observed, which is not present for the pure materials.

The XRD spectra taken on pure pentacene and PTCDI-C_{13} and on the co-evaporated material are shown in Figure 6.14. The complete spectra (Figure 6.14-a) and the zoom on the initial part (Figure 6.14-b) show that the co-evaporated material is not characterized by even one of the diffraction peaks detected for pure materials. At the angular position of about $2\theta = 3.4°$ the trace of a diffraction band can be seen, which corresponds to a reflex from PTCDI-C_{13}, as commented in chapter 5.

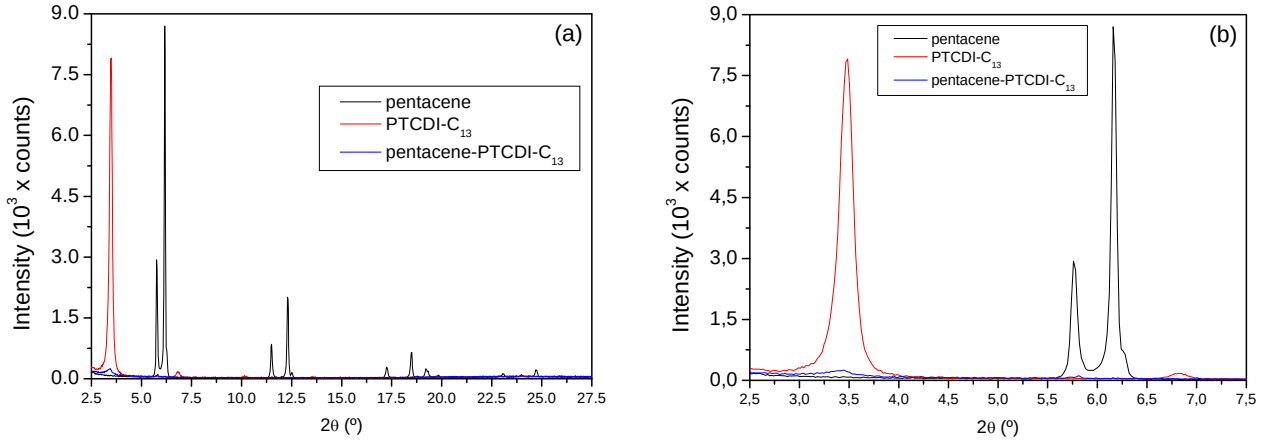

Figure 6.14. (a) XRD spectra of pure materials and the co-evaporated thin film; (b) Detail on the first part of the spectra: no diffraction peak is observed for the co-evaporated thin film.

In Figure 6.15 the results obtained for the optical gap and the energy of Urbach are shown.

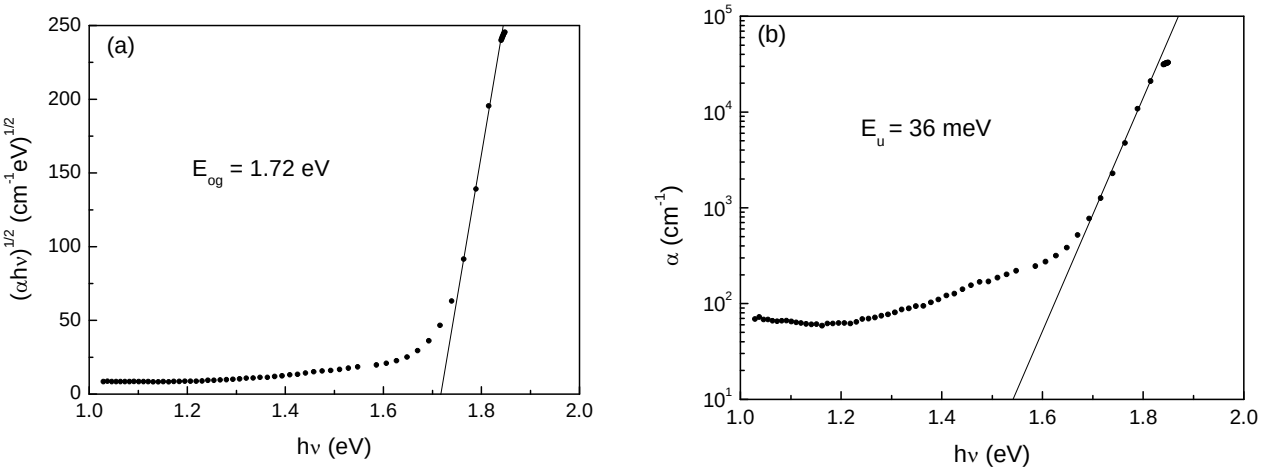

Figure 6.15. (a) Optical gap (E_{og}) of the co-evaporated pentacene-PTCDI-C_{13} thin film; (b) The Urbach energy (E_u).

The optical gap of 1.72 ± 1 eV is slightly lower than the one of pentacene (1.73 eV in Figure 5.3-a) and much lower than the one of PTCDI-C_{13} (2.00 eV in Figure 5.22-a). The same happens for the Urbach energy that is equal to 36 ± 1 meV, value that is lower than the ones of the pure materials: 37 meV for pentacene (Figure 5.3-b) and 48 meV for the perylene derivate (Figure 5.22-b).

In Figure 6.16 the effects of degradation on absorption coefficient and optical transmittance are shown.

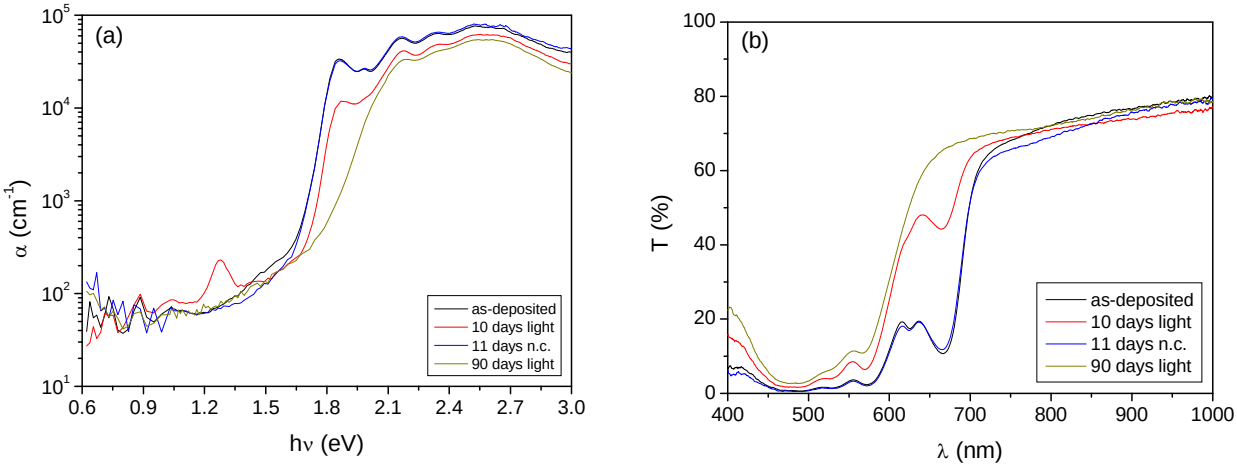

Figure 6.16. Absorption coefficient (a) and transmittance (b) of degraded pentacene-PTCDI-C_{13} thin films: as-deposited film (black line), after 10 days of irradiation treatment (red line), 11 days of exposure to *n.c.* (blue line) and 90 days of irradiation (dark yellow line).

The most striking change in the absorption coefficient (Figure 6.16-a) is the appearance of an absorption peak centred at 1.28 eV, exactly as it happens for pentacene alone, when illuminated for 10 days with light. Surprisingly, such feature disappears when the treatment is prolonged to 90 days, treatment that had never applied before, so we have not any other example of such phenomenon, with pure materials. On the other side, the spectrum of the sample treated for 90 days is radically different, from the original one, in the region between 1.43 and 2.06 eV, where there is a general decrease of the absorption level. A trace of such trend is already observed after 10 days of treatment, where, however, the shape of the curve still remains quite similar to the one measured on as-deposited sample. The treatment for 11 days at normal environmental conditions does not affect the absorption spectrum at all.

The transmittance measurements point out that the treatment in *n.c.* does not have any effect, whereas the treatment with direct light irradiation causes a general increase of the transmission.

In Figure 6.17 the evolution of the optical gap after the degradation processes is shown. After the exposure to light irradiation for 10 days and to *n.c.* for 11 days the gap does not change significantly from the as-deposited value of 1.72 eV, being 1.72 ± 0.01 eV in the first case (Figure 6.17-a) and 1.71 ± 0.01 eV in the second one (Figure 6.17-b). The value changes a lot after 90 days of exposure to light irradiation, since the gap in this case is 1.85 ± 0.01 eV (Figure 6.17-c).

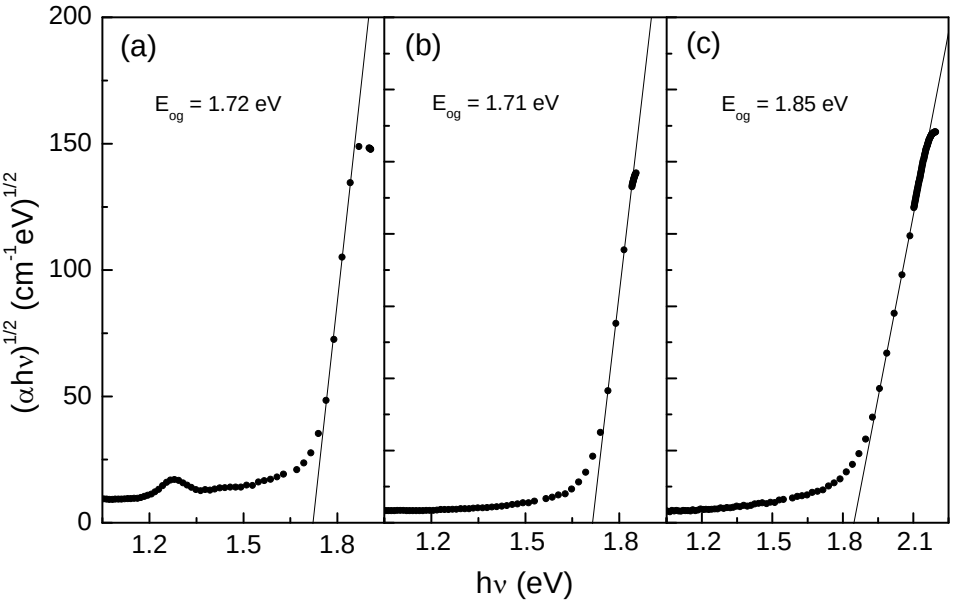

Figure 6.17. Optical gap (E_{og}) of the thin film exposed to light irradiation for 10 days (a), to *n.c.* for 11 days (b) and to light irradiation for 90 days (c).

The change of the Urbach energy with the degradation treatments is shown in Figure 6.18.

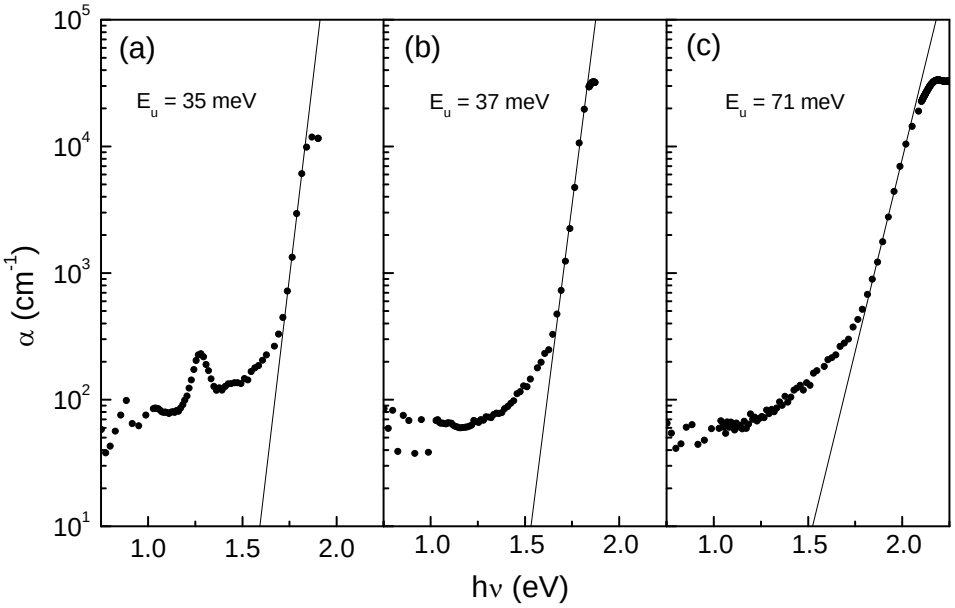

Figure 6.18. Urbach energy (E_u) of the thin film exposed to light irradiation for 10 days (a), to *n.c.* for 11 days (b) and to light irradiation for 90 days (c).

Remembering that the original value is 36 meV, also in this case we can see that the first two treatments do not affect much the energy of Urbach, since it equals the value of 35 ± 1 meV we got

in the first case (Figure 6.18-a) and 37 ± 2 meV in second one (Figure 6.18-b). As in the case of the optical gap, we notice important changes when the sample is exposed to light irradiation for 90 days, since Urbach energy increases to 71 ± 2 meV (Figure 6.18-c), well beyond the limit of the experimental error.

6.1.4 CuPc-fullerene

In this paragraph the first of the three bulk-heterojunctions deposited using copper phthalocyanine as a *p*-type semiconductor will be analyzed. In Figure 6.19 the absorption coefficient and the transmittance of co-evaporated CuPc-fullerene is compared with the ones of pure materials.

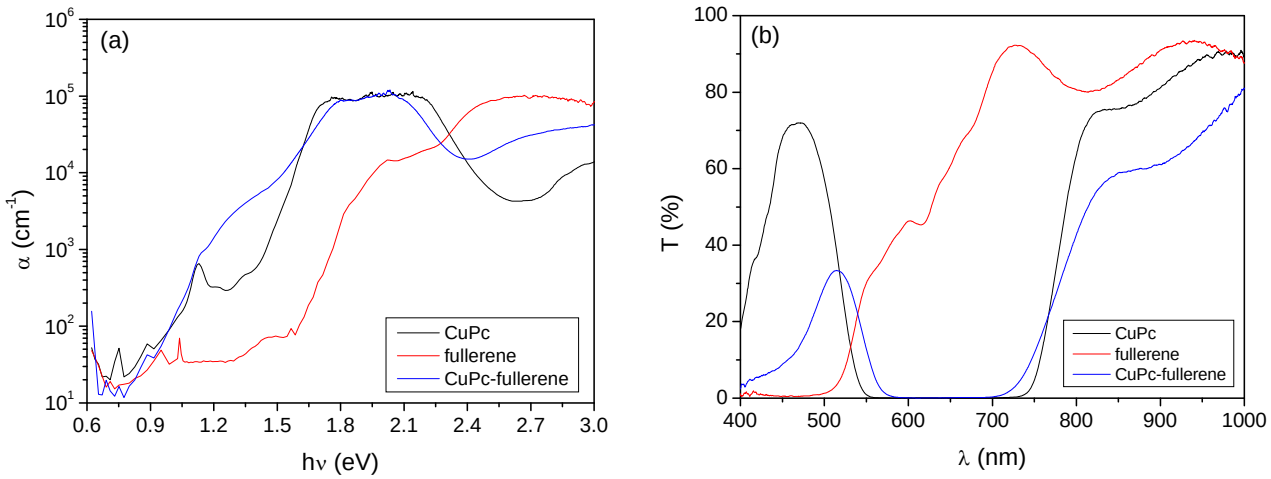

Figure 6.19. (a) Comparison between the absorption coefficients of CuPc, fullerene and co-evaporated material; (b) Comparison between the transmittance spectra.

In the region below 0.94 eV the absorption of the co-evaporated thin film tends to the one of fullerene. In the rest of the spectrum, the result is a mix of the pure materials, prevailing signatures of one or the other depending on which is the most absorptive. Between 1.6 and 2.3 eV the phthalocyanine clearly dominates, while above 2.3 eV the curve resembles the one of fullerene. What makes this measurement interesting is the anomalous absorption in the sub-gap region, between 1.13 and 1.63 eV. The peak located at 1.13 eV, typical for CuPc, disappears due to such a high absorption. This new configuration of the absorption also makes less clear where to locate exactly the exponential decrease and, consequently, where to calculate optical gap and Urbach energy. A general view on the spectra suggests the idea that the co-evaporated material absorbs

much more than the pure ones, due to the sum of the absorptions in the region between 1.5 and 3 eV and also to the anomalous absorption for lower energies.

The transmittance spectra indicate that the co-evaporated material transmits a lower amount of light. The shape of the curve is similar to the one of CuPc but with a lower level of transmission and a different position for the short-wavelength transmission band, which for pure material is centred at 470 nm and for the mix is centred at 516 nm.

In Figure 6.20 the XRD spectra are presented. As in the other cases the co-evaporated thin film does not show the features that characterize the pure materials. This result seems to indicate that the co-evaporated material has grown with an amorphous micro-structure. The zoom on the initial part of the spectra (Figure 6.20-b) clearly shows that the only diffraction peaks that are present are the ones due to CuPc alone. Only a trace of a diffraction reflex is detected close to the angular position $2\theta = 7^{\circ}$ for the mixed materials.

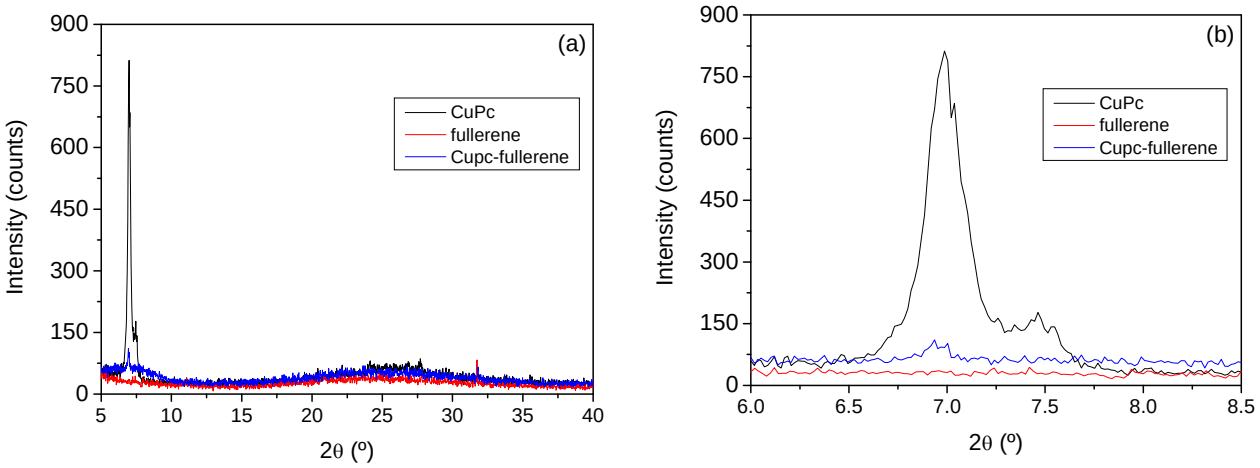

Figure 6.20. (a) XRD spectra of pure materials and the co-evaporated thin film; (b) Detail on the first part of the spectra: in the spectrum of the co-evaporated thin film no diffraction peak is visible.

Given the amorphous nature of the structure obtained by co-evaporating CuPc and C_{60} the optical gap of the thin film has been evaluated by employing Tauc's law. The result obtained for the gap and the Urbach energy are shown in Figure 6.21.

When $(\alpha h\nu)^{1/2}$ has been plotted in function of the energy two regions of the spectrum have been found that can be fitted by Tauc's law: one between 1.65 and 1.78 eV and another one between 1.06 and 1.46 eV. The fit has been evaluated in both cases obtaining a result for the gap of 1.50 ± 0.01 eV and 0.99 ± 0.01 eV, respectively. The presence of two gaps resembles the case of

indirect allowed transitions, where the creation or destruction of phonons is required during the process[103]. Nevertheless, the interpretation of such phenomenon here is somewhat difficult: it could be different and require a theoretical study on organic bulk heterojunctions. Moreover, the value of 1.50 eV seems surprisingly low, even if, by looking at the α spectrum reported above, such result could be expected, due to the pronounced absorption change in the sub-gap region. The energy of Urbach is equal to 77 ± 2 meV, a value that is higher than both the ones of the pure materials: 53 meV for CuPc (Figure 5.9-b) and 63 meV (Figure 5.13-b). The obtained value is quite high for a good semiconductor but it could be expected for a co-evaporated thin film.

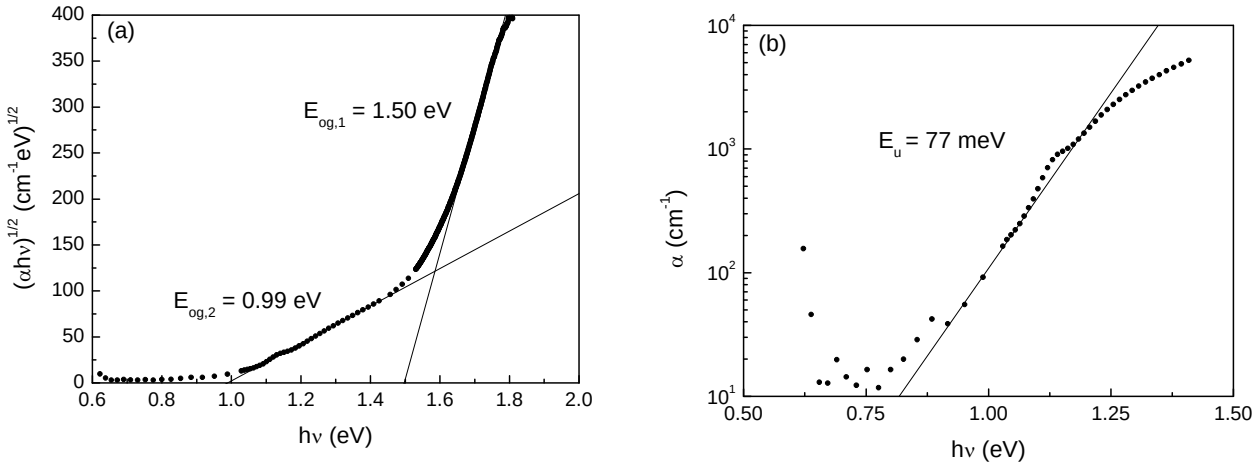

Figure 6.21. (a) Optical gap of the co-evaporated CuPc-fullerene thin film: two regions of good agreement with Tauc's law have been individuated; (b) The Urbach energy.

Returning back to the calculation of the optical gap, the value of 1.50 eV seems surprisingly low if compared with the ones of the other materials here investigated. Pure CuPc and fullerene have optical gaps of 1.64 eV (Figure 5.9-a) and 1.68 eV (Figure 5.13-a), respectively. In lack of a general model for organic semiconductors, as already discussed before in this work, it is worth trying to calculate another fit by plotting α^2 *vs.* $h\nu$, in order to observe the differences between direct allowed transitions model and Tauc one. The result is shown in Figure 6.22. As it happens in the case of fullerene (paragraph 5.1.3), the value of the optical gap changes a lot depending on the law adopted. Moreover, in this case only one gap has been found, with a value of 1.68 ± 0.01 eV, more similar to the ones calculated for the other materials. Such kind of plot also allows to find a better linear part of the spectrum.

The phenomenon of the presence of more than one optical gap, depending on the law employed to calculate the fit, is unique and it had not been observed for the other materials in this work.

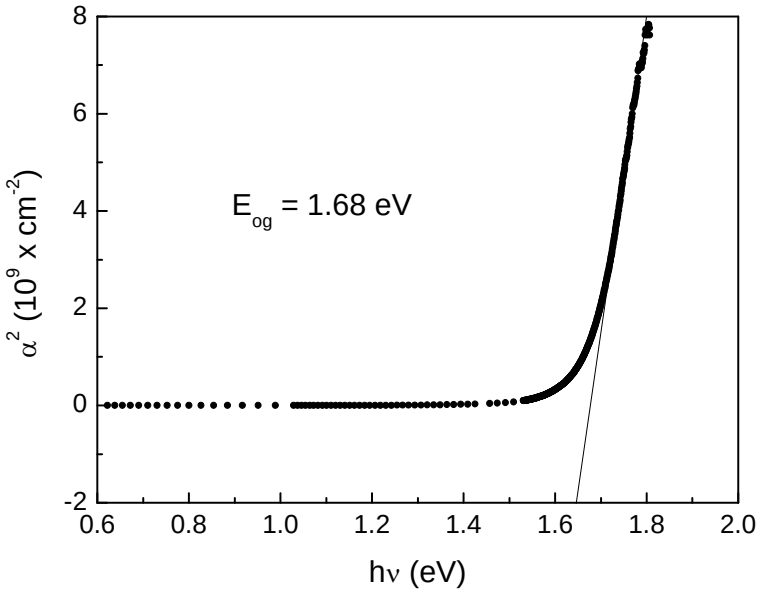

Figure 6.22. New calculation of the optical gap for co-evaporated CuPc-fullerene.

In Figure 6.23 the evolution of the absorption coefficient and the transmittance after the degradation processes performed on co-evaporated CuPc-fullerene thin films is shown.

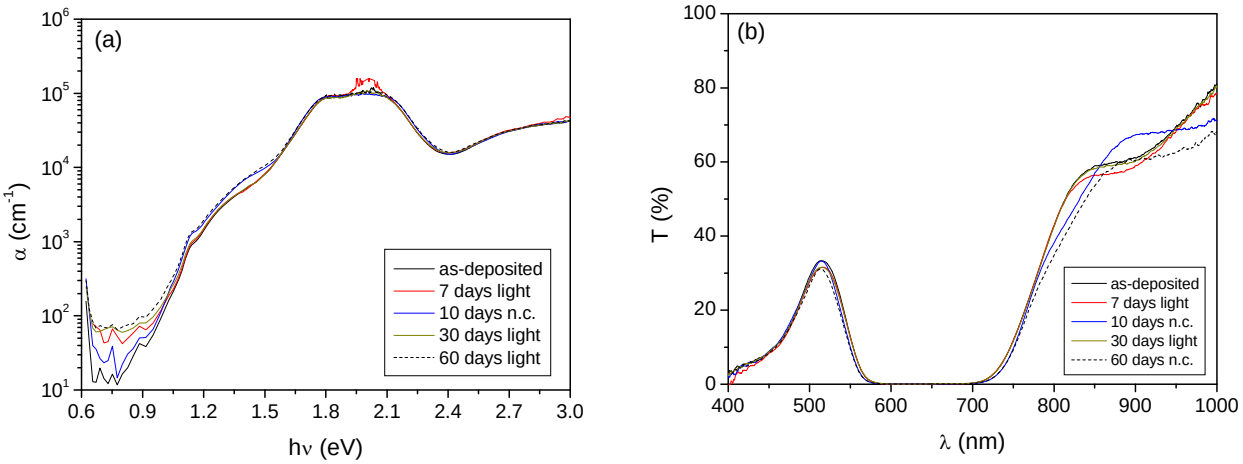

Figure 6.23. Absorption coefficient (a) and transmittance (b) of degraded CuPc-fullerene thin films: as-deposited film (black line), after 7 days of irradiation treatment (red line), 10 days of exposure to *n.c.* (blue line), 30 days of irradiation (dark yellow line) and 60 days of exposure to *n.c.* (black dashed line).

Important changes in the absorption coefficient are observed in the region below 1 eV (Figure 6.23-a). Both degradation processes yield an increase of absorption in such region, by an amount that depends on the exposure time. The treatment with direct light irradiation has more intense effects than the treatment with exposure to the environment. Other degradation effects can be seen

in the region between 1.2 and 1.5 eV, where the absorption also slightly increases. The little band observed at around 2 eV, for the sample treated with light for 7 days, is probably just due to noise affecting the measurement.

The optical transmittances remain quite identical after all of the degradation processes (Figure 6.23-b). The differences that are visible above 800 nm are probably caused by the fact that the measurement could have been performed in slightly different spots of the thin film. As a result, the interferences, related with the thickness of the sample, can be slightly different.

In the following part of the present paragraph the calculations of the optical gap and the energy of Urbach, after the degradation processes, will be shown. Regarding the gap, for reasons of brevity and coherence with the previous part of this work and despite the results obtained for the previous material, only the values obtained by using Tauc's low will be presented. Such law is the one to be used with amorphous semiconductors and XRD characterizations indicate that our co-evaporated thin film is in all probability amorphous (Figure 6.20). Moreover, as it can be argued by looking at the evolution of the absorption coefficient (Figure 6.23), no important change has occurred in the material even after the hardest treatment, leading to the conclusion that the parameters should not have changed much either. Anyway, for completeness of the information Tauc's plots and the results for the gap are shown in Figure 6.24:

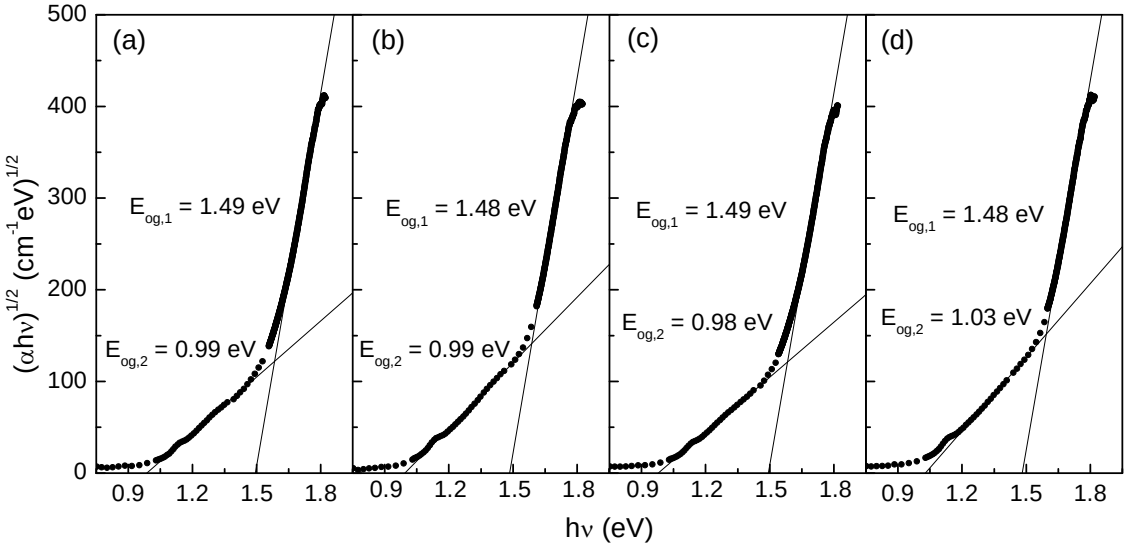

Figure 6.24. Optical gap of the thin film exposed to light irradiation for 7 days (a), to *n.c.* for 10 days (b), to light irradiation for 30 days (c) and to *n.c.* for 60 days (d). In all the cases two values of optical gap can be calculated.

For all the cases here presented two values of optical gap ($E_{og,1}$ and $E_{og,2}$) can be found, which are 1.48-1.49 ± 0.01 eV and 0.98-0.99 ± 0.01 eV, respectively. In both cases the results are not much different from the original values, estimated on the as-deposited sample, of 1.50 and 0.99 eV (Figure 6.21-a). Only when the sample is treated with direct illumination for 60 days, the second gap ($E_{og,2}$) changes by an important amount, increasing to 1.03 ± 0.01 eV.

In Figure 6.25 the evolution of Urbach energy with the degradation processes is presented.

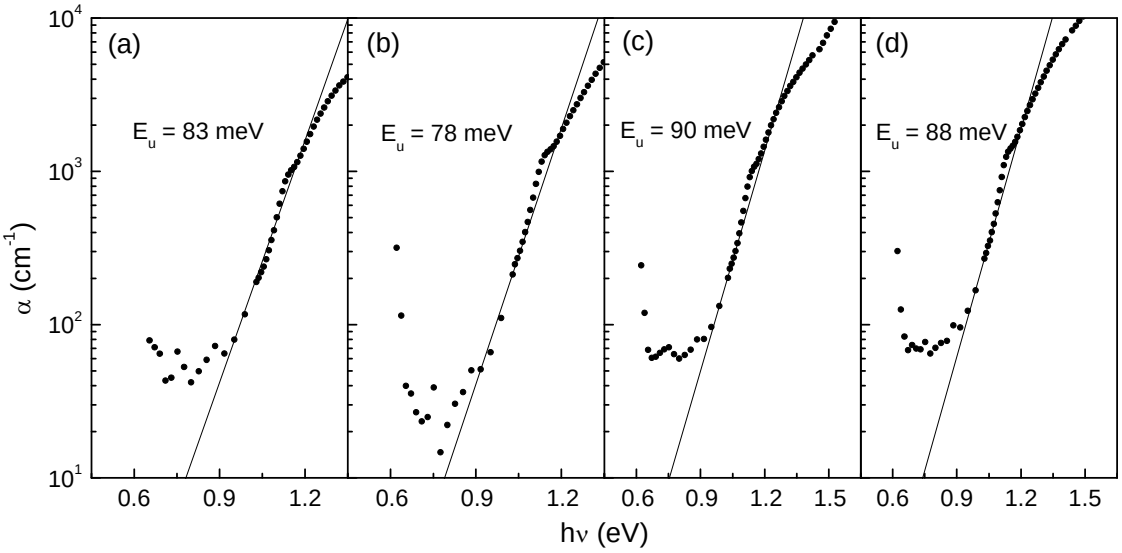

Figure 6.25. Urbach energy of the thin film exposed to light irradiation for 7 days (a), to *n.c.* for 10 days (b), to light irradiation for 30 days (c) and to *n.c.* for 60 days (d).

Given that the original value for Urbach energy was 77 meV (Figure 6.21-b), the treatment with light irradiation causes an increase to 83 meV after 7 days and to 90 ± 3 meV after 30 days of exposure. In the first case the fit has not been possible to calculate using the usual automatic method by Origin®, due to the not clear linearization of this part of the curve. So a manual evaluation has been done for the Urbach law and, for this reason, no error is reported. This result must be taken only as a qualitative indication. After the treatment with *n.c.* for 10 days the Urbach energy is 78 meV and also in this case the calculation has been performed manually. In any case, the difference with the value of the as-deposited sample is very low. After 60 days of the same treatment the parameter increases to 88 ± 3 meV.

6.1.5 CuPc-PTCDA

In Figure 6.26 a comparison between absorption coefficients and transmittances of pure CuPc, PTCDA and co-evaporated material is presented.

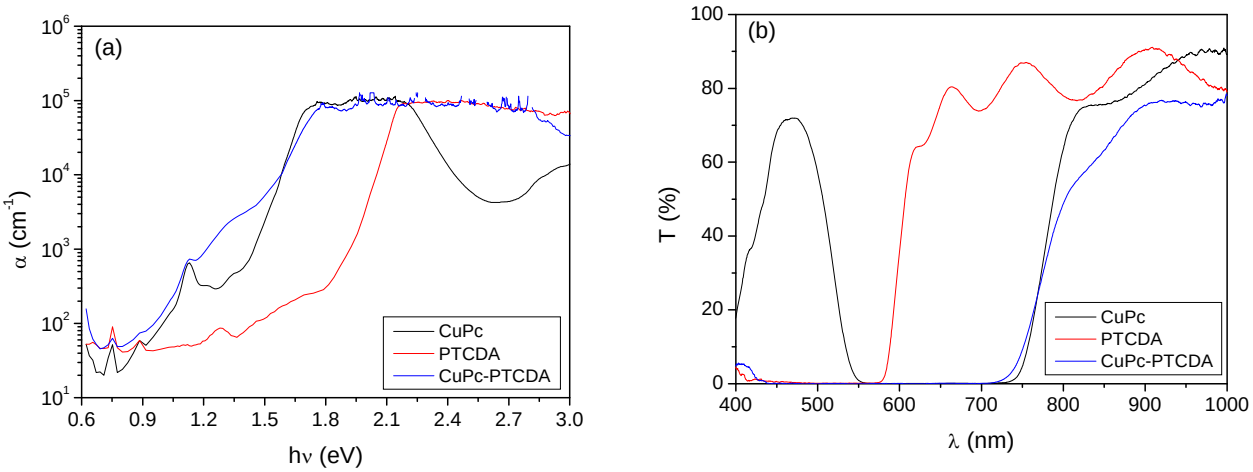

Figure 6.26. (a) Comparison between the absorption coefficients of CuPc, PTCDA and the co-evaporated material; (b) Comparison between the transmittance spectra.

The α of co-evaporated CuPc-PTCDA (Figure 6.26-a) has elements in common with the one of CuPc-fullerene (Figure 6.19-a). In the region between 0.9 and 1.5 eV the absorption is clearly higher and the characteristic absorption peak located at 1.13 eV, related with CuPc, is almost covered by such high-level absorption. The most interesting feature of this measurement can be seen in the high-level absorption region, above 1.5 eV. In fact, the absorption bands of the pure materials are almost perfectly complementary and the co-evaporated material corresponds, point by point, to the one of the most absorptive material: below 2.1 eV CuPc, above that value PTCDA. As a result, the co-evaporated material has a very wide absorption band and its colour is nearly black, thing that would suggest that the optical gap has become narrower and the material absorbs more wavelengths. Nevertheless, some experiment described in the previous chapter indicate that, in order to better define the absorption curve and its features in the high-level absorption region, we should deposit films with much lower thickness. This would avoid the saturation of the transmittance in that region and possible differences in the absorption peaks or in the absorption level would be evident. In the sub-gap region, on the contrary, it is quite clear that there are absorptions that cannot be explained simply in terms of the absorptions observed for the pure materials.

The transmittance (Figure 6.26-b) confirms that the co-evaporated CuPc-PTCDA is much more absorptive, since it begins to grow only near to 750 nm and the transmission band observed for CuPc at around 470 nm here has completely disappeared.

In Figure 6.27 a comparison of the XRD spectra of pure CuPc and PTCDA and the co-evaporated material is shown.

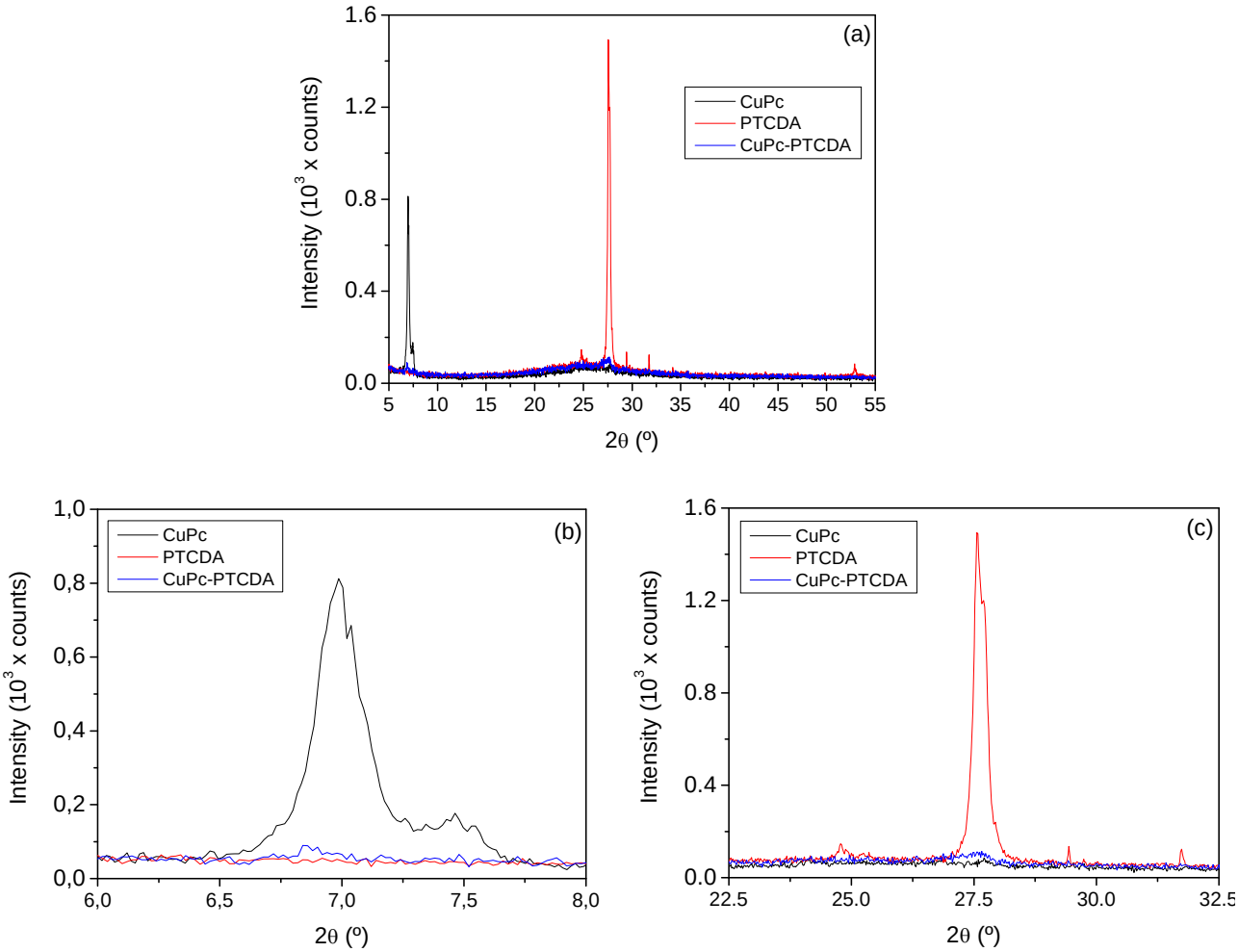

Figure 6.27. (a) Comparison between XRD spectra of pure CuPc (black line) and PTCDA (red line) and co-evaporated CuPc-PTCDA (blue line); (b) Detail on the first group of peaks; (c) Detail on the group of peaks located at the central part of the spectra.

Co-evaporated CuPc-PTCDA does not seem to have an ordered micro-structure. Just traces of diffraction peaks are present at 2θ=6.9º, due to polymorph α of CuPc, and at 2θ=27.6º, which should be associated with PTCDA. The dimensions of the crystallites that determinate such reflexes are probably too small to give a clearly detectable XRD signal. As a consequence, we conclude that the crystalline fraction of this sample is much lower than the amorphous one.

In Figure 6.28 the plots for the calculation of optical gap and Urbach energy are shown. The gap has been evaluated using Tauc's law, which gives results that are similar to the ones already discussed for the case of CuPc-fullerene. Two regions of the curve show linear dependence as a function of the energy and two gaps have been calculated: 1.52 ± 0.01 eV and 1.00 ± 0.01 eV, respectively. The Urbach energy is equal to 112 meV, a very high value, if compared with good amorphous silicon (around 50 meV).

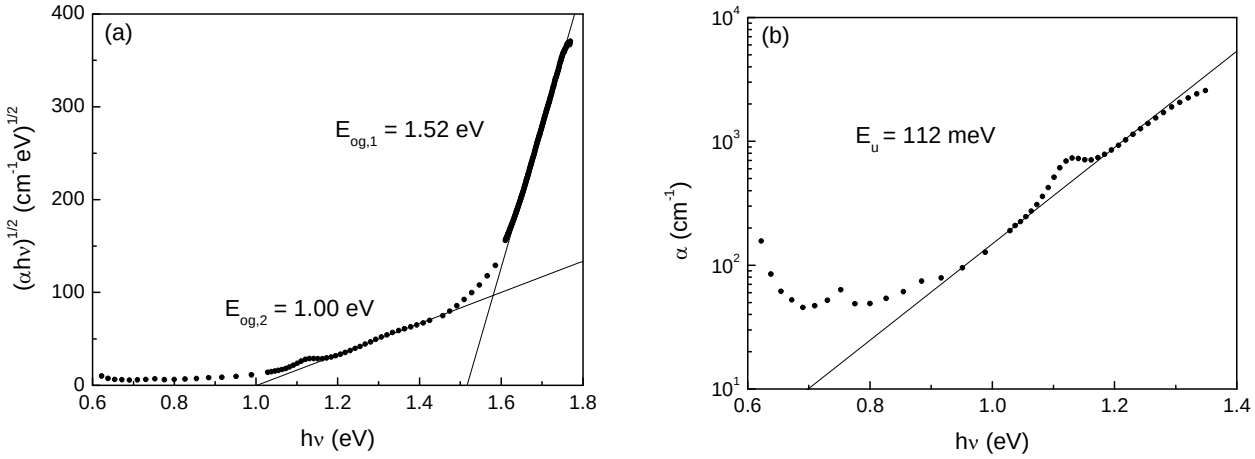

Figure 6.28. (a) Optical gap of the co-evaporated CuPc-PTCDA thin film: two regions of good agreement with Tauc's law have been identified; (b) The Urbach energy.

Starting from here, Tauc's law will be used to calculate the optical gap of amorphous co-evaporated materials, as it is usually the case for inorganic semiconductors.

In Figure 6.29, the effects of degradation on the absorption coefficient and the transmittance are shown. The degradation processes do not have any effect on the absorption coefficient (Figure 6.29-a), with the exception of the treatment at environmental conditions for 60 days, which causes a slight increase in the absorption at energies below 1 eV.

The transmittance spectra (Figure 6.29-b) also indicate that no important changes have occurred in the material after undergoing the degradation treatments. Only variations in the interferences caused by the thickness of the thin film are observed. Nevertheless, such changes should not be caused by any degradation in the samples.

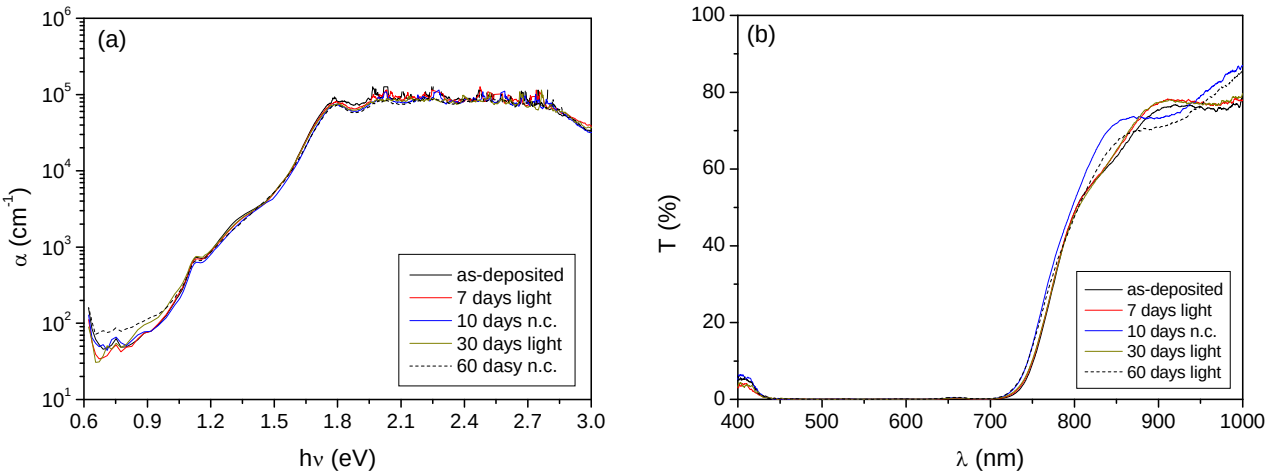

Figure 6.29. Absorption coefficient (a) and transmittance (b) of degraded CuPc-PTCDA thin films: as-deposited film (black line), after 7 days of irradiation treatment (red line), 10 days of exposure to *n.c.* (blue line), 30 days of irradiation (dark yellow line) and 60 days of exposure to *n.c.* (black dashed line).

In Figure 6.30 the evolution of the optical gaps with the degradation processes is shown.

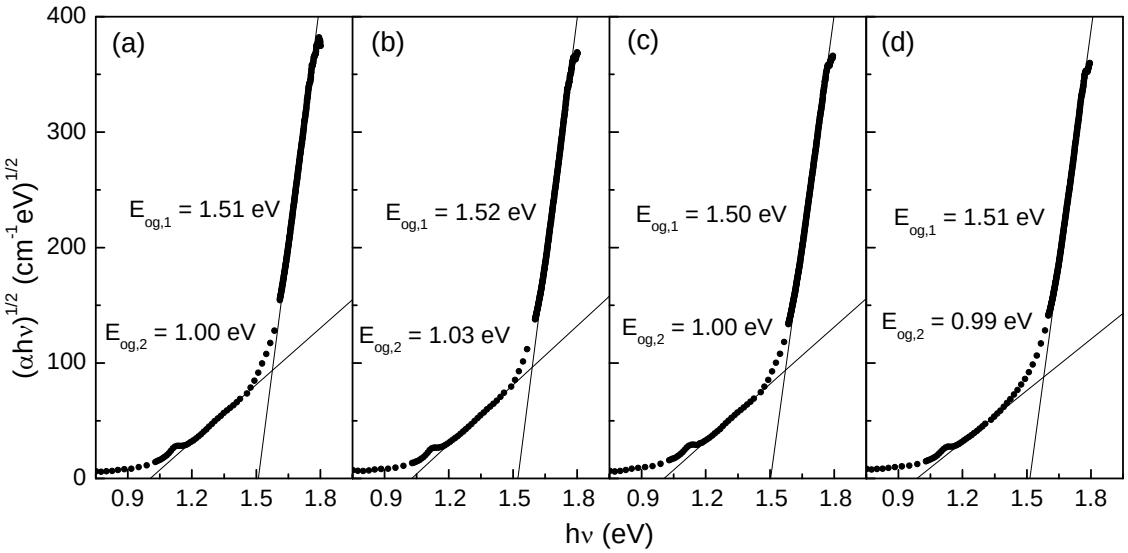

Figure 6.30. Optical gap of the thin film exposed to light irradiation for 7 days (a), to *n.c.* for 10 days (b), to light irradiation for 30 days (c) and to *n.c.* for 60 days (d). In all the cases two values of optical gap can be calculated.

Regarding the higher gap, its value is $E_{og,1}$ = 1.51 ± 0.01 eV when the sample has been irradiated with direct light for 7 days and 1.50 ± 0.01 eV when the treatment has been prolonged to 30 days. When the material has been exposed to normal environmental conditions of light and air, its gap is 1.52 ± 0.01 eV after 10 days and 1.51 ± 0.01 eV after 60 days of treatment.

The second gap remains equal to 1.00 ± 0.01 eV after the irradiation with light, while increases to 1.03 ± 0.01 eV after the exposition to *n.c.* for 10 days and goes back to 0.99 ± 0.01 eV after 60 days of treatment.

The changes in the gap are not much relevant, taking into account the error affecting the calculations, or when compared with the value calculated on the as-deposited sample (Figure 6.28). On one side, also in the case of CuPc mixed with PTCDA the optical gap seems to be surprisingly low, compared with the values of the pure materials: 1.64 eV for CuPc and 2.11 eV for PTCDA. On the other side, the new absorptions found in the sub-gap region are responsible for relevant mutation of absorption spectrum also visible by naked eye, since the sample is characterized by a very dark colour.

In Figure 6.31 the evolution of the Urbach energy with the degradation processes is shown.

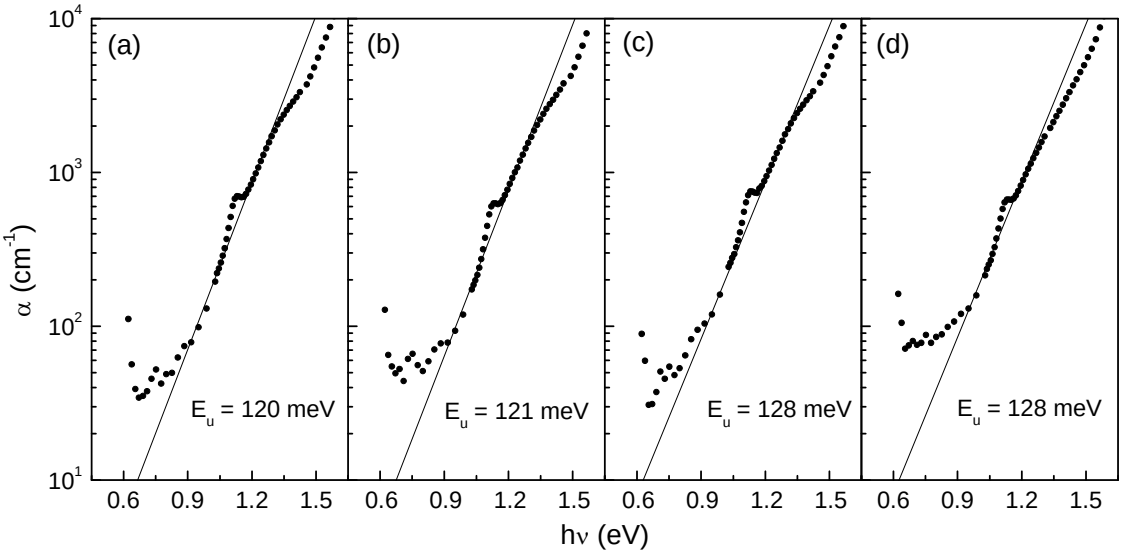

Figure 6.31. Urbach energy of the thin film exposed to light irradiation for 7 days (a), to *n.c.* for 10 days (b), to light irradiation for 30 days (c) and to *n.c.* for 60 days (d).

Urbach energy increases from the as-deposited value of 112 meV to 120 meV after 7 days of irradiation with light and to 128 meV after 30 days of treatment. The process at environmental conditions causes an increase of Urbach energy to 121 meV after 10 days and to 128 meV after 60 days of treatment. In none of these cases the error is reported because the calculations have been done manually.

The results here presented and discussed indicate that the optical properties of such material are very stable against the degradation treatments applied to it in this work, at least during the first few weeks. The unique factor that changes significantly seems to be the Urbach energy, whose error, nevertheless, we do not know.

6.1.6 CuPc-PTCDI-C_{13}

In Figure 6.32 the absorption and the transmittance spectra of co-evaporated CuPc-PTCDI-C_{13} are compared with the ones of the pure materials.

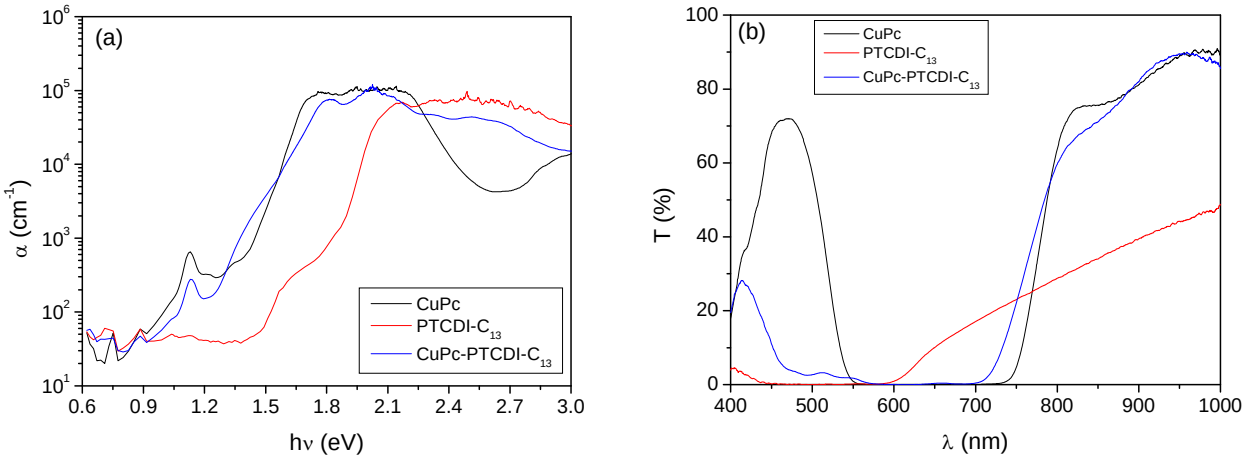

Figure 6.32. (a) Comparison between the absorption coefficients of CuPc, PTCDA and the co-evaporated material; (b) Comparison between the transmittance spectra.

The absorption coefficient of the co-evaporated material contains clear traces of the one of pure CuPc, with the typical absorption peak at 1.13 eV. In the high-absorption region, α values keep close to 10^5 cm^{-1} in the region dominated by CuPc, while in the region dominated by PTCDI-C_{13} the absorption decreases, differently from what noticed in the case of CuPc-PTCDA.

As usual for the co-evaporated materials, the optical transmittance in the visible range of CuPc-PTCDI-C_{13} is lower than the one of pure materials. The transmission peak, due to CuPc and located at 470 nm, is still present but lower in intensity and blue-shifted.

In Figure 6.33 the XRD spectra of pure CuPc and PTCDI-C_{13} are compared with the one of the co-evaporated material.

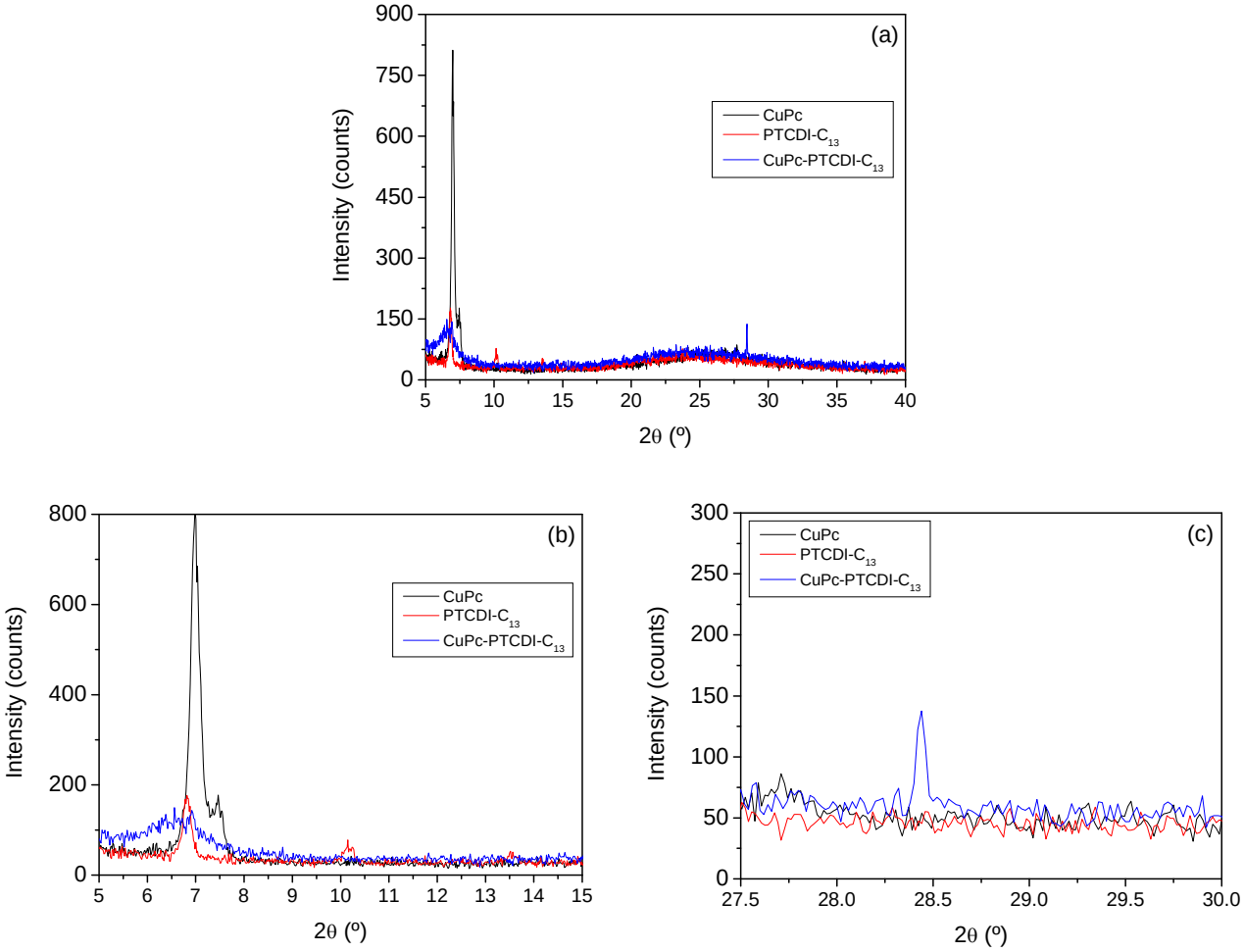

Figure 6.33. (a) Comparison between XRD spectra of pure CuPc (black line) and PTCDA (red line) and co-evaporated CuPc-PTCDA (blue line); (b) Detail on the first group of peaks; (c) Detail on higher angular positions.

The complete spectrum of the co-evaporated sample (Figure 6.33-a) shows some very low intensity features, more visible in the zooms done on the initial part of the spectra (Figure 6.33-b) and on the final part of it (Figure 6.33-c). In the former case, a very broad band centred near the peak of PTCDI-C_{13} is visible, what indicates a partial crystallization of this material. In the latter case, a very sharp and low intensity diffraction peak is observed at the angular position of $2\theta = 28.4º$. Such peak does not correspond to any of the features that characterize the pure materials and, being so sharp, it could be just due to noise in the measurement.

The calculations of the optical gap and the Urbach energy are presented in Figure 6.34.

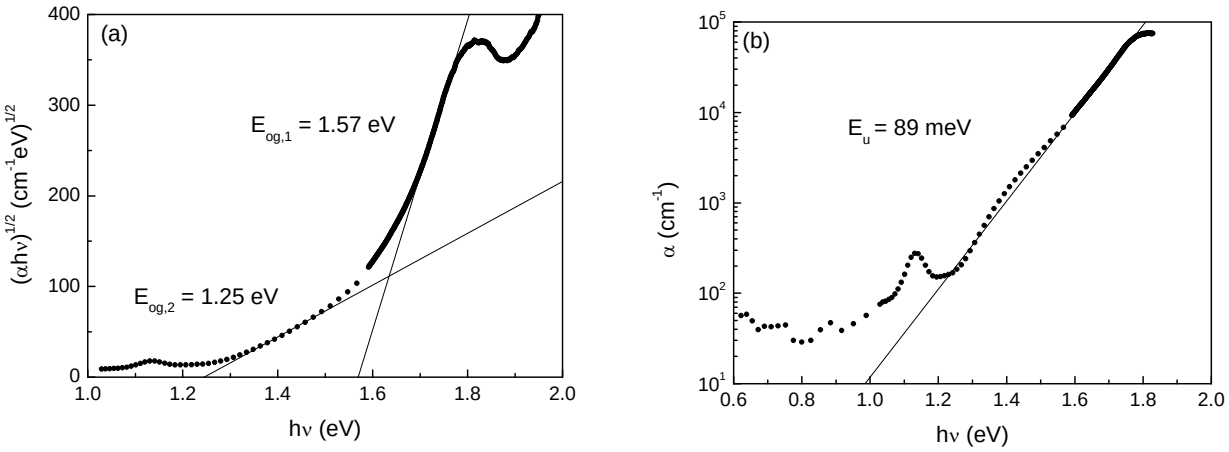

Figure 6.34. (a) Optical gap of the co-evaporated CuPc-PTCDI-C_{13} thin film: two regions of good agreement with Tauc's law have been individuated; (b) The Urbach energy.

As for the previously described co-evaporated thin films containing CuPc, also in this case a double gap has been evaluated. The values obtained for the gaps are $E_{og,1} = 1.57 \pm 0.01$ eV and $E_{og,2} = 1.25 \pm 0.01$ eV. The value obtained for the Urbach energy is 89 ± 1 meV (Figure 6.34-b).

Figure 6.35 shows the evolution of the absorption coefficient and the optical transmittance after the degradation process performed on the co-evaporated thin films. The absorption coefficient (Figure 6.35-a) does not suffer from important changes after the degradation processes. The peak located at 0.89 eV in the spectrum taken from the sample treated for 60 days with direct light irradiation is not probably caused by a physical phenomenon, but by noise.

The transmittance (Figure 6.35-b) confirms what already observed for the absorption coefficient as it stays almost unaltered after any kind of degradation treatment.

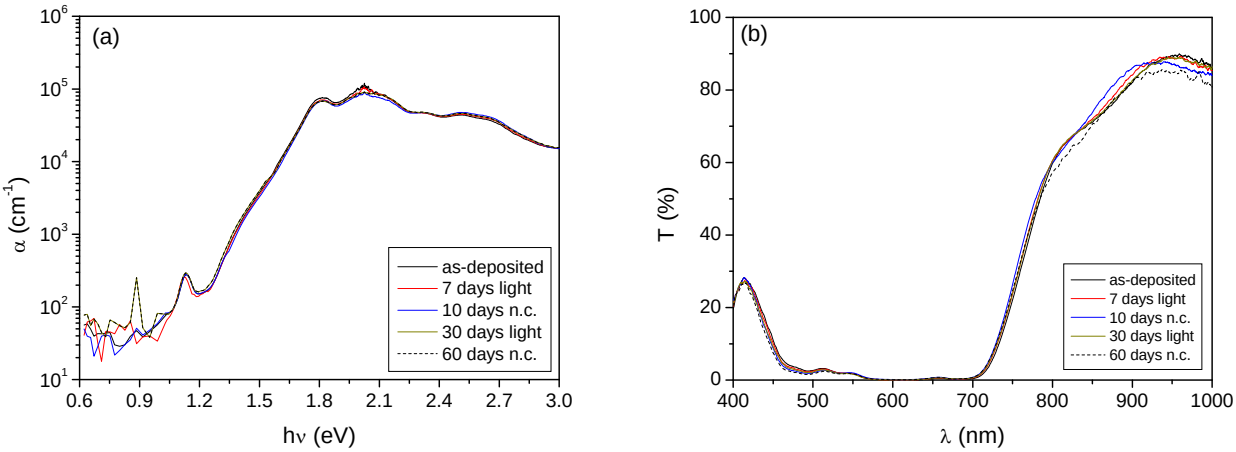

Figure 6.35. Absorption coefficient (a) and transmittance (b) of degraded CuPc-PTCDI-C_{13} thin films: as-deposited film (black line), after 7 days of irradiation treatment (red line), 10 days of exposure to *n.c.* (blue line), 30 days of irradiation (dark yellow line) and 60 days of exposure to *n.c.* (black dashed line).

In Figure 6.36, the results obtained for the optical gaps after performing the degradation processes are presented.

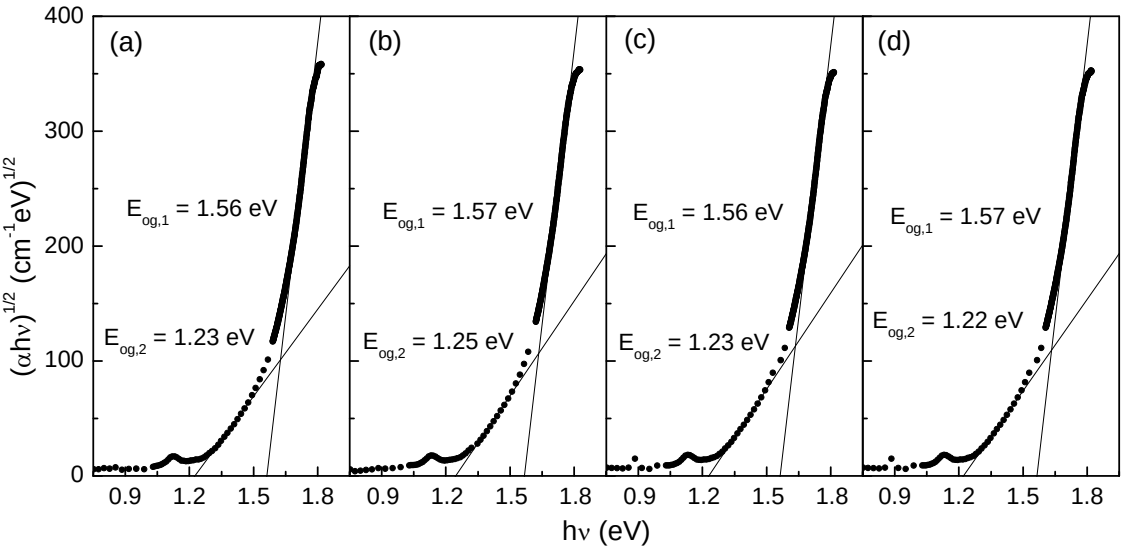

Figure 6.36. Optical gap of the thin film exposed to light irradiation for 7 days (a), to *n.c.* for 10 days (b), to light irradiation for 30 days (c) and to *n.c.* for 60 days (d). In all the cases two values of optical gap can be calculated.

The value of the first gap is $E_{og,1}$ = 1.56-1.57 ± 0.01 eV in all the samples investigated and is almost identical to the one obtained for the as-deposited sample (1.57 eV in Figure 6.34-a). The second gap is $E_{og,2}$ = 1.23 ± 0.01 eV after the treatment with direct light irradiation, while it is 1.25 ± 0.01 eV after 10 days of exposure to *n.c* and 1.22 ± 0.01 eV after 60 days of the same treatment. In general, these four values are slightly lower than the original value of 1.25 eV (Figure 6.34-b), with the exception of the one obtained after 10 days of exposure to air, that is identical.

In Figure 6.37 the Urbach energy is calculated for the samples that have suffered the degradation processes. It has increased from an as-deposited value of 89 meV (Figure 6.34-b) to 91 ± 1 meV, after 7 days of irradiation with light, and to 92 ± 1 meV, after 30 days of the same treatment. On the contrary, the treatment at *n.c.* seems to cause a decrease to 87 ± 1 meV, after 10 days, and an increase to 94 ± 1 meV, after 60 days.

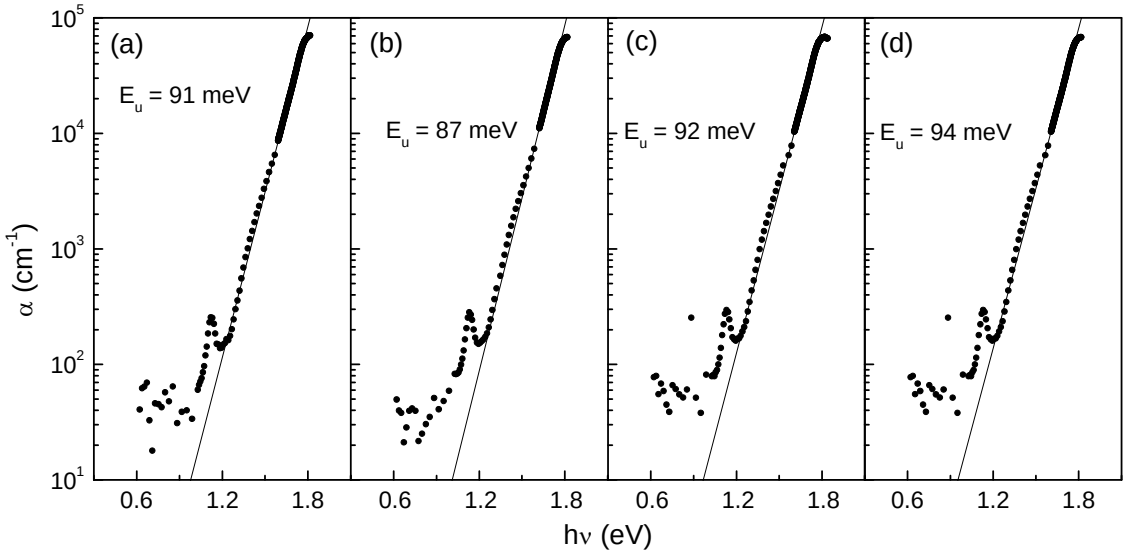

Figure 6.37. Urbach energy of the thin film exposed to light irradiation for 7 days (a), to *n.c.* for 10 days (b), to light irradiation for 30 days (c) and to *n.c.* for 60 days (d).

As a general conclusion for co-evaporated CuPc-PTCDI-C_{13}, we can point out that such combination seems to be the most stable against possible alterations in its optical properties due to the contact with oxidizing agents.

6.2 Annealing treatments

In the previous paragraph it has been demonstrated that when two molecular organic semiconductors are deposited at the same time, the most probable micro-structure to be obtained, at the conditions considered, is amorphous-like. As it has already been anticipated, this phenomenon has already been observed with polymeric semiconductors[91] deposited by spin-coating, a radically different deposition technique. In some cases it is known that to obtain phase separation, with individual crystallization of the two materials, is a fundamental condition to fabricate a well performing solar cell[91].

Annealing treatments have been executed on our co-evaporated thin films and the results will be presented in the present paragraph. The annealing has been performed in a cryostat with a mechanical pump making vacuum in it, at a temperature chosen depending on each material combination. Pentacene is the material with the lowest melting temperature and it is normally evaporated at around 130-140ºC. The rest of materials reach a good deposition rate at temperatures

above 300ºC. So when performing annealing treatments on co-evaporated thin films containing pentacene, the temperature used has been 100 ºC, while for samples containing CuPc the temperature has been 200 ºC or higher. The time of duration of the process has been calculated starting from the instant in which the established temperature has been reached.

6.2.1 Pentacene-fullerene

In Figure 6.38 the XRD spectra taken on pure pentacene and fullerene and on co-evaporated pentacene-fullerene before and after the annealing treatment at 100 ºC for three hours are presented and compared.

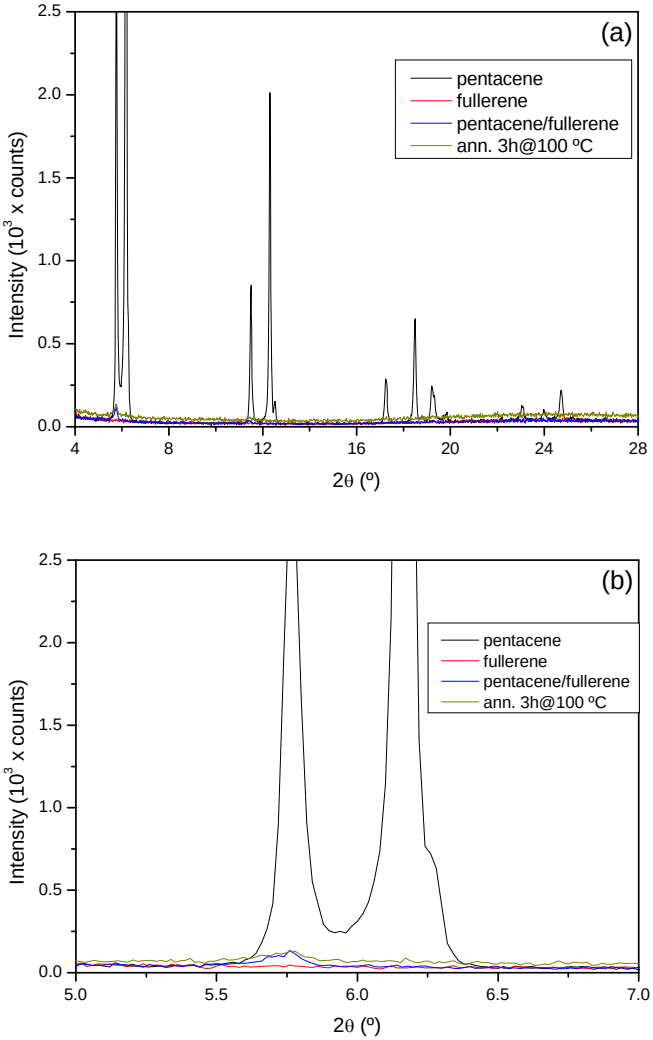

Figure 6.38. Results of the annealing performed at 100 ºC on co-evaporated pentacene-fullerene: (a) part of the spectrum containing the diffraction peaks, (b) detail on the first group of peaks. Because of the very high intensity of some peak the graph has been truncated to be able to distinguish the other features.

In Figure 6.38-a a global view of the part of the spectrum where diffraction peaks have been registered is presented. Moreover, for a clearer vision, a zoom on the first group of peaks is presented in Figure 6.38-b. In both cases the graph has been truncated in the vertical scale, due to the very high intensity of the peaks from pure pentacene.

Only a trace of a diffraction peak associated with pentacene can be observed in the co-evaporated sample, before the annealing, near the angular position $2\theta = 5.75º$. The intensity of such feature does not change after the thermal treatment. Similarly, no other diffraction feature appears after the annealing either from pentacene or from fullerene, suggesting that the treatment has not been sufficient to obtain some improvement in the micro-structure of the thin film.

Since pentacene is evaporated at temperatures between 130 and 140 ºC, no other annealing treatment at higher temperature has been tried.

6.2.2 Pentacene-PTCDA

In Figure 6.39 the XRD spectra of pentacene, fullerene and co-evaporated materials before and after the annealing are presented.

In the global view of the spectra (Figure 6.39-a) the diffraction peaks due to pure pentacene and fullerene are clearly visible and have already been presented. In Figure 6.39-a and Figure 6.39–b zooms on groups of peaks from pentacene and PTCDA, respectively, are presented. No change has been observed after the thermal treatment at 100 ºC for 3 hours, suggesting that no crystallization has occurred, either in pentacene or in PTCDA phases. As in the case of co-evaporated pentacene-fullerene, no other thermal annealing with higher temperature has been tried due to the low evaporation temperature of pentacene.

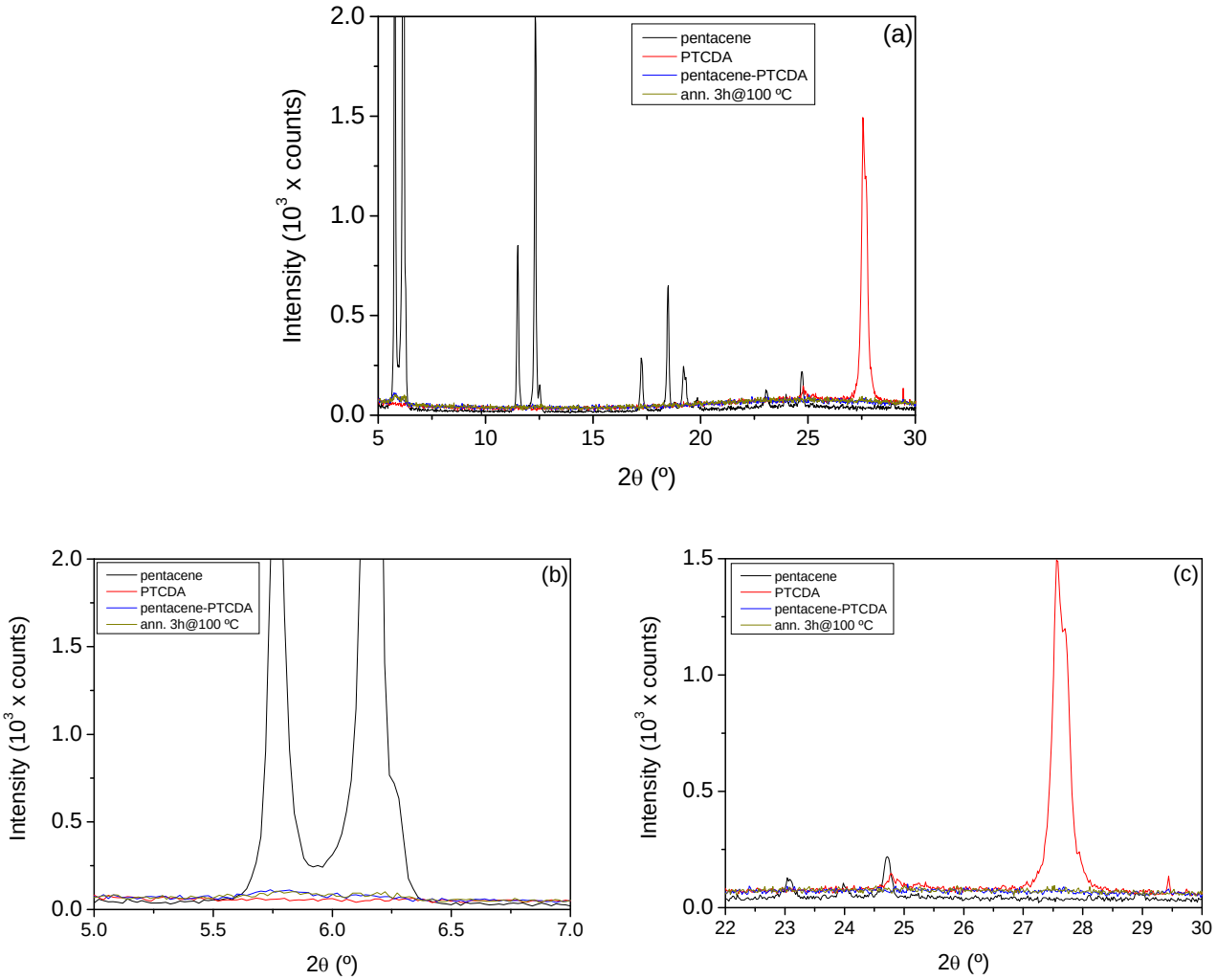

Figure 6.39. Results of the annealing performed at 100 ºC on co-evaporated pentacene-PTCDA: (a) part of the spectrum containing the diffraction peaks, (b) detail on the first group of pentacene peaks and (c) detail on PTCDA group.

6.2.3 Pentacene-PTCDI-C_{13}

In Figure 6.40 the XRD spectra of pentacene, fullerene and co-evaporated materials before and after the annealing are presented. In part (a) of the figure the global view of the spectra is shown where pentacene diffraction peaks dominate upon the less intense ones from the perylene derivate. In the zoom shown in part (b) no change has occurred after annealing for three hours at 100 ºC.

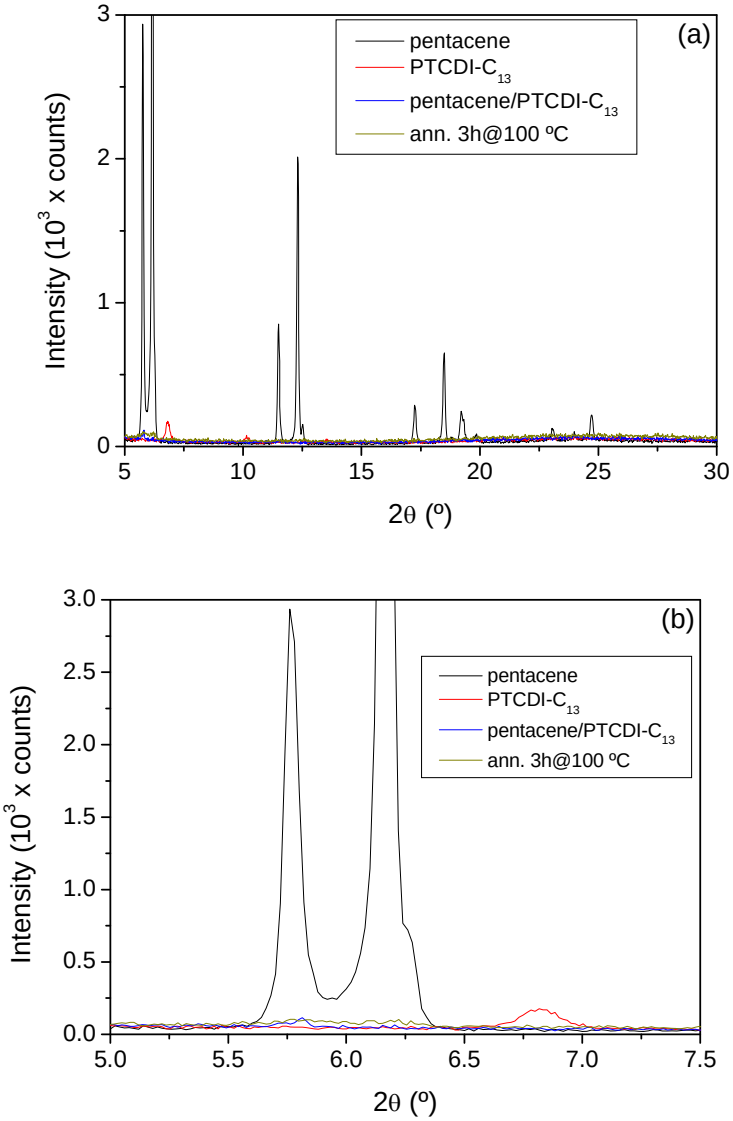

Figure 6.40. Results of the annealing performed at 100 ºC on co-evaporated pentacene-PTCDI-C_{13}: (a) part of the spectrum containing the diffraction peaks, (b) detail on the first group of peaks.

6.2.4 CuPc-fullerene

The XRD spectra in Figure 6.41 show the effects of the annealing on co-evaporated CuPc-fullerene structure. In this figure they are compared with new spectra taken on the co-evaporated sample after two annealing treatments: the first one performed at 200 ºC for 3.5 hours and the second one at 250 ºC for 3 hours. As it has already been discussed, the pre-annealing sample presents only a trace of a diffraction peak near 2θ = 7º. After the first annealing at 200 ºC, a diffraction band, similar to the typical band of CuPc, has appeared (Figure 6.41-b). After the treatment at 250 ºC that band seems to have divided into two sharper and more intense peaks. No

diffraction peak due to fullerene is observed, so it is to be supposed that only CuPc has partially crystallized.

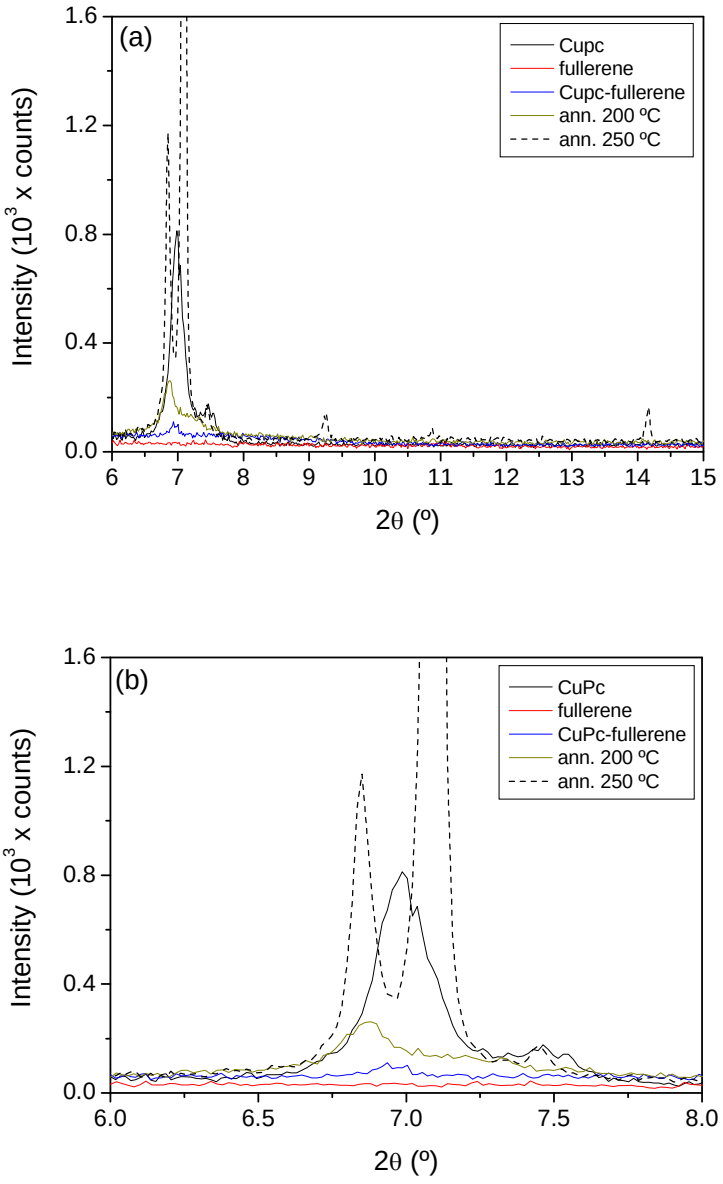

Figure 6.41. Results of the annealing performed at 200 and 250 ºC on co-evaporated CuPc-fullerene: (a) part of the spectrum where changes are noticed, (b) detail on the first group of peaks. In both cases the vertical scale has been truncated to make easier to read the graph.

In Figure 6.42 a fit using a pseudoVoigt function (4.25) of the diffraction peaks from CuPc and of the ones of the annealed co-evaporated sample, are shown. From the fits the angular positions of

the peaks and their FWHM have been estimated. From the obtained data of FWHM the crystal dimension has been evaluated using equation (4.24).

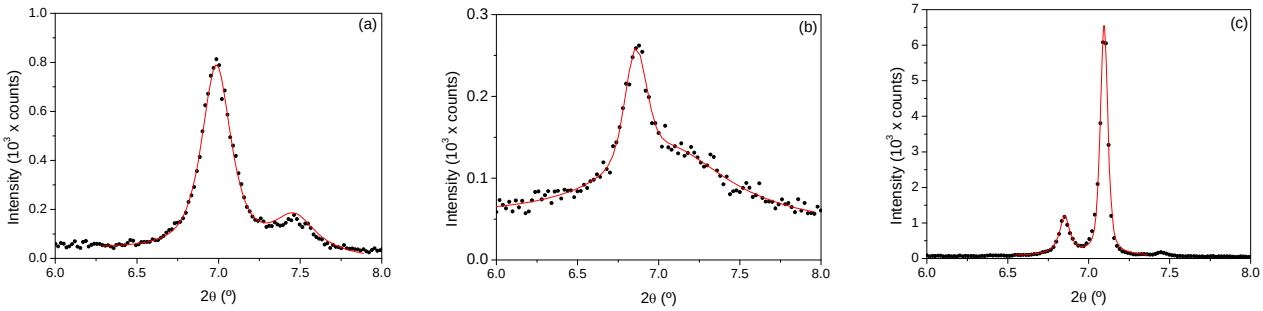

Figure 6.42. Fit of the first diffraction peaks of CuPc (a), of co-evaporated CuPc-fullerene after annealing at 200 ºC (b) and after annealing at 250 ºC (c).

In Table 6.1 the values of angular position and FWHM, as they have been obtained from the fits, are listed together with the resulting crystals dimension:

Sample	Angular position 2θ (º)	FWHM (º)	Crystal dimension (nm)
CuPc	6.987 ± 0.002	0.216 ± 0.005	36.9 ± 0.9
co-evap. ann. @ 200 ºC	6.859 ± 0.003	0.157 ± 0.009	51 ± 3
	7.05 ± 0.04	0.9 ± 0.3	8 ± 3
co-evap. ann. @ 250 ºC	6.851 ± 0.004	0.08 ± 0.01	102 ± 13
	7.095 ± 0.001	0.055 ± 0.002	145 ± 5

Table 6.1. Angular position and FWHM of the first diffraction peaks of CuPc and co-evaporated CuPc-fullerene after annealing at 200 and 250 ºC. The resulting crystal dimension is also shown. In this table the peak located at about 2θ = 7.4º has not been considered.

The errors on angular position and FWHM are the ones given by the software Origin, while the error affecting the crystal dimension is the one obtained by propagating the others during its calculation.

As it can be seen in the table, the sample of pure CuPc is characterized by a diffraction peak located at 2θ = 6.987º and another much less intense one at around 7.4º. Such features have already been discussed in paragraph 5.1.2. As it has also been anticipated, when CuPc is co-evaporated with fullerene, no diffraction peak is observed, indicating that an amorphous structure has been obtained.

After the annealing treatment at 200 ºC a peak located at 2θ = 6.859º, associated with a *d*-spacing of 12.88 Å, and a shoulder centred at 2θ = 7.05º, associated with a *d*-spacing of 12.53 Å, have appeared. Such features are similar to the ones discussed in literature and should correspond to polymorphs α and β, respectively[60]. The crystal dimensions obtained for the two phases are 51 and 8 nm, respectively. After the annealing, partial crystallization occurs in CuPc phase and the polymorph that appears is principally the α one. Respect to the case of CuPc alone, the crystals of α phase in the co-evaporated film are bigger, indicating that the annealing treatment has caused crystallization with an even better grade.

After the annealing at 250 ºC the diffraction peak and the shoulder clearly separate and become much more intense and sharper. In this case the angular positions are 2θ = 6.851º and 7.0946º, respectively, corresponding to an interplanar distance of 12.89 and 12.45 Å. The dimensions of the crystals that have given these reflexes are 102 and 145 nm, respectively.

The thermal treatment at higher temperature has caused two effects: an enlargement of the crystals and a change from a predominant polymorph α to a predominant polymorph β, as it is demonstrated by the fact that the second peak is now much more intense than the first one. These results confirm that 250 ºC is a critical temperature at which CuPc suffers important changes in its micro-structure and that such transformation is also possible when it is mixed with another material. Such conclusion is also confirmed by the appearance of three other peaks located at the angular positions 2θ = 9.25º, 10.87º and 14.16º (Figure 6.41-a), associated with interplanar distances of 9.55, 8.13 and 6.25 nm respectively, and that correspond quite well with the values of 2θ = 9.22º, 10.66º and 14.15º, reported in the literature for polymorph β[63].

6.2.5 CuPc-PTCDA

In Figure 6.43 the XRD spectrum of annealed co-evaporated CuPc-PTCDA is compared with the spectra of pure CuPc and PTCDA and with the original co-evaporated sample.

As it can be noticed by looking at the zooms on two groups of diffraction peaks (Figure 6.43-a,b), the treatment at 200 ºC has hardly had any effect on the micro-structure of the material. Two very low intensity diffraction peaks located at 2θ = 6.89º and 27.55º, and already noticeable in the not-annealed sample, remain unchanged. The first of those peaks is due to polymorph α of CuPc and is associated with an interplanar distance of 12.82 Å, while the second one is due to PTCDA and is associated to an interplanar distance of 3.24 Å. No fit has been calculated for these two peaks since they are too little intense to make a reliable calculation.

On the contrary, the treatment performed at 250 ºC has had effects on the micro-structure of the sample, since a sharp peak has appeared at the angular position 2θ=7.1º, associated with a *d*-spacing of 12.44 Å. Such feature is related with the polymorph β of CuPc that has formed when the annealing temperature has reached the value of 250 ºC. Phase α, on the contrary, seems not be influenced by the thermal annealing, as the PTCDA phase, the reflexes of which also have not changed.

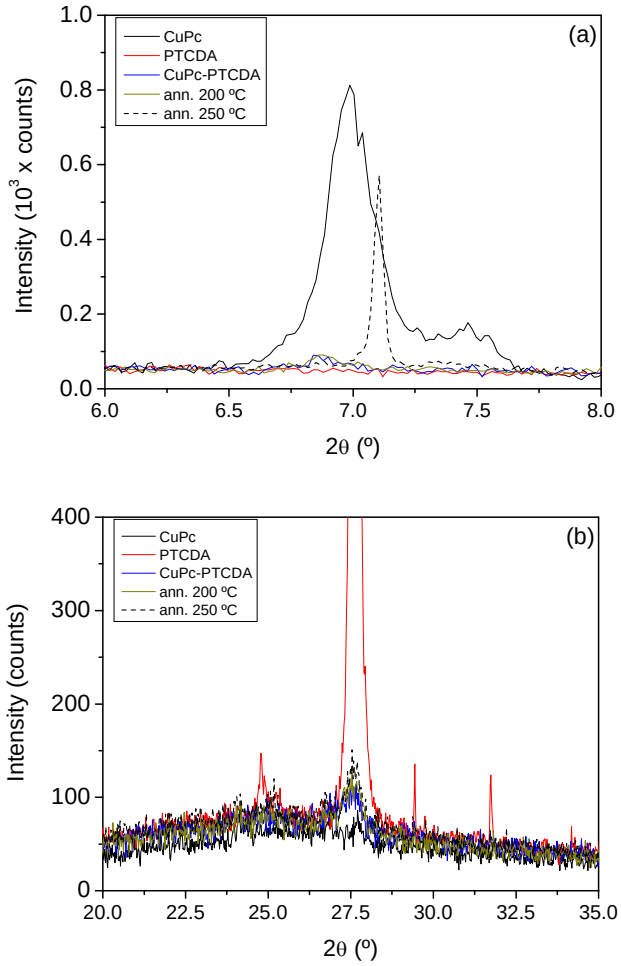

Figure 6.43. Results of the annealing performed at 200 and 250 ºC on co-evaporated CuPc-PTCDA. Two zooms on the only modified parts of the spectra: a group of peaks associated with CuPc (a) and another one due to PTCDA (b). In both cases the vertical scale has been truncated to make easier to read the graph.

In Figure 6.44 the fit of the two diffraction peaks due to CuPc that have appeared after the annealing at 250 ºC is shown:

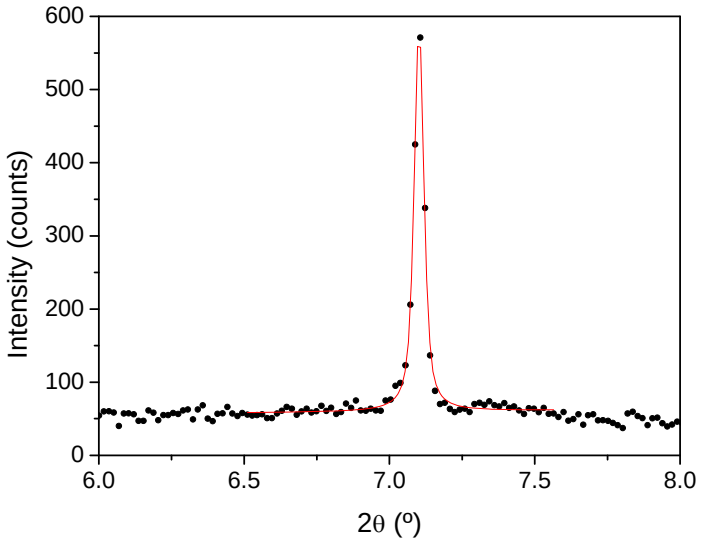

Figure 6.44. Fit of the diffraction peak appeared after the annealing at 250 ºC performed on co-evaporated CuPc-PTCDA.

In Table 6.2 the parameters as they have been obtained from the fit calculated on the diffraction peaks are presented. The data for CuPc have been taken from the previous paragraph.

Sample	Angular position 2θ (º)	FWHM (º)	Crystal dimension (nm)
CuPc	6.987 ± 0.002	0.216 ± 0.005	36.9 ± 0.9
co-evap. ann. @ 200 ºC	-	-	-
co-evap. ann. @ 250 ºC	7.102 ± 0.001	0.040 ± 0.001	199 ± 5

Table 6.2. Angular position and FWHM of the diffraction peak due to CuPc in co-evaporated CuPc-PTCDA, before and after the annealings, compared with the values of pure CuPc. The resulting crystal dimensions are also shown.

6.2.6 CuPc-PTCDI-C_{13}

In Figure 6.45 the spectrum of the annealed co-evaporated CuPc-PTCDI-C_{13} is compared with the ones of pure CuPc and PTCDI-C_{13} and the pre-annealing co-evaporated sample. The figure presents a detail on the three regions where notable changes have been detected after the treatments with temperature.

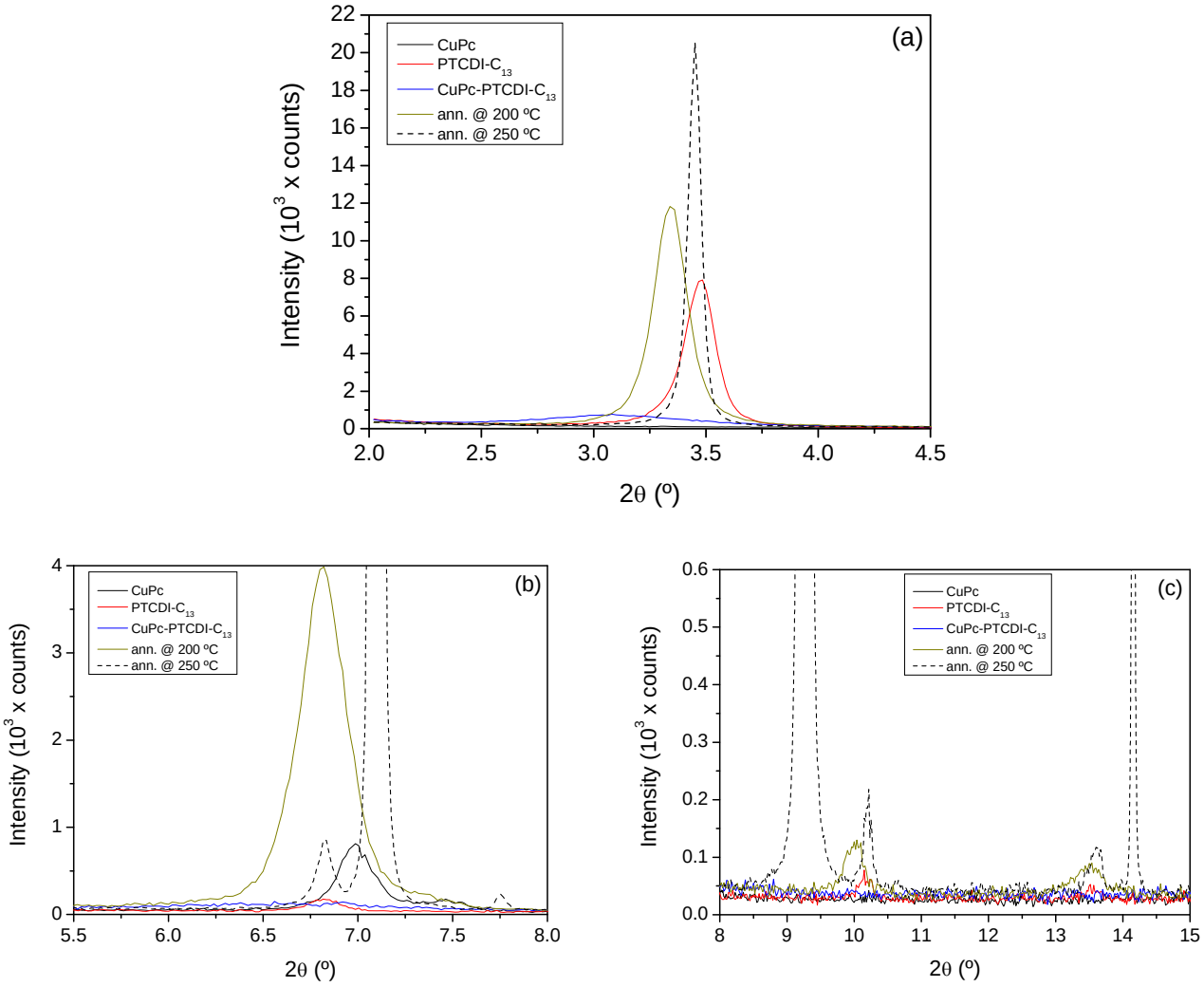

Figure 6.45. Results of the annealing treatments at 200 ºC and at 250 ºC on the structure of co-evaporated CuPc-PTCDI-C_{13}: a zoom on the regions where notable changes are observed.

In the first image (Figure 6.45-a) the evolution of a diffraction peak, due to PTCDI-C_{13}, is shown. Such feature in the as-deposited sample is very little intense and broad, while after the thermal treatments it increases in intensity and gets sharper. Moreover, its angular position changes as a function of the annealing temperature becoming more similar to the one of the peak observed for pure PTCDI-C_{13}.

In the second image (Figure 6.45-b) the familiar evolution of CuPc phase is shown, with the appearance of the peak associated with phase α, after the annealing at 200 ºC, and the transformation to phase β, with the treatment at 250 ºC. As shown in the spectrum taken on pure PTCDI-C_{13}, also this material has one diffraction peak located in this region that could have contributed to the features registered for the co-evaporated sample in this region.

In the third image (Figure 6.45-c) the appearance of other features due to both CuPc and PTCDI-C_{13} is shown. The effect is particularly relevant when the thermal treatment is performed at 250 ºC.

In Figure 6.46 and Figure 6.47 the fit calculated on the diffraction peaks are presented:

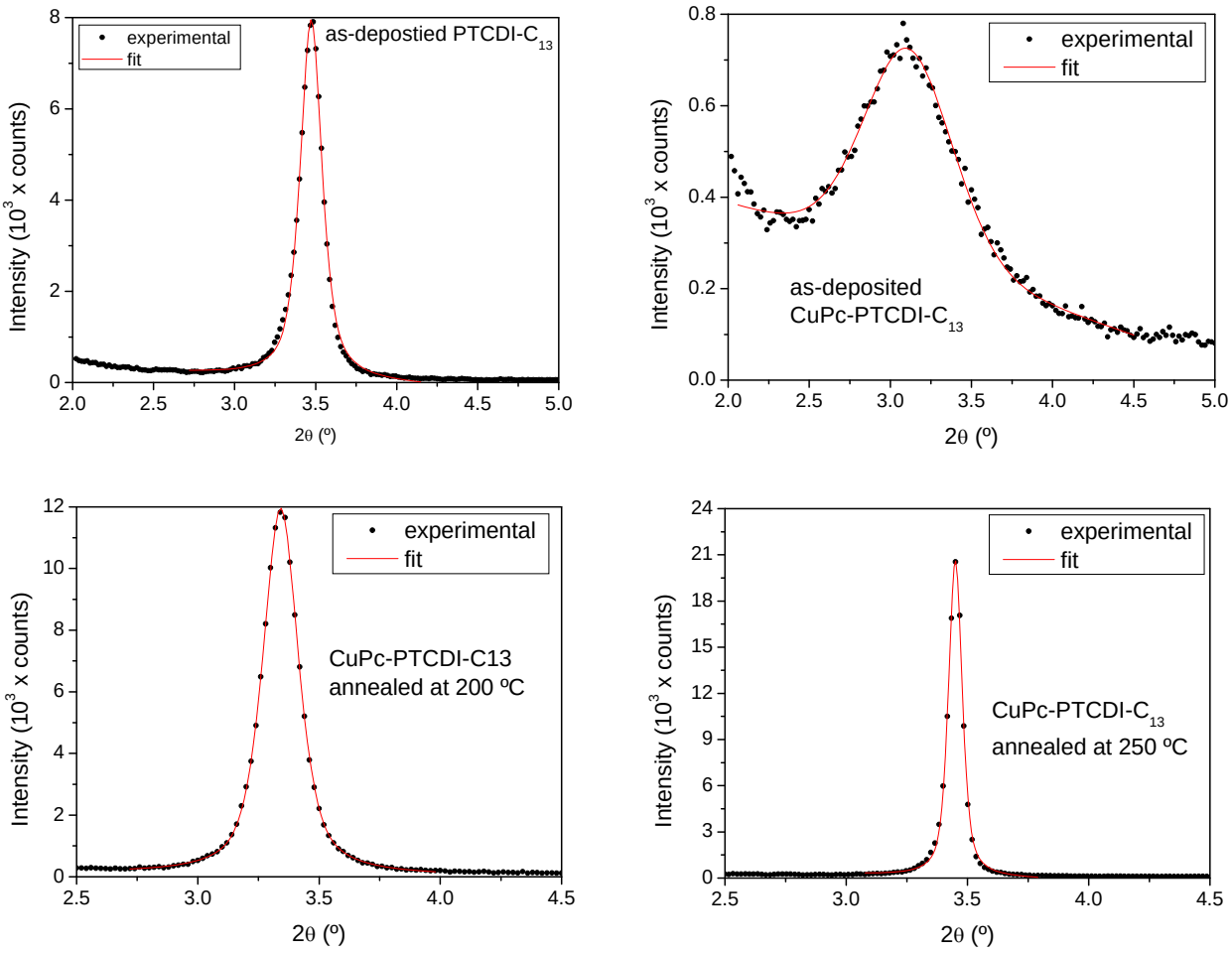

Figure 6.46. Fit of the diffraction peak associated with PTCDI-C_{13} in the pure film and in the co-evaporated one after and before the thermal treatments. The annealing causes an increase in intensity and angular position and a decrease in the FWHM.

The figure shows the fits that have been calculated on the first diffraction peak of pure PTCDI-C_{13} and of the co-evaporated film before and after the two thermal treatments. The features observed in the spectra taken on pure material have already been discussed in chapter 5. Here a fit has been calculated in order to make a comparison with the results obtained for the co-evaporated film.

Figure 6.47 shows the curves for the second group of peaks where a contribution from both CuPc, previously discussed, and perylene have been found. Given that the peak from CuPc has

already been discussed previously, in the figure only the one from pure perylene is compared with the one found for the co-evaporated materials. The effects of the annealing treatments are clearly visible, since the peaks increase a lot in intensity and become sharper.

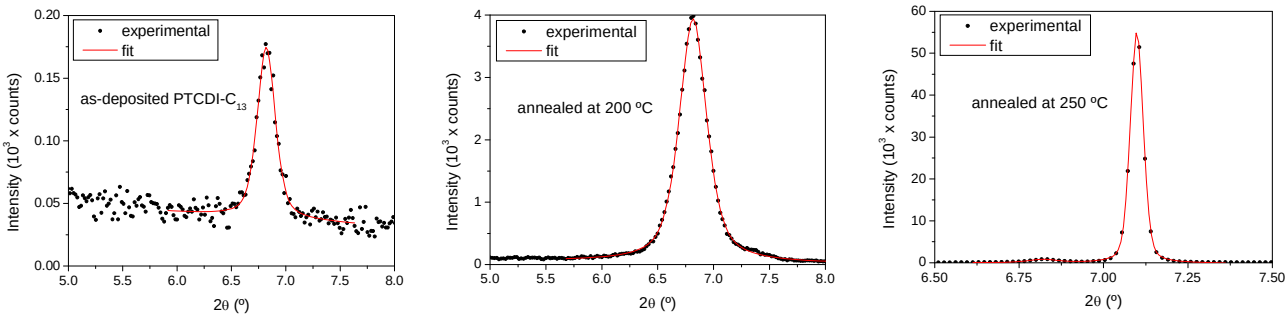

Figure 6.47. Fit of the peaks located near to 2θ = 7º to which both CuPc and PTCDI-C_{13} contribute. The one from pure CuPc is not presented here. For the as-deposited sample there is no peak to fit, while after the annealing at 200 ºC a peak appears that after the treatment at 250 ºC divides into two distinct features.

In Table 6.3 a summary of all the parameters that have been found is presented:

Sample	Angular position 2θ (º)	FWHM (º)	Crystal dimension (nm)
CuPc	6.987 ± 0.002	0.216 ± 0.005	36.9 ± 0.9
PTCDI-C_{13}	3.472 ± 0.001	0.161 ± 0.002	49.4 ± 0.6
	6.820 ± 0.002	0.198 ± 0.006	40 ± 1
co-evap. as-deposited	3.110 ± 0.003	0.66 ± 0.01	12.0 ± 0.2
	6.66 ± 0.02	1.11 ± 0.06	7.2 ± 0.4
co-evap. ann. @200 ºC	3.342 ± 0.001	0.175 ± 0.001	45.4 ± 0.3
	6.816 ± 0.001	0.293 ± 0.002	27.2 ± 0.2
co-evap. ann. @250 ºC	3.450 ± 0.001	0.067 ± 0.001	119 ± 2
	6.82 ± 0.01	0.10 ± 0.03	80 ± 24
	7.099 ± 0.001	0.045 ± 0.001	175 ± 4

Table 6.3. Angular position and FWHM of diffraction peaks of CuPc, PTCDI-C_{13} and co-evaporated CuPc-PTCDI-C_{13} after annealing at 200 and 250 ºC. The resulting crystal dimension is also shown. For CuPc the data already presented in paragraph 6.2.4 are here included. The shoulder located at about 2θ = 7.4º here has not been considered.

The first peak, due to PTCDI-C_{13}, is located at $2\theta = 3.11º$ for the as-deposited sample, and is due to planes with a *d*-spacing of 28.4 Å. After the annealing at 200 ºC such feature moves to $2\theta = 3.3416º$, with an interplanar distance of 26.4 Å. Finally, after the annealing at 250 ºC the peak is located at $2\theta = 3.4501º$, with a lattice parameter of 25.6 Å. As a function of the temperature the angular position of this peak becomes more and more similar to the one registered for pure PTCDI-C_{13} and the interplanar distance diminishes. Such result could be an important indication to improve the transport quality of the material, since a more compact structure could favour the transport of the charge carriers in the semiconductor. The dimension of the crystals in this phase increases from 12 nm, for the as-deposited sample, to 45.4 nm, after the first annealing, and finally becomes 119 nm, after the second one.

Both CuPc and PTCDI-C_{13} contribute to the second group of peaks observed in the spectrum of the co-evaporated material. Regarding perylene, a feature located at $2\theta = 6.82º$ has been found, with an interplanar distance of 13 Å. CuPc, as discussed in the previous paragraphs for annealed samples, contributes with two peaks associated to polymorph α (around $2\theta = 6.85º$) and polymorph β (around $2\theta = 7.09º$). In the spectrum taken on the co-evaporated film a single peak has been registered with angular position $2\theta = 6.66º$, associated with an interplanar distance of 13.3 Å. After the first annealing the peak shifts to $2\theta = 6.816º$ and the distance changes to 13 Å. Finally, after the second annealing the peak divides into two features: one located at $2\theta = 6.82º$, with an associated interplanar distance of 13 Å, and another one located at $2\theta = 7.0985º$, with a distance of 12.4 Å. The dimension of the crystals increases from 7.2 nm in the as-deposited sample to 27.2 nm after annealing at 200 ºC. After annealing at 250 ºC the two new phases that appear are composed by crystals with dimensions of 80 and 175 nm, respectively. Also in this case, an increase in crystals dimension and a more compact structure have been obtained as a function of the temperature. Nevertheless, the peak located at $2\theta = 6.82º$ is probably more due to PTCDI-C_{13} phase, for which a peak has been observed exactly in the same position, than by CuPc, the feature of which is normally located at slightly higher angular values.

6.3 Conclusions about the bulk heterojunctions

To our knowledge, not much investigation has been done about the optical properties of bulk heterojunctions deposited by thermal evaporation, since most of the published works are focused on device performance and optimization.

In this thesis, the first studies carried out in our laboratories on some bulk heterojunctions are presented. All the possible heterojunctions that can be formed between donors and acceptors under investigation have been tried and analyzed. Their optical properties have been explored and compared with the ones of pure materials. The spectra of the mixed materials show, in general, signatures of both components, depending on which of them is the most absorptive in each part of the spectrum. Nevertheless, the absorption spectra are not completely explained in terms of the pure materials, since unexpected absorptions have been observed in the sub-gap region, especially in the cases of pentacene and CuPc when mixed with fullerene and PTCDA. This indicates without any doubt that new states are created in the gap, but it is not clear if they are associated only with more disorder in the structure of the film or also with new species that form as a consequence of the interaction between the two materials. Such phenomenon is less observable, or even absent, when both pentacene and CuPc are co-deposited with PTCDI-C_{13}. Moreover, in many cases the high-absorption band of a co-evaporated thin film is extended to a wider range of energy values than the one of pure materials. As a consequence, the absorption spectrum of the co-evaporated film should have a better coverage of the solar spectrum.

All the samples have been exposed to the same degradation processes as the pure materials. The heterojunctions containing CuPc have revealed as the most stable ones, given that the changes observed in their absorption coefficient are very small, if compared with the ones observed in the other cases. The heterojunctions containing pentacene are less stable and this information could be of help when choosing the materials with which to fabricate organic solar cells.

The optical gap and the Urbach energy have also been evaluated for the co-evaporated samples but, as in the case of the pure materials, the values obtained must be taken just as a qualitative indication due to the difficulty to find a suitable model for organic semiconductors. In Table 6.4 a list of all the results obtained for pure and co-evaporated materials is presented. It is worth noticing that the optical gaps of the heterojunctions are always lower than the ones calculated for the pure materials composing them. The so called band-to-band absorption region of the co-evaporated materials is normally equal to the sum of the ones of pure materials. As a result, the mix of two materials implies a better coverage of solar spectrum. Surprisingly, new absorptions have appeared in the sub-gap region due to defects related with unordered phase and/or new species.

	E_{og} (eV)	E_u (meV)
PURE MATERIALS		
Pentacene	1.73	37
CuPc	1.64	53
Fullerene	1.68	63
PTCDA	2.11	46
PTCDI-C_{13}	2.00	48
BULK HETEROJUNCTIONS		
Pentacene-fullerene	1.67	61
Pentacene-PTCDA	1.71	40
Pentacene-PTCDI-C_{13}	1.72	36
CuPc-fullerene	1.50^{*}, 0.99^{**}	77
CuPc-PTCDA	1.52^{*}, 1.00^{**}	112
CuPc-PTCDI-C_{13}	1.57^{*}, 1.25^{**}	89
$^{*}E_{og,1}$ calculated with Tauc's law $^{**}E_{og,2}$ calculated with Tauc's law		

Table 6.4. The parameters obtained for the bulk-heterojunctions compared with the ones of pure materials.

Once the plots $(\alpha h\nu)^{1/2}$ vs. $h\nu$ have been done for the heterojunctions containing CuPc, another linear region has been found were Tauc's fit was giving a good convergence. From such calculation a second optical gap has been obtained the value of which is much lower that the one of the first gap. By now we have no element to interpret such a result that could be a symptom of the presence of indirect allowed transitions, as it happens for inorganic semiconductors, or of two phases. In case of the latter case being true, these two phases would not be related with the materials composing the heterojunction because the new gaps do not correspond with any of the ones that have been calculated in this work.

A general trend for the Urbach energy, lower for materials that are characterized by some structural order than for amorphous ones, has been evidenced by the XRD spectra with only few exceptions. All the pure materials have very low Urbach energy, if compared with amorphous silicon, with the exception of fullerene, the only pure material whose XRD spectrum demonstrates that it has an amorphous structure. The co-evaporated films generally confirm this trend, with the exception of the ones made of pentacene with PTCDA and PTCDI-C_{13}, which have low values of Urbach energy regardless their unordered structure. It must be noted that the calculation of the

Urbach plot is very affected by any alteration in the spectra. Moreover, in the case of the junctions with CuPc the peak located at 1.13 eV also contributes to make the calculation more difficult. In each case the rule followed, when trying to identify the adequate region where to fit the data, has been to search the lower energies where linearization of the exponential part of the absorption coefficient is obtained. Such rule is the one that must be followed both for the calculation of the Urbach energy and for the optical gap.

Another important aspect is that the XRD characterizations indicate that all of the co-evaporated thin films are nearly or completely amorphous. Annealing treatments have been performed on all of the co-evaporated samples. In the heterojunctions with pentacene, treated at 100 ºC, no change has been observed. On the contrary, the heterojunctions with CuPc show interesting changes when treated at 200 ºC or at 250 ºC. In general, the treatment at 200 ºC causes the increase or appearance of crystallization, as it is evidenced by the data about the crystals dimension. As it could be expected, the treatment at 250 ºC causes the appearance of the polymorph β in the CuPc phase, apart from a further increase in the crystalline fraction. Results like the ones here described indicate that an annealing treatment could be of use for improving the performances of solar cells made with CuPc and the *n*-type semiconductors discussed in this work.

CONCLUSIONS

1. Organic semiconductors have emerged as a novel and promising category of materials for electronic applications. While much work remains to be done to improve our comprehension about the mechanisms that regulate their behaviour, such materials have already attracted much attention for their peculiar properties. The most interesting features that the organic semiconductors show are flexibility, lightweight and low cost device fabrication processes.

2. Among the organic semiconductors two great groups can be distinguished depending on the type of molecules: polymers and small molecules. In this work the latter category of materials has been studied for applications in thin film transistors, diodes and solar cells. The choice of this type of materials was motivated by the experience accumulated, by the investigation groups collaborating in this work, in deposition techniques like thermal vacuum evaporation. Such deposition technique allows a good control of thickness, morphology and other characteristics of the thin films. As a result, the thermal evaporation offers good quality films with adequate properties for electric conduction.

3. Thin films of a group of small molecule semiconductors have been deposited and characterised. The materials analysed are pentacene, CuPc, fullerene, PTCDA and PTCDI-C_{13}. The first two are donor materials, which means materials with good hole conductor properties that work as a *p*-type semiconductor. The other three materials are good electron conductors and work as an *n*-type semiconductor. Such materials have been characterised by different techniques among which Photothermal Deflection Spectroscopy (PDS) has played a major role. By such technique the absorption coefficient α of each material has been calculated, together with optical gap and Urbach energy. The absorption coefficient spectra have suggested that a parallelism can be done with hydrogenated amorphous silicon, whose spectrum shape is determined by the presence of deep and band tail states. The results of the optical gap have been compared with others available in the literature finding good agreement between the data. The films have also been characterised by X-ray diffraction. Such results, with the exception of fullerene, have shown tendency to form polycrystalline solids when deposited in the conditions studied here. Fullerene has shown an amorphous structure.

4. A systematic degradation study has been performed on the semiconductors by measuring the optical spectra of all of the materials. The samples have been optically characterised as-deposited and after being exposed to air (one set of them) and direct light irradiation (another set). Such experiment had the objective to discover if some change occurs in the optical properties of an organic semiconductor when it is exposed to oxidizing agents. CuPc and PTCDA have revealed as the most stable materials, since their absorption coefficient spectra keep unchanged even after a few weeks of degradation treatment. On the contrary, pentacene and fullerene have presented an absorption increase in the sub-gap region. This result indicates that defects have appeared in the materials that could deteriorate their electrical properties acting as traps. The spectrum of PTCDI-C_{13} suffers from changes in its shape and the explanation of such phenomenon is still not clear.

5. A similar systematic study has been performed on all of the possible donor-acceptor combinations. The results obtained have revealed that, when co-evaporated, the molecules have generally more difficulties to arrange in ordered structures. Interestingly, the junctions containing CuPc get more ordered when subjected to annealing treatments at temperatures as high as 200 ºC. If annealed at 250 ºC the order improves even more and, as expected, the appearance of the β polymorph of the phthalocyanine is observed. The study of the degradation performed on the heterojunctions indicates that in general a mixture between two stable materials is stable too. The most stable junctions are the ones composed of CuPc with PTCDA and PTCDI-C_{13}.

APPENDIX A

ORGANIC DEVICES

In this section the first organic devices that have been fabricated in the laboratories of UPC are presented. Many important groups are currently working on this issue and the best results have been obtained doing the whole fabrication process and the following electrical characterisation in nitrogen atmosphere. For this purpose the deposition and the characterisation equipments are usually stored in a glove-box where water and oxygen are present at very low concentration. This way to operate allows to avoid that the semiconductors oxidize, losing their optical and electrical properties. Moreover, the semiconductors are often purified by gradient sublimation before being evaporated. During the period in which the experimental work of this thesis has been done, our laboratories did not have such facilities. Therefore the devices were fabricated and then taken out of the vacuum chamber and put in contact with the atmosphere. As a result, the non optimal conditions in which the devices were fabricated must be taken into account when analyzing the experimental results obtained.

Two types of devices have been fabricated: TFTs using PTCDI-C_{13} as an *n*-type semiconductor and diodes using CuPc as a *p*-type semiconductor. The reasons for choosing such materials lie in their characteristics and in the results discussed in the chapters about material characterisations (chapters 5 and 6). PTCDI-C_{13} has been demonstrated a good electron conductor with an interesting mobility value of $1.7 \cdot 10^{-2}$ $cm^2V^{-1}s^{-1}$ (see chapter 2.4). Furthermore, in chapter 5 we have shown how it is relatively easy to obtain polycrystalline structures with such material, without need of heating the substrate during the deposition process. CuPc is generally used as a *p*-type semiconductor and in this work it has been shown that this material has good tendency to crystallize and form polycrystalline thin films. It is also a very stable material, an important requirement when fabricating organic solar cells.

In the first section of this chapter TFTs fabricated with PTCDI-C_{13} are described and characterised. Four devices have been fabricated changing the substrate temperature in order to determine the effects that such parameter has on the electric performance of the devices. A complete characterization of the devices allows to calculate the density of states in the gap of the semiconductor and to compare the results with the ones obtained by PDS for the same material.

In the second section CuPc diodes are discussed. Also in this case, different samples have been obtained by changing substrate temperature. The I-V curve of such devices has been measured in dark conditions to check their performance. Moreover, the same characterization has been performed with light illumination to see if the devices were sensitive to irradiation. These diodes represent a first step towards solar cell fabrication with small molecule semiconductors by thermal evaporation.

In both cases the device characterisations are preceded by a characterisation of the materials, which is useful to interpret the results.

A.1 PTCDI-C_{13} TFTs

Organic TFTs have been fabricated by using PTCDI-C_{13} as an *n*-type semiconductor, performing the deposition process with different substrate temperatures: 30, 60, 90 and 120 ºC. The substrate has been taken to the required temperature by means of a resistance controlled externally by a PID (proportional-integrative-derivative) system. Once the glass has reached the desired temperature, the material source has been heated to the evaporation temperature and the shutter has been opened.

The structure of the devices is the one shown in Figure:

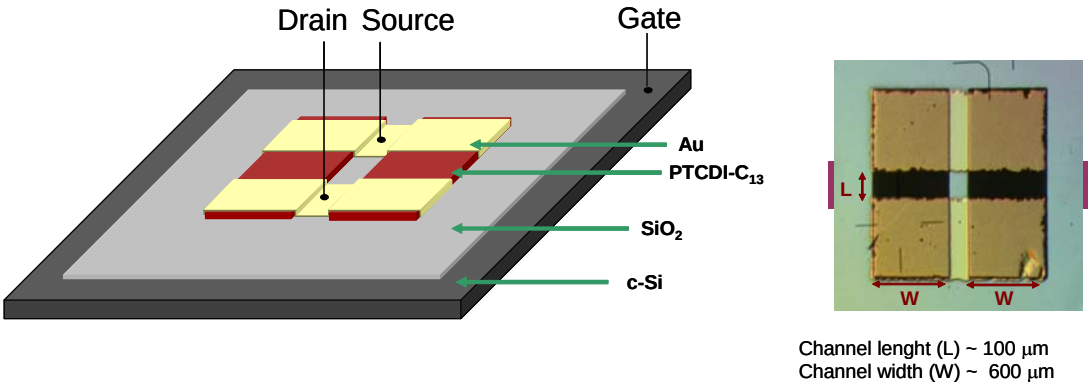

Figure A.1. Structure of the four OTFTs that have been fabricated with PTCDI-C_{13}.

The substrate employed is *p*-type crystalline silicon covered with 150 nm of thermally grown silicon oxide (SiO_2) as a dielectric. 100 nm-thick films of the perylene derivate have been deposited

by thermal vacuum evaporation on the oxide. Gold contacts have also been evaporated in order to form source and drain contacts, while the silicon works as the gate contact. Gold is known to make ohmic contact with *n*-type semiconductors. Both the perylene derivate and gold have been deposited through a shadow mask which allows to obtain a channel width of 600 μm and a channel length of 100 μm. PTCDI-C_{13} thin films have been deposited with a base pressure of 10^{-4} Pa and a deposition rate of 0.5 Å/s. In addition, other four 200 nm thick films have been deposited, in the same conditions, on glass for XRD characterization. All device characterizations have been performed in vacuum in a cryostat.

An XRD analysis has been performed on PTCDI-C_{13} deposited at the different substrate temperatures. In Figure A.1 the spectra of the four films are shown. Four diffraction peaks located at 2θ = 3.43º, 6.77º, 10.11º and 13.57º, respectively, have been observed which correspond to *d*-spacings equal to 25.7, 13.1, 8.77 and 6.5 Å. The four peaks are the typical ones observed for PTCDI.C_{13} and that have already been discussed in chapter 5.

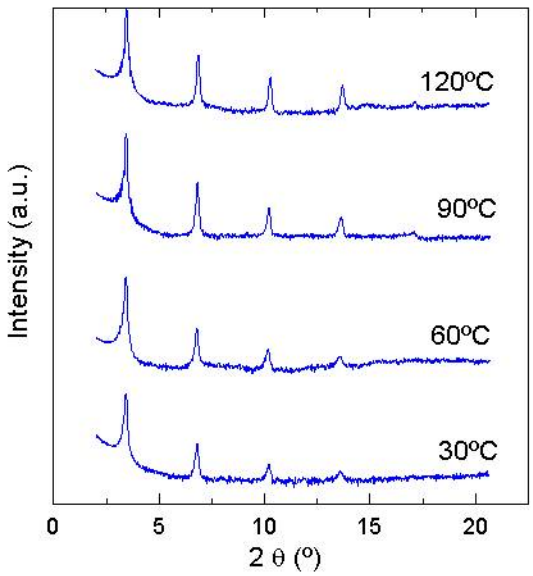

Figure A.1. XRD pattern of PTCDI-C_{13} thin films deposited with different substrate temperatures.

By increasing the substrate temperature the diffraction peaks increase in intensity and become sharper, which indicates an increase in crystallites dimension and in the crystalline fraction of the films. On the contrary, no relevant change in the angular position has been detected. It has been reported that gold, aluminium, silver and chromium are metals that provide good electron injection

into PTCDI-C_{13} and that no dependence is observed between the field-effect mobility and the work function of the metallic contact[124,125].

In Figure A.2 the output characteristic **(**I_{DS} vs. V_{DS}**)** with different gate tensions (V_{GT}) of the TFT deposited at 120 ºC is shown. The device shows the typical characteristics of an *n*-channel field-effect transistor, generating charge accumulation for a positive gate voltage. Neither current crowding for low V_{DS} nor kink effects for higher V_{DS} values were observed, indicating a low contact resistance at the drain and source electrodes with low carrier injection.

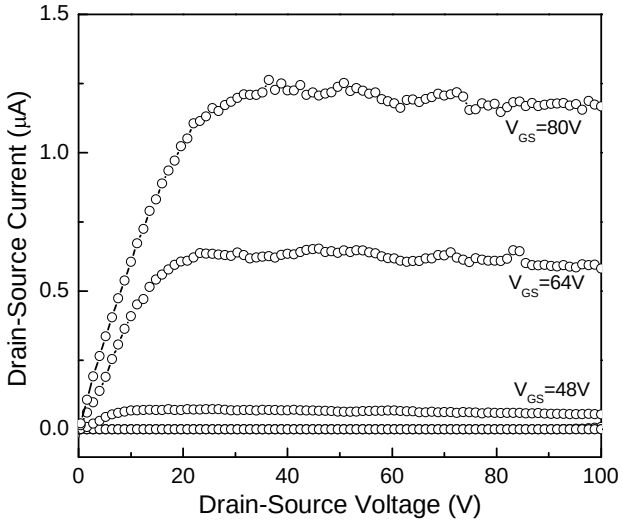

Figure A.2. Output characteristic with different gate tensions (V_{GS}) of the TFT deposited at T_{sub} = 120 ºC.

In Figure A.3 the transfer characteristics (I_{DS} vs. V_{GS}) of the TFTs deposited with the four substrate temperatures are presented. The measurements have been performed applying a drain-source tension of 10 V. All the fabricated devices exhibited clear *n*-type characteristics. They operate in the accumulation mode (electron accumulation) for positive V_{GS} values, while when the gate is negatively biased the channel interface is depleted of carriers (depletion mode). The measured I_{on}/I_{off} ratios were about 10^5 with also acceptable sub-threshold slopes (0.5 V/decade for the sample deposited at 30ºC). The I_{DS} current evidences a strong dependence on the deposition temperature. A shift of I_{DS} to lower V_{GS} values (i.e. lower threshold voltage) is clearly observed when substrate temperature is increased.

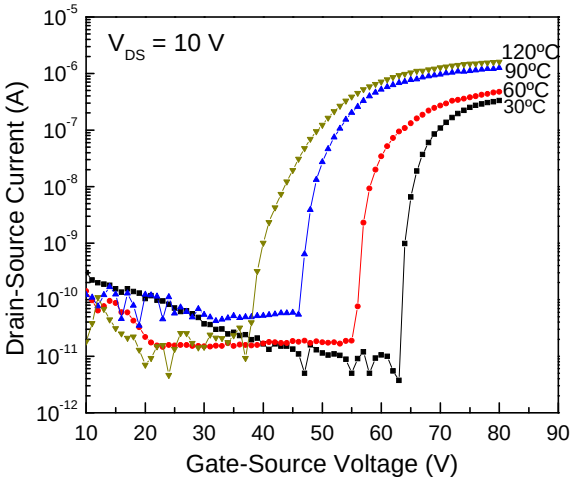

Figure A.3. Transfer characteristic measured with a drain-source tension (V_{DS}) of 10 V on the TFTs deposited with different substrate temperatures

In Figure A.4 the plot $I_{DS}^{1/2}$ vs. V_{DS} in the saturation regime ($V_{GS} = V_{DS}$) is depicted for the four substrate temperatures together with the fits calculated in the linear part of each curve:

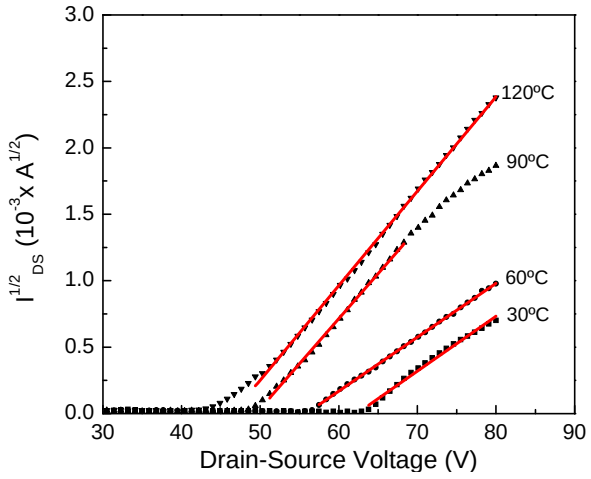

Figure A.4. Plot of the square root of I_{DS} in function of the drain-source voltage (scattered points) in saturation conditions. For each curve a fit of the linear part (red lines) has been calculated in order to evaluate μ and V_t.

Field-effect electron mobility μ and threshold voltage V_t values for the four devices have been calculated using equation (4.27) and the results are listed in Table A.1:

Substrate temp. (º)	μ ($cm^2V^{-1}s^{-1}$)	V_t (V)
30	0.036	61.7
60	0.038	55.8
90	0.092	48.7
120	0.120	46.6

Table A.1. Values of field-effect mobility (μ) and threshold voltage (V_t) obtained by fit calculations in the saturation regime.

The field-effect mobility of the electrons increases with substrate temperature, while the threshold voltage diminishes. These results indicate that an improvement of the electrical performance of the TFT occurs when the substrate is heated during the deposition process of the semiconductor. The values here obtained for both parameters are in good agreement with the ones reported in literature for PTCDI-C_{13} transistors[124].

The XRD analysis has revealed (Figure A.1) that PTCDI-C_{13} thin films present a polycrystalline structure. As it could be expected, the XRD spectra have also shown an increase in the molecular order with substrate temperature. While the carrier mobility within a crystalline grain is high, the scattering effect of the grain boundaries in polycrystalline structures results in reduced mobility. Then, we could attribute the observed dependence of μ and V_t with substrate temperature to the formation of more ordered films at higher deposition temperatures. An increase in the molecular order reduces the amorphous fraction and enhances the transport of charge carriers by increasing the field-effect mobility. Our results are in agreement with those reported by other laboratories. Tatemichi *et al.* reported that the field-effect mobility of PTCDI-C_{13} can be increased orders of magnitude (from $5.4 \cdot 10^{-3}$ to 2.1 $cm^2/V \cdot s$) by annealing the OTFT at an adequate temperature (140ºC). However, the threshold voltage also increased from 44 V to 60 V[78]. Gundlach *et al.* also studied the dependence of μ and V_t values for PTCDI-C_{13} OTFTs fabricated at different substrate temperatures on SiO_2 dielectrics[124]. By contrast, these authors did not find any dependence of μ and V_t with substrate temperature.

In order to get more information about the electronic properties of the PTCDI-C_{13} thin films, the transfer characteristic of the OTFT deposited at 120ºC has been measured, changing the temperature during the measurement over a range of 30–90ºC. The activation energy (E_A) of

channel conductance as a function of gate bias has also been evaluated by employing equations (4.29) and (4.30).

In Figure A.5 the transfer characteristics measured for several temperatures (left side) and the resulting Arrhenius type plot of the drain-source current, in function of temperature, for several gate voltages (right side), are shown. The drain-source current is proven to be influenced by the temperature, according to an Arrhenius type law.

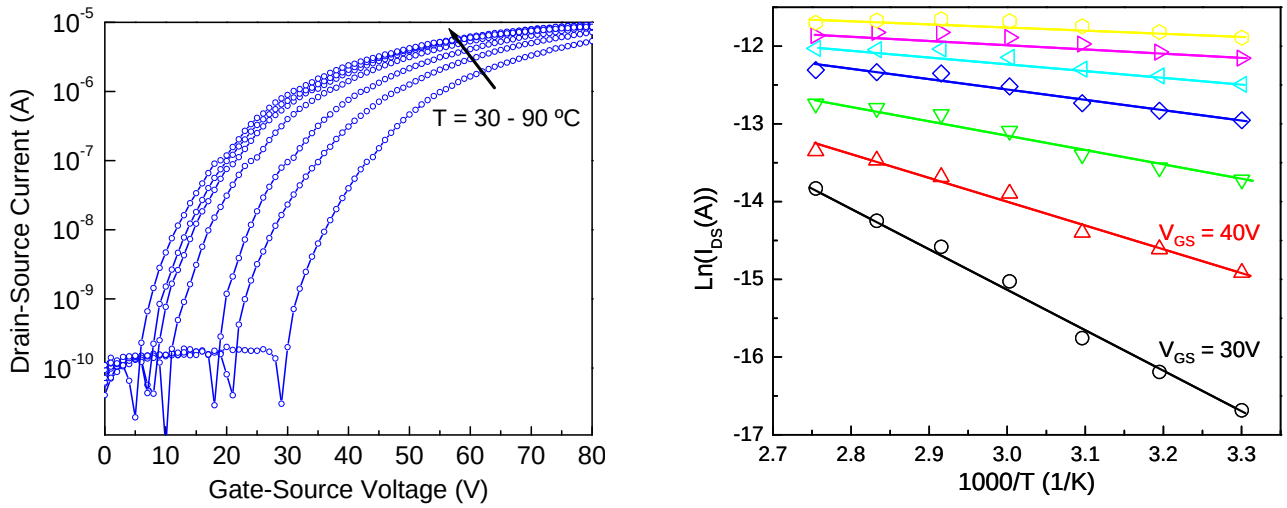

Figure A.5. Transfer characteristic as a function of gate-source voltage for several temperatures (left side) and Arrhenius plot of I_{DS} as a function of temperature and with different gate-source tensions (right side).

In Figure A.6 the activation energy (E_A) in function of the gate tension is shown. The activation energy decreases from 1.4 eV, for a gate tension of 30 V, to about 0.1 eV, for a tension of 80 V. This behaviour could be described in terms of standard semiconductor theory. The dependence of E_A on V_{GS} corresponds to a gradual shift of the Fermi level toward the conduction band as more empty traps become filled by injected electrons from the contacts. The Fermi level moves toward the conduction band by increasing V_{GS} and, consequently, E_A steadily decreases. For low V_{GS} values the Fermi level is far from the conduction band and can enter deeper states resulting in large values of activation energy.

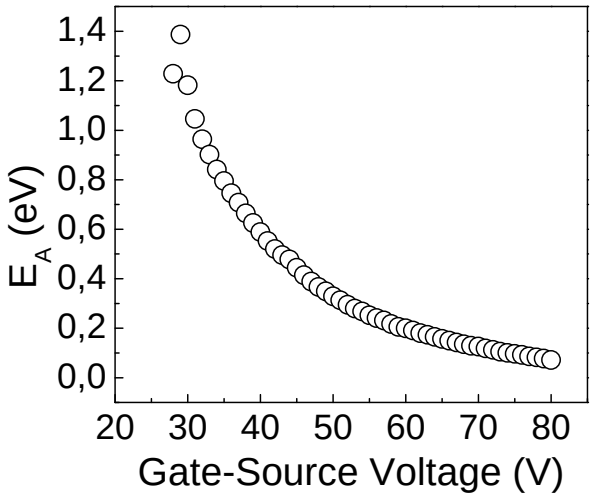

Figure A.6. Activation energy as a function of the tension applied to the gate.

The density of states in the band-gap has been calculated by employing equation (4.35) and is shown in Figure A.7. Remembering the value for the optical gap of 2 eV, calculated in section 5.1.5, the density of localized states is around 10^{17} $cm^{-3}eV^{-1}$ at about 1 eV (in the midgap) and increases one order of magnitude for energy values closer to the conduction band. The DOS distribution could be roughly described by the sum of two exponential contributions (see dashed lines in Figure A.7). The electronic properties of thin film organic semiconductors are usually interpreted assuming, as in the case of hydrogenated amorphous silicon, the presence of localized states in the band gap. Hence, we can attribute the two exponential regimes in the DOS distribution to the presence of deep and band tail states.

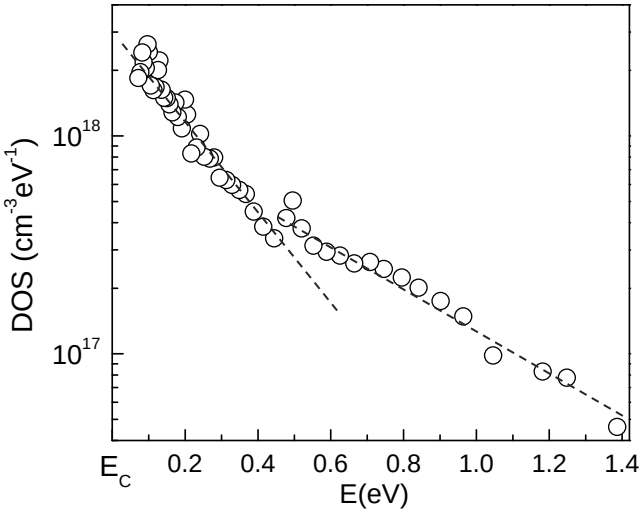

Figure A.7. Density of states in function of the energy. The boarder of the conduction band (E_C) is also indicated in the energy scale as a reference.

The presence of deep (localized) and band tail states in the gap of the organic semiconductors has also been demonstrated by the PDS measurements discussed in the previous chapters. In the sub-gap region, the spectrum of the absorption coefficient gives information about the density of states in the gap. The non-zero absorption coefficient of our materials for energies lower than their optical gap reveals the presence of both deep and tail states and this concept finds confirmation in the results of TFTs here presented.

A.2 CuPc diodes

A.2.1 CuPc thin films deposited with different substrate temperatures

In this section the characterizations performed on CuPc samples deposited on glass with four different substrate temperatures will be presented. All the films were 700 nm thick and have been deposited with a deposition rate of 1 Å/s at substrate temperatures of 30, 60, 90 and 120 ºC.

The thin films have been characterized by X-ray diffraction spectroscopy and the spectrum until 2θ = 30º, is presented in Figure A.8. Three diffraction peaks, located at approximately 2θ = 6.85º, 13.68º and 27.51º respectively, are present in all four samples.

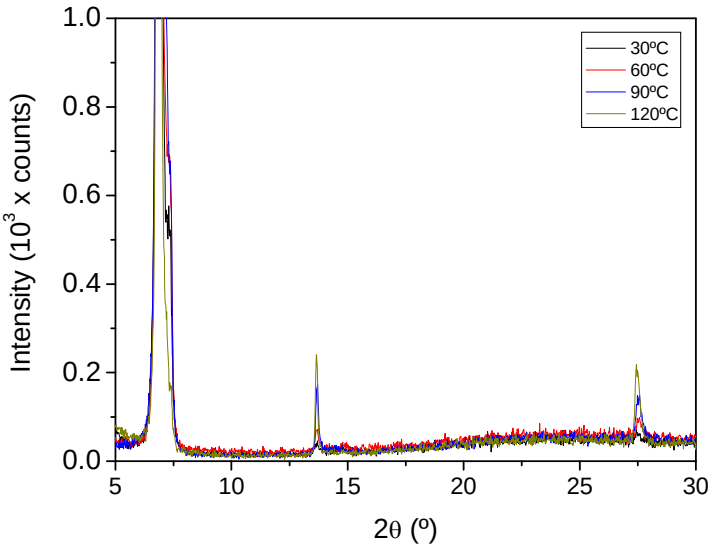

Figure A.8. XRD spectrum of CuPc samples deposited with different substrate temperatures.

When we compare these spectra with the one presented in chapter 5 (Figure 5.8), we notice that in the patterns shown in Figure A.8 there are two more diffraction peaks. We argue that the appearance of such features in this case is due to the different deposition conditions employed. The samples here described have been deposited at a much lower deposition rate (1 Å/s instead of 3 Å/s) than the ones described in chapter 5. A lower rate could have favoured the growing of a more ordered structure, revealed by the appearance of other diffraction features.

In Figure A.9 a zoom on the diffraction peaks is shown:

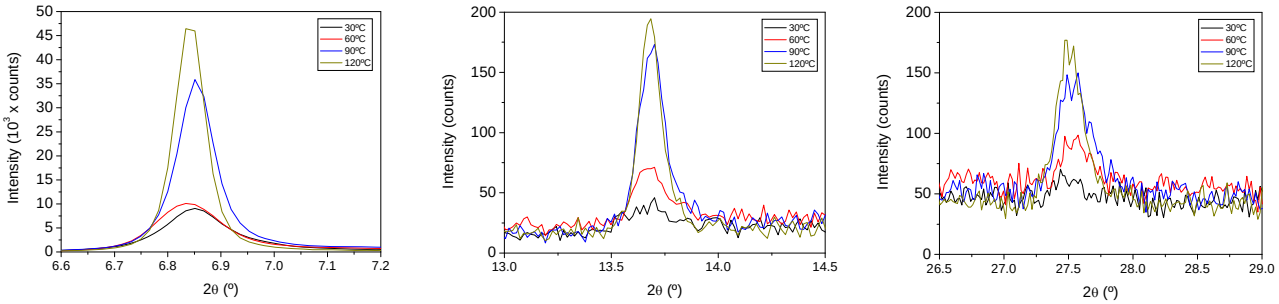

Figure A.9. Zoom on the three diffraction peaks.

In all cases the intensity of the peaks increases with the substrate temperature. This suggests that at temperatures higher than room temperature it is possible to improve the crystallinity of CuPc films. A fit of the first diffraction peak has been evaluated for all the samples using a pseudoVoigt equation (see chapter 4) and is presented in Figure A.10. With the results obtained from the fit a qualitative estimation of the dimension of the crystals present in the films has been done.

The results of peak position and FWHM, obtained from the fits, are listed in Table A.2 with the value of crystal dimension, calculated by the Scherrer equation (4.24). In the calculation of the fits a simple pseudoVoigt equation has been used, without taking into account any effect of instrumental origin like the presence of radiation $K_{\alpha 2}$. Anyway, the equation fits quite well the experimental data and allows us to make an estimation of crystal dimension. The errors indicated in the table for peak position and FWHM are the ones calculated by Origin®, while the one of the crystal dimensions has been calculated from the others. What is really useful, in our case, is to compare the values of crystal dimension for the different samples and to notice that it increases with the substrate temperature with the exception of the sample grown at 60 ºC, whose value stays substantially equal to the previous one.

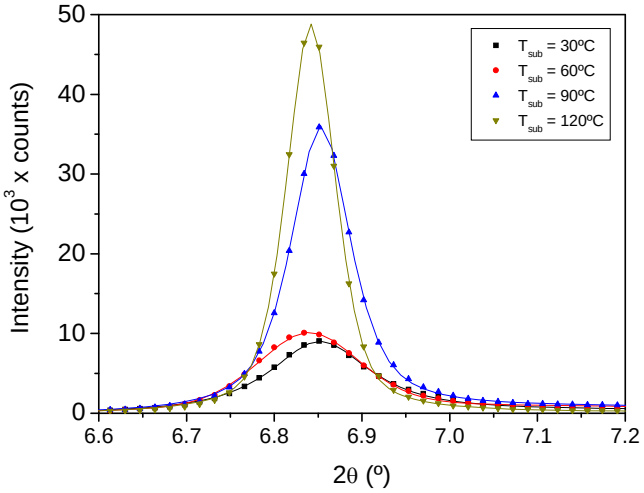

Figure A.10. Fit of the first peak of the four spectra. The scattered points represent the experimental data, while the lines represent the calculated curves.

T_{sub} (ºC)	Peak position 2θ (º)	FWHM (º)	Crystal dimension *d* (nm)
30	6.852 ± 0.001	0.138 ± 0.004	58 ± 1
60	6.839 ± 0.001	0.141 ± 0.002	56 ± 1
90	6.853 ± 0.001	0.081 ± 0.001	98 ± 1
120	6.842 ± 0.001	0.067 ± 0.001	120 ± 1

Table A.2. Angular position and FWHM of the first diffraction peak for each sample; dimension of the crystals (*d*) obtained by Scherrer's equation.

In Figure A.11 the variation of the crystal dimension with the substrate temperature is shown:

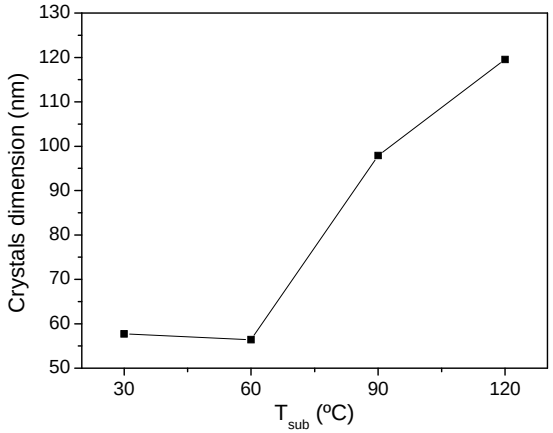

Figure A.11. Variation of the crystal dimension as a function of the substrate temperature.

In Figure A.12, the absorption coefficient and optical transmittance of the samples deposited with different substrate temperatures are presented:

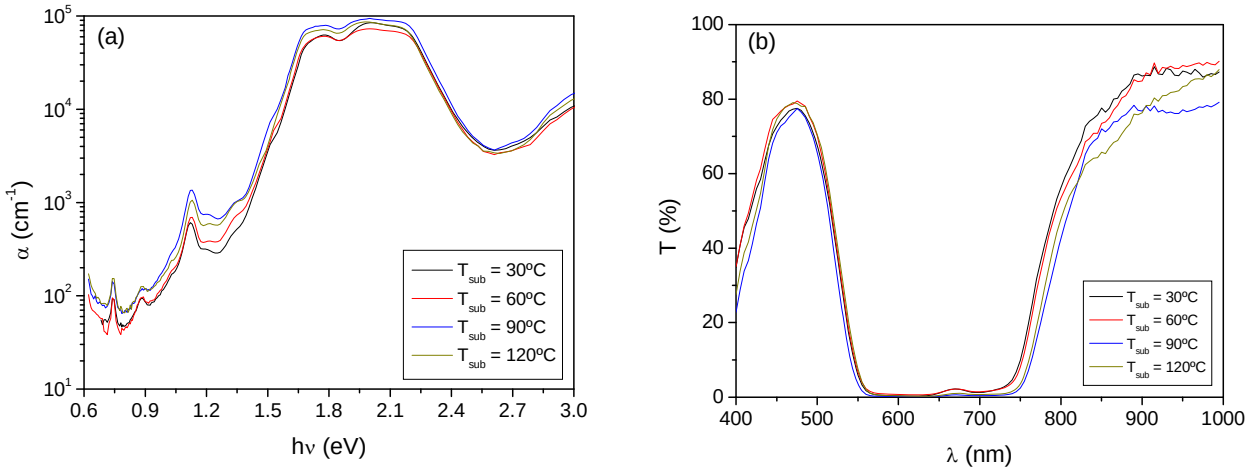

Figure A.12. Absorption coefficients (a) and transmittance spectra (b) of CuPc thin films: comparison between samples deposited with different substrate temperature.

Some changes are observed as a function of the deposition temperature in the absorption coefficient (Figure A.12-a), but no clear trend can be detected. The samples deposited at 30 and 60 ºC have the lowest absorption coefficients. The other two samples have the highest absorption level in the whole range, with the exception of the region included between 0.95 and 1.40 eV where the sample deposited at 90 ºC has higher α.

Regarding the optical transmittance (Figure A.12-b), the thin films deposited with the two highest temperatures have the lowest values. The clearest differences in the spectra are visible for wavelengths higher than 750 nm, but they are probably affected by the interference oscillations that make it difficult to make a comparison.

A.2.2 CuPc devices

A photo and a not-in-scale representation of the CuPc diodes that have been fabricated are presented in Figure A.13. In this case the device structure is the simplest of the ones discussed in chapter 3: a Schottky device where the rectifying contact is between CuPc and Al. The photo presented in the figure below shows that we deposited many 1 mm^2 aluminium contacts, so that we obtained many devices with one deposition process. The semiconductor has been deposited with the

evaporator for organics with the same conditions as indicated in the previous paragraph and, also in this case, samples with different substrate temperatures (30, 60, 90 and 120 ºC) have been fabricated. Metallic contacts have been deposited in the other evaporation system with a base pressure of 10^{-3} Pa.

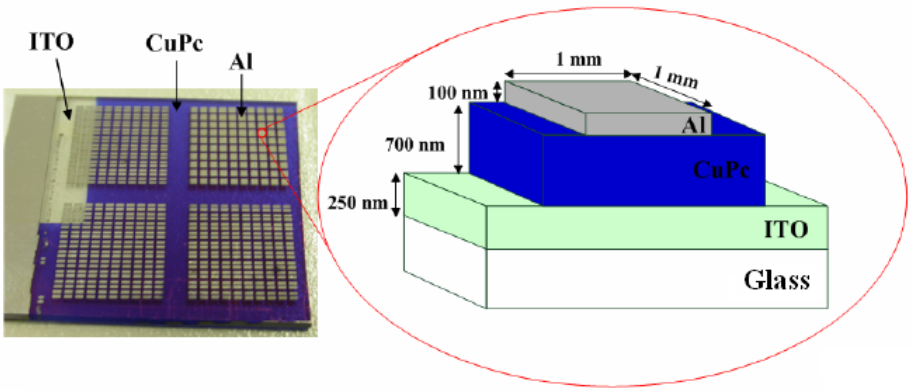

Figure A.13. Photo and structure of CuPc diodes.

In Figure A.14 the J-V characteristics, measured in dark, for the CuPc devices is presented.

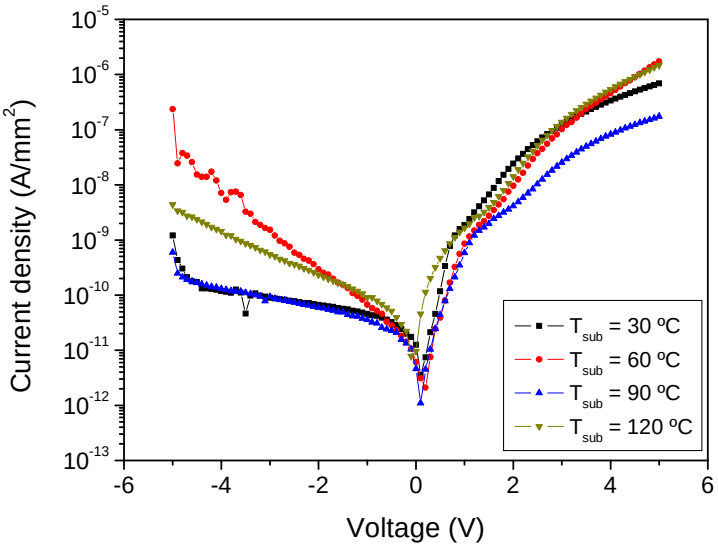

Figure A.14. Dark J-V characteristic of CuPc Schottky devices fabricated with different substrate temperatures under dark conditions.

The devices fabricated at 30 and 90 ºC present the best rectifying properties, since they have the lowest current for inverse polarization (negative values of voltage). The high current measured for negative polarization in the case the other two devices is probably due to current losses caused by pin holes. Such pin holes could be caused by material perforation occurred during the deposition of the metallic contacts.

For polarization values included between 0 and 0.5 V the device fabricated at 120 ºC shows the highest current. In this region the current is regulated by ohmic regime and the charge carriers are thermally generated. The XRD characterization previously performed on thin films reveals that the one deposited at 120 ºC has larger crystals. A higher crystalline fraction could have yield a higher mobility for the charge carriers and better transport properties for that film, explaining the measured current in the ohmic regime.

For higher tension values there are not important differences between the devices, with the exception of the one fabricated at 90 ºC, which has the lowest current.

In Figure A.15 the J-V characteristics of the devices measured under illumination conditions are shown:

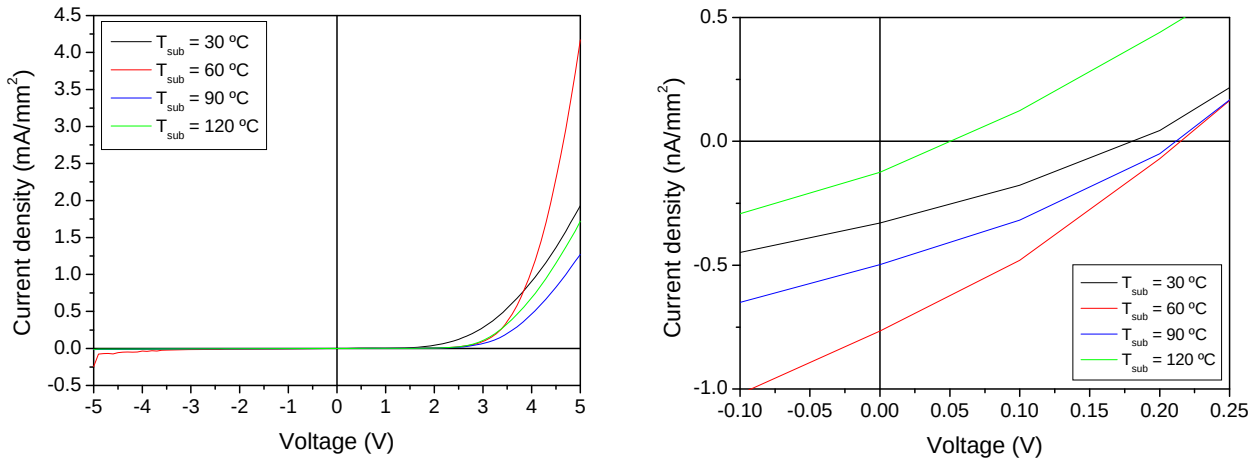

Figure A.15. J-V characteristic of CuPc devices under illumination conditions (left side) and detail on the fourth quadrant (right side).

The light power concentration used to characterize the devices is 248 W/m^2. As it was expected for this kind of devices, the diodes have very poor response to light irradiation. In order to obtain better photovoltaic performances, double layer devices are being investigated but still not presented in this work. Moreover, new equipment, consisting of a glove-box with two internal evaporators

and the possibility to perform J-V characterisations in inert atmosphere, is being installed in order to exclude problems with oxidizing agents.

References

[1] http://nobelprize.org/nobel_prizes/chemistry/laureates/2000/index.html
[2] Hideki Shirakawa, Edwin J. Lewis, Alan G. MacDiarmid, Chwan K. Chang and Alan J. Heeger, J. Chem Soc. Chem. Comm. (1977) 578-580.
[3] - R. McNeill, R. Siudak, J.H. Wardlaw and D.E. Weiss, Aust. J. Chem. 16 (1963) 1056-1075.
- B.A. Bolto and D.E: Weiss, Aust. J. Chem. 16 (1963) 1076-1089.
- B.A. Bolto, R. McNeill and D.E. Weiss, Aust. J. Chem. 16 (1963) 1090-1103.
[4] Yueh-Lin Loo and Iain McCulloch, MRS Bulletin 33 (2008) 653-658.
[5] Martin A. Green, Keith Emery, Yoshihiro Hishikawa and Wilhelm Warta, *"Solar Cell Efficiency Tables (version 34)"* Prog. Photovolt.: Res. Appl. 17 (2009) 320-326.
[6] Plastic Solar Panels by Solarmer: Plastic Solar Panels. © 2009 All Rights Reserved Solarmer Energy, Inc.. [Consulted: December 2009]. Available at http://www.solarmer.com/.
[7] Jean-Michel Nunzi, C. R. Physique 3 (2002) 523–542.
[8] S-S Sun and N.S. Sariciftci, *Organic Photovoltaics: Mechanisms, Materials and Devices*, Taylor & Francis, p. 112.
[9] Peter Peumans, Aharon Yakimov and Stephen R. Forrest, J. Appl. Phys. 93 (2003) 3693-3723.
[10] Yen-Yi Lin, David J. Gundlach, Shelby F. Nelsón and Thomas N. Jacksón, IEEE TRANSACTIONS ON ELECTRON DEVICES 44 (1997) 1325-1331.
[11] D.J. Gundlach, Y.Y. Lin, T.N. Jacksón, S.F. Nelsón, and D.G. Schlom, IEEE Electr. Dev. Lett. 18 (1997) 87-89.
[12] R.E. Blankenship, *Molecular Mechanisms of Photosyntesis*, Blackwell Science, Oxford (2002).
[13] S-S Sun and N.S. Sariciftci, *Organic Photovoltaics: Mechanisms, Materials and Devices*, Taylor & Francis, p. 41.
[14] P. Bernier, S.Lefrant and G. Bidan, *Advances in Syntetic Metals: Twenty Years of Progress in Science and Technology*, Elsevier (1999) p. 99.
[15] Carlo Di Bello, *Principles of Organic Chemistry,* Decibel-Zanichelli (1993) p. 93.
[16] Harald Hoppe and Niyazi Serdar Sariciftci, J. Mater. Res. 19 (2004) 1924-1945.
[17] P. Peumans and S. R. Forrest, Appl. Phys. Lett. 79 (2001) 126-128.
[18] Christopher R. Newman, C. Daniel Frisbie, Demetrio A. da Silva Filho, Jean-Luc Bredas, Paul C. Ewbank, and Kent R. Mann, Chem. Mater.16 (2004) 4436-4451.
[19] D.M. de Leeuw, M.M.J. Simenon, A.R. Brown, R.E.F. Einerhand, Synthetic Metals vol. 87 (1997) 53-59.
[20] P. Bernier, S.Lefrant and G. Bidan, *Advances in Syntetic Metals: Twenty Years of Progress in Science and Technology*, Elsevier (1999).
[21] C.J. Brabec, V. Dyakonov, J. Parisi and N.S. Sariciftci, *Organic Photovoltaics*, Springer (2003).
[22] A.J. Heeger, S. Kivelsón, J.R. Schrieffer and W.-P. Su, Rev. Mod. Phys. 60 (1988) 781-850.
[23] R. Peierls, J. Phys. A Math. Gen. 24 (1991) 5273-5281.
[24] S. Brazovskii, N. Kirova and A.R. Bishop, Opt. Mater. 9 (1998) 465-471.
[25] D. Guo, S. Mazumdar, S.N. Dixit, F. Kajzar, F. Jarka, Y. Kawabe and N. Peyghambarian, Phys. Rev. B 48 (1993) 1433.
[26] D. Moses, M. Sinclair and A.J. Heeger, Phys. Rev. Lett. 58 (1987) 2710.
[27] M. Pope and C.E. Swenberg, *Electronic Process in Organic Crystal and Polymers,* Oxford Science Publications (1999) p. 1.
[28] S.R. Forrest, Chem. Rev. 97 (1997) 1793-1896
[29] M. Pope, Ch.E. Swenberg, *Electronic Processes in Organic Crystals and Polymers*, 2nd Ed. Oxford University Press, New York, (1999).
[30] P. Bernier, S.Lefrant and G. Bidan, *Advances in Syntetic Metals: Twenty Years of Progress in Science and Technology*, Elsevier (1999) p. 135.

[31] S-S Sun and N.S. Sariciftci, *Organic Photovoltaics: Mechanisms, Materials and Devices*, Taylor & Francis, p. 162
[32] S-S Sun and N.S. Sariciftci, *"Organic Photovoltaics: Mechanisms, Materials and devices"*, Taylor & Francis, p. 423.
[33] I.B. Goldberg, H.R. Crowe, P.R. Newman, A.J. Heeger and A.G. MacDiarmid, J. of Chem. Phys. 70 (1979) 1132-1136.
[34] B.R. Weinberger, E. Ehrenfreund, A. Pron, A.J. Heeger and A.G. MacDiarmid, J. of Chem. Phys. 72 (1980) 4749-4755.
[35] H. Thomann, L.R. Dalton, M. Grabowski, Y. Tomkievicz, N. Shiren and T.C. Clarke,Phys. Rev.Lett. 50 (1983) 533-536.
[36] N. Suzuki, M. Ozaki, S. Etemad, A.J. Heeger and A.G. MacDiarmid, Phys. Rev. Lett. 45 (1980) 1209-1213.
[37] H Schaffer, R.H. Friend and A.J. Heeger, Phys. Rev. B 36 (1987) 7537-7541.
[38] C.R. Fincher, M. Ozaki, A.J. Heeger and A.G. MacDiarmid, Phys. Rev. B 19 (1979) 4140-4148.
[39] J. Orenstein and G.L. Baker, Phys. Rev. Lett. 49 (1982) 1043-1046.
[40] J. Orenstein, Z. Vardeny, G.L. Baker, G. Eagle and S. Etemad, Phys. Rev. B 30 (1984) 786-794.
[41] J. Rothberg, T.M. Jedju, S. Etemad and G.L. Baker, Phys. Rev. Lett. 57 (1986) 3229-3232.
[42] J. Chen, A.J. Heeger and F. Wudl, Sol. State Comm. 58 (1986) 251-257.
[43] X. Wei, B.C. Hess, Z.V. Vardeny and F. Wudl, Phys. Rev. Lett. 68 (1992) 666-669.
[44] W. Graupner, J. Partee, J. Shinar, G. Leising and U. Scherf, Phys. Rev. Lett. 77 (1996) 2033-2036.
[45] K.F. Voss, C.M. Foster, L. Smilowitz, D. Mihailovic, S. Askari, G. Srdanov, Z. Ni, S. Shi, A.J. Heeger and F. Wudl. Phys. Rev. B 43 (1991) 51095118.
[46] J.L. Bredas, J.C. Scott, K. Yakushi and G.B. Street, Phys. Rev. B 30 (1984) 1023-1025.
[47] T.-C. Chung, H.H. Daufman, A.J. Heeger and F. Wudl, Phys. Rev. B 30 (1983) 702-710.
[48] K.C. Yee and R.R. Chance, J. Polym. Sci., Polym. Phys. Ed. 16 (1978) 431.
[49] L. Sebastian and G. Weiser, Phys. Rev. Lett. 46 (1981) 1156-1159.
[50] Y. Tokura, T. Koda, A. Itsubo, M. Myabayashi, K. Okuhara and A. Ueda, J. Chem Phys. 85 (1984) 99-104.
[51] T. Hasegawa, K. Ishikawa, T. Koda, K. Takeda, H. Kobayashi and K. Kubodera, Synth. Met. 43 (1991) 3151-3156.
[52] C.H. Lee, G. Yu, D. Moses and A.J.Heeger, Phys. Rev. B 49 (1994) 2396-2407.
[53] C.H. Lee, G. Yu and A.J. Heeger, Phys, Rev. B 47 (1993) 15543-15553.
[54] P. Bernier, S.Lefrant and G. Bidan, *Advances in Syntetic Metals: Twenty Years of Progress in Science and Technology*, Elsevier (1999) p. 123.
[55] V. Bulovic, S.R. Forrest, Chem. Phys. 210 (1996) 13-25.
[56] Jiangeng Xue, Soichi Uchida, Barry P. Rand Stephen R. Forrest, Appl. Phys. Lett. 84 (2004) 3013-3015.
[57] Wei-Bing Chen, Hai-Feng Xiang, Zong-Xiang Xu, Bei-Ping Yan, V. A. L. Roy, Chi-Ming Che and Pui-To Lai, Appl. Phys. Lett. 91 (2007) 191109.
[58] Max Shtein, Jonathan Mapel, Jay B. Benziger and Stephen R. Forrest, Appl. Phys. Lett. 81 (2002) 268-270.
[59] Meng-Sheng Liao and Steve Scheiner, J. Chem. Phys. 114 (2001) 9780-9791.
[60] L. Lozzi, S. Santucci, S. La Rosa, B. Delley and S. Picozzi, J. Chem. Phys. 121 (2004) 1883-1889.
[61] T. Schwieger, H. Peisert, M. S. Golden, M. Knupfer and J. Fink, Phys. Rev. B 66, (2002) 155207.
[62] M. Debe, R. Poirier and K. Kam, Thin Solid Films 197 (1991) 335.
[63] O. Berger, W.-J. Fischer, B. Adolphi, S. Tierbach, V. Melev and J. Schreiber, J. Mater. Sci.: Mater. Electron. 11, (2000) 331-346.

[64] Raffaele Guido Della Valle, Aldo Brillante, Elisabetta Venuti, Luca Farina, Alberto Girlando and Matteo Masino, Organic Electronics 5 (2004) 1-6.
[65] I.P.M. Bouchoms, W.A. Schoonveld, J. Vrijmoeth, T.M. Klapwijk, Synth. Met. 104 (1999) 175-178.
[66] Christine C. Mattheus, Anne B. Dros, Jacob Baas, Gert T. Oostergetel, Auke Meetsma, Jan L. de Boer and Thomas T.M. Palstra, Synth. Met. 138 (2003) 475-481.
[67] A. Vollmer, H. Weiss, S. Rentenberger, I. Salzmann, J.P. Rabe, N. Koch, Surface. Science 600 (2006) 4004-4007
[68] Oana D. Jurchescu, Jacob Baas and Thomas T.M. Palstra, Appl. Phys. Lett. 87 (2005) 052102.
[69] H.W. Kroto, J.R. Heath, S.C. O'Brien,R.F. Curl and R.E. Smalley, Nature 318 (1985) 162-163.
[70] M.D. Pace, T.C. Christidis, J.J. Yin and I. Milliken, J. Phys. Chem. Lett. 96 (1992) 6855-6858.
[71] Leif A.A. Pettersón, Lucimara S. Roman and Olle Inganäs, J. Appl. Phys. **86** (1999) 487-496.
[72] Franz Padinger, Roman S. Rittberger and Niyazi Sariciftci, Adv. Funct. Mater. 13 (2003) 85-88.
[73] T. Ogawa, K. Kuwamoto, S. Isoda, T. Kobayashi, N.Karl, Acta Cryst. B55 (1999) 123-130.
[74] B. Krause, A. C. Dürr, K. Ritley, F. Schreiber, H. Dosch and D. Smilgies, Phys. Rev. B 66 (2002) 235404.
[75] H. P. Wagner, V. R. Gangilenka, A. DeSilva, H. Schmitzer, R. Scholz and T. U. Kampen, Phys. Rev. B 73 (2006) 125323.
[76] A.J. Lovinger, S.R. Forrest, M.L. Kaplan, P.H. Schmidt and T.Venkatesan, J. Appl. Phys. 55 (1984) 476-482.
[77] M. Möbus, N. Karl and T. Kobayashi, J. Cryst. Growth 116 (1992) 495-504.
[78] Shuhei Tatemichi, Musubu Ichikawa, Toshiki Koyama and Yoshio Taniguchi, Appl. Phys. Lett. 89 (2006) 112108.
[79] P. R. L. Malenfant, C. D. Dimitrakopoulos, J. D. Gelorme, L. L. Kosbar and T. O. Graham, Appl. Phys. Lett. 80 (2002) 2517-2519.
[80] K.N. Narayanan Unni, Ajay K. Pandey and Jean-Michel Nunzi, Chem. Phys. Lett. 407 (2005) 95-99.
[81] N.S. Sariciftci, Primary Photoexcitatios in Conjugated Polymers (World Scientific Publ. Co., Singapore, 1998).
[82] Leif A.A. Petterssón, Lucimara S. Roman, and Olle Inganäs, J. Appl. Phys. 86 (1999) 487-496.
[83] J.J.M. Halls, K. Pichler, R.H. Friend, S.C. Moratti and A.B. Holmes, Appl. Phys. Lett. 68 (1996) 3120-3122.
[84] Klaus Petritsch, *Organic Solar Cell Arquitectures*, PhD thesis presented at the Technisch-Naturwissenschaftliche Fakultät der Technischen Universit¨at Graz (Austria) (2000) p.12.
[85] Frederik C: Krebs, Suren A. Gevorgyan and Jan Alstrup, J. Mater. Chem. 19 (2009) 5442-5451.
[86] D. Wöhrle and D. Meissner, Adv. Mater. 3 (1991) 129-138.
[87] C.W. Tang and A.C. Albrecht, J. Chem. Phys. 62 (1975) 2139-2149.
[88] C.H. Lee, G. Yu, D. Moses, K. Pakbaz, C. Zhang, N.S. Sariciftci, A.J. Heeger and F. Wudl, Phys. Rev. B 48 (1993) 15425.
[89] G. Zerza, C.J. Brabec, G. Cerullo, S. De Silvestri and N.S. Sariciftci, Synth. Met. 119 (2001) 637-638.
[90] C.W. Tang, Appl. Phys. Lett.48 (1986) 183-185.
[91] Wanli Ma, Cuiying Yang, Xiong Gong, Kwanghee Lee and Alan J. Heeger, Adv. Funct. Mat. 15 (2005) 1617-1622.
[92] Ajay K. Pandey, K.N.N. Unni and Jean-Michel Nunzi, Thin Solid Films 511-512 (2006) 529-532.
[93] Soichi Uchida, Jiangeng Xue, Barry P. Rand and Stephen R. Forrest, Appl. Phys. Lett. 84 (2004) 4218-4220.
[94] Kristian O. Silvester-Hvid, J. Phys. Chem. B 110 (2006) 2618-2627.

[95] Kevin M. Coakley, Yuxiang Liu, Michael D. McGehee, Karen L. Frindell and Galen D. Stucky, Adv. Funct. Mat. 13 (2003) 301-306.
[96] Kevin M. Coakley and Michael D. McGehee, Appl. Pys. Lett. 83 (2003) 3380-3382.
[97] Wendy U. Huynh Janke J. Dittmer and A. Paul Alivisatos, Science 295 (2002) 2425-2427.
[98] Evan L. Williams, Ghassen E. Jabbour, Qi Wang, Sean E. Shaheen, David S. Ginley and Eric Schiff, Appl. Phys. Lett. 87 (2005) 223504.
[99] Shawn Smith and Stephen R. Forrest, Appl. Phys. Lett. 84 (2004) 5019-5021.
[100] G. Hughes, D. Carty and A.A. Cafolla, Surf. Sci. 585 (2005) 90-96.
[101] Warren B. Jacksón and Nabil M. Amer, Phys. Rev. 25 (1982) 5559-5562.
[102] R.A. Street, *Hydrogenated Amorphous Silicon*, Cambridge Solid State Science Series (1991).
[103] K.V. Shalimova, *Physics of Semiconductors*, Ed. Mir (1975) p. 268.
[104] Jacques I. Pankove, *Optical Processes in Semiconductors*, Ed. Courier Dover (1975) p. 36.
[105] Shaji Varghese, Mercy Iype, E.J. Mathew and C.S. Menon, Mat. Lett. 56 (2002) 1078-1083.
[106] S. Ambily and C.S. Menon, Solid State Commun. 94 (1995) 485-487.
[107] M. M. El-Nahass, F.S. Bahabri and S.R. Al-Harbi, Egypt. J. Sol. 24 (2001) 11-19.
[108] R.A. Street, *Hydrogenated Amorphous Silicon*, Cambridge Solid State Science Series (1991), p. 87.
[109] R.A. Street, *Hydrogenated Amorphous Silicon*, Cambridge Solid State Science Series (1991), p. 88.
[110] Tamihiro Gotoh, Shuichi Nonomura, Satoshi Hirata, Shoji Nitta, Appl. Surf. Sci. 113/114 (1997) 278-281.
[111] J. Bertomeu, J. Puigdollers, J.M. Asensi and J. Andreu, J. of Non-crystalline Solids 164-166 (1993) 861-864.
[112] A. Guinier, *X-Ray Diffraction in Crystals, Imperfect Crystals and Amorphous Bodies*, General Publishing Company, Ltd. (1994) pag.124.
[113] S.M. Sze and Kwok N. NG., *Physics of Semiconductor Devices*, Wiley & Sóns (2007).
[114] T. Globus, H.C. Slade, M.S. Shur, M. Hack, Mat. Res. Soc. Proc. 336 (1994) 883.
[115] L. Goris, K. Haenen, M. Nesládek, P. Wagner, D. Vanderzande, L. De Schepper, J. D'Haen, L. Lutsen and J. V. Manca, J. Mat. Sci. 40 (2005) 1413–1418.
[116] L. Edwards and M. Gouterman, J. Mol. Spectr. 33 (1970) 292-310.
[117] B.H. Schechtmann, W.E. Spicer, J. Mol. Spectr. 33 (1970) 28-48.
[118] E. A. Lucia, F.D. Verdearme, J. Chem. Phys. 48 (1968) 2674-2681.
[119] Qiying Chen, Donghong Hu and Fuxi Gan, Physica B 212 (1985) 189-194.
[120] Meng-Sheng Liao, Steve Scheiner, J. Chem. Phys. 114 (2001) 9780-9791.
[121] Chhaya R. Kant , M.F. Srivastava and R.S. Rawat, Phys. Lett. A 239 (1998) 109-114.
[122] Pavel Janda, Torsten Krieg and Lothar Dunsch, Adv. Mat. 10 (1998)1434-1438.
[123] S. Heutz, A.J. Fergusón, G. Rumbles and T.S. Jones, Org. El. 3 (2002) 119-127.
[124] D.J. Gundlach, K.P. Pernstich, G. Wilckens, M. Grüter, S. Haas, B. Batlogg, J. of Appl. Phys. 98 (2005) 064502.
[125] R.J. Chesterfield, J.C. Mckeen, C.R. Newman, C.D. Frisbie, P.C. Ewbank, K.R. Mann, L. Miller. J. Appl. Phys. 95 (2004) 6396.

Acronym list

A: acceptor semiconductor
a-Si:H: hydrogenated amorphous silicon
Å: ångstrom
a_L: crystalline constant
a.u.: atomic units
BCP: bathocuproine
C_{60}: fullerene
CCl_4: carbon-tetrachloride
CdTe: cadmium telluride
$CHCl_3$: chloroform
CIGS: solar cells with structure $Cu(In:Ga)(S:Se)_2$
CT: charge-transfer exciton
CTC: Charge Transfer Complexe
CN-MEH-PPV: poly(2-methoxy-5-ethylhexyloxy-1,4-phenylenecyanovinylene)
CuPc: copper phthalocyanine
D: donor semiconductor
d_{hkl}: distance between crystalline planes (*d*-spacing)
DOS: density of states
DSC, DSSC: dye sensitized solar cells
E_+, E_-: energy of bonding and anti-bonding molecular orbital
EA: Electroabsorption
E_A: activation energy
E_c: bottom energy level of the conduction band
E_F: Fermi level
E_g, E_{og}: energy gap
E_v: top energy level of the valence band
ENDOR: Electron-nuclear Double Resónance
EQE: External Quantum Efficiency
ESR: Electro Spin Resónance
E_u: Urbach energy
F8BT: poly(9,9-dioctylfluorene-co-benzothidiazole)
FC-40: liquid Fluorinert^{TM}
FF: fill factor
FWHM: full width at half maximum
GaInP: gallium indium phosphide
GaAs: gallium arsenide
I_{max}: current at maximum power point
InP: indium phosphide
ITO: indium tin oxide
HOMO: highest occupied molecular orbital
HWCVD: hot wire chemical vapour deposition
I_{ds}= source-drain current
I_{ph}: photocurrent intensity
I_{sc}: short circuit current
ISC: inter system crossing transitions
k_F: Fermi wave-vector
k_{ISC} : rate constant for inter system crossing transitions
k_{nr} , $k_{nr}^{'}$: rate constants for optical non-radiative transitions

k_r , $k_r^{'}$: rate constants for optical radiative transitions
L: transistor channel length
LCAO: Linear Combination of Atomic Orbitals
LUMO: lowest unoccupied molecular orbital
Me-Ptcdi: *N,N'*-dimethylperylene-3,4,9,10-dicarboxyimide
MOCVD: metal organic chemical vapour deposition
MDMO-PPV: poly[2-metoxy-5-(3',7'-dimethyl-octyloxy)-p-phenylene vinylene]
n.c.: normal air and light conditions
NIR: near infra-red
$NOBF_4$: nitrosónium tetrafluoroborate
o-DCB: 1,2-dichlorobenzene
OLED: organic light emitting device
OMC: organic molecular crystals
ODMR: Optically Detected Magnetic Resónance
OPV: organic photovoltaics
OTFT: organic thin film transistor
p: orbital type *p*
P_{IN}: incident power
p_z: orbital type *p* oriented along *z* direction
P3HT: poly-3-hexylthiophene
PCBM: [6,6]-phenyl–C_{61}–butyric acid methyl ester
PDA: polydiacetilene
PDS: Photothermal Deflection Spectroscopy
PECVD: plasma enhanced chemical vapour deposition
PEDOT:PSS: poly(3,4-ethylenedioxythiphene) : poly(styrenesulfonate)
PFB: poly(9,90-dioctylfluorene-co-bis-N,NO-(4-butylphenyl)-bis-N,NO-phenyl-1,4-phenyldiamine)
PIA: Photoinduced Absorption Spectroscopy
PPP: polyparaphenylene
PPV: poly(phenylene vinylene)
CSS: charge separated states
PID: proportional-integrate-differential
PL: photoluminescence
PTCDA: perylene-3,4,9,10-tetracarboxylic dianhydride
PTCDI: 3,4,9,10-perylenetetracarboxylic diimide
PTCDI-C_8: *N,N*-dioctyl-3,4,9,10-perylenetetracarboxylic diimide
PTCDI-C_{13}: *N,N*-ditridecyl-3,4,9,10-perylenetetracarboxylic diimide
Q: charge of the particle
R_s: series resistance
R_{sh}: shunt resistance
s: spin of the particle
S_n: singlet states
SCLC: space charge limited current
SiO_2: silicon oxide
sp^1,sp^2,sp^3: type of hybridization between orbitals *s* and *p*
SSH: Hamiltonian of A.J. Heeger, J.R. Schrieffer and W.-P. Su
TFL: trap filled limit
TFSCLC: trap filled space charge limited current
TiO_2: titania
T_n: triplet states

TFT: thin film transistor
UVO: ultraviolet generated ozone
V_{gs}: gate-source voltage
V_{max}: voltage at maximum power point
V_{oc}: open circuit voltage
V_t: threshold voltage
W: transistor channel width
XRD: x-ray diffraction
ZnO: zinc oxyde
ZnPc: zinc phtalocyanine
α: absorption coefficient
σ, π: types of chemical bonds
β: coulombic integral
η: efficiency of a photovoltaic system
η_A: efficiency of the absorption process
η_{CC}: efficiency of the charge collection process
η_{CT}: efficiency of the dissociation process
η_{ED}: efficiency of the diffusion process
η_{IQE}: internal quantum efficiency
γ: exchange (or resónance) integral
Ψ_+, Ψ_-: bonding and anti-bonding molecular orbital

Table list

Figure list

Resum en català

1. Introducció

Els semiconductors orgànics han atret molt l'atenció en les últimes dues dècades com a materials que pertanyen a una categoria nova, caracteritzada per propietats químiques i mecàniques completament diferents de les dels materials tradicionals com el silici. La investigació sobre els semiconductors orgànics va començar als anys 60 i 70 amb els treballs de Alan J. Heeger, que va guanyar el premi Nobel l'any 2000 pels seus descobriments sobre la conductivitat del poliacetilè, i de D. E. Weiss amb el seu treball sobre el polipirrol. A dia d'avui aquests materials s'estan aplicant comercialment en la tecnologia OLED (Organic Light Emitting Diode) i presenten un bon potencial en el camp dels transistors en capa prima (Thin Film Transitor - TFT), mentre que encara falta temps per veure'ls aplicats comercialment al fotovoltaic. Tanmateix, empreses com Konarka i Solarmer han anunciat recentment que estarien començant una producció de mòduls fotovoltaics orgànics.

Martin A. Green i els seus col·laboradors publiquen periòdicament unes taules que contenen els valors mes alts d'eficiència obtinguts amb cadascun dels diferents tipus de cèl·lules solars. Actualment les tipologies de tecnologia fotovoltaica que es poden trobar a nivell comercial són principalment de tipus inorgànic. Dins d'aquesta categoria hi ha les cèl·lules de silici cristal·lí (amb una eficiència del 25%), multicristal·lí (20.4%) i amorf (9.5%). A més a més, hi ha les de combinacions d'elements dels grups III i V de la taula periòdica com ara les de GaAs (26.1%) i les d'InP (22.1%) i finalment les de tipus calcogenita com les CIGS [$Cu(In:Ga)(S:Se)_2$] (19.4%) i les de CdTe (16.7%). Les heterounions de més d'una cèl·lula també han donat bons resultats com per exemple en el cas de les de GaInP/GaAs (30.3%) i les GaInP/GaAs/Ge (32.0%). A part de la tecnologia inorgànica, en els últims anys s'han desenvolupat cèl·lules que funcionen amb un mecanisme electroquímic com les cèl·lules sensibilitzades per un pigment (Dye Sensityzed Solar Cells - DSC). La capa activa d'aquestes cèl·lules està formada per un òxid de titani porós, un pigment que absorbeix la llum i un electròlit i han obtingut una eficiència del 10.4%. Finalment en la categoria de les cèl·lules completament orgàniques hi ha les de polímer i les de molècula petita. Aquest tipus de cèl·lula solar és el més nou i encara no ha fet el salt a una aplicació comercial. El record de eficiència actual és del 7.9% amb una cèl·lula polimèrica i el potencial dels materials orgànics fa pensar en un futur prometedor.

Les prestacions menys eficients dels dispositius orgànics indiquen que encara queda molta feina per fer en l'àmbit del desenvolupament dels dispositius mateixos però també en l'àmbit dels

materials. Els resultats no completament satisfactoris són deguts a la baixa mobilitat dels portadors de carrega (10^{-8}-10^{-2} $cm^2V^{-1}s^{-1}$) i la curta longitud de difusió dels excitons (50-100 nm). Tanmateix en el cas del pentacè s'ha observat una mobilitat de portadors de 0.7 $cm^2V^{-1}s^{-1}$, un valor semblant al del silici amorf. A part d'això, els materials orgànics presenten tota una sèrie d'avantatges que pot ser resumida en els següents punts:

- Les tècniques de producció ofereixen gran varietat de possibilitats, flexibilitat i, en alguns casos, baix cost. A més a més ofereixen la possibilitat d'augmentar fàcilment la superfície de treball.
- Els mòduls orgànics poden ser flexibles, lleugers i, per això, fàcilment integrables.
- La gran varietat de materials existents i de materials nous que es poden sintetitzar dóna a aquesta tecnologia un gran potencial de millora pel futur.

La naturalesa ha desenvolupat mecanismes per aprofitar la energia solar i utilitzar-la per dur a terme processos biològics. S'ha pogut calcular que el procés de conversió de l'energia fotònica en energia química, conegut com a fotosíntesi clorofíl·lica, té una eficiència del 20-25%. Aquest mecanisme consisteix en l'absorció de la llum per part d'una antena constituïda per pigments i que condueix l'energia fins al centre on els portadors són dissociats. El potencial químic que es genera és el que mou les reaccions químiques necessàries per dur a terme els processos cel·lulars a les plantes. La fotosíntesi és vista com un exemple natural interessant d'aprofitament de l'energia solar per la seva complexitat, la seva eficiència i la seva estabilitat.

2. Introducció general a la teoria dels semiconductors orgànics

Dins dels materials semiconductors orgànics es distingeixen dues categories depenen de l'estructura de la molècula que els composa: els polímers i els materials de molècula petita. En tot cas, tots aquests materials tenen en comú una estructura que presenta alternança entre enllaços senzills i enllaços dobles. Aquesta configuració, deguda a la hibridació dels àtoms de carboni sp^2, porta a que cadascun dels àtoms de carboni tingui un electró deslocalitzat en tota la molècula. Fonamentalment el mecanisme de transport de càrrega en els materials orgànics es veu així fet possible per la presencia d'electrons deslocalitzats.

Per estudiar els materials moleculars es fa us de la teoria coneguda com a teoria de la combinació lineal dels orbitals atòmics (*Linear Combination of Atomic Orbitals - LCAO*). Per calcular l'energia que els electrons tenen en el sistema es consideren els orbitals atòmics dels àtoms

que composen la molècula i es combinen linealment per obtenir orbitals moleculars. D'aquesta manera es formen bandes energètiques com passa pels sòlids atòmics, com per exemple el silici, una comparable a la banda de valència i una altra a la banda de conducció. El nivell energètic ocupat més alt, en la banda de valència, en anglès és conegut com *Highest Occupied Molecular Orbital* (*HOMO*), mentre que el nivell no ocupat més baix, en la banda de conducció, es diu *Lowest Unoccupied Molecular Orbital* (*LOMO*). La diferència entre aquests dos nivells és el *gap* òptic del material (E_g) i defineix les seves propietats d'absorció. Com passa pels materials inorgànics, per poder tenir portadors de càrrega lliures de circular s'ha d'excitar un electró des de la banda de valència a la de conducció. Durant els darrers anys s'han fet molt estudis per entendre exactament quins són els mecanismes que regulen la generació de portadors de càrrega i la seva naturalesa però encara queden molts punts per aclarir.

Diferentment del que passa amb els semiconductors inorgànics, la fotogeneració de portadors de càrrega passa a través de la formació d'especies excitades, la naturalesa de les quals pot canviar segons el material.

S'ha fet una distinció entre materials polimèrics que tenen un estat fonamental degènere i els que tenen un estat fonamental no degènere. En els primers després de la fotoabsorció es generen partícules conegudes com solitons, afavorides per la possibilitat que l'estructura té d'intercanviar enllaços senzills i dobles per formar dos tipus d'estructures energèticament equivalents (degeneres). Els solitons poden ser vistos com la frontera dins dues fases: una fase *A* i una fase *B* que es distingeixen per la posició dels enllaços dobles. El poliacetilè es un exemple de polímer on les excitacions primàries estables són els solitons.

En canvi, en els polímers on no hi ha degeneració de l'estat fonamental, les dues estructures no són energèticament equivalents i els solitons no són estables. En aquests materials solitons i antisolitons es formen per donar origen a polarons i bipolarons. Materials com poli(fenilè vinilè) (PPV) and poliparafenilè (PPP) pertanyen a aquesta categoria de polímers.

Els materials de molècula petita formen una categoria a part perquè en ells es reconeix que les partícules que es formen són els excitons: parelles electró-forat que cal dissociar per poder obtenir portadors de càrrega.

Segons el tipus de partícula, cadascuna de les descrites anteriorment poden portar càrrega i/o spin amb el qual la interacció amb els camps elèctric i magnètic pot canviar. Diverses són les proves científiques que indiquen la presencia de solitons, polarons i excitons en un material. Tanmateix, com s'ha dit abans, encara queden molts dubtes pel que fa a la naturalesa de les excitacions primàries que es formen en els primers instants en un material il·luminat. En la major part dels casos la literatura científica considera que en tots els materials primerament es formen excitons i

que després aquest poden dissociar-se per donar origen a portadors separats (per exemple polarons). En tot cas, s'ha observat que associats amb aquestes partícules van nivells energètics que es situen en el gap del material. La presència de nivells nous comporta l'aparició de transicions òptiques, abans no existents, que involucren valors d'energia que pertanyen al infraroig proper. Aquests nivells, que apareixen picosegons després de l'absorció de la llum, són responsables de les propietats òptiques no linears dels materials estudiats. Les peculiaritats que caracteritzen a nivell òptic els materials semiconductors s'afegeixen a les ja conegudes en molts altres. Quan un material es excitat per una llum amb energia igual o superior al seu gap òptic, un estat singlet excitat es forma (S_1). L'energia absorbida es pot lliurar mitjançant una sèrie de mecanismes que competeixen entre ells: recombinació radiativa i/o no radiativa del estat de singlet ($S_1 \rightarrow S_0$), formació d'estats de triplet (T_1), recombinació radiativa i/o no radiativa des de l'estat de triplet al estat fonamental de singlet ($T_1 \rightarrow S_0$) i finalment formació de estat de carrega separada (*Charge Separated State - CSS*). La recombinació radiativa de l'estat de singlet és el fenomen anomenat com fluorescència, mentre que la recombinació radiativa del estat de triplet porta al fenomen de la fosforescència.

Aquesta tesi doctoral està focalitzada en l'estudi d'alguns semiconductors de molècula petita dipositats per evaporació tèrmica en buit. Els materials són el pentacè i la ftalocianina de coure (CuPc) com semiconductors de tipus *p* i ful·lerè i dos perilens (PTCDA i PTCDI-C_{13}) com semiconductors de tipus *n*. Aquests materials s'han escollit per les seves propietats que n'han fet materials interessants per a l'aplicació en dispositius electrònics com les cèl·lules fotovoltaiques i els transistors de capa prima. Per exemple, el pentacè ha mostrat una mobilitat dels forats propera a la del silici amorf (1 cm^2/Vs).

3. Aspectes tecnològics

Els mecanismes de dopatge d'un semiconductor orgànic són quatre:

- dopatge químic
- dopatge electroquímic
- fotodopatge
- dopatge interficial

En el primer cas s'introdueixen portadors de càrrega al material mitjançant reaccions químiques oxidatives per obtenir dopatge de tipus *p*, i reductives pel dopatge de tipus *n*. En segon cas les

reaccions d'oxidació o reducció són controlades per via electroquímica. Aquest procés permet un control molt millor del nivell de dopatge. El mecanisme de fotodopatge consisteix en la generació de portadors de càrrega com a conseqüència de la irradiació lluminosa del material. L'últim mecanisme es duu a terme per injecció de portadors des dels elèctrodes.

El mecanisme de generació de corrent elèctric en una cèl·lula solar orgànica es realitza en quatre passos:

1. absorció de fotons i generació d'excitons
2. difusió dels excitons
3. dissociació dels excitons amb generació de portadors
4. col·lecció dels portadors en els elèctrodes

Per cadascun d'aquests passos es defineix un valor d'eficiència: η_A, η_{ED}, η_{CT} i η_{CC}, respectivament. El producte de totes les eficiències es l'eficiència total del dispositiu η.

Els semiconductors orgànics poden ser dipositats en capa prima per moltes tècniques diferents segon les seves propietats químiques. En el cas de materials de molècula petita, la majoria del quals no pot ser dissolta en cap dissolvent orgànic, la tècnica més comuna és l'evaporació tèrmica en buit. Els polímers, en canvi, poden ser processats en solució utilitzant alguna de les moltes tècniques que existeixen i de les quals l'*spin-coating*, l'*screen printing* i l'*inkjet printing* en són uns exemples. La possibilitat de treballar amb materials dissolts també ofereix la oportunitat d'utilitzar màquines *roll-to-roll*: equipaments que permeten dipositar materials en capa prima per damunt d'un substrat flexible enrotllat i fet moure dins de l'unitat de dipòsit. Aquest tipus de procés de fabricació té l'avantatge de poder produir superfícies grans en poc temps, reduint el costos de producció.

Al llarg dels darrer anys s'han desenvolupat diferents estructures de les cèl·lules solars amb l'objectiu de millorar les seves prestacions. Les geometries que s'han estudiat en ordre de temps són tres:

1. cèl·lula de monocapa
2. cèl·lula de doble capa
3. cèl·lula d'heterounió

A la cèl·lula de monocapa, un únic semiconductor, dipositat entre els dos elèctrodes, fa contacte òhmic amb un dels conductors i contacte Schottky amb l'altre. D'aquesta manera s'obté rectificació i el dispositiu funciona com un diode. En aquest tipus de dispositiu els excitons fotogenerats en el semiconductor han de moure's fins arribar al contacte Schottky on dissociar-se. La generació de portadors depèn del camp elèctric i el *fill factor* és de mala qualitat. A més les probabilitats de recombinació per a tornar a formar excitons són molt altes.

La introducció d'una segona capa semiconductora per fer una heterunió porta a tenir rectificació entre els dos semiconductors. Els excitons es dissocien en la interfície entre els semiconductors i els dos portadors de càrrega queden en dues fases diferents. El mecanisme de transferència dels portadors des d'un semiconductor a l'altre és conegut com transferència de càrrega ultra ràpida i és favorable si l'energia d'ionització del material donador és inferior a la suma entre afinitat electrònica de l'altre i l'energia de dissociació de l'excitó. S'ha vist que d'aquesta manera les probabilitats de recombinació són menys altes que en el cas precedent ja que depèn només de la densitat de trampes. El *fill factor* dels dispositius fets amb aquesta geometria és millor.

L'estructura que ha donat els millors resultats és la que preveu barrejar físicament els dos semiconductors per augmentar la superfície d'interfície entre els dos: la coneguda com heterounió en volum. D'aquesta manera s'optimitza al màxim la dissociació dels excitons ja que així tindran poc recorregut per arribar a l'altre semiconductor.

S'han elaborat altres estratègies per a millorar les prestacions de les cèl·lules com ara la selecció d'un dissolvent adequat, l'ús d'additius, l'optimització dels paràmetres de dipòsit, tractaments amb temperatura, l'utilització de polímers que tinguin part donadora i part acceptadora en la mateixa molècula o de nanopartícules.

També s'han elaborat dispositius híbrids amb una unió entre silici i un material orgànic o entre orgànic i nanopartícules inorgàniques. Tanmateix el cas més important és el de les cèl·lules definides com *dye sensitized solar cells* (DSSC), la capa activa de les quals està formada per òxid de titani porós, un pigment que absorbeix la llum i un electròlit.

4. Experimental

4.1 Dipòsit de capes primes

Les capes primes dels semiconductors orgànics que s'han estudiat en aquest treball s'han dipositat mitjançant la tècnica de l'evaporació tèrmica en buit. S'han utilitzat dos equips disponibles

als laboratoris del Departament d'Enginyeria Electrònica de la Universitat Politècnica de Catalunya. Un equip, de la marca Leybold (model Univex 300), està dedicat al dipòsit dels materials orgànics i està equipat amb dues fonts d'evaporació ceràmiques, dos sistemes PID (*Proportional-Integrative-Derivative*) pel control de la temperatura, una bomba mecànica i una turbomolecular per a la generació del buit. El sistema també té integrat un mesurador de gruix de cristall de quars calibrat pels diferents materials.

L'altre sistema s'utilitza pel dipòsit dels metalls per realitzar el contactes dels dispositius. També en aquest cas dues bombes, una mecànica i un altra turbomolecular, s'utilitzen per fer el buit. A diferència de l'altre sistema d'evaporació, només hi ha una font d'evaporació de molibdè sense control de temperatura. Tampoc no hi ha controlador de gruix.

4.2 Tècniques de caracterització òptica

La tècnica de caracterització principal, entre les emprades en aquest treball, és de tipus òptic i és l'espectroscòpia per desviació fototèrmica (*Photothermal Deflection Spectrocopy - PDS*). L'equipament va ser montat en el laboratori i està compost per una font de llum halògena, un trossejador, un monocromador, una cubeta de quars plena d'un líquid transparent (Fluorinert FC-40^{TM}) on es posa la mostra, un làser (635 nm), una sèrie de lents per a focalitzar la llum monocromàtica i el làser, un sensor de posició, un amplificador lock-in i un ordinador. Amb aquest sistema es pot mesurar en un interval entre 400 i 2000 nm, incloent el espectre de la llum visible (VIS) i part de l'infraroig proper (*near infrared - NIR*).

Tal tècnica té com a finalitat la detecció de l'absorció de baix nivell en els materials i es basa en la il·luminació d'una mostra submergida en un líquid transparent i amb propietats tèrmiques adequades. La llum blanca incident passa a través del monocromador i és polsada per un trossejador mecànic. Per efecte de l'absorció en el material, i de la successiva excitació de portadors i la seva recombinació no radiativa, es genera calor a la capa, que es transmès al líquid causant l'aparició d'un gradient de temperatura i, consegüentment, d'índex de refracció. Al mateix temps un làser es fa passar a prop de la superfície de la mostra i en direcció paral·lela a ella. El làser és desviat per efecte de l'índex de refracció de manera polsada amb la mateixa freqüència aplicada pel trossejador a la llum incident. L'angle de desviament del làser és proporcional a l'absorció en la mostra i es mesurat mitjançant un sensor de posició. L'efecte de la desviació per un canvi d'índex de refracció és conegut com a efecte mirall.

Aquesta tècnica permet mesures d'absorció amb una sensibilitat molt superior a la que es pot obtenir amb tècniques tradicionals com la transmitància òptica. D'aquesta manera és possible mesurar l'absorció deguda a la presencia de defectes als quals van associats nivells energètics

localitzats en el gap del material semiconductor. Les dades obtingudes a través de l'amplificador lock-in, calibrades amb mesures de transmitància, permeten calcular el coeficient d'absorció del material (α). Des del coeficient d'absorció és possible calcular paràmetres del material importants com el seu gap òptic i el front d'Urbach, normalment calculats per materials inorgànics com el silici. En aquest cas, per realitzar el càlcul s'han utilitzat les relacions conegudes pels materials inorgànics perquè no s'en coneixen d'específiques dels orgànics.

Per a les mesures de transmitància s'ha utilitzat un equip de Ocean Optics amb una font de llum blanca, un sistema de fibres òptiques per conduir la llum fins a la mostra i des d'ella al detector que està format per una sèrie de díodes que capten les diferents longituds d'ona. Com s'ha dit abans, la transmitància òptica és una tècnica que s'ha empleat de suport al PDS pel calibratge de les mesures però també per calcular l'espectre complet del coeficient d'absorció. S'han efectuat mesures de transmitància de totes les mostres per obtenir l'espectre de transmitància entre 400 i 1000 nm i poder utilitzar les dades en el càlcul del coeficient d'absorció. La tècnica PDS és sensible en la regió sub-gap mentre que la transmitància òptica en la regió d'alta absorció. L'espectre complet de l'alfa s'ha obtingut unint les dues mesures agafades en les respectives parts. Per fer això s'ha hagut de calcular un factor de calibratge per l'espectre PDS que té la característica de no ser absolut.

4.3 Altres tècniques de caracterització

Per estudiar la qualitat de l'estructura de les capes dipositades se les ha caracteritzat per difracció de rajos X amb la configuració Bragg-Brentano. En aquesta configuració l'angle incident i el de reflexió s'han mantingut iguals, respecte a la superfície de la mostra, i es detecten les reflexions provocades per les famílies de plans cristal·logràfics paral·lels a la mateixa superfície. S'ha utilitzat aquesta tècnica per definir si les mostres dipositades per evaporació tenien estructura amorfa, en qual cas no haurien de mostrar cap pic de difracció, o policristal·lina, on s'haurien d'enregistrar els pics de difracció típics del material. S'han comparat els espectres de rajos X obtinguts amb la literatura per poder identificar les famílies de plans cristal·logràfics. S'ha calculat un ajust dels pics, quan n'hi havien, mitjançant una equació de Voigt, formada per una suma de l'equació de Lorentz i de la de Gauss. Amb les dades de l'ajust s'han obtingut la posició angular del pic i la seva amplitud a mitja altura. Finalment s'ha empleat l'equació de Scherrer per a calcular les dimensions dels cristalls que composaven les mostres.

Un altre tipus de caracteritzacions que s'ha utilitzat en aquest treball són les mesures elèctriques dels dispositius. S'han fabricat i caracteritzat elèctricament transistors de capa prima mesurant la

seva característica de sortida (corrent entre *source* i *drain* en funció de la tensió entre els mateixos contactes) i la característica de transferència (corrent entre *source* i *drain* en funció de la tensió entre *gate* i *source*). També s'han realitzat i caracteritzat díodes mesurant la característica I-V (corrent en funció de la tensió aplicada als elèctrodes) del dispositiu fent una mesura sense llum i una altra amb llum amb una potència d'1 sol. Aquestes mesures permeten calcular paràmetres com el corrent de curt circuit, la tensió en circuit obert, el *fill factor* i l'eficiència.

Per totes aquestes mesures s'ha fet servir un equipament instal·lat als laboratoris de la Universitat Politècnica de Catalunya.

5. Anàlisi dels materials

En aquesta secció es presenten els resultats obtinguts de la caracterització dels materials dipositats en capa prima per evaporació i els efectes dels tractaments tèrmics realitzats sobre ells.

5.1 Caracteritzacions de capes primes

Per a cadascun dels materials s'han dipositat capes amb dues combinacions de paràmetres:

Capes gruixudes:

- gruix: 1 μm
- temperatura del substrat: ambient
- ritme de dipòsit: 3 Å/s
- pressió inicial: $6 \cdot 10^{-4}$ Pa

Capes primes:

- gruix: 100 nm
- temperatura del substrat: ambient
- ritme de dipòsit: 0.4 Å/s
- pressió inicial: $6 \cdot 10^{-4}$ Pa

S'han calculat els coeficients d'absorció dels cinc materials trobant que en tots els casos es composen de tres regions: una regió d'alta absorció, associada amb transicions òptiques de banda a banda, una regió exponencial, associada amb cues de banda, i finalment una regió d'absorció baixa, relacionada amb la presència de defectes que causen absorcions per energies inferiors a la del gap del material. Aquesta estructura de l'espectre és semblant a la que s'ha observat pel silici amorf

hidrogenat. Les mesures de difracció de rajos X han mostrat que tots els materials s'han dipositat amb una estructura policristal·lina menys el ful·lerè, l'espectre del qual no mostra cap pic de difracció, indicant que el material és probablement amorf. Com a conseqüència, s'ha calculat el gap òptic mitjançant l'equació general per les transicions directes en un semiconductor en tots els casos excepte pel ful·lerè, pel qual s'ha utilitzat l'equació de Tauc, apropiada per materials amorfs. També s'ha calculat el valor de l'energia d'Urbach trobant que el ful·lerè tenia el valor més alt, confirmant la naturalesa amorfa del material. A la taula següent es mostren els valors del gap, comparats amb valors de literatura calculats per altres mètodes, i de l'energia d'Urbach:

	$E_g^{PDS/T}$ (eV)	$E_g^{fig.3.7}$ (eV)	E_u (meV)
Pentacè	1.73	2.1	37
CuPc	1.64	1.7	53
Ful·lerè	1.68	1.7	63
PTCDA	2.11	2.6	46
PTCDI-C_{13}	2.00	2.0	48

Taula 1. Valors del gap òptic calculats ($E_g^{PDS/T}$), comparats amb valors de literatura ($E_g^{fig.3.7}$), i valors de l'energia d'Urbach.

Les mesures realitzades sobre les mostres més primes han mostrat que en aquests casos els defectes superficials tendeixen a ser més evidents i a fer pujar l'absorció sub-gap.

5.2 Efectes de la degradació sobre les propietats òptiques

S'han exposat algunes mostres d'1 μm a degradació per il·luminació directa amb una potència d'un sol i altres a condicions normals de llum i temperatura (abreviat en *c.n.*). S'ha observat un increment de l'absorció sub-gap, relacionada amb defectes, en el pentacè i el ful·lerè il·luminats amb llum directa. El segon mostra alteracions també en condicions normals, encara que d'intensitat menor. A més, en el cas del pentacè degradat amb llum s'ha observat l'aparició d'un pic d'absorció localitzat en 1.28 eV l'origen del qual no coneixem. Canvis de menor o inexistent entitat s'ha observat en la CuPc, el PTCDA i el PTCDI-C_{13}, mostrant que aquests materials són més estables fins i tot quan són irradiats amb llum directa.

6. Heterounions en volum

S'han dipositat capes compostes per una barreja de dos materials, formant totes les combinacions possibles entre un semiconductor tipus *p* i un tipus *n*, amb proporció 1:1. Les condicions de dipòsit han estat les següents:

- gruix: 1 μm
- temperatura del substrat: ambient
- ritme de dipòsit: 3 Å/s (1.5 + 1.5 Å/s)
- pressió inicial: $6 \cdot 10^{-4}$ Pa

6.1 Caracteritzacions de les heterounions en volum

S'han caracteritzat les propietats òptiques i estructurals de les barreges com s'ha fet pels materials purs i s'han comparat els espectres. En general s'han obtingut espectres del coeficient d'absorció que contenen les característiques dels materials purs que predominen en cada regió. En alguns casos s'ha pogut notar un eixamplament de la regió d'alta absorció que ha resultat ser la suma de les registrades pels materials separats. Absorcions noves en la regió sub-gap han aparegut en els casos de la CuPc i el pentacè dipositats amb el ful·lerè i el PTCDA. S'han mesurat espectres de rajos X i en tots els casos analitzats no s'han observat pics de difracció o s'han evidenciat petites bandes d'intensitat molt petita comparada amb la dels pics en els materials sols. Aquests resultats han portat a concloure que els materials coevaporats tenen tendència a dipositar-se amb estructura amorfa.

També s'han calculat els gaps òptics de les barreges i els valors d'energia d'Urbach. Donats els resultats de les caracteritzacions per rajos X, pel primer paràmetre s'ha empleat l'equació de Tauc pels materials amorfs. Pel que fa al gap, els valors obtinguts en el cas d'utilitzar pentacè com a semiconductor tipus *p* no són gaire diferents dels valors calculats pels materials purs; en canvi, en les mostres que contenen ftalocianina de coure com a semiconductor tipus *p* el gap és clarament més baix i, a més a més és nota l'aparició d'un altre gap a energies molt inferiors. En referència a l'energia d'Urbach, com era d'esperar, els valors de les barreges són en general més alts degut a què a les mostres hi ha un grau major de desordre i, com a conseqüència, de defectes. Tanmateix, dins de totes les mostres produïdes, dues en són excepció: la barreja de pentacè respectivament amb PTCDA i PTCDI-C_{13}.

6.2 Tractaments tèrmics

En la segona part de l'experiment sobre les heterounions s'han efectuat tractaments tèrmics a les mostres per comprovar si podien tenir com a efecte millorar la seva estructura. S'han efectuat els tractaments en un criòstat amb buit generat per una bomba mecànica i amb un temperatura que depenia dels materials: 100ºC per a les mostres que contenien pentacè, que s'evapora a 130-140ºC, i 200 i 250ºC per les mostres amb CuPc, que s'evapora a 300ºC. S'ha calculat un ajust dels primers pics per tots els espectres per verificar s'hi havia canvis de posició angular i d'amplitud, la qual està connectada amb la dimensió dels cristalls presents a la mostra. En el cas de les barreges que contenien pentacè com a semiconductor tipus *p* no s'han notat gaires canvis, mentre que en el cas de la ftalocianina han aparegut alguns pics de difracció típics dels materials. En aquestes mostres, de fet, el tractament a 200ºC ha causat l'aparició de pics de difracció de la fase α en la CuPc, mentre que el tractament a 250ºC ha causat un canvi a la fase β, acompanyat per un augment d'intensitat i una disminució de l'amplitud, el que indica un augment de les dimensions dels cristalls.

8. Conclusions

1. El dels semiconductors orgànics ha emergit com a categoria nova i prometedora de materials per aplicacions electròniques. Mentre que molta feina queda per fer per millorar la nostra comprensió sobre els mecanismes que regulen el seu funcionament, tals materials ja han atret molta atenció per les seves propietats peculiars. Els trets més interessants que els semiconductors orgànics mostren són la flexibilitat, la lleugeresa i la possibilitat de dipositar-los en processos de fabricació de baix cost.

2. Entre els semiconductors orgànics dos grans grups es poden distingir depenent del tipus de molècules: polímers i molècules petites. En aquest treball la segona categoria de materials s'ha estudiat per utilitzar-la en cèl·lules solars i transistors de capa prima. L'elecció d'aquest tipus de materials estava motivada per l'experiència acumulada pels grups d'investigació que col·laboren en aquesta investigació en tècniques de dipòsit com l'evaporació tèrmica en buit. Tal tècnica de dipòsit permet un bon control del gruix, la morfologia i unes altres característiques de les capes primes. Com a resultat, l'evaporació tèrmica permet dipositar capes de bona qualitat amb propietats adequades per a la conducció elèctrica.

3. S'han dipositat i s'han caracteritzat capes primes d'un grup de semiconductors de molècula petita. Els materials analitzats són pentacè, ftalocianina de coure (CuPc), ful·lerè (C_{60}), PTCDA i PTCDI-C_{13}. Els dos primers són materials donadors, que significa que són bons conductors de forats i treballen com a semiconductors de tipus *p*. Els altres tres materials són bons conductors d'electrons i treballen com a semiconductors de tipus *n*. Tals materials han estat caracteritzats per unes quantes tècniques entre les quals: l'Espectroscòpia de Desviació Tèrmica (PDS) ha jugat un paper essencial. Mitjançant aquesta tècnica s'ha calculat el coeficient d'absorciò de cada material, juntament amb el seu gap òptic i l'energia d'Urbach. Els espectres del coeficient d'absorbiment suggereixen que es pot fer un paral·lelisme amb el silici amorf hidrogenat, la forma de l'espectre del qual està determinat per la presència d'estats localitzats en el gap i estats de cua de banda. S'han comparat els resultats del gap òptic, en els límits de disponibilitat, amb altres en la literatura trobant un bon acord entre les dades. Les capes també han estat caracteritzades per difracció de rajos X amb el resultat que tots els materials, amb l'excepció del ful·lerè, mostren tendència a formar sòlids policristal·lins quan estan dipositats en les condicions descrites. El ful·lerè es caracteritzat per tenir una estructura amorfa.

4. S'ha realitzat un estudi sistemàtic de la degradació en els semiconductors mesurant els espectres d'absorció de tots els materials. S'han caracteritzat les mostres òpticament immediatament després del dipòsit i de passar un temps establert en contacte amb aire (un conjunt d'ells) i sota il·luminació (un altre conjunt). Tal experiment tenia l'objectiu de descobrir si ocorre un canvi en les propietats òptiques del semiconductor orgànic quan ha estat exposat a agents potencialment oxidants. El CuPc i el PTCDA s'han revelat com els materials més estables, ja que els seus espectres del coeficient d'absorció es mantenen inalterats fins i tot després d'unes quantes setmanes de tractament de degradació. Al contrari, el pentacè i el ful·lerè presenten un augment en l'absorció a la regió sub-gap. Aquest resultat indica que els defectes que hagin aparegut als materials podrien deteriorar les seves propietats elèctriques. L'espectre del PTCDI-C_{13} pateix canvis en el seu perfil i l'explicació de tal fenomen queda encara per aclarir.

5. Un estudi sistemàtic similar s'ha realitzat per tots els parells possibles entre un donador i un acceptador. Els resultats obtinguts mostraven que, coevaporades, les molècules tenen generalment més dificultats per ordenar-se en una estructura ordenada. Les barreges que

contenen CuPc es tornen més ordenades quan són sotmeses a tractaments tèrmics a la temperatura de 200ºC. Si s'escalfa a 250ºC l'ordre millora fins i tot més i, com esperat, hi ha l'aparició del polimorf β del ftalocianina. L'estudi de degradació realitzat sobre les heterounions indica que, en general, una mescla entre dos materials estables és també estable. Com a resultat, la barreja més estable és el compost de CuPc amb PTCDA.

APENDIX A - Dispositius orgànics

Els primers dispositius orgànics que s'ha realitzat als laboratoris són transistors en capa prima (*TFTs*) de PTCDI-C_{13} i díodes de ftalocianina (CuPc). S'ha dut a terme la fabricació dels dispositius evaporant tant el semiconductor com els contactes per després treure'ls a l'aire per a la caracterització elèctrica.

A.1 TFTs de PTCDI-C_{13}

S'han fabricat transistors utilitzant una oblia de silici com a *gate*, l'òxid de silici com a dielèctric, el PTCDI-C_{13} com a semiconductor de tipus *n* i finalment or per a fer el contactes superiors. La longitud del canal era de 100 μm, mentre que la seva amplitud era de 600 μm. L'or fa un contacte òhmic amb el semiconductor que ha estat dipositat amb 10^{-4} Pa de pressió, un ritme de dipòsit de 0.5 Å/s i amb diferents temperatures: 30, 60, 90 i 120ºC. En els mateixos processos s'han dipositat capes de 200 nm sobre vidre per la caracterització amb rajos X. Amb l'increment de temperatura s'ha notat un increment d'intensitat dels pics de difracció típics del PTCDI-C_{13} i una disminució de la seva amplitud, portant a la conclusió que hi ha hagut un augment de la fase cristal·lina en el material.

La mesura de la característica de sortida dels dispositius ha mostrat el comportament típic d'un dispositiu amb canal de tipus *n*: acumulació de portadors de càrrega per tensions de *gate* positives. La mesura de la característica de transferència mesurada amb 10 V entre *drain* i *source* ha indicat que els dispositius operen en modalitat d'acumulació per tensions V_{GS} positives. A partir de les mesures s'ha calculat la mobilitat dels portadors en el semiconductor observant que hi ha un augment amb la temperatura de dipòsit del semiconductor al mateix temps que hi ha una disminució de la tensió llindar del dispositiu. La millora de la qualitat estructural observada en el semiconductor amb un augment de la seva temperatura de dipòsit va acompanyada amb d'una millora en les prestacions del dispositiu.

De les mesures de la característica de transferència amb diferents temperatures s'ha calculat l'energia d'activació del semiconductor i la densitat d'estats. S'han pogut evidenciar dos règims de

distribució dels estats en funció de l'energia, la qual cosa indica que la presència de cues de banda i d'estats localitzats, tal com havien indicat les mesures de PDS també.

A.2 Díodes de CuPc

Com a segon tipus de dispositiu s'han realitzat díodes utilitzant la ftalocianina de coure com a semiconductor. Aquest tipus de dispositiu es defineix com de tipus Schottky pel fet que el semiconductor orgànic fa contacte Schottky amb un dels dos elèctrodes i òhmic amb l'altre elèctrode.

S'han fabricat díodes dipositant la capa de CuPc sobre vidre recobert amb ITO, amb un ritme de dipòsit de 1 Å/s, un gruix de 700 nm i amb quatre temperatures del substrat: 30, 60 , 90 i 120ºC. Finalment els dispositius s'han acabat amb un contacte d'alumini, també evaporats tèrmicament en buit, amb una superfície d'1 mm^2. Al mateix temps s'han dipositat capes de CuPc sobre vidre per a les caracteritzacions per rajos X.

Les mesures de rajos X han indicat que amb l'increment de temperatura de dipòsit hi ha un augment de la fracció cristal·lina en el material, ja que els pics de difracció típics de la ftalocianina augmenten en intensitat i es tornen mes estrets. També s'han realitzat mesures de PDS que han permès determinar que les mostres dipositades a 30 i 60ºC tenen una absorció més baixa, sobretot en la regió sub-gap, la determinada pels defectes.

S'han caracteritzat elèctricament els dispositius evidenciant que les dipositades a 30 i 90ºC tenen les millors propietats rectificadores. Tanmateix la dipositada a 120ºC entre 0 i 0.5 V, en regim òhmic, té el corrent elèctric més alt degut probablement a la seva millor qualitat cristal·lina, com evidencien les mesures de rajos X. També s'ha controlat la resposta dels díodes amb llum il·luminant-los amb una potència d'1 sol. En general, els dispositius tenen una resposta molt baixa.